

LUMINOSITY AND MASS FUNCTIONS  
OF VERY YOUNG STELLAR CLUSTERS

By

AUGUST A. MUENCH

A DISSERTATION PRESENTED TO THE GRADUATE SCHOOL  
OF THE UNIVERSITY OF FLORIDA IN PARTIAL FULFILLMENT  
OF THE REQUIREMENTS FOR THE DEGREE OF  
DOCTOR OF PHILOSOPHY

UNIVERSITY OF FLORIDA

2002

Copyright 2002

by

August A. Muench

Let us content ourselves with the illusion of similarity, but in truth I tell you, Sir, if I may express myself in prophetic tones, the interesting thing about life has always been in the differences,

From *The History of the Siege of Lisbon* by José Saramago

This work is dedicated to Laura.

## ACKNOWLEDGMENTS

I would like to acknowledge a number of individuals and organizations that provided the direction, care, support and opportunity that have allowed me to enjoy and to research astronomy (in addition to completing this dissertation).

After calmly listening to my description of various observational cosmology projects in which I was interested, my dissertation advisor, Dr. Elizabeth Lada simply pointed out that she was not currently working on any such projects. She then proceeded to detail all the research that had constituted her career so far and the directions she wanted to take, listing project after project that was open to me were I interested. She has not stopped listing the avenues open to me and continues to offer me the chance to work on and lead projects and for this and for her guidance and support I am grateful.

Although I grew up on Tampa Bay and my father fishes commercially on the Bay, I have yet to finalize a good answer to the first question posed to me by Dr. Charles Lada on the tidal patterns in the Gulf of Mexico versus the Atlantic Ocean. Despite this delinquency, I have enjoyed trying to answer the innumerable other questions posed to me by him regarding the data, models and interpretations contained within this work and in our other projects. I have come to greatly appreciate the focus that Charlie and Elizabeth Lada employ when our attention turns to the lucid communication of our results through the words contained in our papers, and their excitement at the moment that implication raises its sometimes dangerous head.

I would like to thank the members of my dissertation committee at the University of Florida for reading, reviewing and providing their comments and questions on this work. I would also like to thank the members of my pre-doctoral committee at the

Center for Astrophysics, Drs. Alyssa Goodman and John Stauffer, who labored through my excessively long progress reports and who gave me consistent and fruitful advice. At the Department of Astronomy, I would like to offer my thanks to Dr. Stanley Dermott, Department Chair, who in fact made my career at the University of Florida possible and to Dr. Richard Elston for his suggestions and guidance in using the Monte Carlo technique. It is also without question that both the Radio and Geoastronomy Division at the Center for Astrophysics and the Department of Astronomy at the University of Florida have been gifted by administrators and program assistants such as Tom Mullen, Janice Douglas, and Ann Elton who with continuous and singular focus work toward creating a supportive environment in which to research our field.

I have also been granted good friends and collaborators such as João Alves, who was my office mate at the CfA. I thank him for sharing his boundless excitement for his work, and I look forward to further collaboration and friendship with him. My fellow WIRE survivor, Lori Allen, has been a wonderful friend to me, is greatly missed, and I wonder on a regular basis when will be our next chance to work together. To Lauren Jones, who has believed in me as a person and as an astronomer from the first time she saw me waiting in the main office between classes, I send my conviction that she has much to offer astronomy. I would like to thank Joanna Levine for her friendship and especially her support for me during this dissertation's end times and to both her and Carlos Roman for their assistance with the reduction of the IC 348 images. My friends and colleagues who are unlisted but who have put up with my spontaneous outbursts about Pluto and white dwarfs amaze me with their loyalty.

My parents, Gus and Betsy Muench and my brothers, Sam and Stephen, have given me their love, interest and support throughout these years. And to my wife and my love and my friend, Laura, I pray that I will find some word or deed that can contain and make clear my gratitude to her for her support as I trudged through this dissertation.

I was supported by the Smithsonian Predoctoral Fellowship program at the Harvard-Smithsonian Center for Astrophysics and as a substitute NASA Graduate Student Research Fellow (grant NTG5-50233). My work was also supported by a grant to Dr. Elizabeth Lada from the National Science Foundation (grant AST-9733367). There is no question in my mind that the success of any individual researcher sits level upon three legs: that of individual commitment, that of unabridged opportunity and that of continuous scientific interaction. All of these aspects were enabled for me by being a Predoctoral Fellow at the CfA.

I would like to extend my thanks to John Bally for permission to reproduce HST images of the proplyds in the Trapezium Cluster, and to Kevin Luhman for data in advance of publication. Portions of this work are based on photographic data obtained using The UK Schmidt Telescope. The UK Schmidt Telescope was operated by the Royal Observatory Edinburgh, with funding from the UK Science and Engineering Research Council, until 1988 June, and thereafter by the Anglo-Australian Observatory. Original plate material is copyright (c) the Royal Observatory Edinburgh and the Anglo-Australian Observatory. The plates were processed into the present compressed digital form with their permission. The Digitized Sky Survey was produced at the Space Telescope Science Institute under US Government grant NAG W-2166. This publication makes use of data products from the Two Micron All Sky Survey, which is a joint project of the University of Massachusetts and the Infrared Processing and Analysis Center/California Institute of Technology, funded by the National Aeronautics and Space Administration and the National Science Foundation. The data products were circa the 2nd Incremental release (March 2000). This document was typeset with the  $\LaTeX$  2 $\epsilon$  formatting system using the document class template ufthesis.cls (v2.0b) and written by Ron Smith (ufthesis@ufthesis.com) at the University of Florida. Any apparent success in the format of this document can almost certainly be attributed to Ron Smith's efforts for which I am grateful.

## TABLE OF CONTENTS

	<u>page</u>
ACKNOWLEDGMENTS . . . . .	iv
LIST OF TABLES . . . . .	x
LIST OF FIGURES . . . . .	xi
KEY TO ABBREVIATIONS . . . . .	xiv
KEY TO SYMBOLS . . . . .	xvi
ABSTRACT . . . . .	xvii
 CHAPTER	
1 INTRODUCTION . . . . .	1
2 MONTE CARLO MODELS OF YOUNG STELLAR POPULATIONS . . . . .	10
2.1 Monte Carlo-Based Population Synthesis Model . . . . .	10
2.2 Fundamental Cluster Parameters . . . . .	11
2.2.1 Initial Mass Function . . . . .	11
2.2.2 The Cluster’s Star-Forming History . . . . .	13
2.2.3 Theoretical Mass-Luminosity Relations . . . . .	14
2.3 Additional Cluster Characteristics and Model Inputs . . . . .	17
2.3.1 Reddening Properties . . . . .	18
2.3.2 Binary Fraction . . . . .	19
2.4 Model Outputs . . . . .	20
2.5 Numerical Experiments . . . . .	21
2.5.1 Different Pre-Main Sequence Evolutionary Models . . . . .	21
2.5.2 Star Formation History . . . . .	29
2.5.3 Initial Mass Function . . . . .	34
2.6 Discussion and an Example from the Literature . . . . .	36
2.6.1 Results and Implications of Numerical Experiments . . . . .	36
2.6.2 An Example from the Literature: The Trapezium Cluster . . . . .	37
2.7 Conclusions . . . . .	44
3 THE FAMOUS TRAPEZIUM CLUSTER IN ORION . . . . .	46
3.1 Near-Infrared Census . . . . .	47
3.1.1 Observations . . . . .	48
3.1.2 Data Reduction and Photometry . . . . .	52

3.1.3	Photometric Comparisons of Datasets	55
3.1.4	Astrometry and the Electronic Catalog	57
3.2	Trapezium Cluster K band Luminosity Function	59
3.2.1	Constructing Infrared Luminosity Function(s)	61
3.2.2	Defining a Complete Cluster KLF	64
3.2.3	Field Star Contamination to the KLF	67
3.3	Trapezium Cluster Initial Mass Function	70
3.3.1	Deriving Distributions of Reddening	70
3.3.2	Modeling the Trapezium Cluster KLF	76
3.3.3	Derived Trapezium Cluster IMF	83
3.4	Discussion	89
3.4.1	Structure of the Trapezium KLF and IMF	89
3.4.2	Sensitivity of Results to Theoretical PMS Models	92
3.4.3	Comparison of IR-Based Trapezium IMFs	97
3.5	Conclusions	101
4	THE YOUNG CLUSTER IC 348 IN PERSEUS	103
4.1	Wide-Field Near-Infrared Images of IC 348	105
4.1.1	FLAMINGOS Observations	105
4.1.2	Infrared Census	108
4.1.3	Cluster Structure	113
4.1.4	Cluster Reddening Properties	119
4.2	Infrared Luminosity Functions of IC 348	123
4.2.1	Constructing Infrared Luminosity Functions	123
4.2.2	Field-Star Correction to the Cluster KLF(s)	124
4.3	Initial Mass Function of IC 348	128
4.3.1	Star Forming History of IC 348	128
4.3.2	Cluster Distance and the Mass-Luminosity Relation	129
4.3.3	Other Modeling Parameters: Reddening and Binaries	133
4.3.4	Modeling the IC 348 Differential KLF(s)	134
4.4	Discussion	138
4.4.1	The KLFs and IMFs of IC 348 and the Trapezium	138
4.4.2	Radial Variation of the IC 348 IMF	142
4.5	Conclusions	146
5	THE YOUNG OPEN CLUSTER NGC 2362	148
5.1	La Silla Observations of NGC 2362	150
5.2	2MASS Observations of NGC 2362	152
5.2.1	Spatial Structure of NGC 2362	152
5.2.2	Source Reddening for NGC 2362	155
5.3	The NGC 2362 Cluster KLF	157
5.3.1	Empirical Field Star KLF	157
5.3.2	NGC 2362 Differential KLF(s)	159
5.4	Comparison to other Young Cluster KLFs	160

5.5	Modeling the NGC 2362 KLF . . . . .	163
5.5.1	Deriving a Mean Age Using a Fixed IMF . . . . .	163
5.5.2	Simultaneous Derivation of a Cluster's Age <i>and</i> its IMF . . . . .	167
5.5.3	NGC 2362 IMF Derived Using a Fixed SFH . . . . .	169
5.6	Discussion . . . . .	172
5.6.1	Age and IMF of NGC2362 . . . . .	172
5.6.2	Age and Spatial Structure of NGC 2362 . . . . .	174
5.7	Conclusions . . . . .	176
6	CIRCUMSTELLAR DISKS AROUND YOUNG BROWN DWARFS . . . . .	178
6.1	Trapezium Brown Dwarfs with Infrared Excess . . . . .	180
6.2	Discussion and Implications . . . . .	184
7	DISCUSSION ON THE STRUCTURE OF THE IMF . . . . .	189
7.1	Young Clusters and the Global IMF . . . . .	189
7.2	Secondary Sub-Stellar Peak in the Cluster LFs . . . . .	192
7.3	New Clues to the Origin of Stars and Brown Dwarfs . . . . .	196
8	CONCLUSIONS AND FUTURE WORK . . . . .	198
8.1	On the Luminosity Functions of Very Young Stellar Clusters . . . . .	198
8.2	On the Initial Mass Functions of Very Young Stellar Clusters . . . . .	200
8.3	Future Work . . . . .	202
8.3.1	Continued Study of the IMF in Young Clusters . . . . .	202
8.3.2	Structure of Young Open Clusters . . . . .	203
8.3.3	Disks around Young Brown Dwarfs . . . . .	204
8.3.4	Model Improvements . . . . .	210
APPENDIX		
A	TABULATED BOLOMETRIC CORRECTIONS . . . . .	211
B	DISTANCE TO THE TRAPEZIUM CLUSTER . . . . .	217
C	SUMMARY OF POPULATION SYNTHESIS FORTRAN CODE . . . . .	222
C.1	FORTRAN Code . . . . .	222
C.1.1	The Control Program . . . . .	222
C.1.2	Rejection Functions . . . . .	226
C.1.3	The FORTRAN Sub-routines . . . . .	228
C.2	Input Parameters and Output Files . . . . .	231
REFERENCES . . . . .		
238		
BIOGRAPHICAL SKETCH . . . . .		
247		

## LIST OF TABLES

<u>Table</u>	<u>page</u>
2-1 Evolutionary models used in numerical experiments . . . . .	23
2-2 Cluster IMF derived from the literature Trapezium KLF . . . . .	40
3-1 Summary of infrared observations of the Trapezium cluster . . . . .	49
3-2 FLWO-NTT near-infrared catalog . . . . .	60
3-3 Three power-law Trapezium IMF parameters and errors . . . . .	79
3-4 Three power-law Trapezium sub-stellar IMF . . . . .	86
3-5 Evolutionary models used to compare M-L relations . . . . .	94
3-6 Comparison of published Trapezium IMFs based on IR photometry . . . . .	100
4-1 Summary of FLAMINGOS observations of IC 348 . . . . .	106
4-2 Comparison of IC 348 photometry to 2MASS catalog. . . . .	109
4-3 IC 348 power-law IMFs derived from model KLFs . . . . .	137
5-1 Age dependence of the IMF slope in NGC 2362 . . . . .	169
A-1 Table of bolometric corrections . . . . .	214
A-1 Table of bolometric corrections . . . . .	215
A-1 Table of bolometric corrections . . . . .	216
B-1 Summary of published distances to the Orion 1d association . . . . .	221

## LIST OF FIGURES

<u>Figure</u>	<u>page</u>
2–1 Example mass functions used in models . . . . .	12
2–2 Definition of the cluster’s star-forming history . . . . .	13
2–3 Theoretical Hertzsprung-Russell diagram . . . . .	17
2–4 Model KLFs: varying physical inputs to evolutionary models . . . . .	24
2–5 Model KLFs: comparing DM94 and DM97 . . . . .	26
2–6 Model KLFs: varying the initial deuterium abundance . . . . .	28
2–7 Model KLFs: truncations in the mass-luminosity relation . . . . .	30
2–8 Model KLFs: varying the star forming history ( $\tau, \Delta\tau$ ) . . . . .	31
2–9 Evolution of mean K magnitude with cluster age . . . . .	32
2–10 Model KLFs: varying the cluster’s age spread . . . . .	33
2–11 Model KLFs: varying the initial mass function . . . . .	35
2–12 Application of models to literature data . . . . .	39
3–1 Comparison of recent Trapezium cluster IR surveys . . . . .	48
3–2 Infrared color composite image of the Trapezium . . . . .	52
3–3 Trapezium cluster: raw near-infrared luminosity functions . . . . .	62
3–4 Trapezium cluster: construction of observed control field KLF . . . . .	63
3–5 Trapezium cluster: deriving $M - A_V$ completeness limits . . . . .	65
3–6 Trapezium cluster: testing contribution of reddened field star KLFs . . . . .	68
3–7 Infrared colors of Trapezium sources . . . . .	71
3–8 Trapezium cluster: extinction probability distribution function . . . . .	73
3–9 Effects of extinction on model cluster LFs . . . . .	74
3–10 Trapezium cluster: infrared excess probability distribution function . . . . .	75
3–11 Trapezium cluster: best-fitting model KLFs and 3 power-law IMFs . . . . .	78

3–12 Trapezium cluster: $\chi^2$ confidence intervals for IMF parameters . . . . .	81
3–13 Trapezium cluster: best fit model KLF to secondary KLF peak . . . . .	83
3–14 Trapezium cluster: overall derived IMF . . . . .	84
3–15 Trapezium cluster: a closer look at the sub-stellar IMF . . . . .	87
3–16 Trapezium cluster: a secondary peak in Trapezium substellar IMF . . . . .	88
3–17 Comparison of theoretical mass-luminosity relations . . . . .	96
3–18 Comparison of theoretical $M$ - $T_{eff}$ -spectral type relations . . . . .	97
3–19 Comparison of trapezium IMFs from IR photometry . . . . .	98
4–1 Infrared color composite image of IC 348 . . . . .	105
4–2 Near-infrared color-magnitude diagrams of IC 348 . . . . .	111
4–3 Infrared color-color diagram of IC 348 . . . . .	112
4–4 Radial profile of the IC 348 cluster . . . . .	115
4–5 Spatial distribution of sources in IC 348 . . . . .	117
4–6 Surface density profile of the IC 348 cluster . . . . .	118
4–7 Extinction maps of the IC 348 FLAMINGOS region . . . . .	120
4–8 Distributions of reddening for IC 348 . . . . .	122
4–9 Raw infrared luminosity functions for IC 348 . . . . .	124
4–10 K-band luminosity functions by sub-region for IC 348 . . . . .	125
4–11 Field star correction to cluster KLFs in IC 348 . . . . .	126
4–12 Differential KLFs for IC 348 . . . . .	127
4–13 Star-forming history of IC 348 . . . . .	130
4–14 Theoretical mass-luminosity relations of IC 348 . . . . .	131
4–15 Modeling the IC 348 KLF: cluster sub-regions . . . . .	135
4–16 Modeling the IC 348 KLF: the composite cluster . . . . .	138
4–17 Comparison of IC 348 and Trapezium KLFs . . . . .	139
4–18 Radial variation in the IC 348 IMF . . . . .	144
5–1 Digitalized sky survey image of NGC 2362 . . . . .	150

5-2	Source distribution of NGC 2362 from 2MASS . . . . .	153
5-3	Radial profiles of NGC 2362 . . . . .	154
5-4	Infrared color-color diagrams for NGC 2362 . . . . .	156
5-5	Field star and cluster KLFs of NGC 2362 . . . . .	158
5-6	Differential KLF(s) of NGC 2362 . . . . .	159
5-7	Comparing the cluster KLFs of NGC 2362, the Trapezium and IC 348 . . . . .	161
5-8	Mean age of NGC 2362 derived from the cluster KLF . . . . .	164
5-9	Model KLF at 5 Myr with Trapezium IMF fit to NGC 2362 . . . . .	165
5-10	Dependence of the NGC 2362 IMF slope on mean age . . . . .	168
5-11	Best fit model KLFs to the NGC 2362 KLF . . . . .	170
5-12	Mass Function of NGC 2362 . . . . .	171
6-1	Selecting candidate brown dwarfs in the Trapezium . . . . .	180
6-2	Trapezium brown dwarfs with near-infrared excess . . . . .	183
6-3	Brown dwarf proplyds . . . . .	185
6-4	L-band observations of brown dwarf candidates . . . . .	187
7-1	Comparison of Trapezium and $\sigma$ Ori IMF . . . . .	193
8-1	Comparison of 2MASS and FLAMINGOS imaging sensitivity . . . . .	206
8-2	Imaging map of the Perseus GMC with FLAMINGOS . . . . .	208
C-1	Model input file: basic cluster and IMF parameters . . . . .	232
C-2	Model input file: relative frequency probability distribution files . . . . .	233
C-3	Model input file: pointers and parameters for evolutionary tracks . . . . .	234
C-4	Model input file: output parameters . . . . .	235
C-5	Example batch file . . . . .	236
C-6	Example(s) of output file headers . . . . .	237

## KEY TO ABBREVIATIONS

2MASS	Two Micron All Sky Survey
AU	Astronomical Unit
CTTS	Classical T-Tauri Stars
ESO	European Southern Observatory
FLAMINGOS	FLoridA Multi-object Imaging Near-IR Grism Observational Spectrometer
FLWO	Fred Lawrence Whipple Observatory
FWHM	Full Width at Half Maximum
GMC	Giant Molecular Cloud
H-R	Hertzsprung-Russell (Diagram)
HBL	Hydrogen Burning Limit
IDL	Interactive Data Language
IMF	Initial Mass Function
IRAF	Image Reduction and Analysis Facility
KLF	K band Luminosity Function
LF	Luminosity Function
LMS	Luminosity Maximum Spike
M-L	Mass-Luminosity (Relation)
NIR	Near-InfraRed
NTT	New Technology Telescope
ONC	Orion Nebula Cluster
PDF	Probability Distribution Function
PMS	Pre-Main Sequence

PSF	Point Spread Function
SFH	Star Formation History
SIRTF	Space InfraRed Telescope Facility
ZAMS	Zero Age Main Sequence

## KEY TO SYMBOLS

$M_\lambda$	Absolute passband magnitude
$m_\lambda$	Apparent passband magnitude
$A_V$	Magnitudes of visual extinction
$BC_\lambda$	Bolometric correction to passband magnitude (K)
$\Delta\tau$	Cluster's age spread (in millions of years)
$f_{bin}$	Binary fraction
$L_\odot$	Units of solar luminosity
$m_j$	Mass breakpoints in a power-law mass function
$M_{Jup}$	Units of a Jupiter mass
$M_\odot$	Units of solar mass
$\Gamma_i$	Index of a power-law mass function
$\tau$	Cluster's mean age (in millions of years)
$T_{eff}$	Effective surface temperature (K)

Abstract of Dissertation Presented to the Graduate School  
of the University of Florida in Partial Fulfillment of the  
Requirements for the Degree of Doctor of Philosophy

LUMINOSITY AND MASS FUNCTIONS  
OF VERY YOUNG STELLAR CLUSTERS

By

August A. Muench

December 2002

Chair: Elizabeth A. Lada  
Major Department: Astronomy

We now know that the star formation process results in freely-floating objects with masses spanning nearly four orders of magnitude. However, both the distribution of these objects' masses at birth and the precise physics responsible for the shape of this initial mass function are poorly known and can be improved upon by focusing on very young star clusters just emerging from their parental molecular clouds. In this dissertation I have investigated the usefulness of the observed luminosity function of a very young cluster as a tool for deriving that cluster's underlying mass function. I find that a cluster's luminosity function is an excellent probe of the initial mass function over the entire range of stellar and substellar mass and can be utilized to acquire the statistics necessary for testing the hypothesis of a universal mass function.

To study the luminosity and mass functions of such clusters I developed a Monte Carlo based population synthesis algorithm applicable to pre-main sequence stars. Using this algorithm I performed numerical experiments testing the sensitivity of model luminosity functions to changes in fundamental cluster parameters. After showing that the luminosity function is intrinsically most sensitive to the form of

the underlying mass function, I studied three young clusters, NGC 2362, IC 348 and the Trapezium, and performed deep near-infrared surveys to construct their K-band luminosity functions. Using the model luminosity function algorithm, I derived each cluster's underlying mass function and found them to be remarkably similar, with all forming broad peaks at subsolar masses. Where these census are sufficiently deep I find that the mass function turns over and declines in number throughout the substellar regime but appears to contain structure near the deuterium-burning limit. Regardless, I find that brown dwarfs do not dominate stars either by number or total mass. Lastly, I use a statistically significant sample of candidate brown dwarfs to show that these objects appear as likely to have been born with circumstellar disks as stars. Combining this finding with the continuity of the shape of the initial mass function across numerous environments suggests that a single physical mechanism may dominate the star formation process.

## CHAPTER 1 INTRODUCTION

Little is known about the similarities or differences between the star formation process that created the first generation of stars in the universe and the process that is forming stars and brown dwarfs in nearby stellar nurseries today. A long standing hypothesis, for example, is that the birth of primordial stars was heavily influenced by the low metallicity of the early universe, and would have preferentially yielded stars more massive than those born today (Yoneyama, 1972; Palla et al., 1983; Bromm et al., 2002). Therefore, one important diagnostic for studying any evolution of the star formation process is the statistical distribution of stellar masses at birth, or the stellar initial mass function<sup>1</sup>. The derivation and comparison of the mass functions for stars in old globular clusters, in the galactic field, in intermediate-age open clusters such as the Pleiades and in extremely young clusters embedded in nearby molecular clouds might reveal similarities or differences that would test the notion of an universal mass function (see the discussion of Kroupa, 2002) and perhaps a dominant star formation process, or that could bring about a better understanding of its stochastic nature (Elmegreen & Mathieu, 1983; Zinnecker, 1984; Adams & Fatuzzo, 1996; Elmegreen,

---

<sup>1</sup> In general, we will refer to the stellar initial mass function as the number of stars per logarithmic unit of mass per unit volume at birth. The choice of logarithmic mass units has both an observational and a theoretical basis. Beginning with Eddington (1924), it has been shown both empirically and theoretically that the luminosity of a main-sequence star scales as a power-law function of the star's mass, e.g.,  $L = M^{3.5}$  over most of the range of stellar mass. Since the standard unit of observational astronomy, the magnitude, is a logarithmic scaling of stellar flux, there exists, therefore, a linear relationship between a star's observed magnitude and its logarithmic mass.

1997). If the formation of stars is a stochastic process and is heavily dependent upon numerous parameters other than time, then the problem becomes one of studying the stellar initial mass function in a variety of physical environments. Because the initial mass function (IMF) is an intrinsically statistical quantity, all such comparisons require numerous samplings of the star formation process, in turn, requiring tools that can probe the stellar mass function over a large volume of space and time.

Since very young, newly formed star clusters are found in environments ranging from the nearby Orion molecular clouds (Lada, 1990) to very massive clusters in the turbulent Galactic Center (Figer et al., 1999), they may provide the ideal laboratory for testing whether the IMF is universal or stochastic. Further, there are a number of other reasons why young star clusters may be particularly valuable for mass function studies. For example, a simple photometric census of the members of a young embedded cluster yields a statistically significant population of stars and brown dwarfs (i.e., substellar – non-hydrogen-burning stars) sharing a common heritage (e.g., age, metallicity, birth environment). Perhaps more important, such a census is relatively complete because very young clusters have not lost significant numbers of members to either dynamical or stellar evolution. Hence, the observed mass function is the cluster's *initial* mass function. Because the youngest star clusters are still embedded within their natal molecular cloud, a near-infrared ( $1 - 3\mu\text{m}$ ) photometric census is often necessary to identify a complete cluster population. One direct product of such an infrared census is the young cluster's stellar infrared luminosity function, which can be used as a tool for studying a cluster's initial mass function. This may be a particularly effective tool for studying the low-mass end of a cluster's mass function because infrared luminosities are relatively easy to derive for young brown dwarfs in these clusters since such intrinsically red substellar sources are at brighter luminosities than at any subsequent point in their evolution. Further, the development of large format imaging arrays sensitive to near-infrared wavelengths has made it possible to obtain

statistically significant and complete samplings of the near-infrared luminosity functions of very young embedded clusters. These recent increases in sensitivity permit not only the study of the substellar mass functions of nearby clusters, but also the construction of infrared luminosity functions for distant young clusters even when little or nothing may be learned about these clusters from spectroscopic measurements. Thus, modern infrared cameras on even modest sized telescopes can efficiently survey numerous young clusters, deriving infrared luminosities for complete populations, and, potentially sampling the initial mass function of the current epoch over a relatively large volume of the local galaxy.

The observed luminosity function for a cluster of stars is the product of the underlying mass function of the cluster members and the derivative of the appropriate mass-luminosity relation:

$$\frac{dN}{dL} = \frac{dN}{d \log M} \times \frac{d \log M}{dL} \quad (1.1)$$

However, until a cluster reaches an age of  $\sim 1$  billion years, some fraction of the stars in the cluster will be in their “pre-main sequence” phase, meaning they have not yet begun to fuse hydrogen in their core. Since brown dwarfs never achieve nuclear burning, these cluster members will never reach the main sequence and will be contracting, cooling and becoming fainter for their entire existence. Thus, the radiant luminosity of a brown dwarf or a pre-main sequence star is derived from its gravitational contraction energy, and the mass-luminosity relation appropriate for these objects is a function of time, hence:

$$\frac{d \log M}{dL} = \frac{d \log M}{dL}(\tau) \quad (1.2)$$

For the very young clusters we will be studying in this work (ages,  $\tau < 10$  Myr), nearly all of the members will be in a pre-main sequence phase. Further, the timescale for assembling a star cluster is an appreciable fraction of the cluster’s mean age during

this period. These facts mean that the derivation of a young cluster’s underlying mass function from its luminosity function is sensitive to the history of star formation in the cluster. Additionally, the time-dependent mass-luminosity relation(s) used to convert between a cluster’s luminosity and mass functions is poorly known. Since there are very few meaningful empirical constraints on the form of the pre-main sequence mass-luminosity relation, we must rely upon theoretical evolutionary models of young stars when estimating this quantity. Finally, the predictions of these evolutionary models vary depending upon how they were computed. Considering these complicated factors, the most common approach to studying the luminosity functions of young star clusters has been to numerically integrate these three fundamental quantities, i.e., the initial mass function, the star-forming history and the theoretical mass-luminosity relation, into synthetic luminosity functions and to use these model luminosity functions to interpret the observational data.

Various groups have modeled the luminosity functions of young clusters using realistic stellar mass functions and appropriate mass-luminosity relationships (e.g., [Zinnecker et al., 1993](#); [Strom et al., 1993](#); [Fletcher & Stahler, 1994a](#); [Lada & Lada, 1995](#); [Megeath, 1996](#)). [Zinnecker et al. \(1993\)](#) were the first to present model K band ( $2.2\mu\text{m}$ ) luminosity functions for very young clusters. For their models they adopted a “coeval” star formation history in which all the stars were formed at a single instant of time. Moreover, they assumed black-body radiation to derive bolometric corrections and assumed a single form for the stellar mass function. Consequently, their models were not very realistic, and they did not attempt to fit or directly compare their models to observed cluster luminosity functions.

[Lada & Lada \(1995, hereafter, LL95\)](#) improved on this work by developing evolutionary models for the K band luminosity functions (KLF) of young clusters ranging in age from  $10^6 < \tau < 10^7$  yr, using empirically determined bolometric corrections and allowing for non-coeval or continuous star formation in the clusters. Moreover,

they directly compared their models to observed infrared luminosity functions of young clusters. However, similar to Zinnecker et al., Lada & Lada assumed a single underlying initial mass function for the stars (i.e., the Miller & Scalo, 1979, field star initial mass function), while employing a single set of the published pre-main sequence evolutionary tracks from (D’Antona & Mazzitelli, 1994). Additional luminosity function models were calculated by Strom et al. (1993) and Kenyon & Hartmann (1995), both of whom compared their models to the de-reddened J ( $1.1\mu\text{m}$ ) and K band luminosity functions of young stars. In these works, model luminosity functions were primarily used as probes of a cluster’s age, but were also employed to test the similarity of the clusters’ underlying initial mass function to that for the field stars. All of these model luminosity functions were constructed for stars with masses between  $0.1$  and  $20 M_{\odot}$ , since the existing evolutionary tracks did not extend into the regime of brown dwarfs ( $M < 0.08 M_{\odot}$ ). Thus, many of their results are only valid as long as there are no, or at least very few, brown dwarfs in these clusters.

It is somewhat difficult to evaluate the success of these early modeling works in developing the luminosity function technique as a tool for deriving the initial mass functions of embedded clusters. First, these models were fundamentally limited by the lack of consistent evolutionary models that included young brown dwarfs. Second, the lack of independent estimates for the star-forming histories of the clusters studied meant that these authors approached the problem needing to constrain both the age and mass function; they frequently constructed their models using a single mass function equivalent to that for field stars. Further, their models were rarely applied *directly* to the observations, instead requiring that the actual data be initially corrected for various observational effects such as reddening. Thus, these efforts were never intended to provide comprehensive models of real data such as one might expect from a true population-synthesis model. In addition, when the models were fit to the data, error estimates or other quantification of the usefulness of the luminosity function method

were not calculated, making it difficult to draw conclusions about the accuracy of this method. In part due to the limitations of these early models and partially resulting from the approach taken by these original authors, the luminosity function method has not yet been used as a tool for deriving and for comparing the initial mass functions of a series of young clusters.

Fortunately, technical improvements in some of these areas have recently been made. For example, evolutionary sequences have been calculated for brown dwarfs with masses as small as that of the planet Jupiter ( $M_{Jup}$ ). In addition, improved age estimates for several clusters such as the Trapezium (Hillenbrand, 1997) and IC 348 (Herbig, 1998) have been made by examining brighter members using either optical spectra or the optical color-magnitude diagram. In light of these technical advances and the constraints placed upon the ages of some nearby young clusters, we undertook a systematic study to determine the usefulness of a young cluster's near-infrared luminosity function as a tool for studying and deriving that cluster's initial mass function.

Based upon the success of prior approaches to studying the luminosity function of a young cluster, we formulated our study using three principles: 1) Our study would concentrate on the products of simple near-infrared surveys of young clusters. 2) We would employ a set of model luminosity functions to interpret the products of these near-infrared surveys. 3) We would study multiple young clusters to test, develop and expand our method(s). From these principles, we developed a series of specific goals:

- Creation of a population-synthesis algorithm for young star clusters that includes all of the fundamental and observational characteristics relevant to the products of a near-infrared survey.
- Design of a series of numerical experiments to systematically test the sensitivity of model luminosity functions to changes in the three fundamental quantities governing the form of the cluster luminosity function (e.g., the star-forming history, initial mass function, and theoretical mass-luminosity relation).

- Construction of the near-infrared luminosity functions of a series of young clusters from deep multi-wavelength near-infrared surveys of these clusters.
- Derivation of the initial mass functions for these clusters through the application of our population-synthesis models to the cluster luminosity functions.
- Comparison of our results to those found via other methods for studying the mass function(s) of young clusters.
- Examination of the hypothesis of a “universal initial mass function” for young clusters by comparing the luminosity and mass functions derived for the clusters in this study.

We accomplished these goals by focusing our efforts in three distinct ways. First, we developed a flexible, Monte Carlo-based population-synthesis algorithm for simulating the observations of young clusters and for creating model luminosity functions that could be applied to cluster data. The second focus of our research has been a series of deep near-infrared surveys of three young clusters, the construction of the infrared luminosity functions for these clusters, and the derivation of these cluster’s mass functions. The third focus of this work is a discussion of evidence that a single process dominates the formation of stars across the mass spectrum down to very small masses (a few times the mass of the planet Jupiter). In summary, we find that a cluster’s near-infrared luminosity function is an excellent probe of the initial mass function of a very young cluster, and that the combination of deep near-infrared surveys with model luminosity functions can be used to accurately derive the initial mass function down to and below the deuterium-burning limit in young nearby star clusters. Further, the evidence that the IMF(s) we derive from modeling the cluster luminosity function are robust relative to other methods suggests that KLF modeling can be applied to a much larger sample of young clusters over a considerable volume of the local galaxy, providing the statistics necessary for establishing the degree of uniformity of the initial mass function through (local) space and time.

We briefly summarize the structure of this work. In Chapter 2 we develop our Monte Carlo based population-synthesis algorithm and use this algorithm to test the theoretical sensitivity of a cluster’s luminosity function to changes in such parameters as age and initial mass function. We then apply these models to the luminosity function for a young cluster constructed from literature data. In Chapters 3 and 4 we describe detailed studies of the luminosity and mass functions for the young Trapezium and IC 348 clusters using deep near-infrared surveys. Blaauw (1964) first compared these two clusters as part of his discussion of OB associations and subsidiary young clusters: “Two very interesting clusters with a different character do, however, occur: the Trapezium Cluster in I Orion, and the cluster near  $\alpha$  Persei in II Per [IC 348]. Their dimensions are much smaller than those of ordinary clusters, and both are of recent origin.” In our study of these nearby clusters, we develop empirical recipes for including reddening into our population-synthesis models and for statistically correcting the observed cluster luminosity function to account for the contamination of our observations by non-member field stars. We then apply our method to the distant open cluster, NGC 2362, in Chapter 5 and examine the usefulness of our method when little is known about a cluster’s age or age spread. In Chapter 6 we present observational evidence for the existence of circumstellar disks around brown dwarfs and discuss how the continuity of disks around young stars and brown dwarfs points towards a common origin for both. We compare the initial mass functions we have derived for these three clusters, and examine the hypothesis for an universal mass function for young clusters in Chapter 7. Here we combine the evidence of a common origin for stars and brown dwarfs and the continuity of the mass function across a number of clusters and environments to discuss what processes might dominate the formation of stars and brown dwarfs. After summarizing our findings in Chapter 8 we briefly detail additional future work that will focus on the new questions raised by this study. We reserve a number of the parts of our study to the appendices. Here we engage in a

brief discussion of the distance to the Trapezium Cluster, and list minor details of our modeling algorithm, including our tabulation of empirical bolometric corrections and descriptions of the computer code used in our population-synthesis algorithm.

## CHAPTER 2 MONTE CARLO MODELS OF YOUNG STELLAR POPULATIONS

### 2.1 Monte Carlo-Based Population Synthesis Model

For use in the interpretation of infrared luminosity functions of young stellar clusters, we created a Monte Carlo-based population synthesis algorithm for pre-main sequence stars. The underlying principle of our population synthesis model is the treatment of the fundamental cluster properties as probability distribution functions that are sampled and integrated using a Monte Carlo rejection method algorithm. Thus, the algorithm was designed to create a synthetic star cluster with members whose ages and masses are drawn from a specified star-forming history (SFH) and underlying initial mass function (IMF). Each synthetic star's mass and age was converted to observable quantities using mass-luminosity (M-L) relations interpolated from a set of theoretical evolutionary models. Additional properties such as reddening due to interstellar extinction or by excess flux from circumstellar disks were also assigned to each synthetic star by using probability distribution functions, while other parameters such as distance and binary fraction were fixed to specific values for the entire cluster. Further, our use of a Monte Carlo formulation also allows us to run multiple numerical simulations of a model cluster, thus giving us a statistical lens to use when comparing our models to real clusters, which typically contain between 100 and 1000 members.

In Sections 2.2 and 2.3, we describe each of the cluster parameters and how it was implemented into our models before detailing a series of numerical experiments in Section 2.5 aimed at testing the sensitivity of a model cluster's luminosity function (LF) to changes in the underlying cluster parameters. In Section 2.6 we discuss the results of these experiments and illustrate the effectiveness of KLF modeling for constraining a cluster's IMF by applying our technique to data taken from the literature

for the famous Trapezium Cluster in Orion. In Section C.1 we briefly detail each of the FORTRAN subroutines that were written to implement this algorithm.

## 2.2 Fundamental Cluster Parameters

### 2.2.1 Initial Mass Function

In our standard model, stars can have masses between 80 and  $0.02 M_{\odot}$ , limits set by the range of evolutionary models available for very high-mass O stars and very low mass brown dwarfs and giant planets. We parameterized the underlying cluster initial mass function with a number of different analytical forms. Throughout this work, we refer to the initial mass function as the frequency of stars per unit *log mass* per unit volume. Since we may suppose that a cluster represents a single star formation event, then there is no purpose in integrating this function over space volume.

A simple power-law function is the most common parameterization of the IMF and that originally used by [Salpeter \(1955\)](#), e.g.,

$$\xi(\log(\frac{M}{M_{\odot}})) = c1 * M^{\Gamma}, \quad (2.1)$$

where  $c1$  is a normalization constant, and  $\Gamma$  is the power-law index. In this form, [Salpeter](#) found that the initial mass function for stars in the field had  $\Gamma = -1.35$  over the mass range from 1 to  $10 M_{\odot}$ . Our standard parameterization of the underlying cluster IMF consisted of power-law segments,  $\Gamma_i$ , connected at break masses,  $m_j$ . For example, for masses between our upper mass limit and the first mass break  $m_1$ , the IMF is described as a power-law with index,  $\Gamma_1$ , and from  $m_1$  to  $m_2$ , the IMF has a power-law index,  $\Gamma_2$ , etc. Cluster IMFs could have as many as five (5) independent power-law segments.

We also used the log-normal distribution as a functional form of the IMF, e.g.,

$$\xi(\log(\frac{M}{M_{\odot}})) = c1 * \exp(-c2 * (\log(\frac{M}{M_{\odot}}) - c3)^2), \quad (2.2)$$

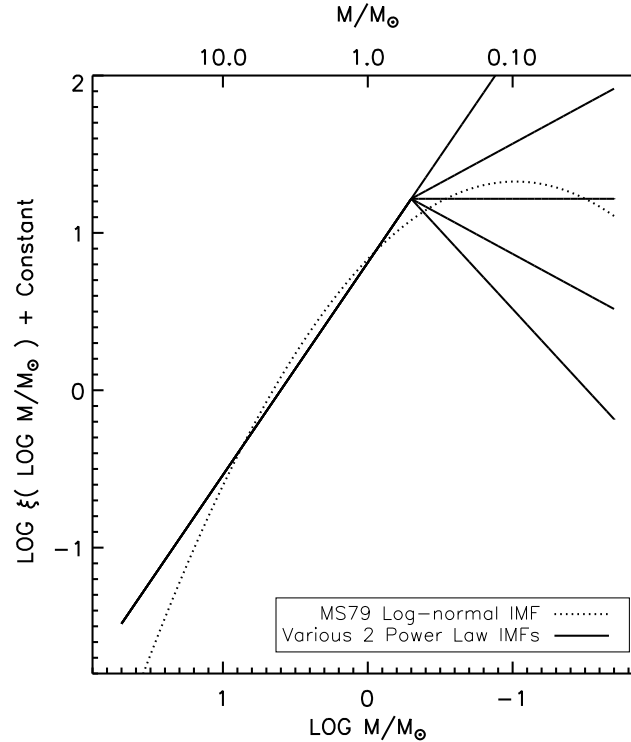


Figure 2–1: Example mass functions used in models. The log-normal form follows the parameterization of [Miller & Scalo \(1979\)](#) and is extended to the lowest masses. Standard two (2) power-law IMFs are shown where the high-mass IMF slope,  $\Gamma_1$ , equals -1.35 (equivalent to [Salpeter \(1955\)](#)) and then breaks at a mass,  $m_1$ , equal to  $0.5M_{\odot}$ . Below the break mass, the IMF is governed by a low mass slope,  $\Gamma_2$ , for which we show five different values: -1.35, -0.40, 0.00, +0.40, and +1.0.

where  $c_1$  is a normalization constant,  $c_2$  equals  $1/(2\log(\sigma)^2)$ ,  $c_3$  equals  $\overline{\log(\frac{M}{M_{\odot}})}$  or the mean log mass of the distribution and  $\sigma$  is the variance of this mean.

Figure 2–1 illustrates these mass function parameterizations. The mean and variance of the log-normal IMF shown correspond to the field star mass function given by [Miller & Scalo \(1979, hereafter, MS79\)](#), having constants of  $c_2 = 1.09$  and  $c_3 = -1.02$  or a mean mass of  $0.0955 M_{\odot}$ <sup>1</sup>. The example two power-law IMFs shown in Figure 2–1 have  $\Gamma_1 = -1.35$ ,  $m_1 = 0.5 M_{\odot}$  and  $\Gamma_2$  varying from -1.35 to +1.0.

<sup>1</sup> This set of log-normal parameters corresponds to the [MS79](#) derivation that used a maximum age of the galactic disk equal to 12 Gyr.

### 2.2.2 The Cluster’s Star-Forming History

For most of the models presented in this work, we assumed a constant star formation rate during the formation of a young cluster. We adopt this characterization partially because it is the simplest such model, and partially because the precision of observations which suggest that a cluster’s SFH is episodic or accelerating (Palla & Stahler, 2000) is certain to be strongly modified by intrinsic errors that would lead to exaggerated star-forming histories (Kenyon & Hartmann, 1990; Hartmann, 2001). Further, we assumed that there is no correlation between mass of a cluster member and when it was formed in the cluster.

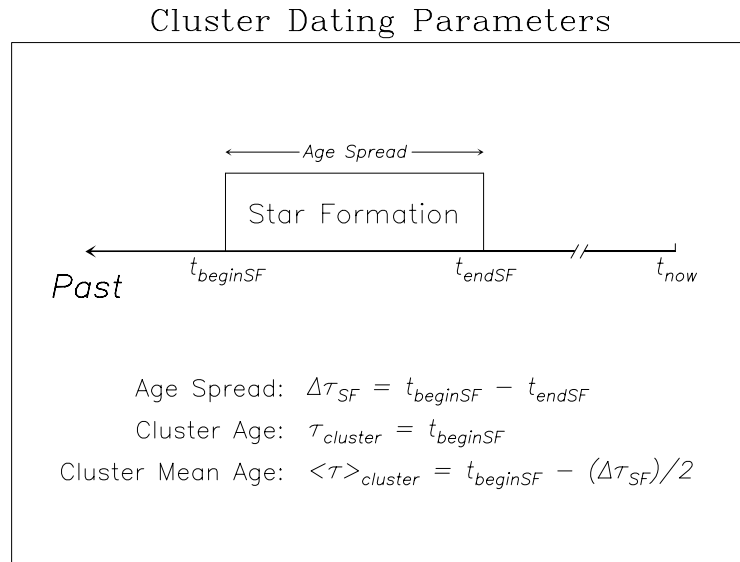


Figure 2–2: Definition of the cluster’s star-forming history. The cluster’s mean age,  $\tau$ , in this simple model is equivalent to the average of the ages of the oldest and youngest stars, assuming a constant star formation rate.

Therefore, we parameterized the SFH using a “mean age”,  $\tau$ , and an “age spread,”  $\Delta\tau$ . For example, a coeval cluster will have no age spread and  $\Delta\tau/\tau = 0.0$ . A cluster with the largest possible age spread would have  $\Delta\tau/\tau = 2.0$  with star formation starting  $2 \times \tau$  years ago and continuing to the present. Figure 2–2 illustrates these definitions. We note that these definitions of the cluster’s star-forming history are different than those used in the models of LL95 and Kenyon & Hartmann (1995). For

these works, the age of the cluster referred to the total timespan since star formation began, which is also the age of the oldest cluster members. Thus, for constant star-forming histories, their “age” would correspond to the “age spread” of our SFH and it would also be equal to twice our derived “mean age.” Our standard model SFH, therefore, approximates any real SFH to first order by using the most common age of the members and a rough age spread. The requirement of a constant star formation rate, however, is not a pre-requisite of our models, and any toy or empirical distribution of age can be used to draw ages for a synthetic cluster.

### 2.2.3 Theoretical Mass-Luminosity Relations

The mass-luminosity relation appropriate for converting the synthetic stars’ masses into observable luminosity is dependent on the evolutionary status of the star. For all the clusters considered here, the youngest ( $1 - 5 \times 10^5$  years) and most massive cluster members ( $M > 5 M_{\odot}$ ) will have already contracted on to the Zero Age Main Sequence (ZAMS) (Palla & Stahler, 1990). For these O and B type members, we converted their mass to bolometric luminosity and effective temperature using a theoretical ZAMS derived from Schaller et al. (1992). No post-main sequence evolution is included for the high and intermediate mass objects, since for the clusters considered here ( $\tau < 10\text{Myr}$ ), only the O stars would have had sufficient time to complete their core hydrogen burning and begin to evolve into giant or supergiant-type stars.

The majority of the cluster members will be in the pre-main sequence phase of their evolution. Since these stars are still contracting, the appropriate mass-luminosity relation is age dependent, and we must rely upon theoretical evolutionary models to convert from the synthetic star’s masses and ages into luminosities. These evolutionary models have been calculated by a number of authors (Henyey et al., 1955; Hayashi, 1961; Iben, 1965; Burrows et al., 1993; Palla & Stahler, 1993; D’Antona & Mazzitelli, 1994; Baraffe et al., 1998), who have explored a variety of different physical inputs and initial conditions to the models. Typically these models track the pre-main sequence

evolution (luminosity and effective temperature) of a star of a particular mass across what is referred to as the theoretical Hertzsprung-Russell (H-R) diagram.

Unfortunately, pre-main sequence (PMS) theoretical models are not typically calculated for the entire mass range from brown dwarfs ( $0.001 M_{\odot}$ ) to high-mass B stars ( $10 M_{\odot}$ ). Because of this, we often had to combine two different sets of PMS tracks to provide a complete mass range. We took the opportunity to use different sets of PMS tracks for high and low mass stars to remove an apparent mass-age correlation found by many authors who have used PMS evolutionary tracks to derive real ages and masses for stars using the H-R diagram (Hillenbrand, 1995; Meyer, 1996; Hillenbrand, 1997). These authors point out that when masses and ages are derived for a cluster of real stars using PMS tracks, a correlation existed such that the more massive stars were systematically *older* than the lower mass stars. Further, these authors suggested that the cause of this correlation is due to the way canonical PMS tracks have been constructed. Canonical PMS tracks evolve the model stars from infinite spheroids, while recent studies suggest that stars evolve during a proto-stellar phase along a specific mass-radius relationship referred to as the proto-stellar birthline (Stahler, 1983; Palla & Stahler, 1990). Using a proto-stellar birthline as the initial condition for PMS tracks will most prominently adjust the predicted luminosities and effective temperatures (as a function of time) for the youngest and highest mass stars, where the stars' proto-stellar (birthline) lifetimes are comparable with these stars' pre-main sequence contraction lifetimes.

Rather than using canonical PMS tracks for model stars with masses greater than solar, we used “accretion-scenario” PMS model calculations by Palla & Stahler (1993) and Bernasconi (1996). Accretion scenario PMS tracks better represent the location of the young intermediate mass stars on the H-R diagrams (Palla & Stahler, 1993; Bernasconi & Maeder, 1996). Yet the accretion-scenario PMS tracks cannot be straightforwardly used with subsolar mass canonical PMS tracks. We adopted the

accretion-scenario tracks listed above for models above  $2 M_{\odot}$  and canonical tracks below  $1 M_{\odot}$  taken from [D’Antona & Mazzitelli \(1994\)](#) and [D’Antona & Mazzitelli \(1997\)](#). Between these two mass limits, we compared the canonical and accretion-scenario calculations. We calculated an average of each accretion-scenario and canonical mass track, weighting the average to result in a smooth conversion from the canonical (subsolar mass) to accretion-scenario (intermediate mass) regimes. We examined the theoretical H-R diagram resulting from our combination of ZAMS, accretion-scenario, averaged, and canonical PMS tracks. These new sets of tracks and resulting isochrones were found to be smooth between all regimes and they were used as input to the modeling algorithm. In [Figure 2–3](#) we show an example of the distribution of mass tracks and isochrones in the H-R diagram. We define our standard set of PMS tracks to be a merger of the [D’Antona & Mazzitelli \(1997\)](#) subsolar mass and [Bernasconi \(1996\)](#) “accretion-scenario” intermediate mass tracks.

Our modeling algorithm uses a cubic spline routine to interpolate between the mass tracks and isochrones on the H-R diagram to derived luminosities and effective temperatures for the masses and ages drawn from the IMF and SFH. Using these luminosities and effective temperatures we converted to an absolute magnitude using the formula:

$$M_{\lambda} = M_{bol,\odot} - 2.5 \times \log(L/L_{\odot}) - BC_{\lambda}(T_{eff}) \quad (2.3)$$

We assumed  $M_{bol,\odot} = 4.75$  and our empirical bolometric corrections were tabulated as functions of effective temperature and were taken from the literature. We list the sources of the bolometric corrections in [Section A](#). Appropriate bolometric correction tables were constructed for I - K bands, allowing for the calculation of red and near-infrared colors, magnitudes and monochromatic luminosity functions.

Lastly, for defining the source of the mass-luminosity relation, we did not account for stars in their proto-stellar phase since the contribution of these extremely young objects to the total population of an embedded star cluster goes as the ratio of the

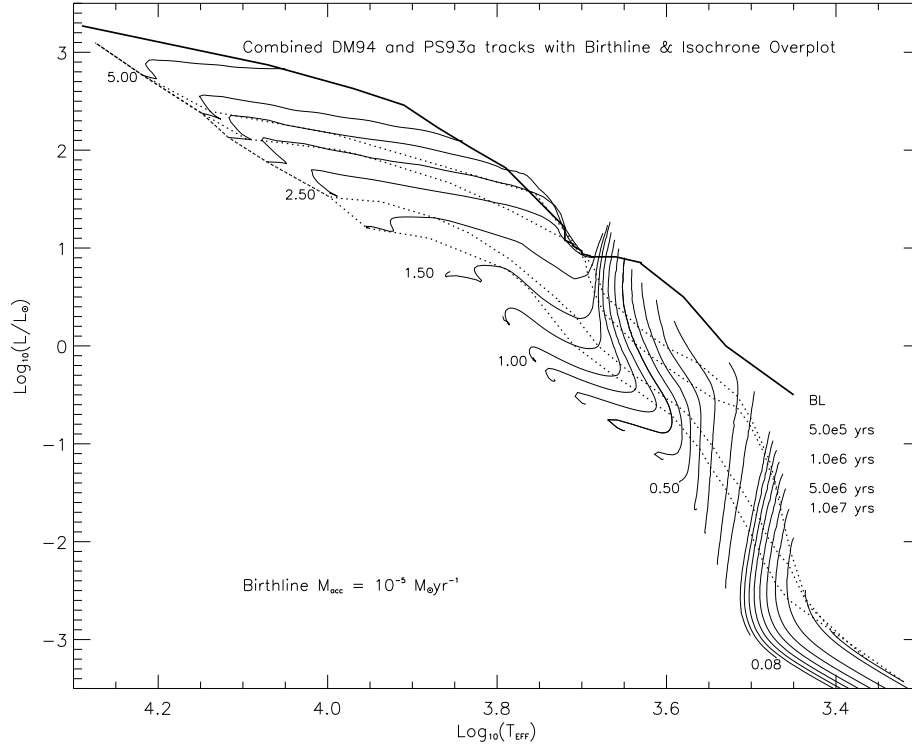


Figure 2–3: Theoretical Hertzsprung-Russell diagram. Pre-main sequence evolutionary tracks from 0.02 to 5  $M_{\odot}$  and isochrones from 0.5 to 10 Myr are shown. The merged tracks are from DM94 and Palla & Stahler (1993). Also shown is the birthline for a proto-stellar accretion rate of  $10^{-5} \frac{M_{\odot}}{\text{yr}}$

duration of the proto-stellar phase ( $\sim 0.1\text{Myr}$ ) to the age spread of the stars in the region ( $\sim 1 - 2\text{Myr}$ ), and hence will be quite small in most cases (Fletcher & Stahler, 1994a,b).

### 2.3 Additional Cluster Characteristics and Model Inputs

In addition to the three fundamental quantities (IMF, SFH, M-L relation) that govern the structure of a young cluster’s luminosity function, there are a number of observational characteristics that must be included into our population synthesis model. Some of these parameters, the distance to a young cluster, for example, are not easily constrained by the analysis we present here, and are subsequently assumed from literature sources, becoming a fixed parameter in our models. For very young clusters, distance is often determined by association with a molecular cloud complex whose systemic velocity is known and has been converted to a distance estimate. In

other cases, some high-mass cluster members are optically visible and are assumed to be on the ZAMS, and these stars are used to derive a distance modulus. The model algorithm always converts from the absolute passband magnitude of the stars,  $M_\lambda$  into an apparent passband magnitude  $m_\lambda$  based on the fixed distance. The cluster's reddening properties and appropriate binary fraction are treated as free parameters, and we describe their inclusion into the modeling algorithm below.

### 2.3.1 Reddening Properties

The mean reddening estimates, e.g.,  $E(B-V)$ , used in traditional open cluster studies are inappropriate for very young clusters because of the large, variable extinction arising from the parental molecular cloud. Although the magnitude of this extinction is decreased by working at near-infrared rather than optical wavelengths, the reddenings are sufficiently large and spatially variable, that a single mean extinction for the entire cluster would be inappropriate. Additionally, hot dust in circumstellar disks around young stars reprocesses the stellar radiation and re-emits it at infrared wavelengths, further reddening a young star's intrinsic infrared colors and increasing the infrared flux observed.

To include these parameters into the modeling algorithm, probability distribution functions (PDFs) are constructed for both of these reddening properties. These PDFs can have either functional (e.g., gaussian) or empirical forms. In both cases, we constrain the cluster's reddening properties from the infrared colors obtained when a young cluster is surveyed. Indeed, two goals of the current luminosity function modeling are to 1) derive recipes for extracting the distributions of reddening from the observed infrared colors themselves, and 2) to use these distributions in our modeling algorithm to recreate not only the cluster's luminosity function, but also to duplicate the distribution of sources in the cluster's infrared color-color and color-magnitude diagrams. We describe our derivation of empirical reddening PDFs in detail in Section [3.3.1](#).

### 2.3.2 Binary Fraction

One observational constraint imposed on our studies of young clusters is the angular resolution limit of our surveys. Thus, the observed luminosity function can be altered by the presence of unresolved multiple stars, by cluster members missed because of chance projections or by confusion due to background stars. Because the clusters we study are reasonably nearby, chance projections do not produce a significant number of false binaries or missed cluster members. Further, we are not observing clusters close to the galactic plane, in the galactic center or in other galaxies so will not consider the latter effect of confusion in our models.

The effects of unresolved binaries and higher order systems on the cluster luminosity function is a well known problem and it depends partially on the underlying IMF of the primaries and of the secondaries (Kroupa et al., 1991). While the typical angular resolution of our surveys allows us to identify some visual binary systems, we can typically probe only to separations of  $\sim 200$  to 300 AU where the binary fraction is observed to be no more than 10-15% (Duquennoy & Mayor, 1991). Hence the majority of the binaries are unresolved and may influence the form of the luminosity function and mass function we derive.

Unresolved binaries have two effects on the form of a cluster's intrinsic luminosity function. First, binaries with mass ratios of  $\sim 1$  will be up to 0.75 magnitudes brighter than the individual members, and will shift the overall form of the luminosity function. Second, binaries with low mass ratio (low mass secondaries to higher mass primaries) will result in cluster members that are completely lost since they will not contribute an appreciable fraction of the total flux of the unresolved system.

We include the existence of unresolved binaries in our Monte Carlo algorithm using a one-parameter binary fraction defined by Reipurth & Zinnecker (1993) as:

$$f = \frac{N_{binaries}}{N_{binaries} + N_{single\ stars}} \quad (2.4)$$

Thus we ignore higher order un-resolved systems (triples, quadruples). We further make the simplifying assumption that the primaries and secondaries are drawn from the initial mass function, and that the distribution of mass ratios is uniform.

To include binaries into our algorithm we follow the formulation of Kroupa (private communication). Simply, after  $N$  stars are sampled from the mass function, a subset are randomly paired into binary systems, (e.g., “systems,”  $N_{sys}$  with the remaining stars becoming “singles,”  $N_{sing}$ ). The number of each type is approximated in the code by the equations:

$$N_{sing} = INT \left( N_{stars} * \frac{1. - f}{1. + f} \right) \quad (2.5)$$

$$N_{sys} = INT \left( (N_{stars} - N_{sing}) / 2. \right) \quad (2.6)$$

Both members of a binary system are assigned the same age and extinction drawn from the star-forming history and the appropriate reddening distribution. If the population synthesis includes flux from a circumstellar disk, each member of a binary is assigned a separate flux excess. The luminosities of the members of the binary system are converted to individual magnitudes, reddened and finally merged (in flux units) to simulate their un-resolved nature.

## 2.4 Model Outputs

Our Monte Carlo based pre-main sequence population synthesis code was scripted to produce a number of different possible simulations. Taking advantage of the code’s Monte Carlo nature, random samples (of  $N$  stars and  $M$  iterations) of any or all of the input distributions (IMF, SFH, reddening distributions) can be derived. Further, synthetic H-R diagrams, infrared color-magnitude and color-color diagrams can be produced for permutations of all of these input parameters.

Finally, model (binned) infrared (IJHK) luminosity functions can be created using parameters that adjust the bin sizes and bin centers. Two model luminosity functions are standard output for each set of input parameters. The first is the luminosity

function constructed from the un-convolved magnitude of every individual star without the effects of reddening or unresolved binaries. The second is an observable model luminosity function which includes these effects. This would be the luminosity function used in modeling young cluster luminosity functions in later chapters, while returning both the intrinsic and observable LFs allows us to make simple direct tests of the impact of various observational quantities. In all cases, the output files are simple ASCII files with headers containing the parameters used in that model run.

## 2.5 Numerical Experiments

Using our Monte Carlo population synthesis code, we performed a series of numerical experiments aimed at evaluating the sensitivity of a young cluster's luminosity function to each of the three fundamental underlying inputs: the theoretical M-L relation, the cluster's star-forming history and the cluster's IMF. We create a suite of model luminosity functions systematically varying each of the three fundamental underlying relations while holding the other two functions constant. For each synthetic model run, we produced model luminosity functions by binning the resulting synthetic magnitudes in half (0.5) magnitude bins as is standard for actual observed cluster luminosity functions. Our standard model cluster for these experiments contained 1000 stars and for each set of fixed parameters we produced typically 50-100 independent luminosity functions. We computed the mean luminosity function from these realizations, and record the one sigma standard deviation of the computed mean of each model luminosity function bin.

### 2.5.1 Different Pre-Main Sequence Evolutionary Models

The evolution of pre-main sequence stars across the H-R diagram and onto the main sequence is not observationally well constrained. Details of PMS evolution rely heavily upon theoretical PMS tracks. These theoretical PMS tracks vary in their predictions depending on the numerical methods and theoretical assumptions used in their creation. Since these PMS tracks are used to convert from a stellar age and mass

to a monochromatic magnitude, the resulting luminosity functions will depend to some degree on the PMS evolutionary models which are chosen. To evaluate how PMS tracks with different input physics, chemical abundances or effective mass ranges affect the shape and form of a model luminosity function, we constructed and compared model luminosity functions calculated assuming different PMS tracks.

For these experiments, we fixed the initial mass function to have a log-normal distribution as described in Equation 2.2. We produced a suite of model clusters with a range of mean ages from 0.2 to 15 Myr and age spreads from coeval to twice the mean age of the model cluster. For the purposes of evaluating the effects of using different input PMS tracks, we only directly compared KLF models having identical star-forming histories.

**D’Antona & Mazzitelli (1994): Differing input physics.** [D’Antona & Mazzitelli \(1994\)](#), hereafter DM94) calculated four different sets of evolutionary PMS tracks varying two input physical parameters, the input opacity tables and the treatments of internal convection. Table 2–1 summarizes the four combinations of input physics and other parameters of the DM94 PMS tracks. Only one of these data sets contained stars with masses less than the hydrogen burning limit. Consequently, we used a common range of stellar masses from 2.5 to 0.1  $M_{\odot}$  to compute different model KLFs using the four sets of DM94 PMS tracks. Figure 2–4 compares synthetic KLFs computed from the DM94 PMS tracks for coeval models with mean ages of 1 and 7 million years, respectively. In Figure 2–4, different symbols correspond to different input opacity tables in the PMS tracks used. For the 1 million year coeval models, the two KLFs corresponding to PMS tracks with Kurucz opacities are essentially indistinguishable, indicating that the KLFs are insensitive to the convection model used. The two model KLFs corresponding to PMS tracks with Alexander opacities exhibit a relatively narrow but significant feature or peak between  $M_K \sim 3-4$  which is not apparent in the KLFs with Kurucz opacities. The position of this spike is different for the two convection

Table 2–1. Evolutionary models used in numerical experiments

Source	Model Name	Opacity Table	Convection Model	$[\frac{D}{H}]^{(a)}$	Mass Range ( $\frac{M}{M_{\odot}}$ )
DM94	ACM	Alexander et al. (1989)	FST <sup>(b)</sup>	2.0	0.018 → 2.5
DM94	AMT	Alexander et al. (1989)	MLT <sup>(c)</sup>	2.0	0.100 → 2.5
DM94	KCM	Kurucz (1991)	FST <sup>(b)</sup>	2.0	0.100 → 2.5
DM94	KMT	Kurucz (1991)	MLT <sup>(d)</sup>	2.0	0.100 → 2.5
DM97 <sup>(e)</sup>	d1.5	Alexander & Ferguson (1994)	FST <sup>(f)</sup>	1.0	0.017 → 1.5
DM97 <sup>(e)</sup>	d2.5	Alexander & Ferguson (1994)	FST <sup>(f)</sup>	2.0	0.017 → 3.0
DM97 <sup>(e)</sup>	d4.5	Alexander & Ferguson (1994)	FST <sup>(f)</sup>	4.0	0.017 → 3.0

<sup>(a)</sup>Deuterium Abundance relative to Hydrogen; In units of  $\times 10^{-5}$

<sup>(b)</sup>Full Spectrum Turbulence Model; [Canuto & Mazzitelli \(1991, 1992\)](#)

<sup>(c)</sup>Mixing Length Theory;  $1/H_p = 1.2$

<sup>(d)</sup>Mixing Length Theory;  $1/H_p = 1.5$

<sup>(e)</sup>DM97 models were initially released in 1997. These models were updated in 1998. The models used were those of the updated calculations.

<sup>(f)</sup>Full Spectrum Turbulence Model; [Canuto et al. \(1996\)](#)

References. — [D’Antona & Mazzitelli \(1994, DM94\)](#); [D’Antona & Mazzitelli \(1997, DM97\)](#)

models used with the Alexander opacities. This feature is due to deuterium-burning which causes a slowing of the stellar luminosity evolution ([Zinnecker et al., 1993](#)) and therefore results in a pile up of stars in the luminosity function. The deuterium-burning spike is absent in the 7 Myr coeval model in Figure 2–4, and in all coeval models with mean ages greater than 2-3 Myr for stars above the hydrogen burning limit. The onset of deuterium-burning is a function of stellar mass. Low mass stars contract more slowly than higher mass stars and begin burning deuterium after high-mass stars. However by 3 Myr, even stars at the hydrogen burning limit would have burned all of their initial deuterium abundance.

A second feature of interest in the KLFs is the spike/dip at  $M_K = 2$  in the 7 Myr coeval model. It is present in all four 7 Myr KLFs and in all KLFs with mean ages greater than 3-4 Myr. This feature is the result of stars reaching a luminosity maximum on radiative tracks before beginning hydrogen burning and moving to

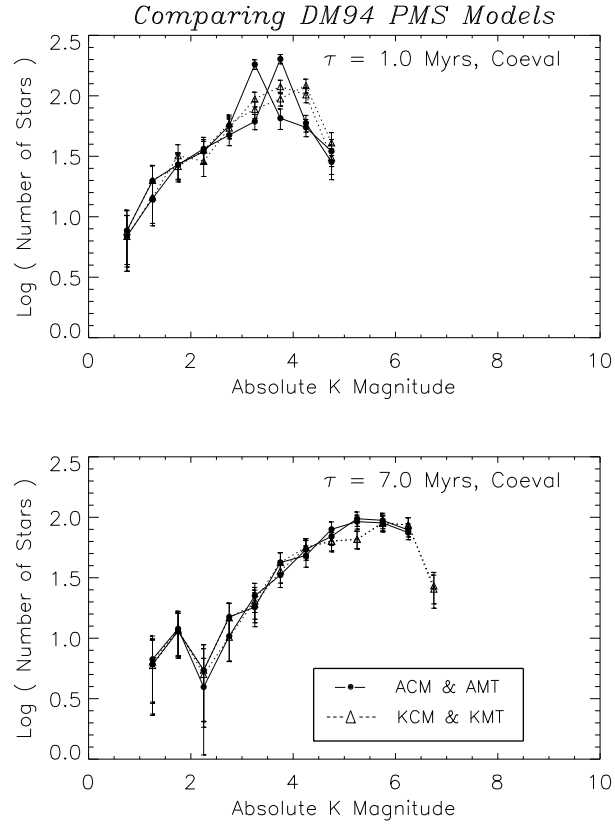


Figure 2–4: Model KLFs: varying physical inputs to evolutionary models. Each model KLF corresponds to a different combination of input physics as described in DM94 (see also Table 2–1). These model KLFs were constructed using a log-normal IMF (see equation 2.2) with a lower mass limit of  $0.1 M_{\odot}$  and having coeval star formation with mean ages of 1 (top) and 7 (bottom) Myr. Different symbols correspond to different input opacity tables used by the PMS tracks. Each bin’s value corresponds to the mean value of that bin for 100 independent realizations of the model KLF. Each realization of the model KLF contained 1000 stars. Error bars correspond to the  $1\sigma$  standard deviation of the mean value of that bin for the 100 iterations.

lower luminosities on the main sequence (Iben, 1965). We refer to this feature as the luminosity maximum spike (LMS). This luminosity maximum spike has been studied by Belikov & Piskunov (1997) in intermediate age (50-100 Myr) clusters and these authors have used it to study the age of the Pleiades open cluster (Belikov et al., 1998).

Model KLFs appear degenerate in the absence of the deuterium-burning spike. The existence of a deuterium spike removes the degeneracy and differentiates between the two different PMS opacity models. Moreover, the position of the deuterium-burning

spike can differentiate between the two convection treatments but only for Alexander opacities. However, only the youngest clusters exhibit a deuterium-burning spike. Model KLFs computed with different PMS tracks and with mean ages greater than 2-3 Myr are essentially indistinguishable from each other and consequently insensitive to the input physics of the PMS models. Note that the deuterium-burning spike is most prominent when deuterium-burning occurs in those stars with masses at the peak of the chosen IMF, which for models discussed here occurs at the hydrogen burning limit (mean ages 1-2 Myr).

Introducing an age spread to the cluster star-forming history diminishes the differences between the KLFs for all four DM94 and at any cluster mean age. While we fully describe the effects of age and age spread on the model KLFs in Section 2.5.2, these results imply that except in the youngest clusters, the KLF will be observationally insensitive to variations in the input physics of the PMS models.

To further study how different PMS tracks affect the model KLFs, we compared the model KLFs using the PMS tracks of DM94 with the models computed using the more recent and improved calculations of D'Antona & Mazzitelli (1997, hereafter DM97). Table 2-1 lists the relevant characteristics of the DM97 tracks. We constructed model KLFs computed with the standard mass range (0.02 to  $80 M_{\odot}$ ) using the DM94 ACM and DM97 d2.5 PMS tracks. These two PMS tracks have similar deuterium abundances but DM97 have advancements to the opacity table and treatment of convection as well as a new equation of state. Figure 2-5 compares model KLFs using these two PMS tracks with a coeval cluster SFH and mean ages of 0.8 and 5 million years. In general the overall shapes of the model KLFs from the two different PMS tracks are quite similar but some minor differences can be quantified. First, the DM97 model KLFs are somewhat narrower and have peaks shifted to slightly brighter magnitudes than those KLFs corresponding to the DM94 ACM tracks. This was a consistent result for all cluster ages and star-forming histories.

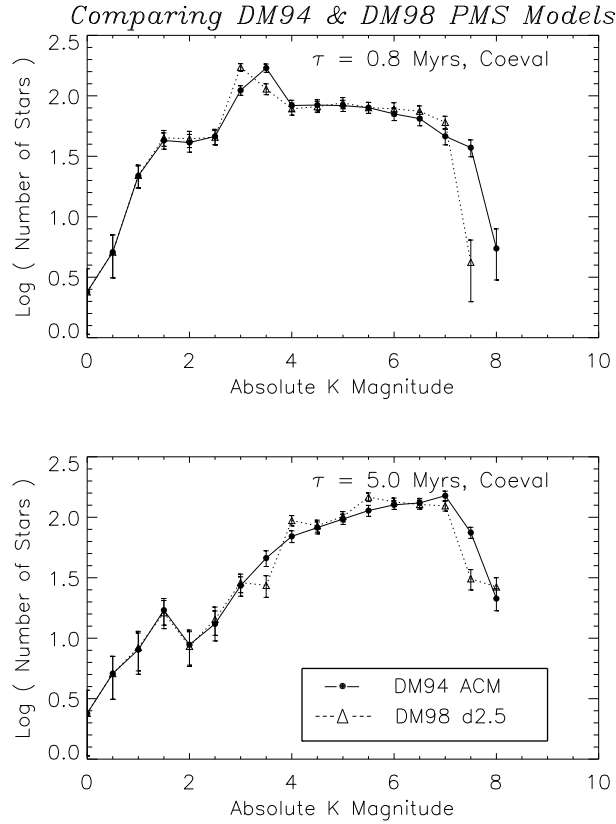


Figure 2–5: Model KLFs: comparing DM94 and DM97. Shown are model KLFs computed using the ACM model from DM94 and the d2.5 model from DM98 (see Table 2–1). These two PMS evolutionary models differ in basic input physics such as opacity table, equation of state and treatment of convection, however, they cover similar mass ranges and have identical deuterium abundances. Upper panel:  $\tau = 0.8$  Myr Lower panel:  $\tau = 5.0$  Myr Both panels correspond to model KLFs for clusters with a coeval star-forming history. Error bars are the same as those in Figure 2–4.

Second, the largest differences between the model KLFs occur at the faint end. This is where DM97 describe the largest differences in their PMS tracks with respect to the DM94 PMS tracks. DM97 PMS tracks have a very different resulting mass-effective temperature relation for low mass stars and brown dwarfs than DM94. Since the K band bolometric correction is fairly insensitive to effective temperature for stars cooler than 3500K (see Section A), these changes do not radically affect the model KLF. Further, DM97 PMS tracks have larger luminosities for the low mass stars and young brown dwarfs compared to DM94. Likewise the DM97 model KLFs are shifted to

brighter magnitudes with respect to DM94 for the faint end of the KLF. However, these differences in the KLFs are relatively small and it would be difficult, observationally, to distinguish between them.

**D’Antona & Mazzitelli (1997): variations in deuterium abundance.** The DM97 PMS tracks were specifically created to study the effects of varying the initial deuterium abundance for PMS evolutionary calculations. It is unclear how much deuterium pre-main sequence stars might contain as they evolve from the birthline toward the main sequence. And there is little observational evidence to constrain this parameter, so it should be considered as an ambiguity in modeling the KLFs. We studied the effects of the deuterium abundance on the KLFs by experimenting with the three PMS tracks presented by DM97. The opacities used by DM97 in their PMS tracks are advancements to those in the DM94 PMS tracks which produced a deuterium-burning spike in the KLFs of Figure 2–4. DM97 input physics and deuterium abundances are summarized in Table 2–1. We produced model KLFs using the three DM97 PMS tracks, d1.5, d2.5, and d4.5, so labeled by their respective deuterium abundance ratios, e.g., the d1.5 set of tracks has a deuterium abundance of  $1.0 \times 10^{-5}$ . Respectively, these three sets of PMS tracks have deuterium abundances of one half, one and two times the interstellar deuterium abundance, which is  $[D/H]_0 = 2.0 \times 10^{-5}$ .

Figure 2–6 compares model KLFs derived from these PMS tracks for mean ages of 2 and 7 Myr and both coeval and  $\Delta\tau/\tau = 2.0$  age spreads. Comparing the coeval models it is clear that increasing the  $[D/H]$  abundance shifts the deuterium-burning spike to brighter magnitudes and increases its size. The deuterium-burning peak disappeared from the d1.5 KLF by 3 Myr, the d2.5 KLFs by 10 Myr and from the d4.5 KLFs not until beyond 10 Myr. For model KLFs shown in Figure 2–6 with the maximum age spread, variations in the KLFs due to changes in the initial deuterium abundance are too small to be observable. The main result here is that variations in the

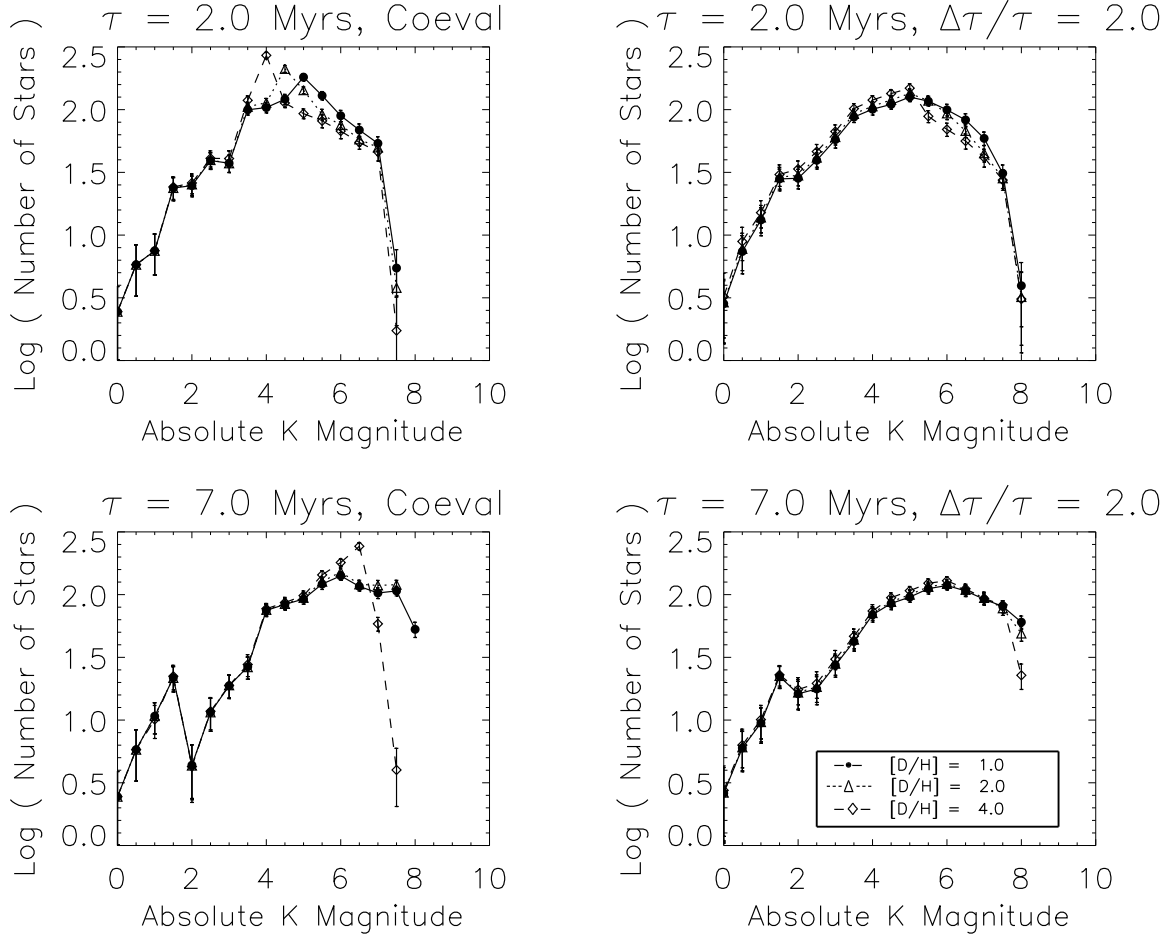


Figure 2–6: Model KLFs: varying the initial deuterium abundance. Each panel compares model KLFs computed with different deuterium abundances at the onset of pre-main sequence contraction. Labels ( $[D/H]$ ) correspond to the ratio of the deuterium to hydrogen abundance in units of  $\times 10^{-5}$  and represent one half, equal to and twice the measured interstellar medium  $[D/H]$ . The model KLFs use log-normal IMF sampled over the entire mass range available for the DM97 PMS models and each panel corresponds to a specific SFH. Error bars are the same as those in Figure 2–4.

$[D/H]$  ratio only produce significant (i.e., observable) differences in the model KLFs of coeval (no age spread) clusters. For these clusters variations in deuterium abundance affects the location and size of the deuterium-burning feature and this occurs only in younger ( $\tau < 3$  Myr) clusters or for the highest deuterium abundances. Once stars have undergone deuterium-burning, their KLFs are identical. Again, the presence of an

age spread dilutes the deuterium-burning feature rendering the form of the cluster KLF independent of the  $[D/H]$  ratio.

**Effective mass ranges for PMS models.** We investigated the effects of using different IMF mass ranges by comparing model KLFs with the standard mass range (0.02 to  $80 M_{\odot}$ ) to model KLFs with a truncated mass range (0.1 to  $2.5 M_{\odot}$ ), i.e., one excluding brown dwarfs, intermediate or high-mass stars. This experiment is useful for comparing our model LFs to prior LF modeling by other authors who typically did not include stars below the hydrogen burning limit or did not include high-mass stars. Figure 2–7 compares model KLFs with truncated and standard mass ranges for two different star-forming histories. For a coeval SFH (upper panel, mean age 3.0 Myr), a truncation in the mass range produces a truncation in the model KLFs at the highest and lowest magnitude bins. However, with an age spread (lower panel, same mean age,  $\Delta\tau/\tau = 2.0$ ), the truncated model KLF is deficient in stars over a wider range of magnitudes, and the two KLFs are similar only over a narrow range of magnitudes. The form of the cluster KLF is clearly very sensitive to the adopted mass range of the underlying IMF.

### 2.5.2 Star Formation History

As shown in the experiments of Section 2.5.1, mean age and age spread have an important effect on the KLF. To more fully explore this, we created model KLFs with a range of mean ages and age spreads, using a single underlying mass function, and a fixed set of PMS tracks. For these experiments, we used the same log-normal IMF as in Section 2.5.1 (see Equation 2.2). As in the previous section, we considered two mass ranges for the IMF, one range with stars down to the  $0.10M_{\odot}$  and one including brown dwarfs with masses down to  $0.02M_{\odot}$ . We adopted our standard PMS evolutionary models described above, i.e., our combination of DM97 d2.5 PMS models, Bernasconi (1996) intermediate-mass PMS tracks, and Schaller et al. (1992)

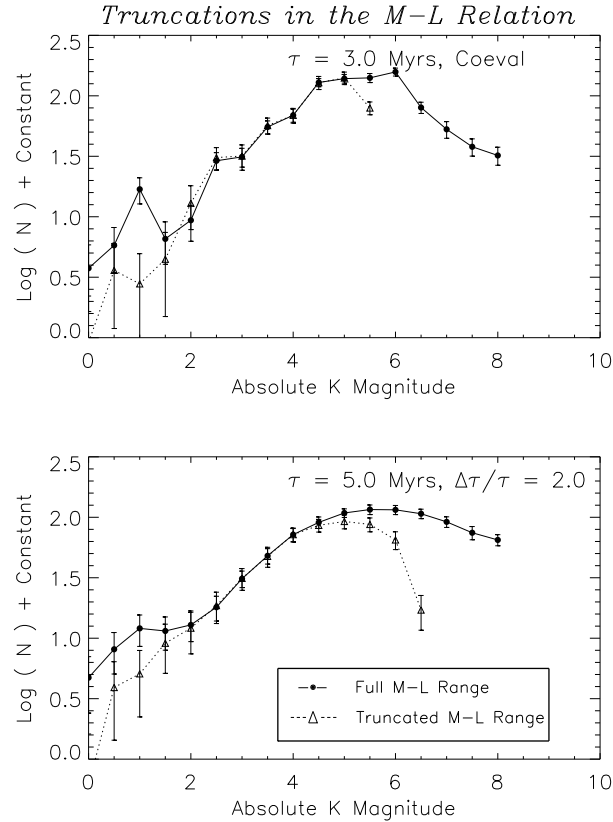


Figure 2–7: Model KLFs: truncations in the mass-luminosity relation. Model KLFs testing the inclusion into model KLFs of high and intermediate mass stars as well as stars at the hydrogen burning limit and brown dwarfs. The mass to luminosity relation was extracted from the ACM PMS model of DM94, intermediate mass PMS tracks from [Palla & Stahler \(1993\)](#) and a ZAMS from [Schaller et al. \(1992\)](#). Two different mean ages and SFH histories are shown for illustration. Upper panel: coeval star-forming history and a mean age of 3.0 Myr. Lower panel: continuous star formation over the age of the cluster with a mean age of 5 Myr. Error bars are the same as those in Figure 2–4.

ZAMS models. We compared the effects of changing the mean age and age spread by studying how model KLFs evolve with time.

Figure 2–8 compares model KLFs with different mean ages and cluster age spreads. Each panel simultaneously displays a one, three and ten million year mean age cluster KLF for a specific  $\Delta\tau/\tau$ . For a given age spread, the models clearly shift to fainter magnitudes with increasing mean age. For small age spreads, the deuterium-burning feature also evolves to fainter magnitudes with time appearing at  $M_K = 3.5$

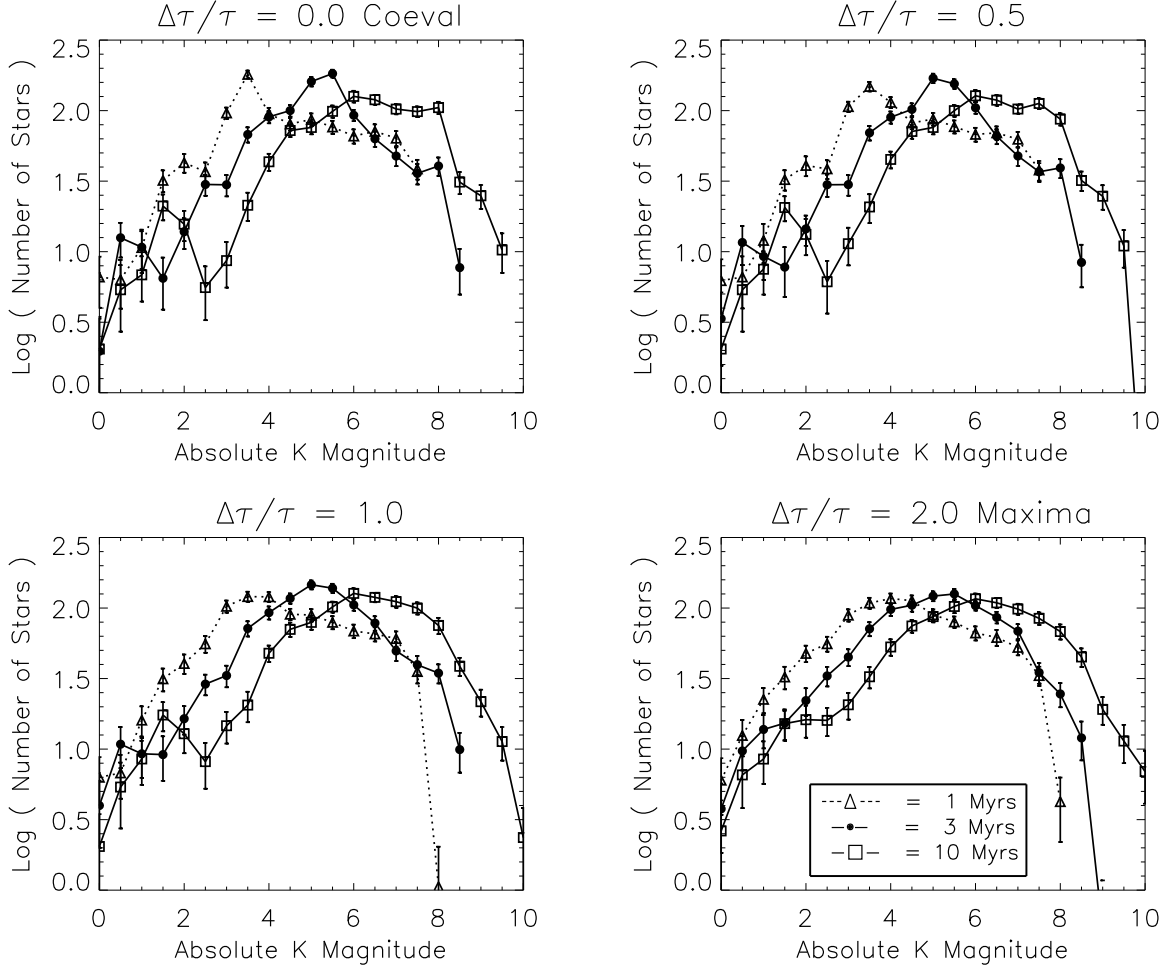


Figure 2–8: Model KLFs: varying the star forming history ( $\tau, \Delta\tau$ ). Each panel displays a different  $\Delta\tau/\tau$  for three mean ages of 1, 3 and 10 million years. Note that from panel to panel, features in the model KLF caused by inflections in the M-L relation are smoothed by the increased age spread. The apparent downward break in the last bin of the model KLFs is primarily due to incompleteness in that bin due to the lower mass limit of the M-L relation at  $0.02M_{\odot}$ . Please see Section 2.5.1 for further explanation of the effects of an artificial truncation in the mass-luminosity relation. Error bars are the same as those in Figure 2–4.

at 1 Myr and  $M_K = 5.5$  at 3 Myr, and  $M_K = 8$  at 10 Myr. To quantify the KLF evolution with time, we calculated the mean K magnitude of the model KLF at each mean age from 0.5 to 10 Myr and for a range of age spreads. In Figure 2–9, we plot the KLF mean magnitude versus the cluster mean age and plot this quantity for the two extrema of  $\Delta\tau/\tau$ . Two sets of curves are plotted, the upper corresponding to an

underlying cluster IMF with brown dwarfs (standard IMF mass range) and the lower to an underlying IMF that truncates at  $0.1 M_{\odot}$ .

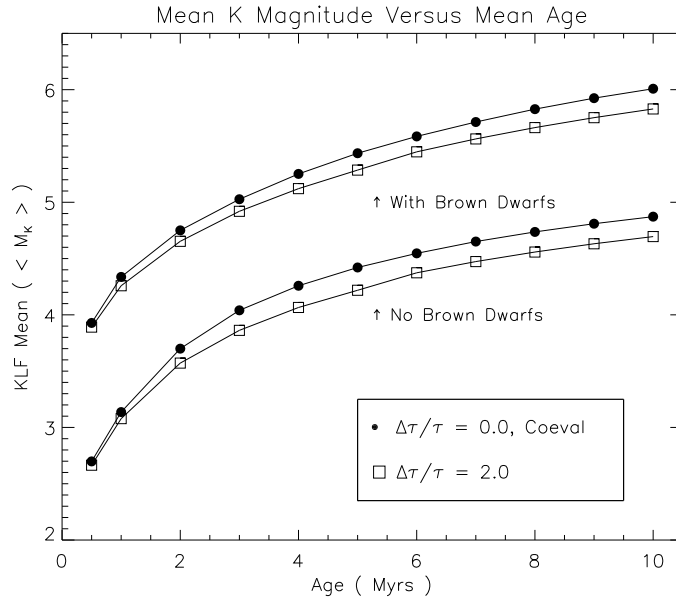


Figure 2–9: Evolution of mean K magnitude with cluster age. The KLF mean refers to the arithmetic mean of the K magnitudes for all synthetic cluster members. Two sets of values are plotted for KLFs having two different underlying IMFs. "With Brown Dwarfs" contains stars below  $0.1 M_{\odot}$  and "Without Brown Dwarfs" has no objects less than  $0.1 M_{\odot}$ . For each set of curves, the KLF mean was plotted for the two extrema of the cluster's age spread,  $\Delta\tau/\tau = 0$  and 2. Error bars are not shown but are within the size of the plotting symbols for a cluster of 1000 stars.

The mean K magnitude of the model KLFs evolves over 2 magnitudes in the first 10 Myr of the cluster lifetime, regardless of the age spread or the mass range over which the IMF was considered. Age spread has little effect except to slightly shift the KLFs to brighter magnitudes. The evolution of the mean K magnitude proceeds most quickly in the first 3 million years where the models evolve by 1 full magnitude. The model KLFs without brown dwarfs naturally have significantly brighter mean values but for these KLFs the mean K magnitude evolves similarly to the standard models. This indicates that the KLFs are more sensitive to changes in the underlying IMF than to changes in the cluster star-forming history. We also studied the width of the model KLFs and found that KLFs widen systematically with time as was shown by LL95.

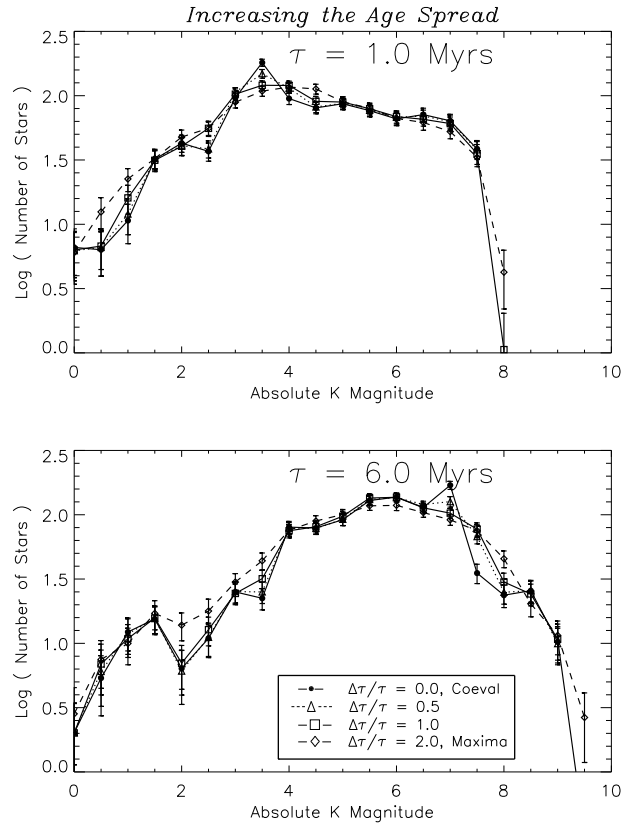


Figure 2–10: Model KLFs: varying the cluster’s age spread. Synthetic cluster KLFs with mean ages of  $\tau = 1$  and  $6$  Myr are shown in top and bottom panels, respectively. In each panel the same four age spreads shown in Figure 2–8 are over-plotted. Upper panel:  $\tau = 1$  Myr. Lower panel:  $\tau = 6$  Myr. Increased age spread erases features in the model KLFs caused by inflections in the mass-luminosity relation. Error bars are the same as those in Figure 2–4.

Variations in the mean cluster age produce more significant changes in the the model KLFs than do changes in the cluster age spread. We show in Figure 2–10, model KLFs for two mean ages and for both of these mean ages we show the four different age spreads from Figure 2–8. For a given mean age, it would be difficult to observationally distinguish clusters with differing age spreads. In detail, models with differing age spreads do exhibit differences in the prominence of the deuterium-burning spike and the maximum luminosity dip/spike. At what point can one distinguish a coeval model KLF from a model KLF with an age spread? To answer this question, we compared model KLFs with increasing age spread to a coeval model of the same mean

age. Using the  $\chi^2$  test, we distinguished the age spread at which the models KLFs no longer appear to be coeval. The general trend from our test is that for an increasing mean age, we require a steadily increasing age spread to distinguish the models from a coeval KLF. For mean ages up to 5 Myr, we could not distinguish model KLFs with age spreads from their coeval counterparts until the age spread exceeded the cluster's mean age ( $\Delta\tau/\tau \sim 1$ ). This changes somewhat between 5 and 10 Myr, since the deuterium-burning feature is present among the brown dwarfs but is not very prominent in the model KLFs. Thus, only a very small age spread is required to erase it from the model KLFs and thus the models no longer appear "coeval" with only a small amount of age spread. Once the deuterium-burning feature is lost from the M-L relation, the models require very large and probably unrealistic age spreads for them to significantly differ from a coeval model of the same mean age.

### 2.5.3 Initial Mass Function

We varied the underlying initial mass function of a young cluster to test the influence of the input IMF on the model KLFs. In previous sections we used a single IMF equivalent to the log-normal (MS79) mass function and only changed the mass limits to this IMF. To test the sensitivity of the KLF to variations in the underlying IMF, we adopted a two segment power-law IMF as defined in Section 2.2.1 and in Equation 2.1

In these experiments, we varied  $\Gamma_1$  values from -2.5 to -0.25,  $m_1$  from  $0.06$  to  $1.5 M_\odot$  and  $\Gamma_2$  values from -1.35 to +2.0. Figure 2–11 displays some of the model KLFs and the corresponding underlying IMFs. The cluster star-forming history used for these models has a mean age of 5 Myr and a  $\Delta\tau/\tau = 1.0$ , or an age spread of 5 Myr. We show model KLFs normalized to the bright end of the KLF where the underlying IMF power-law indices have identical  $\Gamma_1$  slopes equal to -1.35. This example uses a  $m_1 = 0.5 M_\odot$  and five  $\Gamma_2$  values equal to -1.35, -0.40, 0.0, +0.40 and +1.35. The most

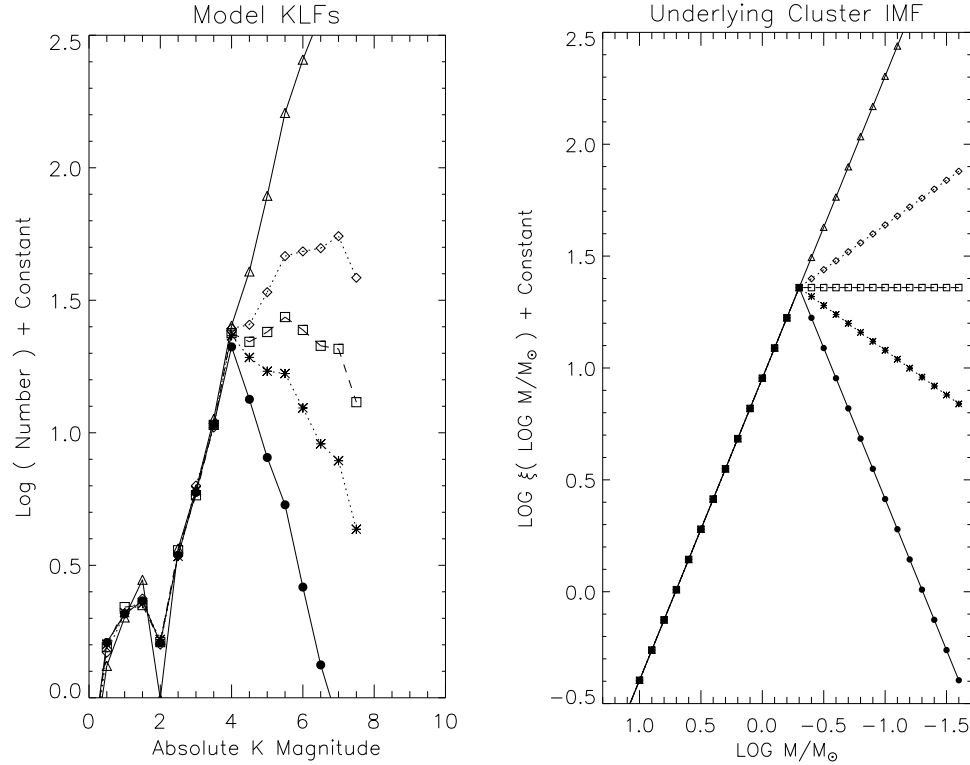


Figure 2–11: Model KLFs: varying the initial mass function. This plot illustrates the sensitivity of the model KLFs to changes in the form of the underlying power-law IMF (see Equation 2.1). The different model KLFs are normalized to their bright LF slopes where their underlying IMFs are identical. The left panel shows the model KLFs corresponding to the underlying IMFs shown in the right hand panel. Symbols are identical for underlying IMFs and the resulting model KLF.

steeply rising KLF corresponds to a single [Salpeter](#) power-law IMF over the entire mass range.

Model KLFs display variations due to changes in all three parameters of the two power-law IMF. In Figure 2–11, the effects of changing  $\Gamma_2$  are large and the differences between KLFs with a slightly rising and a slightly falling IMF below the break mass are significant. Varying the  $m_1$  produces shifts in the peak of the model KLFs. Another result of these tests is that over the range of K magnitudes governed by a single underlying IMF power-law, the model KLF tends to be characterized by a power-law like slope. This is true both for the bright and faint slopes of the model KLFs away from the turnover caused by the  $m$  parameter in the model IMF.

Other than a steep downward drop seen in the last bin of the model KLFs, the model KLFs closely mimic the underlying IMF, decreasing or increasing in number where the IMF is rising or falling. The drop in the last bin of the model KLFs is a byproduct of the limits of the PMS tracks and can be understood by reviewing the comparisons of truncated and extended M-L relations in Section 2.5.1 and Figure 2–7. Simply this turnover is the result of truncating the mass range for the underlying IMF at  $0.02M_{\odot}$ . In summary, these calculations clearly show that the shape of the model KLF is very sensitive to variations in the underlying cluster IMF. Indeed, modest variations in the cluster IMF produce significantly greater responses in the model KLFs than do variations in the SFH and PMS model input physics.

## 2.6 Discussion and an Example from the Literature

### 2.6.1 Results and Implications of Numerical Experiments

From these numerical experiments which evaluate the sensitivity of the K-band luminosity function to variations in three of its fundamental physical parameters: its underlying IMF, its star-forming history, and its mass-to-luminosity relation, we find that the KLF of a young cluster is more sensitive to variations in its underlying IMF than to either variations in the star-forming history or the PMS mass-to-luminosity relation.

We also find that variations in the cluster mean age can produce a significant response in the KLF of a young cluster. In particular, we find that the KLF systematically evolves with time. Both the mean magnitude and the width of the KLF increase with increasing mean age, confirming the results of earlier modeling (LL95). At the same time, variations in the cluster age spread are found to have a small effect on the form of the KLF and would likely be difficult to distinguish observationally.

Except for the youngest and purely coeval clusters, we find that the synthetic KLFs appear relatively insensitive to the adopted PMS evolutionary models (at least for the range of PMS models considered here). In the youngest coeval clusters, the

location and size of the deuterium-burning spike in the KLF was found to depend sensitively on the PMS tracks adopted for the underlying stars. However, we find that even a small amount of age spread broadens the spike and would make it observationally difficult to detect.

We conclude from these experiments that the KLF of a young stellar population can be used to place interesting constraints on the form of the cluster's underlying IMF, provided an independent estimate of the cluster mean age is available. The most direct method of determining the mean age of a young cluster is to obtain optical or infrared spectra and place the objects on the H-R diagram. Through comparison to theoretical PMS tracks, the ages of the stars are determined and a mean age for the cluster derived.

From spectroscopic observations, one can also simultaneously derive the individual masses of the stars and with complete spectra for all cluster members, an independent and more direct determination of the IMF results. However because of spectroscopic sensitivity limits, the determination of masses is usually only possible for the bright stellar population. Since the monochromatic K magnitude of the cluster members can be acquired for stars much fainter than the limit of spectroscopic methods, the analysis of the near-infrared (NIR) luminosity function is a particularly powerful tool for investigating the IMF of faint stars in distant clusters or stars at and below the hydrogen burning limit in nearby clusters. Determining the fraction of cluster members at and below the hydrogen burning limit is a holy grail of present stellar research. The application of the luminosity function method to a nearby populous cluster would provide a first glimpse into the brown dwarf population formed at the time of a typical open cluster's birth.

### **2.6.2 An Example from the Literature: The Trapezium Cluster**

The Trapezium cluster is an excellent system for evaluating the KLF modeling techniques developed in this paper. It is the most densely populated and best studied

nearby ( $D \sim 400\text{-}450\text{pc}$ ; see Section B) cluster, and the central part of a much larger cluster known as the Orion Nebula Cluster (ONC). The ONC has recently been studied by [Hillenbrand \(1997\)](#), who used optical spectroscopy to obtain a mean age for the cluster of  $0.8 \times 10^6$  years and to construct an IMF for stars with masses primarily in excess of the hydrogen burning limit (HBL). In addition, infrared imaging surveys have been made of both the Trapezium cluster ([Zinnecker et al., 1993](#); [McCaughrean et al., 1995](#)) and the ONC ([Ali & Depoy, 1995](#)) enabling the construction of the cluster KLF from these literature data. For comparison with our models, we consider only the KLF for the Trapezium cluster, the 5' by 5' central core of the ONC.

We constructed a KLF of the Trapezium by combining the cluster KLFs published by [Zinnecker et al. \(1993\)](#) and [McCaughrean et al. \(1995\)](#). Our adopted KLF for the Trapezium is shown in the top panel of Figure 2–12. The [Zinnecker et al.](#) KLF includes the bright stars but is not complete at and below the HBL. The [McCaughrean et al.](#) KLF extends to very faint magnitudes, well below the HBL for a one million year old cluster, 400pc distant, but because of source saturation, is incomplete for and does not include bright stars. Neither of these referenced cluster KLFs were corrected for contamination by foreground or background field stars. In addition, neither was corrected for the effects of nebular contamination which would confuse the completeness of the surveys. However, we compared this combined Trapezium KLF to the literature KLF from the [Ali & Depoy \(1995\)](#) survey of the entire ONC and found good agreement in the location of the turnover, bright and faint ends of the two KLFs, although the [Ali & Depoy](#) survey was not as sensitive as that represented by the [McCaughrean et al.](#) KLF. We reiterate that the extent to which this literature based KLF represents the true Trapezium KLF is uncertain because we cannot account for field star or nebular contamination.

Here our goal is to find the simplest functional form of an underlying IMF whose resulting model KLF best fits the observed KLF. We constrained the star-forming

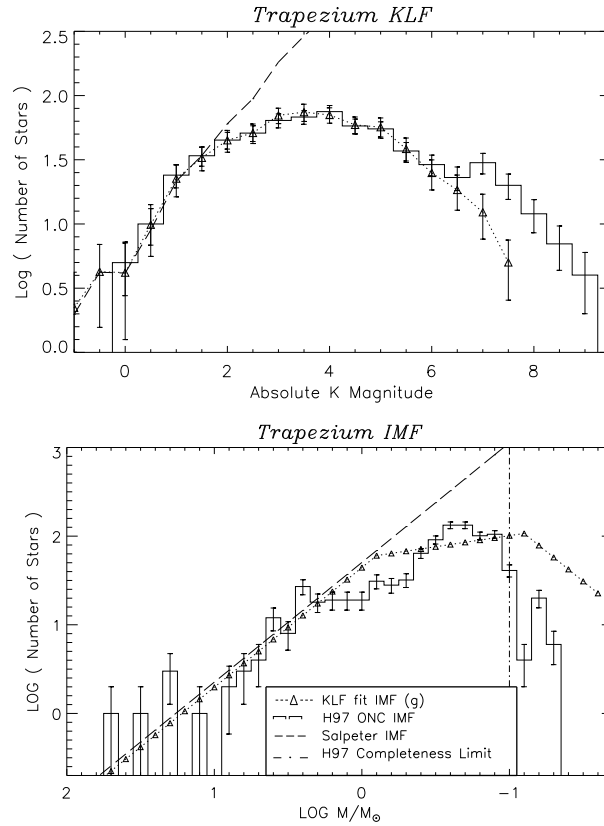


Figure 2–12: Application of models to literature data. Top panel: Literature Trapezium KLF compared to the best fit model KLF (fit from  $M_K = -0.5$  to 6.5). Also shown: a model KLF created using a single power-law [Salpeter IMF](#). The cluster KLF error bars are  $1\sigma$  counting statistics. The model KLF error bars are described in Figure 2–4. Lower panel: KLF derived Trapezium IMF compared to the Orion Nebula Cluster IMF derived by [Hillenbrand \(1997\)](#) using an optical spectroscopic study (histogram). Also shown: the [Salpeter IMF](#) and the mass completeness limit of the optical analysis. For comparison, model IMF (g) is scaled to the same number of stars as the Hillenbrand IMF above the latter completeness limit. Error bars for the Hillenbrand IMF reflect  $1\sigma$  counting statistics.

history of the Trapezium cluster by using the mean age from [Hillenbrand \(1997\)](#) i.e., 0.8 million years. We allowed an age spread of 1.2 million years ( $\Delta\tau/\tau = 1.5$ ) about this mean age, corresponding to constant star formation from 0.2 to 1.4 million years ago. We inspected the observed KLF and determined that a single power-law IMF could not satisfy the observations since the KLF has a peak and turnover well above the completeness limits of the two surveys. Therefore we began with a simple

Table 2–2. Cluster IMF derived from the literature Trapezium KLF

$N_\Gamma^{(a)}$	Name	$\chi^2$ Prob.	$\Gamma_1$	$m_1$	$\Gamma_2$	$m_2$	$\Gamma_3$
2	a	0.38	...	...	-0.50	0.10	+1.00
3	b	0.71	-0.75	0.25	0.00	0.10	+0.75
3	c	0.86	-1.00	0.40	0.00	0.08	+1.00
3	d	0.88	-1.00	0.60	-0.25	0.10	+1.00
3	e	0.93	-0.75	0.25	-0.25	0.10	+0.75
3	f	0.99	-1.00	0.70	-0.25	0.08	+1.00
3	g	0.99	-1.35	0.80	-0.25	0.08	+1.35
4 <sup>(b)</sup>	h	0.96	-1.70	1.00	-0.20	0.10	+0.75
4 <sup>(b)</sup>	i	0.99	-1.70	1.00	-0.20	0.08	+1.00

<sup>(a)</sup>Number of power-laws,  $\Gamma$ , in the derived IMF.

<sup>(b)</sup>Above  $10M_\odot$ , this IMF has a  $\Gamma_0$  equal to -1.30.  $\Gamma_1$ ,  $m_1$ , and  $\Gamma_2$  were fixed.

2 power-law IMFs. We next used a three power-law IMF with a flat (zero slope) IMF in the middle. For symmetry, the two outer power-law slopes were set to have equal but opposite sign slopes. We varied these outer slopes to have absolute values between 0.25 and 2.00 and adjusted the mass range over which the middle slope of the IMF was flat. Finally as a third set of experiments, we allowed the slope of the middle power-law to vary, still holding the outer two slopes to have equal but opposite sign slopes.

We produced a suite of model KLFs for these different IMFs and compared them to the combined Trapezium KLF using a chi-square fitting procedure. Simply, we normalized model KLFs to the observed KLF such that the model and observed KLFs contain the same number of stars between absolute K magnitudes,  $M_K = 0$  and 6.5. We then calculated the  $\chi^2$  statistic and probability over this K magnitude range. To derive a best fit, we compared a suite of model KLFs varying a single IMF parameter, e.g, the middle slope  $\Gamma_2$  or one of the  $m_j$  values and then determining the  $\chi^2$  minima for that variable. Model KLFs were created for a range of possible IMF parameters and compared to the Trapezium KLF in this way.

Best fit model IMFs for each of the tested functional forms of the IMF are listed in Table 2–2. Two power-law fits in general were not good. Symmetric flat topped IMFs fit better and finally a slightly rising IMF across the middle provided a best fit with  $\chi^2 \sim 1$ . Some variation in each of the parameters still allowed for a fit of  $\chi^2 \sim 1$  and examples are listed in Table 2–2. The IMFs (f) and (g) produced best fits to the data and for purposes of discussion, we adopt IMF (g) as representative of the Trapezium IMF and repeat its parameters here:

$$\frac{dN}{d \log M} = \begin{cases} M_{\star}^{\Gamma} & ; \quad \Gamma = \begin{cases} +1.35 & : \quad 0.08 M_{\odot} > M_{\star} \\ -0.25 & : \quad 0.80 M_{\odot} > M_{\star} > 0.08 M_{\odot} \\ -1.35 & : \quad M_{\star} > 0.80 M_{\odot} \end{cases} \end{cases} \quad (2.7)$$

The model KLF corresponding to IMF (g) is shown in the top panel of Figure 2–12 compared to the combined Trapezium KLF and compared to a model KLF calculated with the single power-law slope Salpeter field star IMF over the entire standard mass range.

From our modeling of the observed KLF for the Trapezium cluster we find that the predicted IMF has a rising slope for intermediate mass stars, flattens around a solar mass, reaches a peak near the HBL and turns over below the hydrogen burning limit. There are several comparisons between the observed and modeled Trapezium KLF and between the ONC IMF derived by Hillenbrand and our derived IMF (g) which should be made. First, there exists a significant "tail" to the observed Trapezium luminosity function which is not accounted for in the model KLFs. No attempt was made to account for these very faint stars as cluster members because if they were, they would require ages much older than the distribution suggested by the H-R diagram or lower masses than provided by our standard PMS tracks we are using. We instead suggest that these are either extremely embedded cluster members or heavily extincted background field stars ( $A_V > 20 - 30$ ). We base these suppositions on the fact that the Trapezium is at the core of a blister H II region on the front of a dense molecular

cloud, and because secondary peaks in young cluster luminosity functions are often evidence of a background population seen in projection towards the cluster. Either of these possibilities would in turn imply that our derived IMF is in fact an upper limit to actual IMF below the hydrogen burning limit. Experiments studying the effects of extinction on the model KLF by [Megeath \(1996\)](#) and [Comerón et al. \(1996\)](#) found that while extinction tended to shift a luminosity function to fainter magnitudes, the slope(s) of the KLF were preserved. Thus, the steeply falling slope at the low mass end of the derived Trapezium IMF is reflective of the actual underlying IMF. However, the true IMF may turnover at a larger mass than that implied by our present models.

In the lower panel of Figure 2–12, the mass function derived from the Trapezium KLF is compared to that derived from spectroscopic observations by [Hillenbrand \(1997\)](#). The two mass functions are generally very similar. In particular, these two mass functions agree very well at the high-mass end ( $M_{\star} > 2.0 M_{\odot}$ ). For masses in the range  $2.0 M_{\odot} > M_{\star} > 0.5 M_{\odot}$  the IMF derived from modeling the luminosity function contains more stars than that derived by [Hillenbrand](#). It is not, however, clear how significant this difference is given the possible systematic uncertainties involved in both methods of determining the IMF. Further, these two IMFs sample different volumes of the Orion Nebula region. For masses below  $M_{\star} < 0.1 M_{\odot}$ , the IMF derived from the KLF modeling also contains considerably more stars than the spectroscopic IMF. However, this difference is also not likely to be significant either since the spectroscopic IMF of [Hillenbrand \(1997\)](#) is not complete below  $0.1 M_{\odot}$ .

Lastly, we can investigate whether the field star IMF (FSIMF) could also produce a KLF which reasonably matched the literature Trapezium KLF. To test this, we used the recent field star IMF parameterization from [Scalo \(1998\)](#). [Scalo \(1998\)](#) suggested a

multiple power-law IMF with the form:

$$\frac{dN}{d \log M} = \left\{ M_{\star}^{\Gamma} \ ; \ \Gamma = \begin{cases} -1.30 & : \ M_{\star} > 10.00 M_{\odot} \\ -1.70 & : \ 10.00 M_{\odot} > M_{\star} > 1.00 M_{\odot} \\ -0.20 & : \ 1.00 M_{\odot} > M_{\star} > 0.10 M_{\odot} \end{cases} \right. \quad (2.8)$$

Comparing the IMF in Equation 2.7 to the field star IMF in Equation 2.8, one finds that these two IMFs are quite similar, although for stars in the range of  $10.0 > M/M_{\odot} > 1.0$ , the Scalo IMF is steeper than the IMF in Equation 2.7. In addition, the Scalo FSIMF does not extend below the hydrogen burning limit. To facilitate comparison to the Trapezium data, we added a fourth power-law to the Scalo IMF to account for the faintest stars. We varied  $m_2$ , the mass at which the fourth power-law begins, between  $0.06$  and  $0.1 M_{\odot}$ . In addition, we varied the slope of the fourth power-law,  $\Gamma_4$  between  $-1.0$  and  $+2.0$ . The best fits with this IMF are also listed in Table 2–2. Using this modified field star IMF did yield a  $\chi^2 \sim 1$  with an IMF that breaks near the hydrogen burning limit and falls with a similar steep slope as in the prior IMF fits.

To the extent that our adopted KLF represents the true KLF of the cluster, our modeling suggests that the IMF for brown dwarfs in the Trapezium cluster falls relatively steeply with decreasing mass. However, because contamination due to reddened background stars and incompleteness due to nebular confusion has not properly been taken into account in the construction of this literature Trapezium KLF, the form of the derived IMF below the hydrogen burning limit should be regarded with appropriate caution. As shown in Lada & Lada (1995) and Lada et al. (1996), one can use control-field observations (which are not available for this dataset) to gauge the completeness and membership at the faint end of the LF. Also, our present modeling has not included the effects of extinction and infrared excess. Hillenbrand et al. (1998), using the (I-K) diagnostic, found an average K band excess of 0.35 among identified optically visible cluster members. This average excess is smaller than the bins we have used to construct the Trapezium KLF, and therefore should have only a minor effect.

Overall, we conclude from our modeling that the IMF of the Trapezium cluster is well represented by a three power-law mass function with a high-mass slope between -1.00 and -1.7, a break in slope between 1 and  $0.6M_{\odot}$  followed by a relatively flat or slightly rising slope to the hydrogen burning limit. From our luminosity function modeling, we then found, for the first time that the Trapezium IMF falls with a steep slope  $\sim +1$  into the brown dwarf regime.

## 2.7 Conclusions

After developing a Monte-Carlo based model luminosity function algorithm, we performed a series of experiments aimed at studying how the pre-main-sequence mass-to-luminosity relation, star-forming history and initial mass function each affect the form of the luminosity function for populations of young pre-main sequence stars. Using models of the near-infrared luminosity function and varying these primary inputs, we have derived the following simple conclusions about model near-infrared luminosity functions:

1. We find that the KLF of a young cluster is considerably more sensitive to variations in its underlying IMF than to either variations in the star-forming history or the PMS mass-to-luminosity relation.
2. PMS luminosity functions evolve in a systematic manner with increasing mean age and age spread. They evolve to fainter magnitudes and widen systematically with age.
3. The KLFs of young stellar populations are found to be generally insensitive to variations in the adopted PMS mass-to-luminosity relations. In the youngest, coeval clusters, the presence of deuterium-burning can produce significant features in the KLF which are sensitive to the adopted mass to luminosity relation. However even a small departure from a purely coeval star-forming history will render these features difficult to detect observationally.

We then undertook a preliminary examination of the Trapezium Cluster using data taken from the literature. We apply our models to the K band luminosity function of the Trapezium and are able to derive an underlying Trapezium IMF which spans a

range of stellar mass from  $5 M_{\odot}$  to  $0.02 M_{\odot}$ , well into the brown dwarf regime. The IMF we derive is the simplest multiple power-law function which can reproduce the observed luminosity function of the cluster given the mean age and star-forming history derived from previous optical spectroscopic studies (Hillenbrand, 1997). The derived IMF for the Trapezium cluster consists of three power law segments, has a peak near the hydrogen burning limit and steadily decreases below the hydrogen burning limit and throughout the brown dwarf regime. We derive a brown dwarf mass spectrum of the form  $dN/d\log m \sim m^{+1}$  ( $0.08 > M/M_{\odot} > 0.02$ ). However, the form of the IMF below the hydrogen burning limit must be regarded with caution since the faint end of the observed cluster KLF has not been adjusted for the possible effects of background star and nebular contamination. Above the hydrogen burning limit, the Trapezium IMF we derive from its KLF also appears consistent with that recently advocated for field stars by Scalo (1998).

## CHAPTER 3 THE FAMOUS TRAPEZIUM CLUSTER IN ORION

In Section 2.6.2 we explored the monochromatic K band luminosity function for the well-studied Trapezium Cluster in Orion, which we constructed from literature sources. While we found good agreement between the mass function derived from modeling the cluster’s luminosity function and that IMF found for this cluster using a spectroscopic analysis of the optically visible members, luminosity function modeling enabled the derivation of the cluster’s substellar IMF, which was not possible from the optical/spectroscopic analysis. We concluded from the application of these first-order models to the Trapezium Cluster KLF that model luminosity functions are indeed useful for studying the mass functions of young clusters.

However, the models we applied to the Trapezium cluster did not include other observational characteristics of a young cluster that may affect the conversion between the luminosity and mass functions. Having only the monochromatic Trapezium KLF taken from the literature with no color or completeness information prevented our studying these observational effects in detail. Further, we concluded that we could not fit our models to the entire luminosity range of the literature KLF because of structure that we attributed to heavily reddened cluster members or background field stars. To improve upon this modeling and to standardize the formula for applying the model luminosity functions to the products of a deep near-infrared survey of a young embedded cluster, we have constructed over a three year period of observations a multi-epoch, multi-wavelength near-infrared census of the Trapezium Cluster that we describe in Section 3.1. Using this detailed near-infrared census of the Trapezium, we have expanded our analysis of this cluster’s K band luminosity function and its underlying Initial Mass Function. In Section 3.2, we construct the cluster’s KLF, exploring both

the contribution of background field stars, and the completeness of our survey as it probes the cluster’s parental molecular cloud. We rederive the cluster’s underlying IMF in Section 3.3, refining our techniques to include the effects of source reddening and to fit the model KLFs to the data. In our revised analysis we are able to probe the cluster’s KLF to fainter magnitudes and derive the cluster’s mass function down to the deuterium-burning limit. With these new results, we discuss in Section 3.4 the relationship between the form of a cluster’s KLF and its derived IMF, and we compare our Trapezium IMF derived in this chapter and in Chapter 2 to the Trapezium IMF derived by other authors using different methods. We illustrate the relative robustness of the pre-main sequence mass-luminosity relation as predicted by different theoretical evolutionary models of young stars.

### 3.1 Near-Infrared Census

To derive a complete multi-wavelength census of the sources in the Trapezium Cluster, we performed infrared observations during 1997 December, 1998 November and 2000 March using two telescopes: the 1.2m telescope at the Fred Lawrence Whipple Observatory (FLWO) at Mt. Hopkins, Arizona (USA) and the European Southern Observatory’s (ESO) 3.5m New Technology Telescope (NTT) in La Silla, Chile. These observations yielded the multi-epoch, multi-wavelength FLWO-NTT infrared catalog that contains  $\sim 1000$  sources. Subsets of this catalog have been published previously in the [Lada et al. \(2000\)](#) and [Muench et al. \(2001\)](#) studies of the frequency of circumstellar disks around stars and brown dwarfs in the Trapezium Cluster. We detail below the observations, data reduction, and photometry involved with the construction of the catalog. We also include summaries of the photometric qualities of the datasets and an explanation of the electronic version of the final FLWO-NTT infrared catalog.

### 3.1.1 Observations

We summarize in table 3–1 the characteristics of the three observing runs used to obtain the infrared photometry that comprise the FLWO-NTT Near-Infrared Catalog of the Trapezium Cluster. We compare the area(s) covered by the FLWO-NTT catalog to those of other recent IR surveys in figure 3–1.

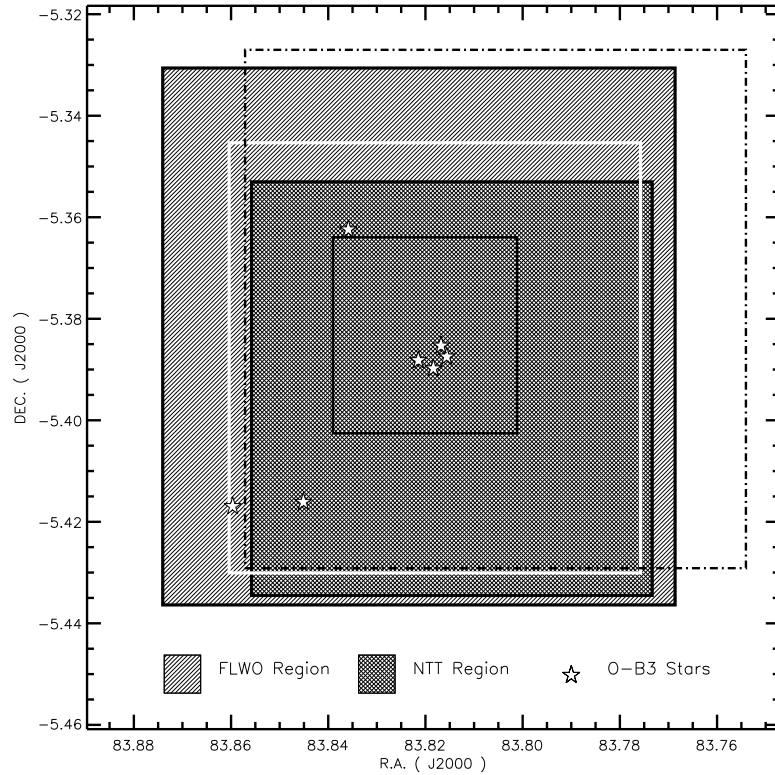


Figure 3–1: Comparison of recent Trapezium cluster IR surveys. The two shaded regions represent the  $6'.5 \times 6'.5$  FLWO survey and the  $5' \times 5'$  NTT survey presented in this work. Also shown are the HST-NICMOS survey (Luhman et al., 2000, solid black border), the Keck survey (Hillenbrand & Carpenter, 2000, solid white border), and the UKIRT survey (Lucas & Roche, 2000, broken black border). The locations of luminous cluster members, spectral types B3 and earlier, are shown as white stars.

**Whipple Observatory – 1997 and 1998: 1.2m JHK-bands.** Initial infrared observations of the Trapezium Cluster region were made on 14, 15, 16 December 1997 with the FLWO 1.2m telescope at Mt. Hopkins, Arizona using the STELIRcam dual channel infrared camera. The STELIRcam instrument allows simultaneous infrared

Table 3–1. Summary of infrared observations of the Trapezium cluster

Observatory <sup>(a)</sup>	Date YYYY / MM / DD	Passband <sup>(b)</sup>	Plate Scale <sup>(c)</sup> Beamsize
FLWO	1997 / 12 / 14	H	0.596 / 3.58
FLWO	1997 / 12 / 14	K	0.596 / 3.58
FLWO	1997 / 12 / 15	H	0.596 / 3.58
FLWO	1997 / 12 / 15	K	0.596 / 3.58
FLWO	1997 / 12 / 16	J	0.596 / 3.58
FLWO	1998 / 11 / 04	J	0.596 / 3.58
FLWO	1998 / 11 / 04	H	0.596 / 3.58
FLWO	1998 / 11 / 04	L	0.596 / 3.58
NTT	2000 / 03 / 14	K <sub>S</sub>	0.288 / 1.73
NTT	2000 / 03 / 14	H	0.288 / 1.73
NTT	2000 / 03 / 14	J	0.288 / 1.73
NTT	2000 / 03 / 14	K <sub>S</sub>	0.288 / 1.73

<sup>(a)</sup>FLWO: Fred Lawrence Whipple Observatory; NTT: New Technology Telescope.

<sup>(b)</sup>Filter central wavelength  $\lambda$  ( $\mu\text{m}$ ): FLWO- J) 1.25, H) 1.65; K) 2.20; L) 3.50; . NTT- J) 1.25; H) 1.65; K<sub>S</sub>) 2.16.

<sup>(c)</sup>Plate scale: arcsec/pixel; Beamsize: diameter of photometry beam (arcsec)

observations using two  $256 \times 256$  pixel InSb arrays and employing a dichroic mirror to divide wavelengths long-ward and short-ward of  $1.9 \mu\text{m}$ . A cold lens assembly allows three changeable fields of view and for all our FLWO observations the camera was configured to have  $2'.5 \times 2'.5$  field of view with a plate scale of  $0''.6$  /pixel. We surveyed the Trapezium Cluster region in a  $3 \times 3$  mosaic pattern, centering on the bright O7 star HD 37022 ( $\Theta$  1c Orionis) and overlapping  $\sim 34''$  between mosaic positions. Our observational technique was to observe 3 on-cluster mosaic positions followed by 1-2 non-nebulous off-fields which were used both for the creation of accurate sky/flat fields and for field star estimation. These off-fields were centered at at R.A. =  $05^h26'$ ; DEC. =  $-06^\circ00'$  (J2000) and were determined to be free of molecular material by inspection of the Palomar Sky Survey Plates and the 100 micron dust opacity maps of [Wood et al. \(1994\)](#). On 14 December 1997,  $H_{\text{barr}}$  ( $1.65 \mu\text{m}$ ) and  $K_{\text{barr}}$  ( $2.2 \mu\text{m}$ ) images were obtained for all 9 mosaic positions, and 7 of the 9 mosaic positions were repeated at H and K band on 15 December.  $J_{\text{barr}}$  ( $1.25 \mu\text{m}$ ) images of all 9 mosaic positions were obtained on 16 December 1997. Each mosaic position was observed with nine dithers of 1 minute each (4 co-additions of 15 seconds) and with  $12''$  spacing, yielding an effective integration time of 9 minutes per field. The Trapezium Cluster region was observed at optimal airmass ( $1.25 < \sec(z) < 1.50$ ). The resulting JHK mosaics mutually covered an on-cluster area of approximately  $6'.5 \times 6'.5$ . Conditions were photometric throughout all three nights with seeing estimates ranging from 1.2 – 1.7 arc-seconds (FWHM).

To improve the photometry of bright sources and increase the dynamic range of our data, we used STELIRcam at the FLWO 1.2m telescope to obtain additional short exposure J and H band images on 4 and 5 November 1998. The Trapezium Cluster region was again observed in a  $3 \times 3$  mosaic but with the telescope in nodding mode taking a single 12 second (12 co-additions of 1 second each) image at each mosaic position followed by an identical off-field exposure at a nod position  $450'$  to the west.

After finishing all 9 mosaic positions, the center of the mosaic was shifted by a small random amount ( $5 - 10''$ ) and the pattern was repeated. Nine repetitions of the mosaic yielding a total effective integration time of 108 seconds per band and these images were observed at transit, with a range of airmasses of 1.24 - 1.28. The resulting JH mosaic images covered an area of  $7' \times 7'$  or slightly larger than the FLWO 1997 observations. Conditions were again photometric with seeing estimated at  $1.6 - 1.8''$ . In this dataset only the brightest 8 stars (all OB spectral types) were saturated.

**European Southern Observatory – 2000: 3.5m JHK<sub>S</sub>-bands.** Our NTT images of the Trapezium Cluster were obtained under conditions of superb seeing ( $\sim 0.5''$  FWHM) on 14 March 2000 using the SOFI infrared spectrograph and imaging camera. The NTT telescope uses an active optics platform to achieve ambient seeing and high image quality, and the SOFI camera employs a large format  $1024 \times 1024$  pixel Hawaii HgCdTe array. To obtain a single wide field image of the Trapezium Cluster, we configured SOFI to have a  $4'.95 \times 4'.95$  field of view with a plate scale of  $0''.29$  /pixel. Each exposure consisted of 9 separate dithers each randomly falling within  $20''$  of the observation center. Each individual dither was the co-average of eight 1.2 second exposures, yielding an total effective integration time of 86.4 seconds for each combined image. We display a JHK<sub>S</sub> color composite image of the NTT region in Figure 3–2.

We observed the Trapezium Cluster with identical sequential pairs of on and off-cluster dithered images. During one hour on 14 March 2000, we obtained four image pairs of the Trapezium Cluster and off-cluster positions. These were, in temporal order, at K<sub>S</sub> ( $2.162 \mu\text{m}$ ), H ( $1.65 \mu\text{m}$ ), J ( $1.25 \mu\text{m}$ ) and again at K<sub>S</sub>, and the on-cluster images had FWHM estimates of  $0.53''$ ,  $0.55''$ ,  $0.61''$  and  $0.78''$ . Seeing estimates of stars in the paired non-nebulous off-cluster image(s) yielded similar if not marginally higher resolution point spread functions (PSF). Observations were taken near transit with a very small range of airmass ( $1.138 < \sec(z) < 1.185$ ).



Figure 3–2: Infrared color composite image of the Trapezium. Taken with SOFI at the ESO NTT telescope, La Silla, Chile, March 2000. North is up and east is left and the field of view is  $5' \times 5'$ .

### 3.1.2 Data Reduction and Photometry

Data reduction of the FLWO and NTT images was performed using routines in the Image Reduction and Analysis Facility (IRAF) and Interactive Data Language (IDL). Our standard data reduction algorithm was described in [Lada et al. \(2000\)](#) for the FLWO images, and it was subsequently used for the NTT images. Simply, individual dithered frames were reduced using sky and flat field images derived from the non-nebulous off-cluster dithered images which were interspersed with the on-cluster images. Each set of reduced dithered frames were then combined using a standard “shift-and- add” technique. While all the FLWO data was linearized after

dark-subtraction using a system supplied linearity correction, linearization coefficients were not obtained for the NTT data. “Sky” flat-fields constructed from the NTT images were compared to system flat-fields which are regularly taken and monitored by the NTT staff. While the NTT system flat-fields were found to vary by only 2-3% over long periods of time, when we compared our sky flat-fields to the system flat-fields, significant small scale variations (5-10%) were revealed across the array. We concluded this was due to our relatively short NTT integration times which results in poor sampling of the intrinsically non-flat SOFI array. Therefore, we substituted the system supplied flat-fields into our reduction procedure. The high resolution of our NTT images results in moderate under-sampling of the point spread functions; we tested to see if sub-pixel linear reconstruction (drizzling) of our images would improve our data quality. Since our images have only a few dithers (9), the drizzle algorithm did not improve our result over standard integer “shift-and-add.”

Each reduced image was characterized with a FWHM estimate of the stellar PSF and an estimate of the pixel to pixel noise. The stellar FWHM was estimated by selecting 10-20 stars per image using IMEXAM and averaging their “enclosed” FWHM measurements. Roughly thirty 100 pixel boxes were placed randomly across each image from which to measure the pixel-to-pixel noise. While a single pixel to pixel noise estimate for an nebulous image is not likely accurate, we used it in the IRAF DAOFIND algorithm to search for objects  $5\sigma$  above the noise threshold. The found sources were then marked on the images, and each source was inspected by eye to remove obvious false detections and include objects missed by DAOFIND. This manual check and selection process was bolstered by using the numerous repeat observations in our data set to ensure a source’s validity. We use our off-field non-nebulous images to estimate the formal detection sensitivity and find  $10\sigma$  limits of: 18.5 at J, 17.7 at H and 16.8 at K for our deep 1997 FLWO observations; 15.3 at J and 15.1 at H for our

shallow 1998 FLWO observations, and 19.75 at J, 18.75 at H and 18.10 at  $K_S$  for our 2000 NTT observations.

The 1997 and 1998 FLWO observations all had FWHM estimates between 2.2 and 3.0 pixels and are, therefore, marginally sampled. We employed the IRAF DAOPHOT (Stetson, 1987) point spread function (PSF) fitting routine to derive photometry for these sources. Our procedure was to perform multi-aperture (2-10 pixel radii) photometry on all the sources on each image, to select 20 stars on each image from which to derive a PSF, and in an iterative fashion, to create the PSF, subtract nearest neighbors and to re-create the PSF until a good PSF was derived. Final PSF photometry was extracted using the ALLSTAR routine and the subtracted images were visually inspected for faint stars missed near bright stars. We used a PSF fit radius of 3 pixels or a beam of  $3.6''$  for our PSF photometry, and set the sky annulus to a 10 pixel radius. Our PSF procedure employed the sky-fitting routines (Parker, 1991) implemented in the DAOPHOT package which we found in artificial star tests to decrease our photometric errors in nebular regions by a factor of two.

The 2000 NTT images had FWHM estimates ranging between 1.8 and 2.1 pixels, and these images are therefore marginally under-sampled and not easily suitable for PSF photometry. Further, the SOFI field of view suffers from coma-like geometric distortions on the northern 10- 15% of the array. For these two reasons, we decided to perform only aperture photometry on the NTT images. Multi-aperture photometry was performed on sources detected in the NTT image using annuli with radii from 2 to 10 pixels. The sky was measured from the mode of the distribution of pixel values in an annuli from 10 to 20 pixels. From inspection of the curves of growth of both isolated and nebulous sources, we chose a 3 pixel radius ( $1.8''$  beam) for most of our NTT sources. Additionally, the choice of small apertures allowed us to minimize the effects of nebular contamination and crowding on the stellar PSF. For faint sources in very confused or highly nebulous regions, we repeated the photometry with a 2 pixel

aperture and a sky annulus from 7 to 12 pixels. The change in sky annulus does not significantly affect our photometry because the fraction of the stellar PSF beyond 7 pixels contains less than 5% of the flux, and the errors resulting from including this flux in the sky estimate are smaller than the errors introduced from using too distant a sky annulus on the nebulous background.

Aperture corrections were derived for our data by choosing  $\sim 15$  relatively bright stars as free of nebular contamination as possible. We performed multi-aperture photometry on them and using the IRAF MKAPFILE routine to visually inspect the stellar curves of growth and calculate corrections. Since small apertures were used to minimize the effects of the bright nebular background, the resulting corrections which constituted a somewhat substantial fraction of the stellar flux. Aperture corrections were carefully checked by comparing the corrections derived for on (nebulous) and off-cluster positions, which are interspersed in time with the on-cluster frames, and found to agree or to correlate with changes in seeing. Because the 1997 and 1998 FLWO observations were performed on the same photometric system and under similar conditions, their aperture corrections were similar and fairly constant between mosaic positions. The average aperture correction from the 3 pixel fitting radius to the 10 pixel sky radius was -0.35 magnitudes. For the NTT images photometered using apertures, a typical 3 pixel aperture correction was -0.14 magnitudes and for those stars photometered using a 2 pixel aperture, a correction of -0.34 was used.

### **3.1.3 Photometric Comparisons of Datasets**

We report in the electronically published catalog all the photometry from the FLWO and NTT observations. Further, we explored any photometric differences between the FLWO and NTT observations because both systems will be merged to construct the cluster's luminosity function, since they do not have the same dynamic range. These differences include the filter systems, the methods and effective beam-sizes of the photometry and the epochs of the observations. We tested if any color

terms were present due to differing photometric (filter) systems, we compared the magnitudes and colors of 504 sources common to both the NTT and FLWO photometry. We compared the (J - H) and (H - K) colors of the NTT photometry to the FLWO photometry and fit these comparisons with linear relations. The (J-H) colors were well fit by a linear relation (slope  $\sim 1$ ); however, we found an offset,  $\Delta(J - H) \simeq 0.10$  magnitudes between the two systems. A similar comparison to the photometry of sources in the Two Micron All Sky Survey (2MASS) catalog <sup>1</sup> indicated this offset was at J band and was restricted to the FLWO sources. Comparison of 2MASS photometry to the NTT photometry revealed no systematic offsets. A comparison of the FLWO and NTT (H - K) colors was also well fit by a linear relation (slope  $\sim 0.97$ ) though this slope suggests that for the reddest sources, the NTT (H - K<sub>S</sub>) color is bluer than the FLWO (H - K) color.

Further, it was evident from these comparisons that while the global filter systems are quite similar, the difference in the NTT and FLWO photometry of individual sources was larger than expected from *formal* photometric errors <sup>2</sup>. From our fake star experiments and from the photometry of sources in overlap regions on mosaicked frames, we determined our *measured* photometric error is 5% for the majority of our sources increasing up to 15% for the sources at our completeness limit. However, when comparing sources common to both the FLWO and NTT data (well above our completeness limit), we derived  $1\sigma$  standard deviations of  $\sim 0.22$  for magnitudes and  $\sim 0.18$  for colors. Very similar dispersions were derived when comparing our FLWO photometry to the [Hillenbrand et al. \(1998\)](#) or 2MASS catalogs or when comparing our

---

<sup>1</sup> A current un-restricted search of the 2MASS First and Second Incremental Point Source and Extended Source Catalogs currently returns only 171 sources.

<sup>2</sup> the quadratic sum of uncertainties from aperture corrections, zeropoint and airmass corrections, flat fielding error and sky noise

NTT data to the [Hillenbrand & Carpenter \(2000\)](#) H and K band dataset. We attribute a portion of this additional photometric noise between the different datasets to the intrinsic infrared variability of these pre-main sequence sources which has been found for stars in this cloud to have an average of 0.2 magnitudes at infrared wavelengths ([Carpenter et al., 2001](#)). We note that the difference in the beamsize used for the FLWO and NTT photometry and by the various other published data sets will also contribute a degree of added photometric noise due to the presence of the strong nebular background, thus making the NTT photometry preferable to the FLWO data for its higher angular resolution.

### 3.1.4 Astrometry and the Electronic Catalog

Astrometry with reasonably high precision was performed by matching the XY pixel locations of a large number ( $> 50$ ) of the observed sources to the equatorial positions of these sources listed on the 2MASS world coordinate system and deriving full plate solutions using the IRAF CCMAP routine. Mosaic positions of the 1997 and 1998 observations were shifted to fall onto a common XY pixel grid defined by the K band FLWO 1997 mosaic images. To create the common K band XY grid, sources in the overlap regions between mosaic positions were matched and global offsets calculated. The two camera arrays of the FLWO STELIRcam instrument are not centered precisely on the sky and the J and H band coordinates were transformed using the IRAF GEOMAP routine into the K band XY coordinate grid. The NTT positions were aligned to the NTT J band image. For the FLWO plate solution, 161 2MASS sources were matched to the FLWO XY coordinates yielding a plate scale of  $0.596''/\text{pixel}$  and an astrometric solution with rms errors of  $\sim 0.10''$ . An independent solution of 82 NTT sources matched to the 2MASS database yielded a plate scale of  $0.288''/\text{pixel}$  and an astrometric solution having rms errors  $\sim 0.07''$ .

We construct the electronic version of the FLWO-NTT catalog based upon all the sources detected by our FLWO and NTT observations, and we compliment our

electronic catalog by including sources identified in other catalogs and falling within our survey area, but that were saturated, undetected or unresolved by our observations. Since our final catalog covers a substantially different area than comparable deep infrared surveys and includes numerous new sources, we chose to assign new source designations for our final catalog. These are based upon the IAU standard format that includes a catalog acronym, a source sequence, and source specifier. For the catalog acronym, we chose MLLA, based upon the initials of the last names of the authors. This acronym is currently unused in the Dictionary of Celestial Nomenclature. We chose to sequence the catalog using a running number incremented from 00001 to 01010. We use a specifier only where necessary to distinguish unresolved sources, typically employing the designations (A), (B), etc. NTT astrometry is preferentially used in the final catalog. For undetected or unresolved sources, we made every effort to include astrometry from the source's identifying catalog if the original catalog could be globally aligned to the FLWO-NTT catalog. We list cross-references based on the most comprehensive or deep surveys; these include the [Hillenbrand \(1997\)](#), [Hillenbrand & Carpenter \(2000\)](#), [Luhman et al. \(2000\)](#) and [McCaughrean & Stauffer \(1994\)](#) designations. For sources lacking cross-references in these catalogs, we list their 2MASS designations (circa the 2nd Incremental 2MASS Point Source Catalog) where possible. The LR2000 designations are based on their derived equatorial coordinates and due to significant astrometric errors do not correspond to the positions we derive in the FLWO-NTT catalog. For example, we find off-sets of  $-0.42''$  in RA and  $0.44''$  in DEC between our positions and those of LR2000. After removing these offsets, we still find median residuals of  $0.44''$  between our coordinates and those of LR2000 with errors as large as  $1''$ ; this is in contrast to the rms residuals of  $0.1''$  between our catalog and the 2MASS and HC2000 positions. Hence we do not list the LR2000 position-dependent designations except where necessary to identify sources undetected by final catalog.

The entire FLWO-NTT Trapezium Cluster catalog has been published electronically in the recent work, [Muench et al. \(2002\)](#). To illustrate what was publically released in that catalog, we have supplied a sample table here, consisting of only a subset of the sources available in the electronic version.

### 3.2 Trapezium Cluster K band Luminosity Function

We restrict our subsequent analysis of the cluster's luminosity and mass function to the area surveyed by our deeper NTT observations. Our observations detected 749 sources within this region. The completeness of this sample at the faintest magnitudes is difficult to quantify because of the spatially variable nebular background. The formal  $10\sigma$  detection limits of our catalog in the NTT region are 19.75 at J, 18.75 at H and 18.10 at  $K_S$  based upon the pixel to pixel noise in non-nebulous off-cluster observations that were taken adjacent in time to the on-cluster images. To better estimate our actual completeness limits, we performed artificial star experiments by constructing a stellar PSF for each of our images and using the IRAF ADDSTAR routine to place synthetic stars in both the off-cluster and the nebulous on-cluster images. A small number of synthetic stars (30-70) with a range of input magnitudes were randomly added across each image and were then recovered using the DAOFIND routine. This was repeated a large number of times (40-200) to achieve sufficient signal to noise for these tests. In off-cluster images, the derived 90% completeness limits agreed well with the estimated  $10\sigma$  detection limits. In the on-cluster images, the completeness limits were reduced to 90% completeness limits of  $J \sim 18.15$ ,  $H \sim 17.8$ , and  $K_S \sim 17.5$  with slightly brighter limits in the dense central core ( $0.5'$  radius from  $\theta^1C$  Orionis). We also carefully compared our source list to those published by other recent surveys for the NTT region. To our resolution limit, we detected all the sources found by the [Hillenbrand & Carpenter \(2000\)](#), hereafter, HC2000) Keck survey except for one, all but two sources from the [Luhman et al. \(2000\)](#) Hubble Space Telescope NICMOS survey, but we could not identify nine sources listed in [Lucas & Roche](#)

Table 3–2. FLWO-NTT near-infrared catalog

Seq.	Spec.	R.A. (J2000)		Dec. (J2000)		J	FLWO (Mag)		FLWO (Err)		NTT (Mag)			NTT (Err)			Phot Flag	H97 ID	HC2000 ID	Other ID
							H	K	H	K	J	H	K <sub>s</sub>	J	H	K <sub>s</sub>				
00001		5 35 22.45	-5 26 10.9	14.59	13.68	99.00	12.40	0.02	0.06	-1.00	0.26									
00002		5 35 26.57	-5 26 09.6	16.24	15.41	99.00	99.00	0.04	0.01	-1.00	-1.00									
00003		5 35 11.65	-5 26 09.0	13.51	11.63	10.56	9.21	0.04	0.01	0.02	0.02									
00004		5 35 15.97	-5 26 07.4	14.12	12.25	99.00	10.30	0.02	0.01	-1.00	0.04									
00005		5 35 09.21	-5 26 05.7									17.01	16.18	15.65	0.05	0.04	0.06			
00006		5 35 20.13	-5 26 04.2									14.57	13.01	12.27	0.01	0.01	0.01			0535201-052604(4)
00007		5 35 04.48	-5 26 04.1	12.14	11.25	10.89	10.15	0.03	0.04	0.03	0.03									0535044-052604(4)
00008		5 35 05.18	-5 26 03.4	13.54	12.88	12.52	12.04	0.01	0.01	0.03	0.12								0	262
00009		5 35 11.48	-5 26 02.6	9.91	9.06	8.84	8.47	0.05	0.01	0.02	0.02								0	365
00010		5 35 22.57	-5 26 02.1									17.18	16.56	16.37	0.09	0.08	0.08			
00011		5 35 06.92	-5 26 00.5	13.48	13.14	12.54	11.43	0.02	0.05	0.02	0.06	13.39	12.56	12.19	0.01	0.01	0.01		0	299
00012		5 35 24.34	-5 26 00.3	13.09	12.42	12.12	11.38	0.08	0.03	0.02	0.10	13.05	12.37	12.02	0.01	0.01	0.01		0	3101
00013		5 35 10.48	-5 26 00.3	13.01	12.25	11.82	11.11	0.03	0.03	0.02	0.05	12.92	12.07	11.66	0.01	0.01	0.01		0	3104
00014		5 35 10.76	-5 26 00.0	15.54	13.61	12.60	11.72	0.04	0.08	0.02	0.09	15.42	13.60	12.57	0.01	0.01	0.01		0	
00015		5 35 15.42	-5 25 59.5	13.72	12.84	12.38	11.56	0.01	0.02	0.02	0.06	13.68	12.78	12.26	0.01	0.01	0.02		0	3103

Note. — FLWO: Fred Lawrence Whipple Observatory, Mt. Hopkins, Arizona; NTT: New Technology Telescope, European Southern Observatory, La Silla, Chile.

References. — [Hillenbrand \(1997, H97\)](#); [Hillenbrand & Carpenter \(2000, HC2000\)](#)

(2000, hereafter, LR2000) UKIRT survey. Further, it is our finding of 58 new sources within our NTT region and un-reported by prior catalogs that adds support to the deep and very sensitive nature of our census.

### 3.2.1 Constructing Infrared Luminosity Function(s)

The FLWO and NTT observations overlap considerably in dynamic range with 504 stars having multi-epoch photometry. For our analysis, we preferentially adopt infrared luminosities from the NTT photometry because it has higher angular resolution and it is an essentially simultaneous set of near-infrared data. For 123 stars that are saturated in one or more bands on the NTT images, the FLWO photometry was used. This transition from NTT to FLWO photometry is at approximately  $J = 11.5$ ,  $H = 11.0$ , and  $K = 11.0$ . For the brightest 5 OB stars, saturated on all our images, we used JHK photometry from the [Hillenbrand et al. \(1998\)](#) catalog. Photometric differences between the FLWO and NTT datasets are small (see section 3.1.3) and will not affect our construction of the Trapezium Cluster infrared luminosity function(s).

In Figure 3–3, we present the raw infrared Trapezium Luminosity Functions (LFs). We use relatively wide bins (0.5 magnitudes) that are much larger than the photometric errors. In Figure 3–3(a), we compare the J and H band LFs for stars in this region. In the Figure 3–3(b), we compare the K band LF of the NTT region to that K band LF constructed in Section 2.6.2. As was observed in previous studies of the Trapezium Cluster, the cluster’s infrared luminosity function (J, H, or K) rises steeply toward fainter magnitudes, before flattening and forming a broad peak. The LF steadily declines in number below this peak but then rapidly tails off a full magnitude above our completeness limits.

For our current derivation of the Trapezium IMF, we use the Trapezium K band Luminosity Function, rather than the J or H LFs. We do so in order to minimize the effects of extinction on the luminosities of cluster members (see Section 3.3.1), to maximize our sensitivity to intrinsically red, low luminosity brown dwarf members of this

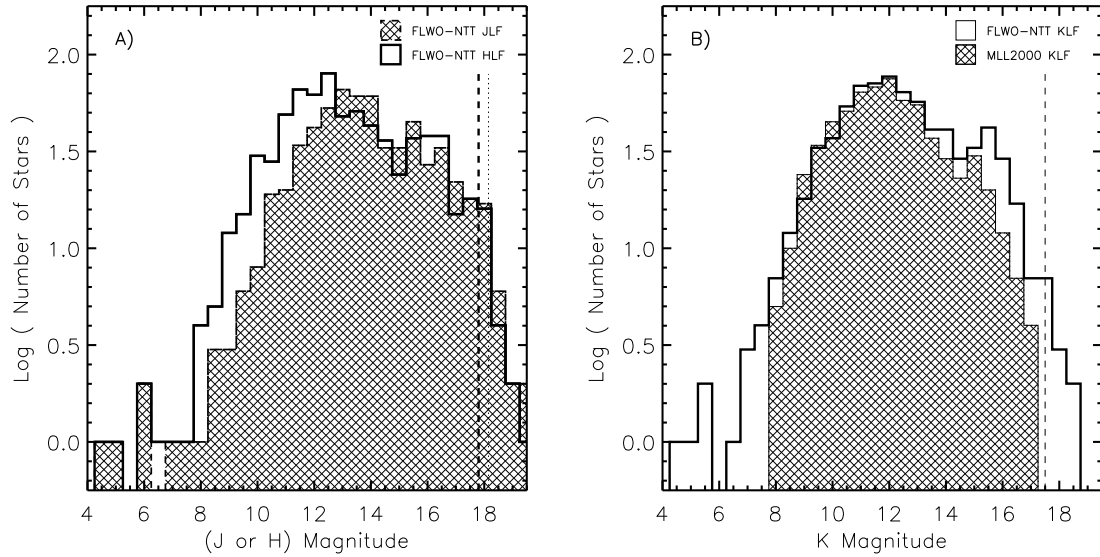


Figure 3–3: Trapezium cluster: raw near-infrared luminosity functions. A) Trapezium Cluster J and H band Luminosity Functions. The Trapezium HLF is the open histogram and the Trapezium JLF is the shaded histogram. Completeness (90%) limits are marked by a solid vertical line at 18.15 (J) and a broken vertical line at 17.8 (H). B) Trapezium Cluster K band Luminosity Function. The Trapezium KLF constructed from the FLWO-NTT catalog is compared to the literature KLF constructed in Section 2.6.2. The  $K=17.5$  90% NTT completeness limit is demarked by a vertical broken line.

cluster, and to make detailed comparisons to our study of the literature Trapezium KLF in Section 2.6.2. For example, the new FLWO-NTT Trapezium KLF contains significantly more stars at faint ( $K > 14$ ) magnitudes than the literature KLF constructed in Section 2.6.2. Interestingly, a secondary peak near  $K = 15$  seen in that KLF (see Figure 2–12) (originally [McCaughrean et al., 1995](#)) is much more significant and peaks at  $K=15.5$  in the new FLWO-NTT KLF. Similar peaks are not apparent in the J or H band LFs constructed here, though [Lucas & Roche \(2000\)](#) report a strong secondary peak in their Trapezium HLF. Such secondary peaks in young cluster luminosity functions have often been evidence of a background field star population contributing to the source counts (e.g., [Luhman et al., 1998](#); [Luhman & Rieke, 1999](#)).

To account for the possible field star contamination, we systematically obtained images of control fields away from the cluster and off of the Orion Molecular Cloud. The FLWO off-cluster field(s) were centered at approximately R.A. =  $05^h26^m$ ; DEC.

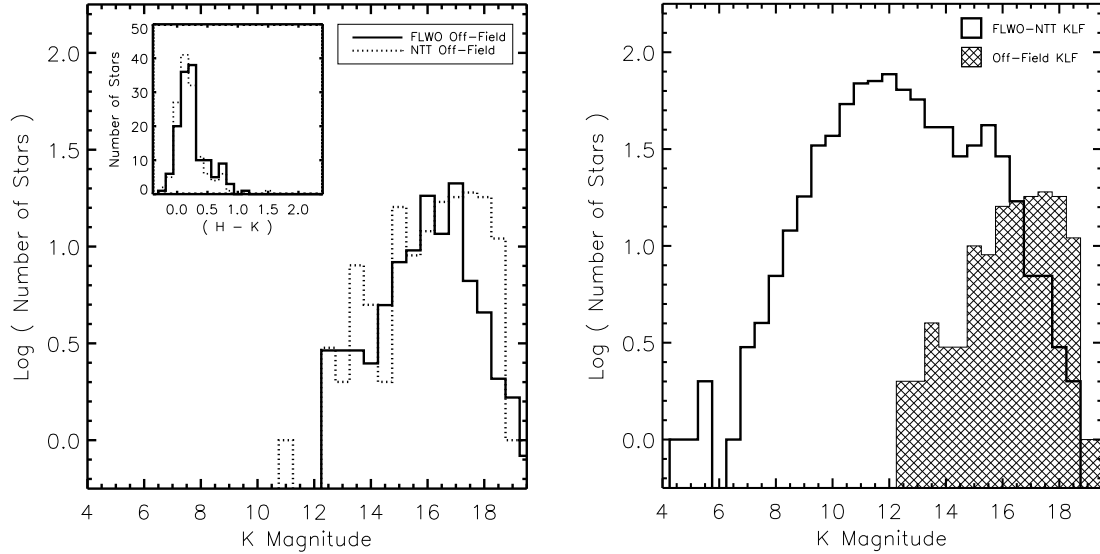


Figure 3–4: Trapezium cluster: construction of observed control field KLF. A) The two histograms are the off-field KLFs obtained as part of the FLWO and NTT observations. The NTT off-fields are approximately 2 magnitudes deeper than the FLWO off-fields, but the FLWO off-fields covered twice the area of the NTT off-fields. Both are scaled to the size of the Trapezium NTT region. The inset diagram shows the distribution of H-K colors for these two off-fields. Their similar narrow widths indicate they are free of interstellar extinction; B) The weighted average of the FLWO and NTT field stars KLFs is compared to the Trapezium Cluster KLF constructed in Figure 3–3(b).

$= -06^{\circ}00'$  (J2000) and were roughly twice the area of the NTT off-fields. The NTT off-cluster region was centered at R.A. =  $05^h37^m43^s.7$ ; DEC. =  $-01^{\circ}55'42''.7$  (J2000). Figure 3–4(a) displays the two off-field KLFs (scaled to the same area) from these observations and in the inset, their (H - K) distributions. The relatively narrow (H - K) distributions indicate that the two off-fields sample similar populations and that they are un-reddened. We constructed an observed field star KLF by averaging these luminosity functions, weighting (by area) toward the FLWO off-fields for K brighter than 16th magnitude, the completeness limit of that dataset, and toward the more sensitive NTT off-fields for fainter than K = 16. In Figure 3–4(b), we compare the resulting field star KLF to the Trapezium KLF of the NTT region. It is plainly apparent from the raw control field observations that while field stars may contribute to the Trapezium Cluster

IR luminosity function over a range of magnitudes, their numbers peak at magnitudes fainter than the secondary peak of the on-cluster KLF and do not appear sufficient in number to explain it.

### 3.2.2 Defining a Complete Cluster KLF

We determine the completeness of our FLWO-NTT Trapezium Cluster KLF by constructing and by analyzing the cluster’s infrared (H - K) versus K color-magnitude diagram. For the purposes of our analysis, we adopt the following parameters for the Trapezium: a cluster mean age of 0.8 Myr (Hillenbrand, 1997) and a cluster distance of 400 pc. As seen in Figure 3–5(a), the luminosities of the Trapezium sources form a continuously populated sequence from the bright OB members ( $K \sim 5$ ) through sources detected below our completeness limits.

To interpret this diagram, we compare the locations of the FLWO-NTT sources in color-magnitude space to the cluster’s mean age isochrone as derived from theoretical pre-main sequence (PMS) calculations. Because the DM97 models include masses and ages representative of the Trapezium Cluster we will use these tracks to define a complete cluster sample from Figure 3–5(a). Differences among pre-main sequence tracks should not have significant effect upon our analysis of the color-magnitude diagram (see Section 3.4.3). It is clear from this diagram that the cluster sources are reddened away from the theoretical 0.8 Myr isochrone, which forms a satisfactory left hand boundary to the sources in this color-magnitude space. This isochrone, however, does not span the full luminosity range of the observations and a number ( $\sim 40$ ) sources lie below the faint end of the DM97 isochrone. As a result, our subsequent analysis that makes use of the DM97 models will be restricted to considering only those sources whose luminosities, after correction for extinction, would correspond to masses greater than the mass limit of the DM97 tracks, i.e.,  $0.017 M_{\odot}$  or roughly 17 times the mass of Jupiter ( $M_{Jup}$ ). Despite the lower mass limit imposed by these PMS

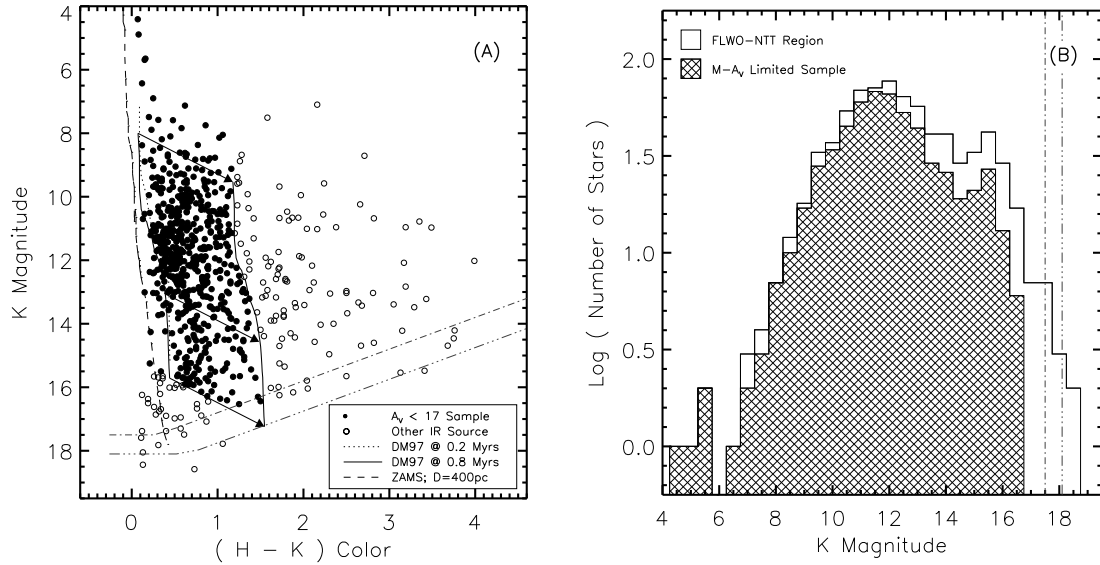


Figure 3–5: Trapezium cluster: deriving  $M - A_V$  completeness limits. A) Trapezium Cluster  $(H - K) / K$  color-magnitude diagram for the NTT region. Stars selected to fall into our mass & extinction limited sample are indicated by filled circles. The distribution of sources in this color-magnitude space is compared to the location of the pre-main sequence 0.2 and 0.8 Myr isochrones from DM97. Reddening vectors ( $A_V = 17$ ) shown for 2.50, 0.08 and 0.02  $M_{\odot}$  stars at the cluster’s mean age (0.8 Myr). The zero-age main sequence (Kenyon & Hartmann, 1995; Bessell, 1995) is shown for 03-M6.5 stars at a distance of 400pc. B) Effects of mass/extinction limits on the cluster KLF. Comparison of the  $M - A_V$  limited KLF derived from (A) to the raw Trapezium KLF (see Figure 3–3b). Sensitivity ( $K = 18.1$ ) and completeness ( $K = 17.5$ ) limits are shown as vertical broken lines.

tracks, our infrared census spans nearly three orders of magnitude in mass, illustrating the utility of studying the mass function of such rich young clusters.

Extinction acts to redden and to dim sources of a given mass to a brightness below our detection limits. To determine our ability to detect extinguished stars as a function of mass, we draw a reddening vector from the luminosity (and color) of a particular mass star on the mean age isochrone until it intersects the  $10\sigma$  sensitivity limit of our census. We can detect the 1 Myr old Sun seen through  $A_V \sim 60$  limits magnitudes of extinction or a PMS star at the hydrogen burning limit seen through  $\sim 35$  magnitudes. For very young brown dwarfs at our lower mass limit ( $17 M_{Jup}$ ), we probe the cloud to  $A_V = 17$  magnitudes. We use this latter reddening vector as a boundary to which

we are complete in mass, and we draw a mass and extinction ( $M - A_V$ ) limited subset of sources bounded by the mean age isochrone and the  $A_V = 17$  reddening vector and mark these as filled circles in Figure 3–5(a). Our  $M - A_V$  limits probe the vast majority of the cluster population, including 81% of the sources the color-magnitude diagram.

In Figure 3–5(b) we present the  $M - A_V$  limited KLF, containing 583 sources. Thirty-two sources, detected only at K band (representing only 4% of our catalog), were also excluded from our further analysis. The median K magnitude of these sources is  $K = 15$ , and we expect that these are likely heavily reddened objects. We compare the  $M - A_V$  limited KLF to the un-filtered Trapezium KLF. Clearly, heavily reddened sources contributed to the cluster KLF at all magnitudes and their removal results in a narrower cluster KLF. However, the structure (e.g., peak, slope, inflections, etc.) of the KLF remains largely unchanged. The secondary peak of the cluster KLF between  $K \sim 14 - 17$  seems to be real since it is present in both the raw and the  $M - A_V$  limited KLFs, though we have not yet corrected for background field stars.

There are at least three possible sources of incompleteness in our mass/extinction limited sample. The first arises because sources that are formally within our mass and extinction limits may be additionally reddened by infrared excess from circumstellar disks and, hence, be left out of our analysis. However, this bias will affect sources of all masses equally because infrared excess appears to be a property of the young Trapezium sources over the entire luminosity range (Muench et al., 2001). Second, the Trapezium Cluster is not fully coeval and our use of the cluster’s mean age to draw the  $M - A_V$  sample means that cluster members at our lower mass limit ( $17 M_{Jup}$ ) but older than the cluster’s mean age ( $\tau > 0.8\text{Myr}$ ) will be fainter than the lower boundary and left out of our sample. Further, sources younger than the mean age but below  $17 M_{Jup}$  will be included into the sample. This “age bias” will affect the lowest mass sources, i.e.,  $< 20 M_{Jup}$ . Third, because of the strong nebular background, our

true completeness limit (see Section 3.1) is brighter than our formal  $10\sigma$  sensitivity for approximately 60% of the area surveyed. The resulting sample incompleteness only affects our sensitivity to sources less than  $30 M_{Jup}$  and with  $A_V > 10$ . We do not correct the Trapezium KLF to account for these effects or biases.

### 3.2.3 Field Star Contamination to the KLF

The lack of specific membership criteria for the embedded sources in the Trapezium Cluster requires an estimate of the number of interloping non-cluster field stars in our sample. Some published studies, for example LR2000 and Luhman et al. (2000), assume that the parental molecular cloud acts as a shield to background field stars; whereas HC2000 suggests that the background contribution is non-negligible. HC2000 estimates the field star contribution using an empirical model of the infrared field star population and convolving this model with a local extinction map derived from a molecular line map of the region. This approach may suffer from its dependence upon a field star model that is not calibrated to these faint magnitudes and that does not include very low mass field stars. As we show, there are also considerable uncertainties in the conversion of a molecular line map to an extinction map. For our current study, we use our observed K band field star luminosity function (see Figure 3–4) to test these prior methodologies and to correct for the field star contamination. We point out that no such estimate can account for contamination due to young, low mass members of the foreground Orion OB1 association.

We compare in Figure 3–6 the effects of six different extinction models upon our observed field star KLF. In panels A and B, we tested simple Gaussian distributions of extinction centered respectively at  $A_V = 10$  and 25 magnitudes with  $\sigma = 5$  magnitudes. In both cases, the reddened field star KLF contains significant counts above our completeness limit and “background extinction shields” such as these do not prevent the infiltration of field stars into our counts. In the second pair of reddened off-fields (panels C and D), we followed the HC2000 prescription for

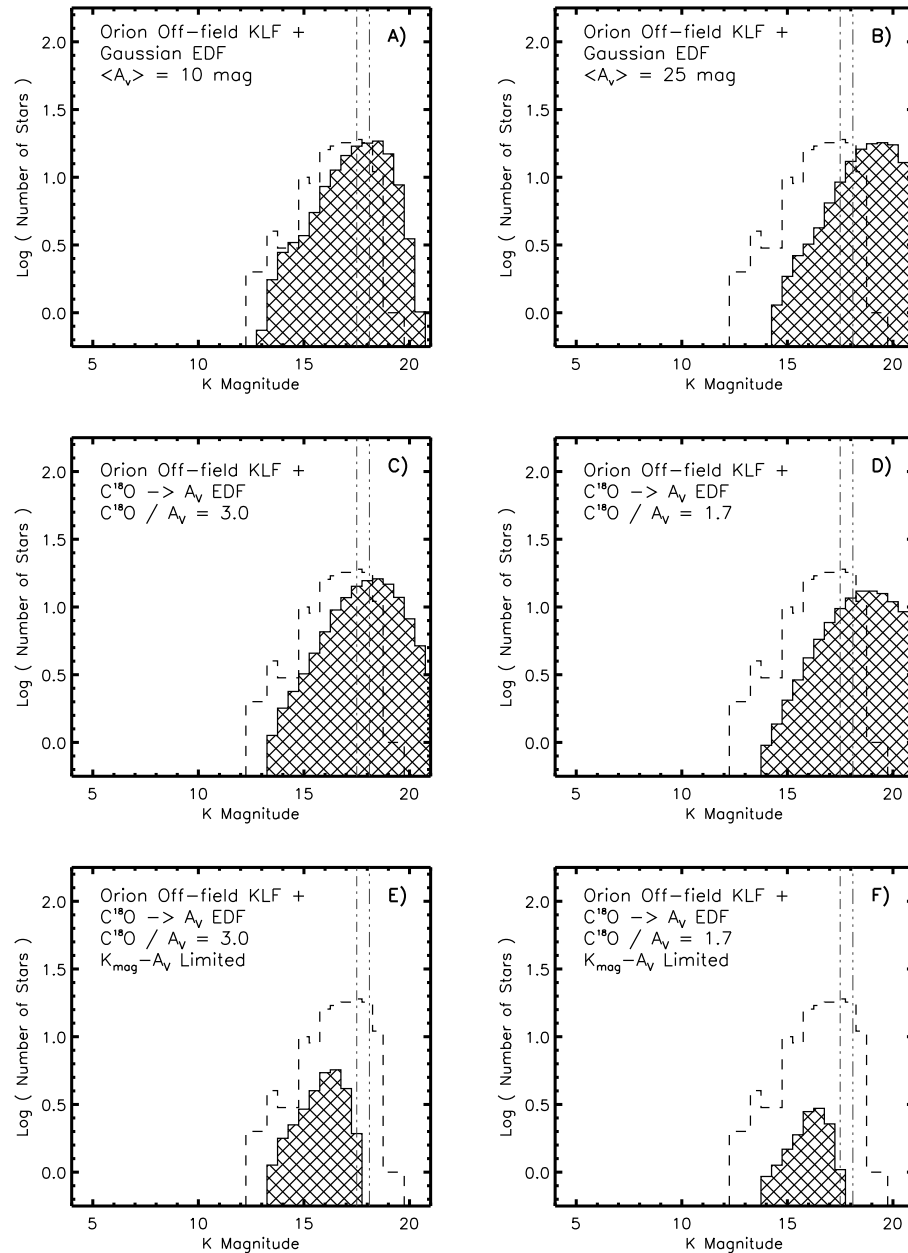


Figure 3–6: Trapezium cluster: testing contribution of reddened field star KLFs. Panels A & B: The observed off-field KLF (Figure 3–4b) reddened by “background shields” of extinction in the form of gaussian distributions centered at  $A_V = 10$  (panel A) and 25 (panel B); Panels C & D: The observed off-field KLF reddened by an extinction map converted from a  $C^{18}O$  map. The two panels represent the variation in the reddened off-field as a function of the uncertainty in the  $C^{18}O$  to  $A_V$  conversion; Panels E & F: The same experiment as performed in C & D, but these have been filtered to reflect the actual contribution due to the  $M - A_V$  limits.

estimating background field stars by convolving our observed field star KLF with the  $C^{18}O$  map from [Goldsmith et al. \(1997\)](#) converted from column density to dust extinction. We note that there is substantial uncertainty in the conversion from  $C^{18}O$  column density to dust extinction. There is at least a factor of 2 variation in this conversion value in the literature, where [Frerking et al. \(1982\)](#) derived a range from 0.7 – 2.4 (in units of  $10^{14} \text{ cm}^2 \text{ mag}^{-1}$ ) and [Goldsmith et al. \(1997\)](#) estimated a range of values from 1.7 – 3. Either the result of measurement uncertainty or the product of different environmental conditions, this variation produces a factor of 2 uncertainty in the extinction estimates from the  $C^{18}O$  map. In short, we find that a  $C^{18}O \rightarrow A_V$  ratio of 3.0 (panel C) results in twice as many interloping background field stars as would a value of 1.7 (panel D; equivalent to that used by [HC2000](#)).

In panels E and F of Figure 3–6 we derive the same reddened off-field KLFs as in the prior pair, but they have been filtered to estimate the actual contribution of field-stars to our  $M - A_V$  limited sample. These filters, which were based upon on the K brightness of the lower mass limit of our PMS models and on the derived extinction limit of the  $M - A_V$  sample, were applied during the convolution of the field star KLF with the cloud extinction model such that only reddened field stars that would have  $A_V < 20$  and unreddened K magnitudes  $< 16$  would be counted into filtered reddened off-field KLF. The extinction limit was expanded from 17 to 20 magnitudes to account for the dispersion of the H-K distribution of un-reddened field-stars ( $\sim 0.2$ ). A factor of 2 uncertainty remains. [Alves et al. \(1999\)](#) derive a more consistent estimate of the  $C^{18}O \rightarrow A_V$  ratio from near-infrared extinction mapping of dark clouds, suggesting a median ratio of 2.1. Adopting  $C^{18}O \rightarrow A_V = 2.1$ , we estimate there are  $\sim 20 \pm 10$  field stars in our  $M - A_V$  limited KLF. From these experiments, we find, however, that both the raw and reddened off-field KLFs always peak at *fainter magnitudes* than the secondary peak of the Trapezium KLF, and that the subtraction of these field-star corrections from the Trapezium KLF do not remove this secondary peak.

These findings suggest that the secondary KLF peak is a real feature in the Trapezium Cluster’s infrared luminosity function.

### 3.3 Trapezium Cluster Initial Mass Function

We analyze the Trapezium Cluster’s K band luminosity function constructed in section 3.2 using our model luminosity function algorithm described in Section 2. Our goal is to derive the underlying mass function or set of mass functions whose model luminosity functions best fit the Trapezium Cluster KLF. We have improved our modeling algorithm by including statistical distributions of the reddening properties of the cluster. We have also improved our analysis by applying the background field star correction from Section 3.2.3 and by employing improved fitting techniques for deriving IMF parameters and confidence intervals. Before deriving the cluster IMF, we use the extensive color information available from the FLWO-NTT catalog to explore the reddening (extinction and infrared excess) properties of the Trapezium sources. In Section 3.3.1, we use this information to create recipes for deriving the probability distributions functions of extinction and excess which can be folded back into our modeling algorithm during our derivation of the Trapezium IMF. We present the new model luminosity functions and fitting techniques in Section 3.3.2 and summarize the derived IMF in Section 3.3.3.

#### 3.3.1 Deriving Distributions of Reddening

**Extinction probability distribution function.** We use the extensive color information provided by our FLWO-NTT catalog to construct a probability distribution function of the intra-cluster extinctions (hereafter referred to as the Extinction Probability Distribution Function or EPDF) based upon the color excesses of individual Trapezium sources. Because the stellar photospheric (H - K) color has a very narrow distribution of intrinsic photospheric values it should be the ideal color from which to derive line of sight extinction estimates, as shown, for example, in the [Alves et al. \(1998\)](#) study of the structure of molecular clouds. In Figure 3–7(a) we show the

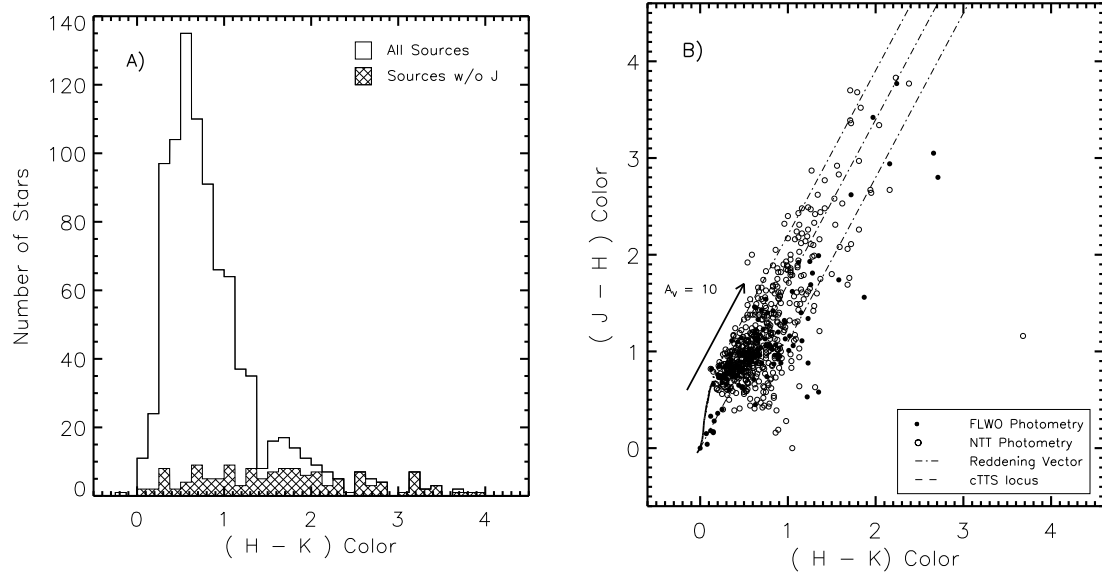


Figure 3–7: Infrared colors of Trapezium sources. A) Histogram of the observed  $(H - K)$  color for the FLWO-NTT Trapezium sources. The subset of these sources which lack J band measurements are indicated by the shaded histogram; B) Trapezium Cluster  $(H - K)$  vs  $(J - H)$  color-color diagram for the NTT region. Symbols indicate if the source’s colors were taken from the FLWO catalog (filled circles, JHK) or the NTT catalog (open circles, JHK<sub>S</sub>).

histogram of observed  $(H - K)$  color for all our Trapezium Cluster sources. This histogram peaks at  $(H - K) = 0.5$  and is quite broad especially when compared to the narrow unreddened photospheric (field-star)  $(H - K)$  distributions seen in Figure 3–4(a). This broad distribution may be in part the result of extinction; however, as recently shown in Lada et al. (2000) and Muench et al. (2001), approximately 50% of these Trapezium Cluster sources, independent of luminosity, display infrared excess indicative of emission from circumstellar disks. This is illustrated in Figure 3–7(b) where it is clear that there are both heavily reddened sources ( $A_V \sim 35$ ) and sources with large infrared excesses (falling to the right of the reddening band for main sequence objects). If the  $(H - K)$  color excess were assumed to be produced by extinction alone without accounting for disk emission, the resulting extinction estimates would be too large.

Meyer et al. (1997) showed that the intrinsic infrared colors of stars with disks are confined to a locus (the classical T-Tauri star locus or cTTS locus) in the  $(H - K)/(J$

- H) color-color diagram. We derive individual  $A_V$  estimates for sources in the (H - K)/(J - H) color-color diagram by dereddening these stars back to this cTTS locus along a reddening vector defined by the [Cohen et al. \(1981\)](#) reddening law. Sources without J comprise  $\sim 20\%$  of the catalog and as shown in [Figure 3–7](#), their (H - K) colors appear to sample a more heavily embedded population, implying extinctions as high as  $A_V \sim 60$ .  $A_V$  estimates are derived for these sources by assigning a typical star-disk (H - K) color = 0.5 magnitudes, and de-reddening that source. Sources near to but below the cTTS locus are assigned an  $A_V = 0$ . The individual extinctions are binned into an extinction probability distribution function (EPDF) as shown in [Figure 3–8](#). Also shown are the effects of changing the typical star-disk (H - K) color assumed for those stars without J band. Little change is seen. Compared to the cloud extinction distribution function, which was integrated over area from the  $C^{18}O$  map, the cluster EPDF is very non-gaussian and peaks at relatively low extinctions,  $A_V = 2.5$ , having a median  $A_V = 4.75$  and a mean  $A_V = 9.2$ . Further, the cluster EPDF is not well separated from the reddening distribution provided by the molecular cloud. Rather the cluster population significantly extends to extinctions as high as  $A_V = 10 - 25$ , near and beyond the peak of the cloud extinction function. Ancillary evidence of this significant population of heavily reddened stars is seen in the color-color diagram ([Figure 3–7b](#)) which clearly illustrates the extension of the cluster to regions of the molecular cloud with  $A_V > 10$ . Lastly, it is clear that the deep nature of our survey has allowed us to sample both the majority of the embedded cluster, and the cloud over the full range of density.

In our revised model luminosity function algorithm, we randomly sample the cluster’s EPDF to assign an  $A_V$  to each artificial star in the model LF. The effect of the EPDF on the model luminosity function is wavelength and reddening law ([Cohen et al., 1981](#), in this case) dependent. In [Figure 3–9](#) we construct model I, J, H, and K luminosity functions, reddening each by the Trapezium Cluster EPDF. The effect of the

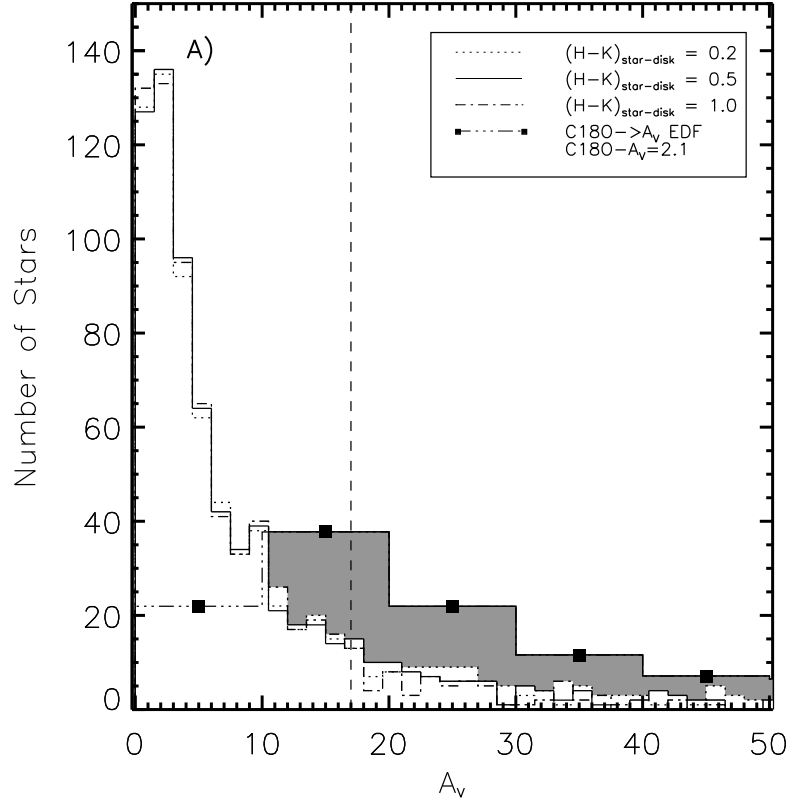


Figure 3–8: Trapezium cluster: extinction probability distribution function. Plotted are three variations in the EPDF under different assumptions of the typical  $(H-K)_{\text{star-disk}}$  color for the 20% of the stars lacking J band measurements. See Section 3.3.1 for derivation. It is compared to the extinction probability distribution function integrated from the  $C^{18}O \rightarrow A_V$  map. Note that they are not well separated distributions. A broken vertical line indicates the  $A_V = 17$ ,  $M - A_V$  limit.

EPDF on the intrinsic I and J band LFs is profound, rendering the reddened I band LF almost unrecognizable. Yet at longer wavelengths, specifically at K band, the effects of extinction are minimized. We note that the overall form of the reddened model K band luminosity function has not been changed by the Trapezium EPDF in a significant way, e.g., the peak of the model KLF is not significantly blurred and the faint slope of the KLF has not been changed from falling to flat. This suggests that our modeling of the literature Trapezium KLF in Section 2.6.2, which did not account for reddening due to extinction, is generally correct. However, we likely derived too low of a turnover

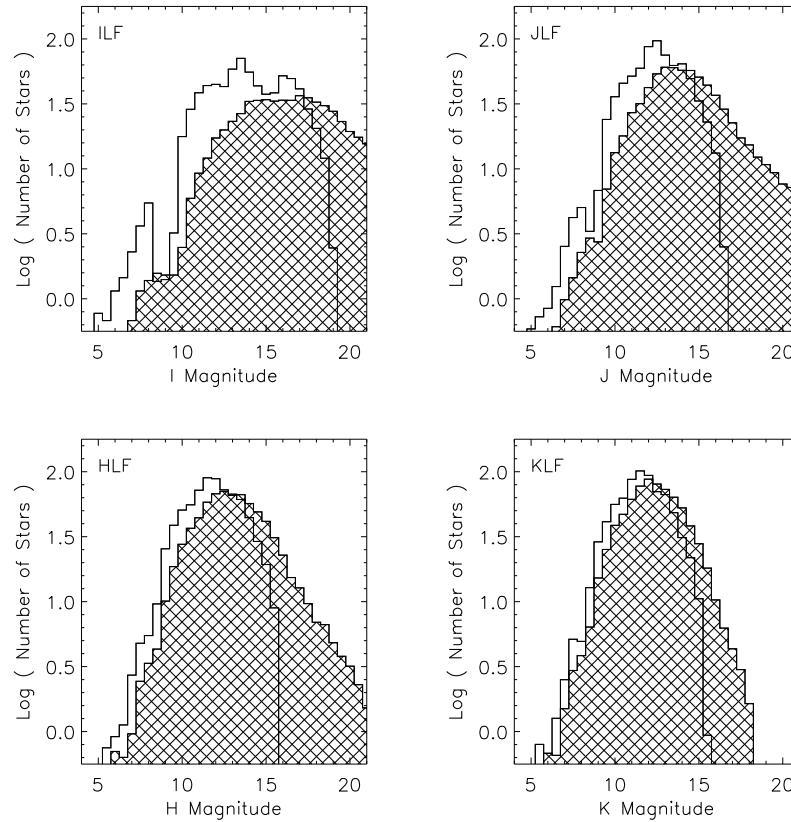


Figure 3–9: Effects of extinction on model cluster LFs. Model luminosity functions of the Trapezium (using the Trapezium IMF of Equation 2.7 and derived in Section 2.6.2) is convolved with the Trapezium Cluster EPDF at four different wavelengths. Reddening effects are most significant at I and J bands and are minimized at K band.

mass for the Trapezium IMF because reddening shifted the intrinsic LF to fainter magnitudes.

**Infrared excess probability distribution function.** Because we wish to use the Trapezium K band LF to minimize the effects of extinction, we must also account for the effects of circumstellar disk emission at K band. The frequency distribution of the resulting excess infrared flux is not a well known quantity, and when previously derived, it has depended significantly upon additional information derived from the spectral classification of cluster members (Hillenbrand et al., 1998; Hillenbrand & Carpenter, 2000). One of the goals of this present work is to construct

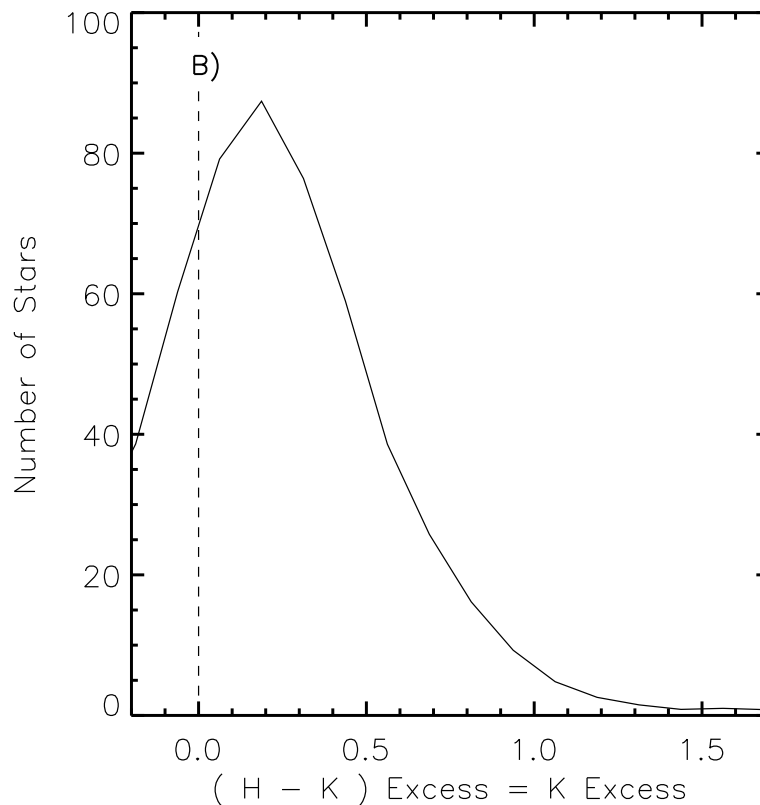


Figure 3–10: Trapezium cluster: infrared excess probability distribution function. The derived  $H-K_S$  color excess distribution function is assumed to reflect a magnitude excess at  $K$  band alone.

a recipe for deriving the  $K$  band excess distribution directly from the infrared colors of the cluster members.

To derive a first-order infrared excess probability distribution function (IXPDF) for the Trapezium Cluster sources, we simply assume that any excess  $(H - K)$  color (above the photosphere, after removing the effects of extinction) reflects *an excess at  $K$  band alone*, realizing this may underestimate the infrared excess of individual sources. We only use the sources having JHK measurements and lying above the cTTS locus in the color-color diagram. We remove the effects of extinction from each source's observed  $(H - K)$  color using the same method described above, i.e., dereddening back to the cTTS locus. However, the photospheric  $(H - K)$  color for each star cannot be discreetly removed from this data alone. The photospheric infrared colors of pre-main

sequence stars appear to be mostly dwarf-like (Luhman, 1999), and therefore, we used the observed field star (H - K) distribution shown in Figure 3–4(a) as a probability distribution of photospheric values. We derive the IXPDF by binning the de-reddened (H - K) colors into a probability function and then subtracting the distribution of photospheric colors using a Monte Carlo integration.

The Trapezium Cluster IXPDF is shown in Figure 3–10. The IXPDF peaks near 0.2 magnitudes with a mean = 0.37, a median = 0.31, and a maximum excess of  $\sim 2.0$  magnitudes. Probabilities of negative excesses were ignored. The IXPDF is similar to the (H - K) excess distribution shown in HC2000 and derived in Hillenbrand et al. (1998) yet extends to somewhat larger excess values. Each artificial star in our models is randomly assigned a K band excess (in magnitudes) drawn from the IXPDF.

### 3.3.2 Modeling the Trapezium Cluster KLF

To model the Trapezium Cluster KLF, we apply the appropriate field star correction derived in section 3.2.3 to the  $M - A_V$  limited KLF constructed in Section 3.2.2. We fix the Trapezium Cluster’s star-forming history and distance to be identical to that used in Section 2.6.2. Specifically, these are a distance of 400pc (m-M=8.0; see appendix B) and a star-forming history characterized by constant star formation from 1.4 to 0.2 Myr ago, yielding a cluster mean age of 0.8 Myr (Hillenbrand, 1997) and an age spread of 1.2 Myr. We adopt our standard set of merged theoretical pre-main sequence tracks from Section 2.2.3<sup>3</sup>. Our merged standard set of tracks span a mass range from 60 to  $0.017 M_{\odot}$ , allowing us to construct a continuous IMF within this range. We incorporated the cluster’s reddening distributions derived in Section 3.3.1

---

<sup>3</sup> Our standard set of theoretical tracks are a merger of evolutionary calculations including a theoretical Zero Age Main Sequence (ZAMS) from Schaller et al. (1992), a set of intermediate mass (1-5  $M_{\odot}$ ) “accretion-scenario” PMS tracks from Bernasconi (1996), and the low mass standard deuterium abundance PMS models from D’Antona & Mazzitelli (1997) for masses from 1 to  $0.017 M_{\odot}$

into our modeling algorithm and chose our standard functional form of the cluster IMF; specifically, an IMF constructed of power-law segments,  $\Gamma_i$  connected at break masses,  $m_j$ . We find that an underlying 3 power-law IMF produced model KLFs that fit the observations over most of the luminosity range, corresponding to masses from 5 to  $0.03 M_\odot$ . In Section 5, we utilize our  $\chi^2$  minimization routine to identify those 3 power-law IMFs that best fit the observed KLF within this mass range, and we estimate confidence intervals for these IMF parameters in Section 5. We find that that the faint Trapezium brown dwarf KLF, corresponding to masses less than  $0.03 M_\odot$ , contains structure and a secondary peak that are not well fit by the 3 power-law IMF models. In Section 5 we model this secondary KLF peak using a corresponding break and secondary feature in the cluster brown dwarf IMF between  $0.03$  and  $0.01 M_\odot$ .

**Results of  $\chi^2$  fitting: best fit three power-law IMFs.** Our  $\chi^2$  minimization procedure calculates the reduced  $\chi^2$  statistic and probability for a particular model KLF fit to the Trapezium KLF over a range of magnitude bins. Parameters for the underlying three power-law IMF are taken from the best fit model KLFs, and we fit both reddened and unreddened model KLFs. The 3 power-law IMF derived from these fits is summarized in Table 3–3. We found that the results of our model fits were dependent upon the dynamic range of K magnitude bins over which the models were minimized. Specifically, we find that our results are very sensitive to the formation of a secondary peak in the Trapezium KLF at  $K = 15.5$ , which remains despite the subtraction of the field star KLF.

We derive good model KLF fits ( $\chi^2 \text{ prob} \sim 1$ ) when fitting between the  $K = 7.5$  bin and the  $K = 14.5$  bin (see Figure 3–11a), the same luminosity range we modeled in Section 2.6.2. Within this fit range, we find an optimal Trapezium IMF nearly identical to that found in Equation 2.7, even after accounting for reddening. The derived IMF rises steeply from the most massive stars with  $\Gamma_1 = -1.3$  before breaking to a shallower IMF slope of  $\Gamma_2 = -0.2$  at  $0.6 M_\odot$  ( $\log m_1 \sim -0.2$ ). The derived IMF

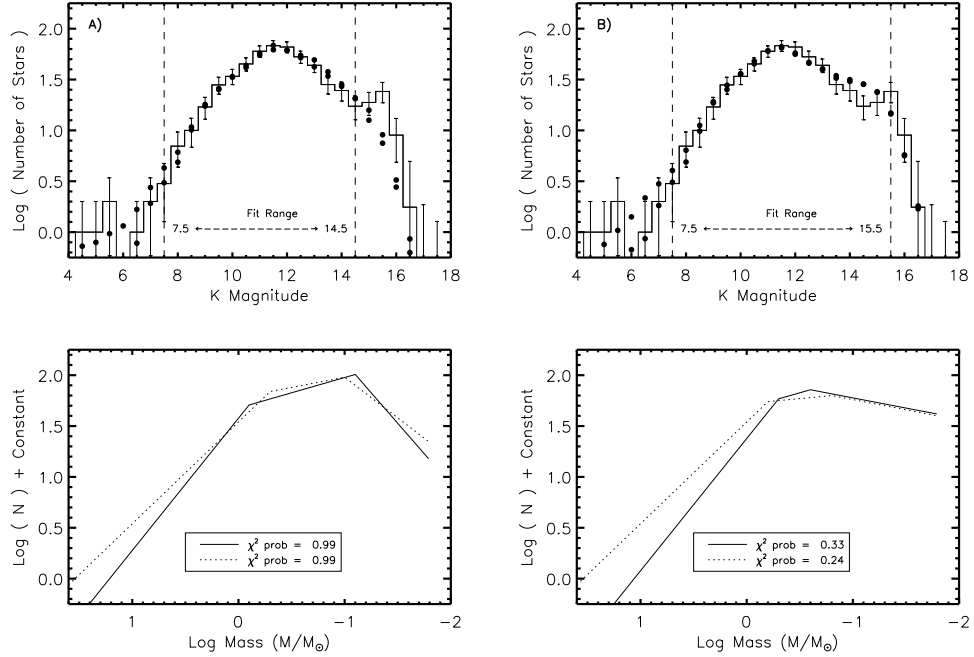


Figure 3–11: Trapezium cluster: best-fitting model KLFs and 3 power-law IMFs. Top panels: the  $M - A_V$  limited, background subtracted Trapezium KLF (histogram) and best fit reddened model KLFs (unconnected filled circles). Bottom panels: the resulting underlying IMFs and corresponding chi-sq probabilities. Panel (A) shows models fit between  $K=7.5$  and  $14.5$ , the same range fit in Section 2.6.2 and Figure 2.7(a). Panel (B) shows three power-law IMF fits to the secondary peak in the cluster KLF at  $K=15.5$ , which correspond to low  $\chi^2$  probability due to the presence of structure and the secondary KLF peak.

peaks near the hydrogen burning limit ( $0.10 - 0.08 M_{\odot}$  or  $\log m_2 = -1.0 - 1.1$ ) and then breaks and falls steeply throughout the brown dwarf regime with  $\Gamma_3 \sim +1.0$ . We also derive good fits to  $K=15$  (just before the secondary peak in the cluster KLF), with the resulting IMF peaking at slightly higher masses ( $0.13 - 0.10 M_{\odot}$ ) and falling with a slightly shallower slope,  $\Gamma_3 \sim +0.7$  to  $0.8$ . The unreddened luminosities of this fit range correspond to a mass range from  $5.0$  to  $0.03 M_{\odot}$ .

However, we cannot produce model KLFs based upon a three power-law IMF that adequately fit the secondary peak in the Trapezium KLF. For example, our best fit to the secondary peak in Figure 3–11(b) is inconsistent with the overall form of the faint KLF, being unable to replicate both the falling KLF at  $K = 14.5$  nor the

Table 3–3. Three power-law Trapezium IMF parameters and errors

Parameter <sup>(a)</sup>	Range	$m_K$ <sup>(b)</sup>	Best Fit <sup>(c)</sup> ( $\pm$ )		Best Fit <sup>(d)</sup> ( $\pm$ )	
$\Gamma_1$	$-1.0 \longleftrightarrow -2.0$	14.5	-1.16	0.16	-1.24	0.20
$\log m_1$	$+0.1 \longleftrightarrow -1.1$	14.5	-0.17	0.10	-0.19	0.13
$\Gamma_2$	$-0.4 \longleftrightarrow +0.4$	14.5	-0.24	0.07	-0.16	0.15
$\log m_2$	$+0.1 \longleftrightarrow -1.4$	14.5	-1.05	0.05	-1.00	0.13
$\Gamma_3$	$-0.4 \longleftrightarrow +2.0$	14.5	1.10	0.25	1.08	0.38
$\Gamma_1$	...	15.0	-1.13	0.16	-1.21	0.18
$\log m_1$	...	15.0	-0.19	0.11	-0.22	0.11
$\Gamma_2$	...	15.0	-0.24	0.15	-0.15	0.17
$\log m_2$	...	15.0	-1.00	0.10	-0.92	0.13
$\Gamma_3$	...	15.0	0.82	0.15	0.73	0.20
$\log m_2$	...	15.5	-0.89	...	-0.77	...
$\Gamma_3$	...	15.5	0.30	...	0.30	...
$\log m_2$	...	16.5	...	...	-0.72	...
$\Gamma_3$	...	16.5	...	...	0.23	...

<sup>(a)</sup>The parameters  $\Gamma_i$  are the power-law indices of the IMF which here is defined as the number of stars per unit  $\log(\frac{M}{M_\odot})$ . The parameters  $m_j$  are the break masses in the power-law IMF and are in units of  $\log(\frac{M}{M_\odot})$ .

<sup>(b)</sup>Faintest KLF bin fit by Model KLF.

<sup>(c)</sup>Model fits without Source Reddening.

<sup>(d)</sup>Model fits accounting for Source Reddening.

Note. — All tabulated fits derived using our standard set of PMS tracks (primarily from DM97).

secondary peak at  $K = 15.5$ . Such structure in the faint Trapezium KLF implies similar non-power law structure in the underlying IMF, while our current models based upon a three power-law IMF essentially assign a single power-law IMF slope for the entire brown dwarf regime. We will explore this structure in the faint brown dwarf KLF and IMF in Section 5, but first we examine the confidence intervals for the derived 3 power-law IMFs.

**Results of  $\chi^2$  fitting: range of permitted three power-law IMFs.** Our  $\chi^2$  fitting routine also allows us to investigate the range of permitted cluster IMFs from modeling the cluster KLF. We illustrate the range of IMFs and the effects of source reddening on our fits in Figure 3–12 and summarize the corresponding constraints on the IMF parameters in Table 3–3. In each panel, we plot the contours of  $\chi^2$  probability for two of the 5 dependent IMF parameters while restricting the other three parameters to a best fit model. In each panel we also display contours for fits with (solid) and without (dashed) source reddening, and we examine the dependence of these parameters for models fit to the  $K=14.5$  and  $K=15.0$  bins.

In all our fitting experiments (here and in Section 2.6.2), the high-mass slope of the cluster IMF,  $\Gamma_1$ , was well constrained with slopes measured between -1.0 and -1.3. Based on this result, we fix  $\Gamma_1$  to equal -1.3. Panels (a) - (c) in Figure 3–12 display the ranges of the other 4 IMF parameters when fitting to a  $K$  limit = 14.5. Panel (a) plots the dependence of the two break masses,  $m_1$  and  $m_2$ . The fits for these parameters are well behaved with 90% contours have a typical width of 0.1-0.2 dex in units of log mass. Source reddening has two clear effects upon our fit results. When source reddening is included, the high-mass break,  $m_1$ , decreases and the low mass break,  $m_2$ , increases. The second effect is that the size of the 90% confidence contour increases when source reddening is included into the model fits. Panel (b) displays the dependence of the low mass break,  $m_2$ , on the middle power-law slope,  $\Gamma_2$ .  $\Gamma_2$  is fairly well constrained to be slightly rising to lower masses, and the permitted range of  $m_2$

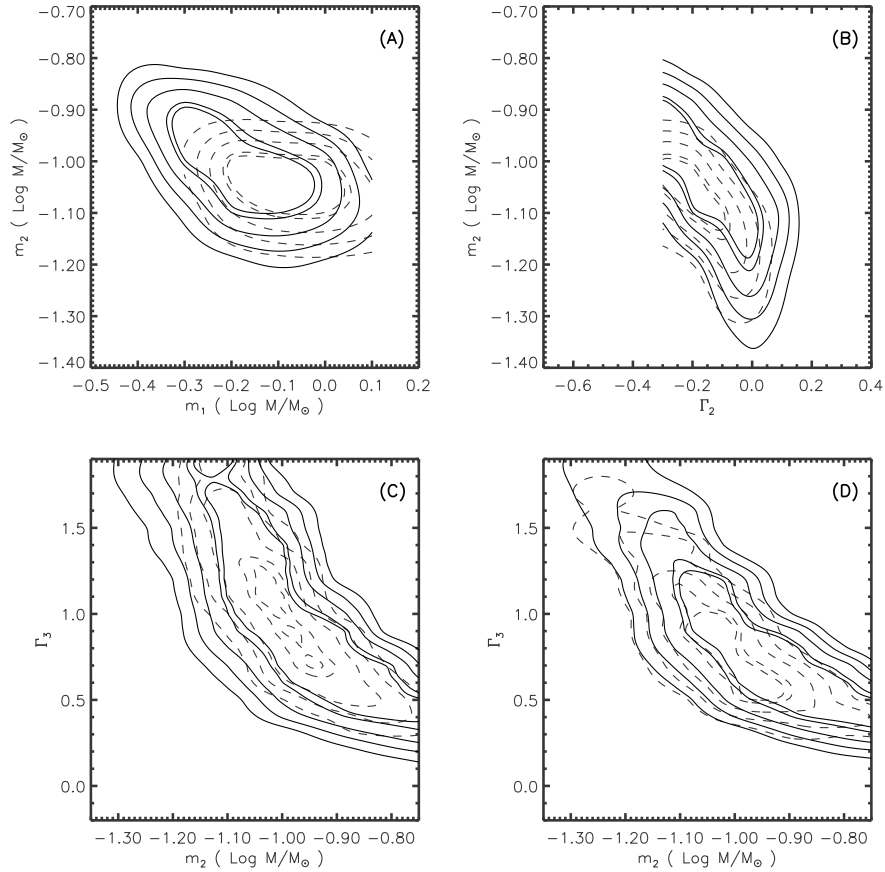


Figure 3–12: Trapezium cluster:  $\chi^2$  confidence intervals for IMF parameters. Contours of  $\chi^2$  probability for the 5 parameters of the underlying three power-law IMF. Two parameters are compared in each panel while fixing the other three to a best fit value. Solid contours are best fit ranges from models that include source reddening. Dashed contours are from best fit models without source reddening. Contour levels are shown at intervals 95, 90, 70, 50 and 30% confidence. Panels (A) to (C) are shown for fits to  $K=14.5$  and panel (D) is shown for fits to  $K=15$ .

is again roughly 0.1 - 0.2 dex, centered near  $0.1 M_{\odot}$  ( $\log m_2 \sim -1$ ). Accounting for source reddening again shifts the low-mass break to slightly higher masses, increases the size of the 90% contour, and in this case, flattens the central power-law.

Panel (c) displays the dependence of  $\Gamma_3$  upon the second break mass,  $m_2$ . Though  $m_2$  is fairly well constrained to have values between  $0.13$  and  $0.08 M_{\odot}$ , the low mass power-law slope,  $\Gamma_3$ , has a large range of possible slopes from 0.50 to 1.50 within the 90%  $\chi^2$  contour for models with source reddening. Panel (d) plots the same parameters

as panel (c) but for fits to the  $K$  limit = 15. These fits give somewhat flatter  $\Gamma_3$  slopes and somewhat higher mass  $m_2$  breaks, but are actually slightly better constrained. As discussed in the previous section, our model KLFs employing a 3 power-law IMF do not provide good fits to the secondary peak in the KLF. As the fit range shifts to fainter magnitudes,  $\Gamma_3$  flattens, but the total  $\chi^2$  confidence depreciates due to the secondary peak. We explore the IMF parameters necessary to fit this secondary peak in the next section.

**Fitting the secondary peak in the Trapezium cluster KLF.** In contrast to our expectations when we interpreted the literature Trapezium KLF in Section 2.6.2, the departure from a power-law decline and the formation of a secondary peak at the faint end of the Trapezium KLF remains after correcting for reddened background field stars. When we attempt to fit the faint KLF using an underlying three power-law IMF, we find that our model KLFs, while producing excellent fits over the majority of the Trapezium KLF, could not simultaneously reproduce the formation of the secondary peak. Since there is no known corresponding feature in the mass-luminosity relation (see Section 3.4.2), we hypothesize that the KLF's break from a single continuous declining slope at  $K > 14.5$  ( $M < 30 M_{Jup}$ ) and the formation of a secondary KLF peak directly imply a similar break and feature in the cluster IMF. Further, the rapid tailing off of the cluster KLF below this secondary peak also directly implies a similar rapid decline or truncation in the underlying IMF, as was also discussed in LR2000.

We modeled the secondary KLF peak by adding a fourth, truncated, power-law segment,  $\Gamma_4$ , to the three power-law IMFs derived in section 5. The truncation of the fourth power-law segment enabled us to model the rapid tailing off of the cluster KLF below the secondary peak, but was also dictated by the artificial low mass cut off present in the adopted merged PMS tracks, which for the substellar regime come from DM97. As such, the truncation mass of the model IMF was arbitrarily set to  $0.017 M_{\odot}$ . We found that this 4 power-law truncated IMF produced good  $\chi^2$  model KLF

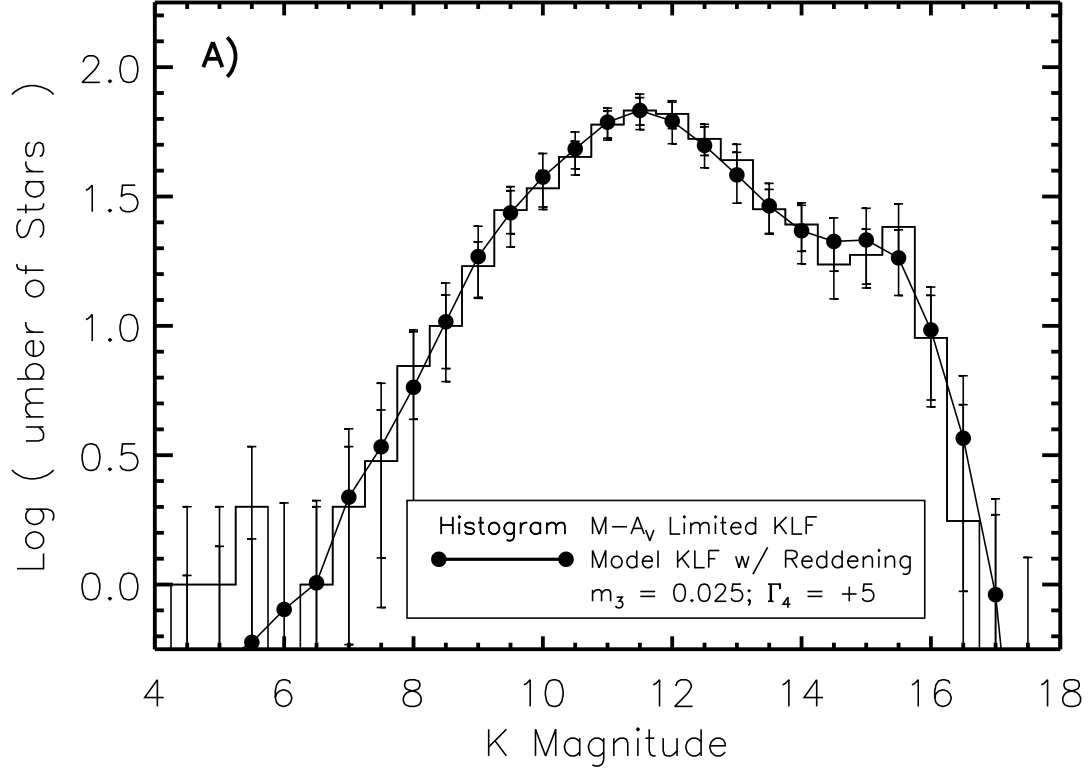


Figure 3–13: Trapezium cluster: best fit model KLF to secondary KLF peak. The Trapezium  $M - A_V$  limited KLF fit over the entire luminosity range using a four power-law IMF with a lower mass truncation ( $\sim 17 M_{Jup}$ ). The brown dwarf IMF breaks from a steady decline ( $\Gamma_3 = 0.73$ ) between 0.03 and  $0.02 M_\odot$  and rises to the mass truncation. Above the  $m_3$  mass break the IMF is that described in Table 3–3 for fits to  $K = 15$ .

fits to the secondary KLF peak. The best fit model KLF shown in Figure 3–13 has an underlying brown dwarf IMF that breaks from a steady decline at  $m_3 = 0.025 M_\odot$  and then rises steeply with  $\Gamma_4 \sim -5$  before truncating at the lower mass limit. Examination of the confidence intervals for the  $m_3$  and  $\Gamma_4$  parameters showed that higher mass breaks ( $m_3 \sim 0.035$ ) required flatter  $\Gamma_4$  slopes, but they had worse  $\chi^2$  and peaked before the observed peak at  $K=15.5$ . This suggests that were the slope of the mass-luminosity relation continuous (and constant) toward lower masses, the exact location of the secondary IMF peak would shift to somewhat lower masses than we can derive using the truncated PMS tracks.

### 3.3.3 Derived Trapezium Cluster IMF

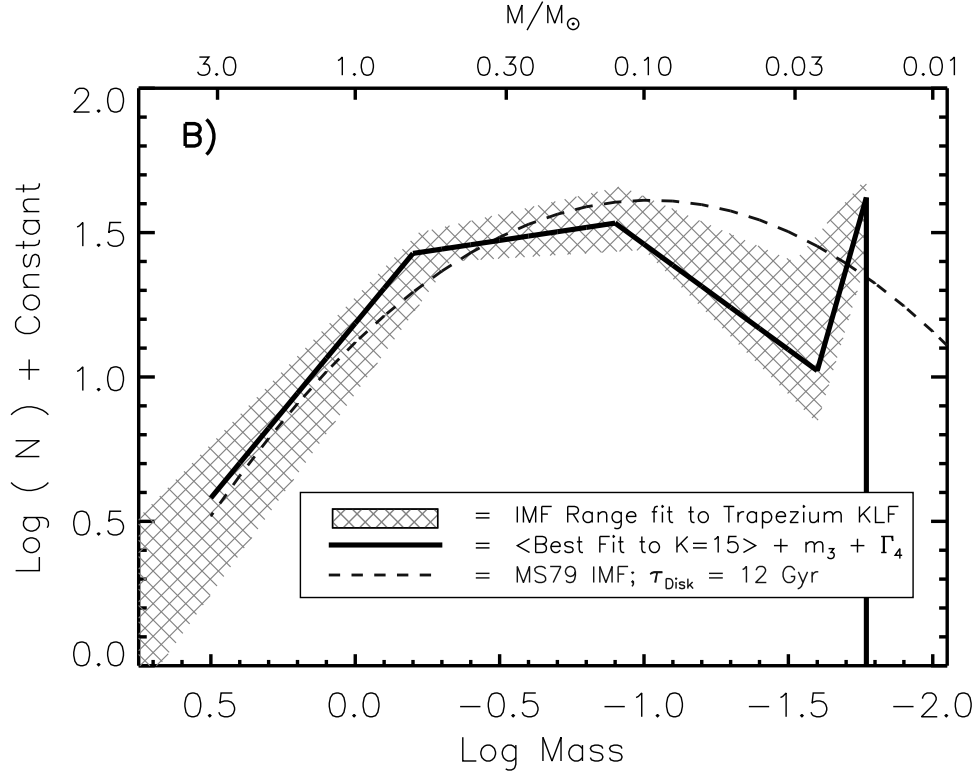


Figure 3–14: Trapezium cluster: overall derived IMF. Hatched areas are derived from the range of 90% confidence contours for KLF fits. Solid line is the best fit Trapezium IMF listed in Equation 3.1. The Trapezium IMF is also compared to the log-normal Miller & Scalo (1979) field star IMF.

**The overall cluster IMF.** Figure 3–14 shows our overall best fit Trapezium IMF and graphically displays the range of cluster IMFs permitted by our modeling of the Trapezium KLF using our standard set of merged PMS tracks. We adopt the following four power-law function with a truncation at the lowest masses for the underlying IMF of the Trapezium:

$$\frac{dN}{d \log M} = \begin{cases} M_{\star}^{\Gamma} & ; \quad \Gamma = \begin{cases} -1.21 & : M_{\star} > 0.600 M_{\odot} \\ -0.15 & : 0.600 M_{\odot} > M_{\star} > 0.120 M_{\odot} \\ +0.73 & : 0.120 M_{\odot} > M_{\star} > 0.025 M_{\odot} \\ -5.00 & : 0.025 M_{\odot} > M_{\star} > 0.017 M_{\odot} \end{cases} \\ 0 & ; M_{\star} = 0.017 M_{\odot} \end{cases} \quad (3.1)$$

We find that despite the use of deeper, more complete observations, the application of detailed mass and extinction limits to the cluster sample, the inclusion of source reddening into the model luminosity function algorithm and the correction of our infrared census for reddened field stars, our derived Trapezium IMF is not a significant revision over that found by studying the literature KLF. We find that the inclusion of source reddening into our modeling algorithm, while providing a more accurate representation of the cluster properties, results in cluster IMFs that have very similar power-law slopes and break masses as fits without source reddening, especially when fit to the same luminosity range. Source reddening does indeed blur the precision of the IMFs we can derive. For example, our Trapezium IMF in Equation 2.7 derived without accounting for source reddening is somewhat broader and peaks to slightly lower mass than the IMF derived here with source reddening. Though the overall derived IMF has not significantly changed from our findings in Section 2.6.2, our more complete infrared census and improved understanding of the field-star population do allow us to explore the Trapezium IMF at lower masses than Section 2.6.2. We find that the secondary peak of the observed Trapezium KLF is not the result of background field stars, and we derive a corresponding secondary peak in the low mass brown dwarf IMF between 10 and 30  $M_{Jup}$ . However, because of the restriction imposed by the low mass limit of the PMS tracks, both the precise location and amplitude of the secondary peak and the precise form of the IMF below 17  $M_{Jup}$  are somewhat uncertain.

**A closer look at the substellar IMF.** To better define the secondary peak in the Trapezium IMF, we consider only the substellar regime of the Trapezium KLF ( $K \geq 13$ ), where we can employ a different set of PMS tracks that cover the corresponding brown dwarf regime but also extend to masses less than the limit of our standard merged PMS tracks. The Burrows et al. (1997, hereafter, B97) PMS models are available from 0.12 to 0.001  $M_{\odot}$  (1  $M_{Jup}$ ), and for the relevant age range of the Trapezium. While the mass to K luminosity relation is relatively robust between

Table 3–4. Three power-law Trapezium sub-stellar IMF

IMF Parameter ( $\phi$ )	Fit to K=16.0			Fit to K=16.5		
	$\langle \phi \rangle$	$1\sigma$	median( $\phi$ )	$\langle \phi \rangle$	$1\sigma$	median( $\phi$ )
Fits to $M - A_V$ KLF w/o Off-field Correction						
$\Gamma_1$	+1.39	0.22	+1,30	+1.36	0.18	+1.30
$m_1$	0.0214	0.0022	0.020	0.0220	0.0025	0.020
$\Gamma_2$	-4.87	1.52	-5.00	-5.50	2.01	-5.00
$m_2$	0.0125	0.0012	0.012	0.0137	0.0005	0.014
$\Gamma_3$	+3.70	2.60	+4.00	+5.70	1.59	+6.00
Fits to $M - A_V$ , Off-field Corrected KLF <sup>(a)</sup>						
$\Gamma_1$	+1.53	0.13	+1,60	+1.51	0.14	+1.60
$m_1$	0.0217	0.0024	0.020	0.0228	0.0025	0.025
$\Gamma_2$	-5.43	1.95	-6.00	-5.04	2.00	-4.00
$m_2$	0.0130	0.0008	0.013	0.0137	0.0008	0.014
$\Gamma_3$	+3.87	2.47	+4.00	+5.61	2.25	+6.00

<sup>(a)</sup>  $M - A_V$  KLF has limits of  $A_V \leq 9$  and  $M \geq 0.01 M_\odot$

Note. — Fits to Sub-Stellar Trapezium KLF using B97 tracks.

different sets of PMS tracks, the B97 PMS models do display a somewhat flatter mass-luminosity relation for substellar objects than do DM97. We re-derived the cluster's  $M - A_V$  limited, background corrected Trapezium KLF following our prescription in Section 3.2.2 but using the B97 isochrone. Since the nebular background decreases our survey's completeness to heavily reddened ( $A_V > 10$ ), very low mass ( $M < 0.03 M_\odot$ ) brown dwarfs, we draw this  $M - A_V$  sample to our completeness limit rather than our  $10\sigma$  sensitivity limit to ensure the precision of the substellar IMF. The resulting  $M - A_V$  limited KLF from the extended B97 isochrone samples the cluster population to a predicted mass limit of  $0.01 M_\odot$  and an  $A_V = 9$ .

New model KLF fits (see Figure 3–15a) that employ the B97 tracks and use a three power-law underlying substellar IMF yield a power-law brown dwarf IMF falling with a similar but somewhat steeper slope than our standard tracks (see summarized

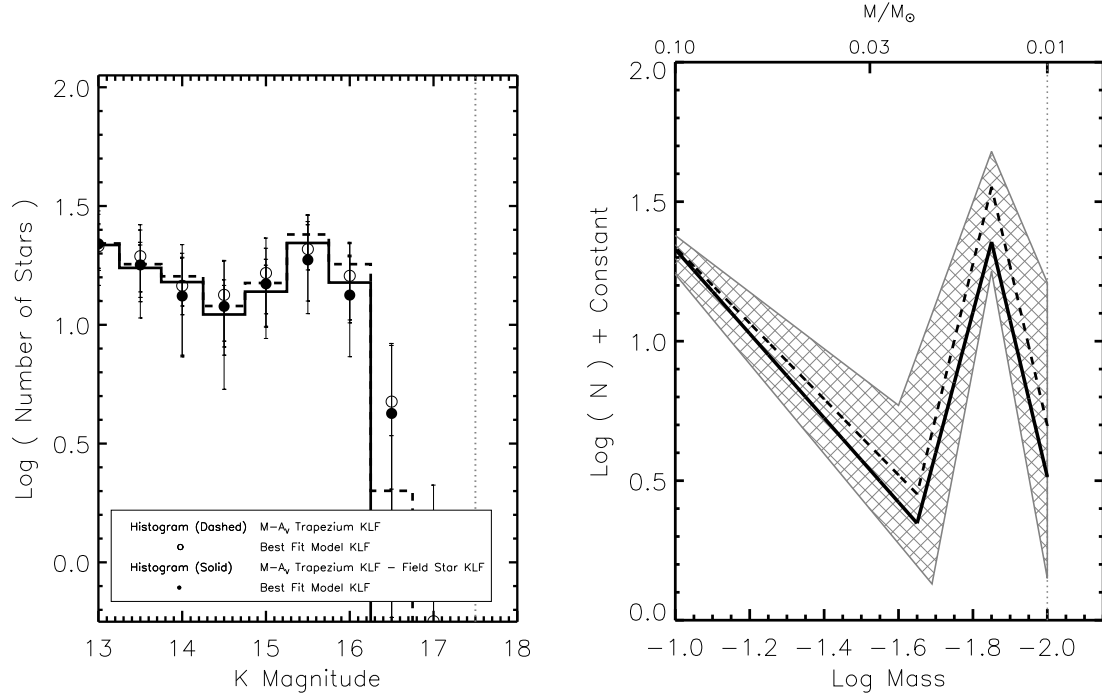


Figure 3–15: Trapezium cluster: a closer look at the sub-stellar IMF. A) The Trapezium Sub-Stellar  $M - A_V$  KLF is compared to best fit model KLFs using the B97 tracks. Two fits are shown: with field star correction (observed - solid histogram; model - filled circles); and without field star correction (observed - dashed histogram; model - open circles). Error bars for the observed KLFs are from counting statistics. Those for the model KLFs are the  $1\sigma$  bin variation from 50 model iterations. The vertical dotted line demarks the  $K=17.5$  completeness limit. B) Derived Sub-Stellar Trapezium IMF using the B97 tracks. Our mass completeness limit ( $0.01 M_{\odot}$ ) is displayed as a vertical dotted line. The IMF fit range allowed by the KLF modeling is shaded with the best fit 3 power-law IMFs from fits with and without background correction are shown (see also Table 3–4).

IMF parameters in Table 3–4)<sup>4</sup>. Similar to DM97, the B97 tracks require the presence of a significant secondary peak that departs from the power-law function at  $m_3 \sim 0.02 M_{\odot}$  and rises very steeply with  $\Gamma_4 = -5$  as shown in Figure 3–15(b). Further, the extended mass range of the B97 tracks allows us to resolve the location

<sup>4</sup> Fitting the substellar sample drawn to an  $A_V < 17$  with model LFs using B97 tracks yielded a power-law decline closer to that derived from our standard merged models

of the secondary peak: our fits require a peak near the deuterium-burning limit, i.e.,  $13 - 14 M_{Jup}$ , followed by a rapidly declining IMF with a slope of  $\Gamma_5 = +5$  down to  $10 M_{Jup}$ . The sharp decline in the substellar IMF below this peak is *not* the result of the application of the off-field correction. Fits to Trapezium substellar KLF without correcting for background field stars yield nearly identical cluster IMFs (see Figure 3–15(a) and Table 3–4). Further, the sharp decline in our derived substellar IMF below the deuterium-burning limit and independent of the background correction confirms a similar, straightforward interpretation of the observed rapid turn down in the cluster KLF and dearth of sources in the  $(H - K)/K$  color magnitude diagram nearly a full magnitude above our completeness limits (see Figure 3–5).

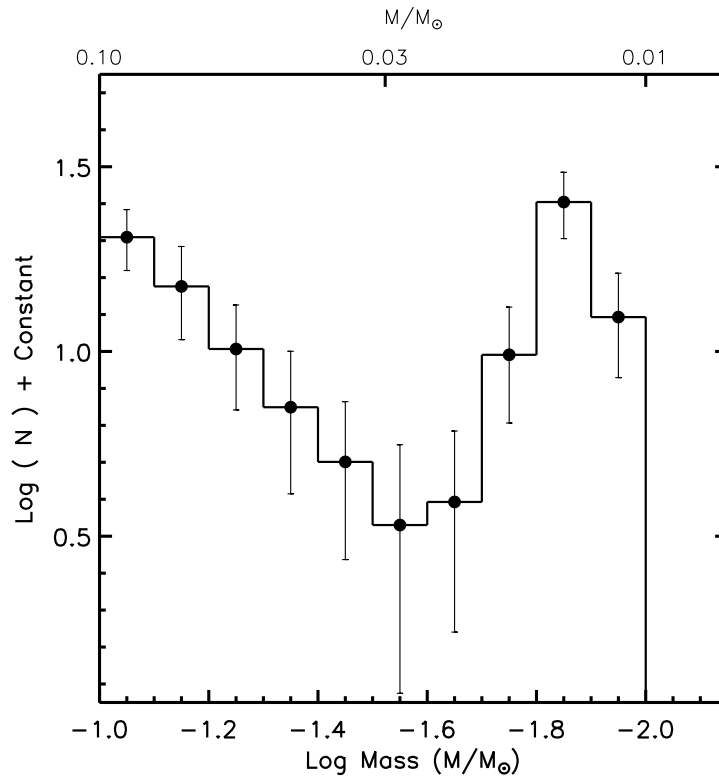


Figure 3–16: Trapezium cluster: a secondary peak in Trapezium substellar IMF. Shown is a Monte Carlo simulation of the Trapezium Sub-Stellar IMF from fifty (50) samples of 150 brown dwarfs drawn from the best fit Trapezium Sub-Stellar IMF derived from B97 tracks. The plotted histogram is the average of the iterations, and the error bars represent the derived  $1\sigma$  standard deviation of each IMF bin from the Monte Carlo simulation.

Lastly, this feature in the IMF appears to be a statistically significant departure from the power-law decline of the brown dwarf IMF as was implied by our  $\chi^2$  fitting in Section 5. We ran a Monte Carlo simulation of the derived Trapezium substellar IMF for a population of 150 brown dwarfs. In Figure 3–16 we show the resulting histogram form of the average simulated cluster IMF. Using equally sized bins in log mass units, we calculated the statistical variation in an IMF bin as a function of 50 drawn samples. From these plotted  $1\sigma$  error bars, it is clear that the derived secondary peak is a significant statistical result. In addition, these results imply that a statistically significant identification of such a feature at the tail of the IMF requires the examination of a rich substellar population such as that provided by the Trapezium Cluster.

### 3.4 Discussion

#### 3.4.1 Structure of the Trapezium KLF and IMF

**The stellar regime.** From our careful construction and improved modeling of the Trapezium Cluster KLF, we are able to derive the underlying Trapezium Cluster IMF, spanning the entire mass range from OB stars to substellar objects near the deuterium-burning limit. We find that the stellar Trapezium IMF first rises steeply with a Salpeter-like power-law slope from high-mass stars to near  $0.6 M_{\odot}$  where the IMF flattens and forms a broad peak extending to the hydrogen burning limit. There the IMF turns over and declines into the brown dwarf regime. From our modeling experiments in Chapter 2, we knew that where an underlying IMF has a power-law form, the young cluster’s model KLF also has a power-law form. Further we found that peaks in the model KLFs can arise both due to peaks in the underlying IMF and from features in the M-L relation. From our current modeling of the Trapezium KLF, we find that these conclusions about the relationship between the structure of the KLF and IMF are unchanged by the presence of source reddening. The power-law slope of the bright end ( $K < 11.5$ ) of the cluster KLF reflects the power-law slope of the

derived IMF. The formation of the primary KLF peak is also similar to the structure of the underlying IMF we derive. The broad main peak of the Trapezium KLF is formed by a combination of a peak in the underlying stellar IMF and a feature in the theoretical mass-luminosity relation due to deuterium-burning. Moreover, we find that our KLF modeling has allowed us to disentangle these two effects. The main KLF peak at  $K = 11 - 11.5$  corresponds to PMS stars between  $0.4$  and  $0.2 M_{\odot}$ , which according to the DM97 PMS models are undergoing deuterium-burning at the mean age of this cluster, while the derived IMF has a broad peak at somewhat lower masses ( $0.2-0.08 M_{\odot}$ ) than the KLF peak would to first order imply. Lastly, our detailed KLF modeling has determined that the turn-over and decline in the cluster KLF does reflect a similar turn-over and decline of the Trapezium IMF across the hydrogen burning limit and is not solely a product of the deuterium-burning spike (e.g., [Zinnecker et al., 1993](#)).

**The substellar regime.** As in our work in Section 2.6.2, our KLF modeling technique has permitted us to derive the Trapezium substellar IMF, while the improved depth of our IR census has allowed us to extend this derivation from  $0.03 M_{\odot}$  down to near the deuterium-burning limit. Our KLF modeling that now includes source reddening confirms that the steady decline of the cluster KLF between  $K = 12$  and  $K = 15$  reflects a steady power-law decline in the substellar IMF. Independent of our modeling results, however, no more than  $22^{+4}_{-2}\%$  of the sources are substellar objects<sup>5</sup>.

The secondary peak in the brown dwarf regime of the cluster KLF at  $K=15.5$  and the subsequent rapid decline of the cluster KLF, however, do not correspond to any known features in the theoretical mass-luminosity relations we have examined (see Section 3.4.2 and Figure 3–17). Moreover, detailed KLF modeling using two different

---

<sup>5</sup> Error based upon the uncertainty in the hydrogen burning limit due distance and cluster mean age.

sets of PMS tracks require both the presence of a break from a single power-law decline of the Trapezium brown dwarf IMF around  $0.02 - 0.03 M_{\odot}$  and the formation of a significant, secondary IMF peak. Using the B97 tracks, this IMF peak is located near the deuterium-burning limit,  $13-14 M_{Jup}$ , and is followed by a rapid decline to lower masses. Although both sets of PMS tracks suggest the presence of a secondary peak, the precise details (e.g., location and amplitude) may be track dependent. For example, in the Trapezium substellar IMF found using the B97 tracks, 36% of the brown dwarfs in the cluster are found in the secondary IMF peak while 64% have their mass distribution governed by the power-law regime. For the IMF found using our standard merged tracks, these numbers are 15 and 85%, respectively, however the truncation of the tracks at the lowest masses will slightly skew these latter percentages.

One proviso to the derivation of a significant IMF peak at the deuterium-burning limit is the contamination of our IR census by non-cluster members. Though, we have accounted for the background field star contribution to the cluster KLF, we have also shown that there is reasonable uncertainty in the cloud extinction properties. Additionally, the large beamsize of the  $C^{18}O$  map may mask low extinction holes in the molecular cloud. Since there are  $\sim 75$  sources in the secondary peak of the  $M - A_V$  limited KLF before background subtraction, our current background field star estimate would have to be off more than a factor of two to remove any feature from the IMF at these low masses; it would have to be off by a factor of 4, however, to account for all of the brown dwarf members. Alternately, our IR census may be contaminated by the presence of low mass members from the intervening but only slightly older Orion OB1c association. While these sources cannot create such a secondary peak, they could contribute to the overall KLF and IMF. Since these sources are somewhat older, they would appear at fainter magnitudes, skewing the KLF and IMF to lower masses and producing an over-estimate of the number of brown dwarfs. Though spectroscopic follow up of a few of these faint sources would separate out

background stars (and provide a good test of the  $C^{18}O \rightarrow A_V$  conversion), members of the foreground OB1 association would be difficult to spectroscopically separate from actual Trapezium cluster members because even at these older ages they will not have evolved very much in temperature or surface gravity. However, as we have shown, the derived turn down in the “sub-brown dwarf” IMF below the deuterium-burning limit appears independent of background correction.

We conclude, therefore, that if the mass-luminosity relation for low mass brown dwarfs is reasonably robust and does not contain a previously unidentified feature, and our estimate of the contamination of our infrared census by non-cluster members is accurate, then the existing structure of the faint cluster KLF can only be created by a break from a single declining power-law brown dwarf IMF, the formation of a corresponding peak in the underlying Trapezium IMF near the deuterium-burning limit, and a rapid decline of the IMF into the planetary mass regime.

### 3.4.2 Sensitivity of Results to Theoretical PMS Models

The accuracy of an IMF derived for a young stellar cluster is intrinsically dependent upon the robustness of the conversion from observables to a mass function (or individual masses) provided by the theoretical evolutionary models. In Chapter 2, we came to the somewhat surprising conclusion that model KLFs were fairly insensitive to differences in the evolutionary PMS models from which the mass-luminosity relations were drawn. This was despite that fact that the detailed physics (e.g., opacities, model atmospheres, internal convection theory, and initial conditions) involved with calculating the theoretical PMS evolutionary models are poorly constrained and that changes in the assumed physics of these models have been shown to produce significant differences in the locations of evolutionary tracks and isochrones on the theoretical HR diagram (D’Antona & Mazzitelli, 1994, 1997; Baraffe et al., 1998; D’Antona, 1998; Siess et al., 2000; Baraffe et al., 2002). Our findings in Chapter 2 would also appear to disagree with recent summaries of the IMF in young clusters which concluded,

based upon the track variations in the HR diagram, that the accuracy of current PMS models are the primary uncertainty to the form of the derived IMF (Meyer et al., 2000). Therefore, we explore in more detail the dependence of the theoretical mass-luminosity relation relevant for luminosity function modeling upon the different PMS tracks.

In Figure 3–17 we compare the theoretical mass-infrared luminosity (K magnitude) relations converted from six sets of theoretical PMS models for a progressive series of young cluster mean ages. In Table 3–5 we summarize the different input physics and parameters used by various PMS models. The sets of theoretical PMS models were taken from literature sources and converted to observables using a single set of bolometric corrections (see Section A). Remarkably, the theoretical mass-K magnitude relations are fairly degenerate between the different PMS models, and those differences that do exist are the largest at very young ages ( $\tau < 1$  Myr), agreeing with the recent analysis of (Baraffe et al., 2002). Consequently, this implies that for the Trapezium Cluster there will be some uncertainty in our derived mass function due to the PMS tracks. On the other hand, while the models of B97 and Siess et al. (2000) display the most significant variations in their predicted M-L relations, we have shown in Section 3.3.3 that the substellar Trapezium IMF derived from KLF modeling using the B97 tracks is not significantly different than that found using the DM97 tracks. As we concluded in Section 2.5.1, most differences in the mass-luminosity relations due to differences in input physics are much smaller than we could ever observe and will not impact our modeling results. This result may be understood by considering the fact that the luminosity of a PMS star is determined by very basic physics, simply the conversion of gravitational potential energy to radiant luminosity during the Kelvin-Helmholtz contraction. And this primarily depends on the general physical conditions in the stellar interior (e.g., whether the interior is radiative or partially to fully convective). The luminosity evolution at the youngest ages ( $< 1$  Myr) will depend, however,

Table 3–5. Evolutionary models used to compare M-L relations

Model Name	$\tau_{min}$ <sup>(b)</sup> (Myr)	$M_{max}$ ( $M_{\odot}$ )	$M_{min}$ ( $M_{\odot}$ )	Initial <sup>(c)</sup> Conditions	$[\frac{D}{H}]$ <sup>(d)</sup>	Opacity <sup>(e)</sup> Table	EOS <sup>(f)</sup>	Convection <sup>(g)</sup> Model	Atmosphere <sup>(h)</sup> Model
DM94	0.1	2.50	0.020	Canonical	2.0	OPAL92+Alex89	MHD	FST-1	Gray
B97	0.1	0.15	0.001	Canonical	2.0	?	SC	?	Non-Gray
DM97	0.1	3.00	0.017	Canonical	2.0	OPAL92+Alex94	MHD+OPAL	FST-2	Gray
BCAH98	1.0	1.40	0.020	Canonical	2.0	OPAL96+Alex94	SCVH	MLT-1.0	Non-Gray(NextGen)
PS99	0.1	6.00	0.100	Birthline	—	OPAL96+Alex94	PTEH	MLT-1.5	Gray
SDF00	0.1	7.00	0.100	Canonical	2.0	OPAL96+Alex94	PTEH(r)	MLT-1.6	Analytic Fit

(a) All models used standard solar metallicity ( $Z=0.02$ ).

(b) Minimum Age (Myr) listed by the models.

(c) Initial Physical Conditions from which the tracks are evolved. Canonical: the model stars are evolved from “infinite” spheroids; Birthline: the PS99 models begin with spherically accreting (single accretion rate,  $10^{-5} M_{\odot} yr^{-1}$ ) protostars evolving along the birthline before beginning their PMS contraction phase.

(d) Deuterium abundance relative to hydrogen, in units of  $10^{-5}$ . The initial D/H for the PS99 models was  $2.0 \times 10^{-5}$ , however this is significantly modified by the burning of deuterium during the model’s proto-stellar phase.

(e) Opacity Table (interior not atmosphere): Alex89 (Alexander et al., 1989); OPAL92 (Rogers & Iglesias, 1992); Alex94 (Alexander & Ferguson, 1994); OPAL96 (Rogers et al., 1996)

(f) Convection Model: FST (Full Spectrum Turbulence. FST-1: Canuto & Mazzitelli (1991, 1992), FST-2: Canuto et al. (1996)); MLT-1.X (Mixing Length Theory,  $1.X = \alpha = 1/H_p$ )

(g) Equation of State: MHD (Mihalas et al., 1988); SC (Saumon & Chabrier, 1991, 1992); SCVH (Saumon et al., 1995); PTEH (Pols et al., 1995, r: Revised by SDF), OPAL (Rogers et al., 1996)

(h) Treatment of Atmosphere: Analytic Fit (SDF00) is a 1D fit of  $T(\tau)$  to atmosphere models; NextGen (Hauschildt et al., 1999)

on the initial conditions of the contracting PMS star as it exits its proto-stellar stage, though these differences are quickly erased (Baraffe et al., 2002).

This is significantly different than the situation for mass functions derived by placing the stars on the theoretical HR diagram using spectroscopic and photometric observations. Because most young stars have late type K-M spectral types, they are on nearly vertical Hayashi contraction tracks in the HR diagram. As a result a star's mass derived from the HR diagram is primarily a function of its assigned effective temperature, i.e., its observed spectral type. We illustrate this dependence in Figure 3–18(a) where we plot the predicted effective temperatures as a function of mass for stars in a 1 Myr old cluster. In contrast to the quite similar mass-luminosity relations, a star's mass derived based upon its spectral type is uncertain due to differences in the PMS models by factors of 3 (or more). The conversion from spectral type to mass is made worse by the uncertain conversion of spectral type to effective temperatures for late type sources, resulting from their sub-giant gravities (Luhman, 1999). Such uncertainties will undoubtedly result in spectroscopically derived IMFs that vary substantially as a function of PMS tracks used (compare, for example, the Luhman et al., 2000, derivation of the Trapezium IMF from DM97 and BCAH98 tracks). Further, these track differences, while decreasing with time, are not resolved by 5 Myr as shown in Figure 3–18(b). In summary, the uncertainties in the PMS models primarily manifest themselves in variations in the predicted effective temperatures of the young stars rather than the predicted luminosities.

We do not surmise that luminosity function modeling, which employs mass-luminosity relations, is free from systematic dependencies. As concluded in Chapter 2, a cluster's mean age must be known in order to derive a cluster's initial mass function from its luminosity function; this can only be derived from placing the stars on the theoretical HR diagram. In general, however, age is a function of luminosity for low mass stars on the HR diagram and will be more or less similar when derived

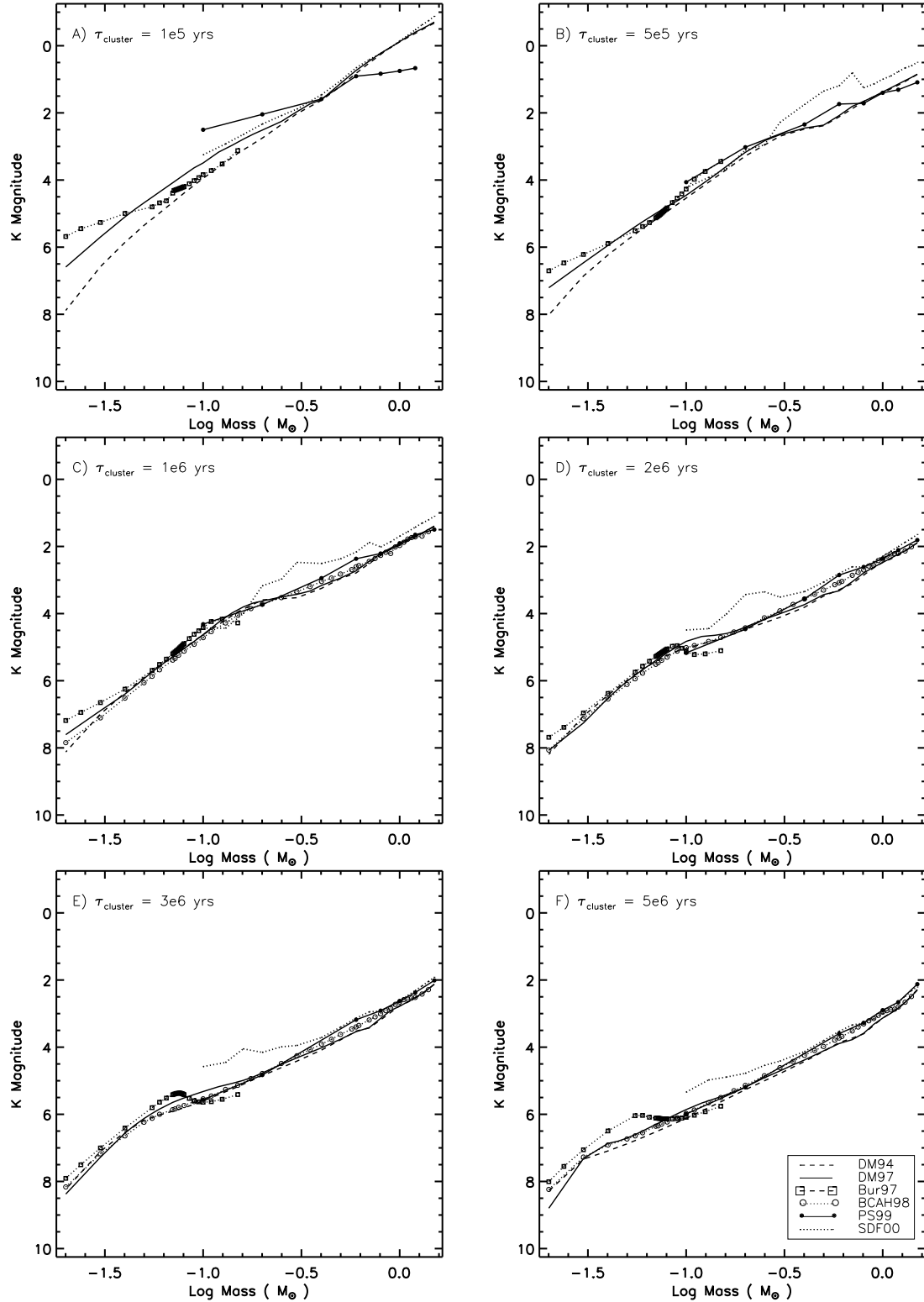


Figure 3–17: Comparison of theoretical mass-luminosity relations. Theoretical pre-main sequence mass-luminosity (infrared K band) relations were extracted from six different sets of evolutionary models (see Table 3–5). In all cases the intrinsic model quantities (luminosity, effective temperature) were converted to K magnitudes using a single  $T_{\text{eff}}$ -bolometric correction relationship. Shown for 6 sets of cluster mean ages: 0.1 (a); 0.5 (b); 1 (c); 2 (d); 3 (e), and 5 (f) Myr. [Baraffe et al. \(1998\)](#) models do not include models for ages less than 1 Myr.

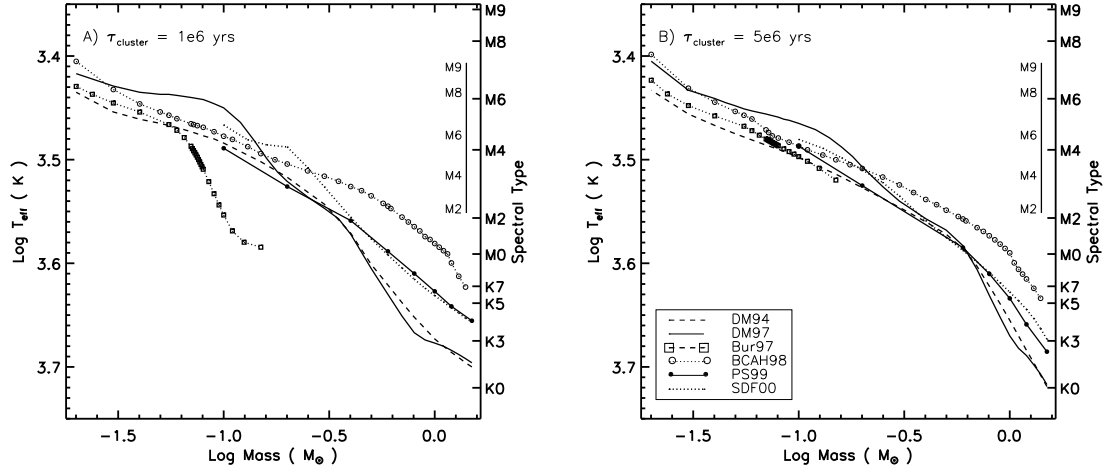


Figure 3–18: Comparison of theoretical  $M$ - $T_{eff}$ -spectral type relations. (Figure adopted and revised from [D’Antona, 1998](#)). The spectral type - effective temperature - mass relationships were taken directly from the 6 sets of PMS models at 1 (A) and 5 (B) Myr. Also shown is the gravity (dwarf vs sub-giant) dependence of the spectral type to effective temperature calibration for late type PMS stars. Because very young subsolar mass stars and brown dwarfs are primarily on vertical Hayashi contraction tracks in the HR diagram, there is theoretically a close correspondence between effective temperature and mass. The effective temperature to spectral type scale (right hand y-axis) is a cool dwarf scale (summed from [Kenyon & Hartmann, 1995](#); [Bessell, 1995](#); [Wilking et al., 1999](#)). The inset spectral sequence is the hotter sub-giant temperature-spectral scale tuned by [Luhman & Rieke \(1999\)](#).

from these PMS models. The exception again occurs at the youngest ages, where the definition of a star’s age may differ if the models include the proto-stellar lifetimes. Even in the case of the [Palla & Stahler \(1999, hereafter, PS99\)](#) models, which begin as protostars accreting along an initial mass-radius relationship or birthline in the HR diagram ([Stahler, 1983](#)), the mass-luminosity relations are not substantially divergent from canonical theoretical models except at the very youngest ages.

### 3.4.3 Comparison of IR-Based Trapezium IMFs

In addition to our initial modeling in of the Trapezium in Section 2.6.2 and our present study, a number of other authors have recently derived Trapezium IMFs based upon deep infrared observations. While all of these derivations make use of the same set of theoretical pre-main sequence models for converting observations to mass

(functions), they use somewhat different cluster parameters and employ a variety of different methodologies. Systematic uncertainties might arise due to varying of cluster parameters such as distance, due to different assumptions about the cluster population such as field star contamination or from simple observational effects such as survey area or the wavelength regime analyzed. Further, it is not understood how closely different methods can arrive at the same IMF.

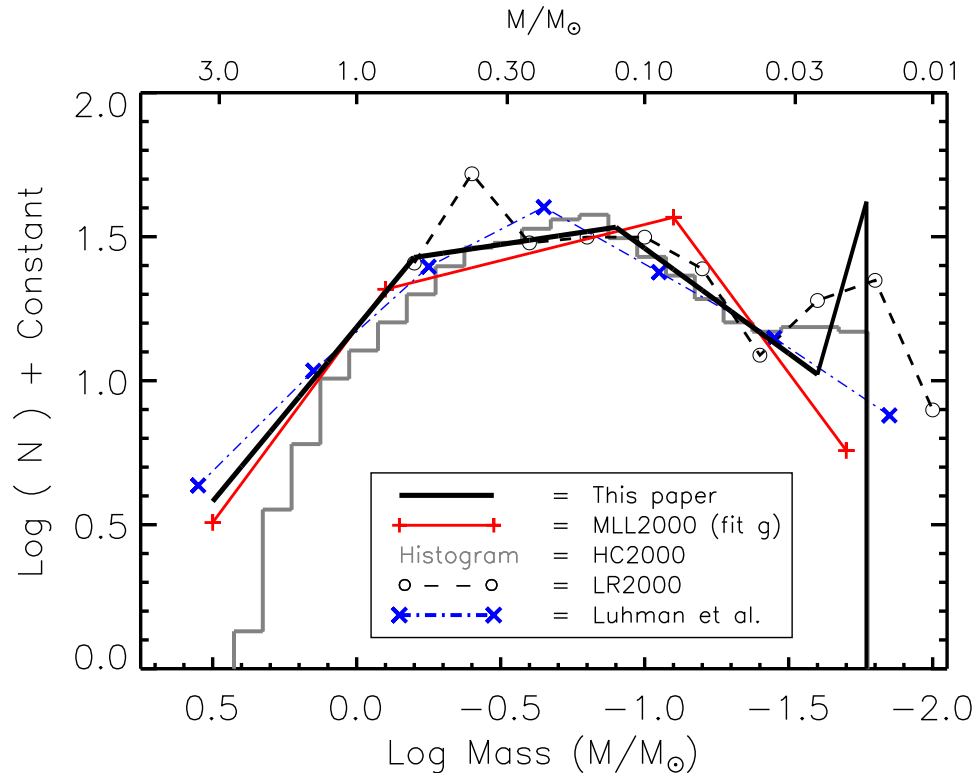


Figure 3–19: Comparison of Trapezium IMFs from IR photometry. All derivations used the DM97 PMS tracks for masses less than  $1 M_{\odot}$ . Table 3–6 summarizes differences among the derivation methods. The HC2000 Trapezium IMF corresponds to their  $A_V < 10$  limited sample. The “MLL2000” IMF is fit (g) from Table 2–2.

In Figure 3–19 we compare the IMFs derived by us in Section 2.6.2, and in Section 3.3 to those derived by LR2000, HC2000 and Luhman et al. (2000). Globally, these IMFs are remarkably similar. They all have Salpeter-like high-mass slopes, all reach a broad peak at subsolar masses and all decline in frequency with decreasing mass below the hydrogen burning limit with brown dwarf IMF slopes between +1

and +0.5. After inspecting the different methods and cluster parameters used by these authors, which we summarize in Table 3–6, this result should be in part expected. When different methods use the same PMS tracks (in this case DM97;  $M < 1 M_{\odot}$ ) and essentially the same star-forming histories, the resulting IMFs should basically agree.

The cluster parameters used by these workers are not exactly homogeneous. Further, there are slight variations between these IMFs that might be due in part to observational effects. For example, the truncation or turn down in the high-mass end of the LR2000 and HC2000 IMFs is due to bright source saturation in these surveys, not to a real IMF feature. At the low mass end, the IMF derivations appear to diverge below  $30 M_{Jup}$  (-1.5 in log solar mass units) with a “spike” in the LR2000 IMF but no feature in the Luhman et al study. Because LR2000 surveys the largest area while the Luhman et al. (2000) study surveys the smallest area, one might suspect that this difference is due to an increase in field star contamination or, perhaps, counting statistics for the smaller study. The latter is the most likely explanation since both our study and that of HC2000 survey similar large areas and apply field star corrections while finding substellar IMFs that contain either a secondary peak or a plateau at the lowest masses.

Lastly, the methodologies employed range from a purely statistical approach (e.g., our LF modeling) to the derivation of individual masses of the stars via a hybrid combination of spectroscopy and infrared colors (e.g., Luhman et al.). It is unclear how to make detailed comparisons of these methods, however, in general, the LR2000, HC2000 and our LF modeling primarily depend upon the theoretical mass-luminosity relation extracted from the PMS tracks. The stellar portion of the Luhman et al IMF depends upon the theoretical HR diagram, while the substellar depends upon the predicted infrared colors and magnitudes. One apparent difference between the resulting IMFs that might be related to the different methods is the exact location of the IMF’s “peak,” or what is sometimes termed the “characteristic” mass. This

Table 3–6. Comparison of published Trapezium IMFs based on IR photometry

Work Name	IMF Method	Distance (pc), (m-M)	$\tau, \Delta\tau$ <sup>(a)</sup> (Myr)	Extinction? <sup>(b)</sup>	IR Excess? <sup>(b)</sup>	Field Star <sup>(b)</sup> Correction?	$A_V$ Limit?	IMF Peak ( $\frac{M}{M_\odot}$ )	Area <sup>(c)</sup> ( $\square$ pc)	Comments <sup>(d)</sup>
chapter 2	Model KLF Fit	400, 8.00	0.8, 1.2	Not Included	Not Included	Not Included	None	0.08	0.34	Literature K only
HC2000	(H-K)/K	480, 8.40	0.4, 1.0	Derived	Empirical	Reddened Galaxy Model	$A_V < 2.5, 10,$ no limit	0.15	0.35	Keck H, K
LR2000	$M_J \rightarrow M_\odot$	440, 8.22	1.0, 0.0	Derived	Assumed None	Assumed None	(J-H) < 1.5	0.40	0.50	UKIRT I, J, H
Luhmen et al	IR Spectra + Colors	450, 8.27	0.4, $\sim 1$	Derived	Assumed None	Assumed None	$A_H < 1.4$	0.25	0.073	NICMOS F110, F160
chapter 3	Model KLF Fit	400, 8.00	0.8, 1.2	EPDF Derived	IXPDF Derived	Reddened Obs. KLF	$A_V < 17$	0.10	0.34 (0.57)	FLWO + NTT J, H, K

<sup>(a)</sup>Cluster mean age and age spread used by authors. For [Luhman et al. \(2000\)](#), an empirical star forming history was used by the authors and those tabulated here are approximate characterizations.

<sup>(b)</sup>Listed if and how these quantities: extinction, excess and the contribution of background field stars, were included into that work's IMF derivation.

<sup>(c)</sup>Size (area) of surveys in  $\square$  parsec assuming  $D = 400$ pc. The two values for this work are for the NTT/FLWO overlap region and the larger FLWO region.

<sup>(d)</sup>Comments include location of observation(s) and broadband filters used.

Note. — All IMF derivations used the [DM97](#) pre-main sequence models for masses less than  $1 M_\odot$ .

References. — HC2000: [Hillenbrand & Carpenter \(2000\)](#); LR2000: [Lucas & Roche \(2000\)](#); Luhmen et al: [Luhman et al. \(2000\)](#)

“peak” mass varies between IMF derivations by 0.7 dex in log solar mass units. It is not immediately apparent that internal uncertainties in the IMF derivations could cause this scatter. For example, the “peak” of the Trapezium IMF from Section 2.6.2 is revised only 0.1 dex by the inclusions of source reddening. For methods that depend upon mass-luminosity relations, the resulting IMF will be dependent upon the assumed cluster distance and age; modest changes in these parameters should result in slightly different M-L relations and slightly different IMFs. However, there is no strict correlation between “peak” mass and the cluster age or distance used. Hence, we conclude that specific IMF details such as the exact location of “peak” mass cannot be securely identified by these methods; although, we can conclude that the Trapezium IMF peaks at subsolar masses somewhere between  $0.3 M_{\odot}$  and the hydrogen burning limit.

### 3.5 Conclusions

Using a new and very complete near-infrared census of the Trapezium Cluster, we have performed a detailed analysis of the Trapezium Cluster’s K band luminosity function and its underlying mass function. Following our earlier work in Chapter 2, we expanded our luminosity function modeling to include the effects of source reddening, and we studied in detail the field star contribution to the cluster KLF. We applied our new models to the Trapezium KLF to explore its structure and to derive the cluster’s initial mass function. From this analysis we draw the following conclusion(s):

1. The Trapezium Cluster IMF rises in number with decreasing mass and forms a broad peak at subsolar masses between  $0.3 M_{\odot}$  and the hydrogen burning limit before declining into the brown dwarf regime. Independent of modeling details, no more than  $\sim 22\%$  of the young sources fall below the hydrogen burning limit, placing a strict limit on the brown dwarf population in this cluster.
2. The Trapezium Cluster substellar IMF breaks from a single declining power-law slope between  $0.02$  and  $0.03 M_{\odot}$  and forms a significant secondary peak near the

deuterium-burning limit ( $\sim 13 M_{Jup}$ ). We derive these results through detailed analysis of the likely field star contamination and from our modeling of the cluster’s faint KLF using two different sets of theoretical mass-luminosity relations, although the precise details of this peak do depend upon the PMS models. Regardless, this peak may contain between 15 and 36% of all the substellar objects in this cluster. Below this peak the substellar IMF declines rapidly toward lower masses suggesting that the yield of freely floating, planetary mass objects during the formation of the Trapezium Cluster was extremely low.

3. We find that source reddening (due to infrared excess and extinction) has only modest effects upon our modeling of the Trapezium cluster’s luminosity function. Source reddening tends to broaden the IMFs derived and blur the precision with which we can derive IMF parameters. However, the Trapezium IMF we derive here after accounting for source reddening and field stars is not a substantial revision over that Trapezium IMF we derived in Chapter 2.

4. Pre-main sequence luminosity evolution and the resulting age dependent mass-luminosity relations are relatively robust results of most modern PMS evolutionary models, except at the very youngest ages where the models are affected by initial conditions. Conversely, the predicted effective temperatures, hence predicted spectral types, are considerably less robust. This suggests that modeling a cluster’s K band luminosity function is likely to produce a faithful representation of the true IMF of the cluster. Further, we find that the different published methodologies used for deriving the Trapezium IMF from near-infrared photometry produce nearly identical results, although the precise location of a “peak” or characteristic mass for the Trapezium cannot be securely identified.

## CHAPTER 4 THE YOUNG CLUSTER IC 348 IN PERSEUS

Infrared detector technology has often provided the impetus for new, sensitive, and revealing studies of young clusters and star-forming regions. At the very early stages of this technology, for example, the young partially embedded IC 348 cluster, which is the focus of this chapter, was investigated in the infrared using a single channel photometer by [Strom et al. \(1974\)](#) who used this instrument to discover heavily embedded sources at the interface of the cluster with the Perseus Molecular Cloud.

The development of array format IR cameras yielded very large surveys of giant molecular clouds (GMCs) (e.g., the Orion B GMC; [Lada et al., 1991](#)) and young clusters such as IC 348. These intensive surveys often consisted of large mosaics containing tens to hundreds of individual frames; the [Lada & Lada \(1995, hereafter, LL95\)](#) survey of IC 348 required, for example, twenty four separate tiles to cover the cluster's central parsec. Recent advancements to infrared detector technology have permitted the development of wide-field infrared cameras that provide a motivation to revisit large area IR surveys of GMCs and young clusters.

The very sensitive and contiguous coverage provided by these wide-field cameras allows, for example, the simultaneous coverage of large cluster areas and the efficient census taking of candidate young brown dwarfs as small 10 Jupiter masses ( $M_{Jup}$ ) found deeply embedded ( $A_V \sim 5 - 10$ ) in the parental cloud. Combining such a wide-field IR census with tools for studying the characteristics of the stars and brown dwarfs in young clusters such as the construction and modeling of their luminosity functions ([Muench et al., 2000, 2002](#)), permits the testing of various hypotheses about the cluster's initial structure and mass function. For example, one often cited advantage to studying the mass function of very young clusters is that few members will have been

lost due to the cluster's dynamical expansion. Recent N-body experiments, however, have shown that considerable dynamical evolution may occur in clusters within one million years after the expelling of the molecular gas (Kroupa et al., 2001). Other simulations suggest that some mass segregation could be primordial (Bonnell et al., 2001). Thus, the combination of wide-field infrared imaging with luminosity function modeling may provide important clues about the spatial distribution of stellar masses while the cluster is still embedded in the parental cloud.

IC 348 has been the target of a number of wide-field studies since the Lada & Lada IR survey. Wide-field optical (Luhman, 1999), H $\alpha$  (Herbig, 1998) and X-ray imaging (Preibisch et al., 1996) have all reinforced the LL95 finding that IC 348 is spatially extended on the sky and partially embedded at the edge of the Perseus GMC. In our current wide-field near-IR imaging, we are able to survey in a single image an area encompassing nearly all the boundaries of these past surveys while probing very low mass sources ( $0.01 M_{\odot}$ ) over a much larger cluster volume (larger extinction) than prior studies. We use the results of our infrared census to examine the cluster's structure, reddening and relationship to the Perseus Molecular Cloud in Section 4.1. Following from our analysis of the Trapezium cluster's luminosity and mass function in Chapter 3, we construct the K band luminosity function for IC 348 in Section 4.2. In Section 4.3 we employ our model luminosity function algorithm to derive and to study the IMF of IC 348, encompassing with our wide-field surveys much larger area than past IMF studies which have concentrated on the central core of the cluster (Luhman et al., 1998; Najita et al., 2000). From this analysis, we compare our results for IC 348 and the Trapezium and discuss in Section 4.4 the impact of spatial and statistical IMF variations on meaningful comparisons of the IMFs for different clusters.



Figure 4–1: Infrared color composite image of IC 348. For orientation, north is up while east is left and the field of view is  $20.5 \times 20.5'$ . The bright blue star to the north by northwest is  $\alpha$  Persei. The cluster's interface with the Perseus Molecular Cloud is clearly outlined by a series of nebular features and enshrouded or heavily reddened sources along the southern edge of the image. The series of blue-green-red sources to the south by southwest of the cluster center is the asteroid 545 Messalina.

## 4.1 Wide-Field Near-Infrared Images of IC 348

### 4.1.1 FLAMINGOS Observations

We obtained wide-field near-infrared images of the IC 348 cluster using the FLoridA Multi-object Imaging Near-IR Grism Observational Spectrometer (FLAMINGOS, [Elston, 1998](#)) on the 2.1m telescope at the Kitt Peak National Observatory,

Table 4–1. Summary of FLAMINGOS observations of IC 348

Target	Filter	Julian Date	Exp. (sec)	Dithers	Total Exp. (sec)	Airmass	Seeing ( $''$ )	$5\sigma$ (mag)	Flat-Field type
IC 348	K	2452257.82961	20	49	980	1.139	1.60	16.81	dome
IC 348	H	2452257.85944	20	48	960	1.262	1.81	17.69	sky
IC 348	J	2452257.88446	20	46	920	1.414	1.87	17.70	sky
Off 1	K	2452260.81462	30	30	900	1.112	2.10	16.97	dome
IC 348	$K_S$	2452313.60532	60	16	960	1.007	1.48	17.72	dome
IC 348	H	2452313.62027	60	14	840	1.020	1.49	18.04	sky
IC 348	J	2452313.68697	60	24	1440	1.176	1.67	18.82	sky
Off 2	$K_S$	2452316.58424	60	16	960	1.001	1.59	17.74	dome

Arizona (USA) during December 2001 and February 2002. The FLAMINGOS instrument employs a 2K HgCdTe “HAWAII-2” imaging array, which when configured on the 2.1m Kitt Peak telescope yields a  $20.5' \times 20.5'$  field of view with a derived plate scale at K band of  $\sim 0.608''/\text{pixel}$ .

On both 14 December 2001 and 08 February 2002 dithered sets of IC 348 images were obtained with FLAMINGOS in the J, H and K (or  $K_S$ ) passbands. These image sets were also obtained within a narrow window of time (1.5 - 2.5 hrs) and a restricted range of airmass ( $\sec z < 1.4$ ). We list the details of these observations in table 4–1. Briefly, we employed a large number (15-50) of short (20-60 sec) non-repeating dithers to yield total integration times of approximately 14-24 minutes, depending upon the passband. Conditions on both nights appeared photometric, with no apparent cloud cover, stable background sky counts, and seeing estimates between 1.6 and 1.9 $''$  on 14 December 2001 and 1.5 – 1.7 $''$  on 08 February 2002.

Two wide-field off-cluster K (or  $K_S$ ) images were similarly obtained on 17 December 2001 and 11 February 2002. These two non-overlapping regions lie approximately 1 degree east of IC 348, along a line of constant galactic latitude with the young cluster. Their equatorial field centers were: 1)  $03^h48^m21^s9$ ; DEC.=  $+31^\circ38'06''7$  (J2000); 2)  $03^h48^m19^s4$ ; DEC.=  $+31^\circ08'34''7$  (J2000). Additional details of these off-field observations are also listed in table 4–1.

The sets of dithered images were reduced using the April 2002 version of the FLAMINGOS data reduction pipeline (Elston et al, in preparation), using relevant dark frames obtained on each observing night and either local sky or dome flat-fields, depending upon the filter. Local sky flat-fields were used for J and H bands, while dome flats were used for K or  $K_S$  passbands. Briefly, the FLAMINGOS data reduction pipeline is based upon a two-pass, object masking routine that permits the creation of star-free median sky frames from the target images while following standard techniques for the reduction of near-infrared data. To take advantage of the relatively large number of dithers in our datasets, the pipeline employs the drizzle IRAF routine (Fruchter & Hook, 2002) to allow for linear sub-pixel image reconstruction during the final combination of the dithered frames. In summary, 6 reduced cluster images (2 at each passband) were obtained, in addition to two K band off-field images.

In Figure 4–1 we display a (false) color composite near-infrared image of IC 348 using the J, H, and  $K_S$  FLAMINGOS images from our February 2002 observations. A number of interesting cluster features are outlined by low-level nebulosity. These include the cluster core, which displays deep red nebulosity suggestive of somewhat higher extinction, and the interface between the IC 348 cluster and the molecular cloud all along the southern edge of the image. This interface region also includes numerous signposts of very recent star formation including the HH-211 infrared jet (McCaughrean et al., 1994), the enshrouded IR source deemed the “Flying Ghost” nebula (Strom et al., 1974; Boulard et al., 1995), a dark lane suggestive of a flared edge-on disk-like structure, and a number of bright infrared sources detected only in the K band.

A few image artifacts can also be seen in this figure. These include geometric distortions of the stars in the northeast corner of the image, red and green glint features due to internal reflections along the south edge of the cluster, and coma like ghosts south-southwest of the cluster center, resulting from a long time constant in one

amplifier of the HAWAII-2 array. On the other hand, the alternating blue-green-red source south-southwest of the cluster center is not an image artifact but is instead the asteroid 545 Messalina.

#### 4.1.2 Infrared Census

**Photometry and calibration.** We characterized each reduced image by deriving estimates of the FWHM of the stellar point spread function and the pixel-to-pixel noise in the background sky using the IMEXAMINE IRAF routine, although the pixel-to-pixel noise is correlated in drizzled images. The resulting seeing estimates and  $5\sigma$  detection limits are listed in table 4–1. We found that the slightly better seeing and longer exposure times of the February data yielded detection limits approximately 1 magnitude fainter than the December observations. Sources were initially identified on each reduced image using the stand alone S-Extractor package (Bertin & Arnouts, 1996). In an iterative fashion, accurate centroids were calculated for the detected sources using the CENTER IRAF routine, and marked on the reduced images, after which the images were manually searched to identify false detections or to add sources missed near bright stars. The source lists for each of the 6 on-cluster images were then cross-correlated to identify and check those sources not appearing on all the images.

Multi-aperture photometry was performed on the sources using the APPHOT IRAF package and the instrumental magnitudes were corrected out to the beginning of the sky annulus using photometric curves of growth calculated from  $\sim 20 - 30$  bright stars using the MKAPFILE IRAF routine. From the corrected multi-aperture photometry, we chose to use the smallest beamsize that simultaneously gave the most consistent photometry when compared to larger apertures. Because of a spatially varying PSF due to geometric distortions present in the final images, we resorted to using a rather large aperture (radius = 5 pixels; beamsize =  $6''$ ), which yielded aperture corrections typically of order  $\leq -0.06$  magnitudes. Absolute calibration of the instrumental photometry was performed using zeropoint and airmass corrections

Table 4–2. Comparison of IC 348 photometry to 2MASS catalog.

Date	Target	Passband	Magnitude <sup>(a)</sup> Range	Number of Matches	1 $\sigma$ Noise	Median <sup>(b)</sup> Offset
14 Dec 2001	IC 348	J	11.00 – 15.50	343	0.067	0.050
14 Dec 2001	IC 348	H	11.00 – 14.50	345	0.053	0.049
14 Dec 2001	IC 348	K	11.00 – 13.75	280	0.051	0.075
17 Dec 2001	Off	K	11.00 – 13.75	103	0.033	0.073
08 Feb 2002	IC 348	J	12.00 – 15.50	334	0.068	0.085
08 Feb 2002	IC 348	H	12.00 – 14.50	267	0.066	0.086
08 Feb 2002	IC 348	K <sub>S</sub>	11.75 – 13.75	210	0.078	0.079
11 Feb 2002	Off	K <sub>S</sub>	11.75 – 13.75	98	0.078	0.077

<sup>(a)</sup>For the magnitude range compared for the FLAMINGOS and 2MASS photometry of IC 348, the bright limit depended upon the source saturation in the FLAMINGOS images while the faint limit depended upon the increase in the RMS noise of the 2MASS data with magnitude.

<sup>(b)</sup> Median Offset = 2MASS - FLAMINGOS<sub>absolute</sub>.

derived from [Persson et al. \(1998\)](#) standard stars which were observed on the same night as the targets. For secondary calibration, we calculated and removed median offsets of order  $\sim 0.04 - 0.08$  magnitudes between our absolute photometry and the 2MASS photometric system.

**Accuracy.** We quantified our photometric accuracy by matching our data to the 2MASS catalog, yielding over 670 matches in the cluster region and more than 500 sources matched in each of the off-field images. We also directly compared our December and February on-cluster data. We list the results of these photometric comparisons in table 4–2. This table includes the magnitude range of the comparisons based on the FLAMINGOS saturation and 2MASS photometric limits, the  $1\sigma$  dispersion between the datasets and the secondary calibration offsets applied in Section 4.1.2.

While the 17 December off-field data display a dispersion of  $\sim 3\%$  at K band relative to the 2MASS catalog, we find JHK dispersions in the December 14 on-cluster data are larger than expected from purely photometric errors, with the K band scatter

4% larger in the on-cluster frame than that found in the off-cluster frame taken three days later under similar sky conditions. We attribute some of this additional scatter to the intrinsic variability of young PMS stars in IC 348 (Herbst et al., 2000), which in the infrared typically peaks at J band (Carpenter et al., 2001) (i.e., for our IC 348 data  $\sigma_K = 0.05$  versus  $\sigma_J \sim 0.07$  mag).

Between 03 - 11 February 2002, oil from the primary mirror cell contaminated the FLAMINGOS dewar window. This had a negligible effect on our J and H band photometry since these data were flat-fielded with local, contemporaneous sky flats. However, the K data were flat-fielded using non-contemporaneous dome flat-fields and display a 4 – 6% increase in the photometric scatter relative to the FLAMINGOS data obtained in December and to the 2MASS catalog. This scatter does not affect the analysis or conclusions of this paper.

**Results.** After considering the different saturation, detection and noise limits of the December and February IC 348 FLAMINGOS data, we produced a single working source list with photometry drawn from both FLAMINGOS datasets. Simply, we chose to use the December K band data down to  $m_K \sim 15.5$ . Below this value we transition to the intrinsically deeper February  $K_S$  data. In the J and H bands we averaged the two datasets between the saturation and the detection limits of these respective catalogs, recording the  $1\sigma$  standard deviation between the two observations. For the brightest 39 stars, which were saturated in one or more bands on all of our images, we substituted the 2MASS photometry for our FLAMINGOS photometry. Finally, for the faintest objects ( $m_J > 18.5$ ;  $m_H > 17.5$ ;  $m_K > 17.0$ ) we used smaller aperture photometry (radius = 3.5 pixels, aperture correction =  $\sim -0.12$  mag).

In Figure 4–2 we present the infrared color-magnitude diagrams (J-H vs H and H-K vs K) for the FLAMINGOS IC 348 region without filtering for photometric error. We compare the distribution of sources in these diagrams to the location of pre-main sequence isochrones taken from the D’Antona & Mazzitelli (1997) and

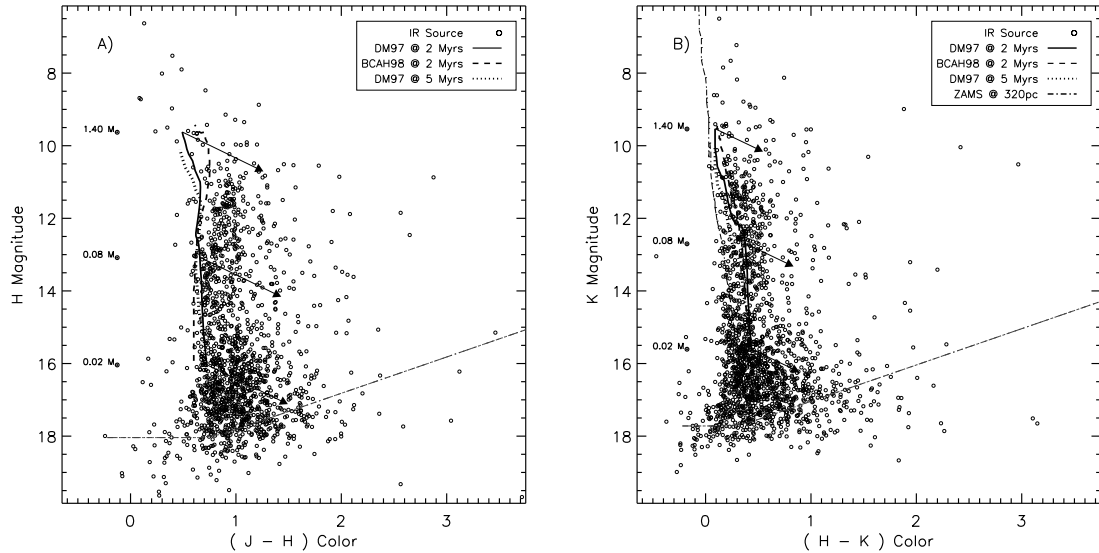


Figure 4–2: Near-infrared color-magnitude diagrams of IC 348. No radial or photometric criteria have been applied to the sources in these diagrams. The locations of the sources in these diagrams are compared to the location of the DM97 and Baraffe et al. (1998) pre-main sequence isochrones for 2 and 5 Myr at 320 pc. Reddening vectors (Cohen et al., 1981) with length  $A_V = 7$  are drawn for 1.4, 0.08 and 0.02  $M_\odot$  PMS objects at the cluster’s mean age. A) J-H/H color-magnitude diagram containing 1534 sources (82% of total); B) H-K/K color-magnitude diagram containing 1739 sources (93% of total).

Baraffe et al. (1998) evolutionary models. For these comparisons we assume a cluster mean age of 2 Myr and a distance of 320 pc (see sections 4.3.1 and 4.3.2 for further discussion of these parameters). Using these cluster parameters, we find that we are sensitive to a 2 Myr old  $80M_{Jup}$  brown dwarf seen through  $\sim 30$  magnitudes of extinction or a  $10M_{Jup}$  source near the deuterium-burning limit seen at an  $A_V = 7$  (using Burrows et al., 1997). Three general characteristics of the sources projected towards our IC 348 FLAMINGOS region are clearly seen: 1) The color-magnitude diagrams indicate a cluster region having only modest reddenings relative to other star-forming regions with the vast majority of the sources having  $A_V < 7$ ; 2) There is a density of sources between  $10 < m_K = m_H < 15$  that is closely outlined by the PMS isochrones and represents a range of magnitude space that is dominated by likely cluster members; 3) Below  $m_K = m_H = 15$  the color-magnitude distribution

appears to become dominated by field-stars (and likely galaxies) as indicated by a rapid increase and steady broadening in the density of sources on these plots. All of these features were seen in individual datasets (December vs February) and are not modified if we change any of the parameters for merging the data.

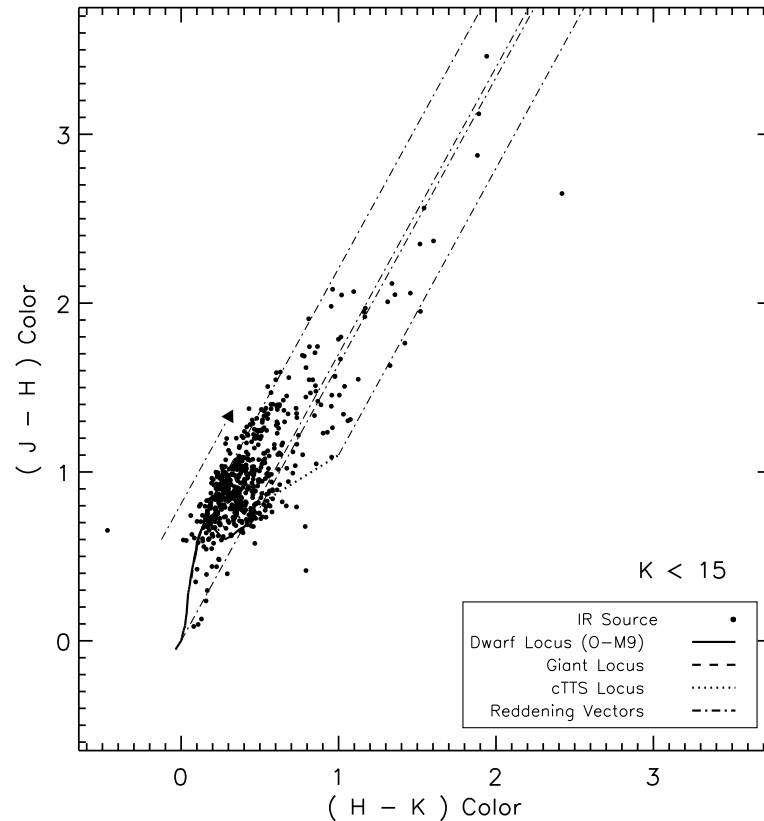


Figure 4–3: Infrared color-color diagram of IC 348. Diagram is filtered on magnitude ( $m_K < 15$ ) but not by photometric error. This observed color distribution is compared to the intrinsic colors of field dwarfs (O-M9, [Bessell & Brett \(1988\)](#); [Kirkpatrick et al. \(1999\)](#)), classical T-Tauri stars with optically thick disks ([Meyer et al., 1997](#)), and giants.  $\sim 12\%$  of the sources display excess infrared emission in this diagram. A reddening vector of length  $A_V = 7$  illustrates the modest reddenings seen by the majority of the cluster.

In Figure 4–3, we display the infrared H-K vs J-H color-color diagram for sources in the IC 348 region. We include sources most likely to be cluster members by using characteristics (2) and (3) of the color-magnitude diagrams listed above to apply a somewhat arbitrary  $m_K = 15$  magnitude limit. There are 580 sources with  $m_K < 15$  of

which 563 have JHK photometry; we display all of these in the color-color diagram without filtering for error. Again, it is clear that the cluster region is only marginally reddened with the nearly all of the sources having  $A_V < 7$ . The overwhelming majority of the sources fall within a reddening band bounded by the reddening vectors for the giant branch and the tip of the M dwarf sequence (M9). While 1 source has IR colors significantly to the left of the reddening band, 66 sources have infrared colors which fall to the right of the reddening vector for M9 dwarfs. These sources fall into a region of infrared excess in the color-color diagram, which because IC 348 is a very young cluster are considered to be likely cluster members with optically thick circumstellar disks. Finally, 42 of these sources having infrared excesses greater than their  $1\sigma$  photometric noise, and we note that these filtered sources are uniformly distributed as a function of H band magnitude. We now use these basic results to examine the structure of the IC 348 cluster.

#### 4.1.3 Cluster Structure

For our subsequent analysis of the luminosity and mass function of IC 348 we wish to select that portion of the FLAMINGOS wide-field image that provides the best sampling of the overall cluster. Studying a region somewhat similar in size to the FLAMINGOS area, [LL95](#) used a surface density analysis to show that IC 348 could be broken into 9 apparent sub-clusterings spread across their survey region. Although subsequent wide-field H $\alpha$  ([Herbig, 1998](#)) and optical ([Luhman, 1999](#)) surveys covered areas similar to [LL95](#), most studies of the IMF of IC 348 have concentrated on the central [LL95](#) sub-cluster, IC348a ([Herbig, 1998](#); [Luhman et al., 1998](#); [Najita et al., 2000](#)) and have not included the other [LL95](#) sub-clusters. While these optical and H $\alpha$  studies may systematically under-estimate the cluster size due to extinction or miss members that do not display H $\alpha$  emission, they have confirmed that the cluster is in fact spread over an area larger than the IC348a region. Using the deeper wide-field near-infrared imaging provided by our FLAMINGOS observations, we re-investigated

the structure of the IC 348 cluster by calculating the cluster’s radial profile and by examining the spatial distribution of sources.

**Cluster radius.** In Figure 4–4 we construct the radial profile of sources in the FLAMINGOS IC 348 region, centering on the IC 348a sub-cluster. We use only those sources  $m_K < 15$  and calculate the surface density in stars per square degree using both annuli of equal width and annuli having constant areas. We compare the resulting radial profiles to the field star surface density calculated from our off-field data. Clearly the cluster exceeds the unreddened background surface density over most of the FLAMINGOS region. Further, the cluster extends over an area considerably larger than the IC348a sub-cluster, whose radius was given as 0.47 pc (5.05′) in LL95 and over an area larger than the radius of 4′ calculated by Herbig. The cluster appears to dip to the unreddened background surface density at a radius of  $\sim 10 - 11'$ ; however, since this is also the radius at which the profile begins to clip the edge of the survey region, we cannot confidently rule out a larger cluster radius using the current FLAMINGOS images. At the distance of IC 348, this translates to a cluster radius of  $\sim 1$  pc, similar to the effective radius of 1.19 pc derived by Carpenter (2000).

To provide a means for comparing our study to that of other authors, we broke our FLAMINGOS cluster region into two sub-divisions based upon the radial profile and further assigned these two sub-regions primarily functional names, e.g., the cluster “core” sub-region with a radius = 5′ and the cluster “halo” region between the cluster “core” and a radius of 10.33′, corresponding to the largest unclipped radius permitted by the current FLAMINGOS survey. The core region is approximately the IC 348a sub-cluster but is slightly larger than that area studied by Luhman et al. (1998) and Najita et al. (2000), while the halo region covers an area approximately 3.3 times that of the core and encompasses the stars contained in the LL95 sub-clusters b-i.

Although our construction of the cluster’s radial profile has allowed us to divide the spatial extent of IC 348 within our survey region, we found that it followed

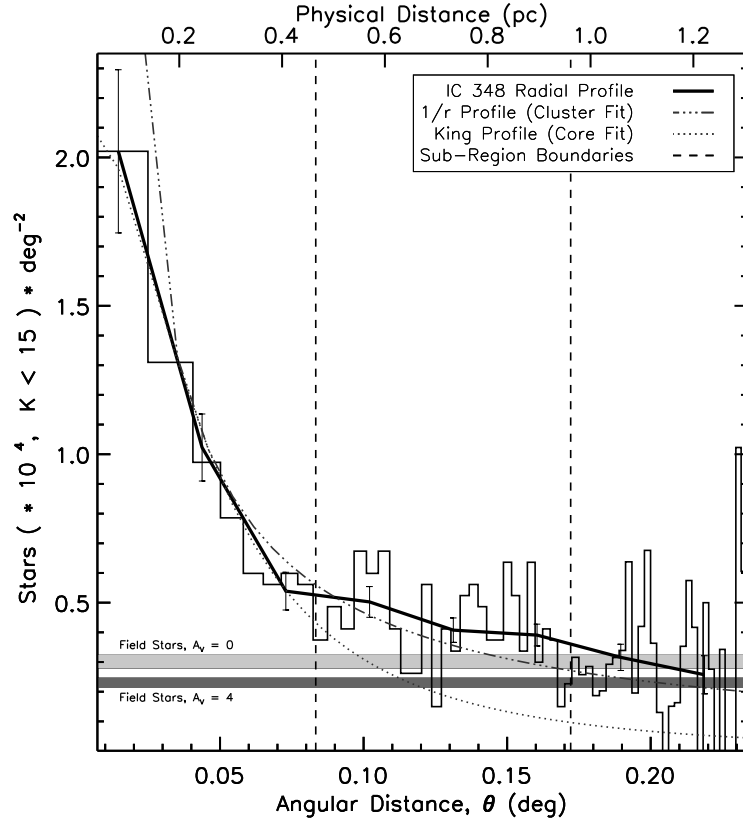


Figure 4–4: Radial profile of the IC 348 cluster. Surface density (in stars per square degree) is measured in circular annuli, centering on the location of the LL95 sub-group IC348a. Profiles are calculated using annuli of equal area (histogram with bins of decreasing width) and annuli with equal radial steps (heavy solid line with error bars). First annuli width was  $R_0 = 1.75'$ . Profiles are compared to the unreddened background surface density (lightly shaded band; width =  $2 \times$  the  $1\sigma$  deviation of background, see text.) and the background surface density reddened by  $A_V \sim 4$ . Also shown: the division of cluster into sub-regions (vertical dashed lines, see text); a  $1/r$  profile fit to the entire cluster region (dot-dashed line;  $\chi^2 \sim 4.9 \times 10^{-4}$ ); and a King profile fit to the cluster core (dotted line;  $r_{core} = 0.25\text{pc}$ ;  $\chi^2 \sim 1$ ). Note: bins with  $R \geq 10.33'$  have been geometrically corrected to account for the survey boundaries and the conversion from angular to physical scale (upper x-axis) is calculated for a distance of 320 pc.

neither a simple  $r^{-1}$  nor a King profile. We fit both analytical profiles to the cluster's constant area annuli profile, varying the radial extent of the fits, and for the King profile, allowing both the core and tidal radii to vary freely. Neither analytic profile provided reasonable  $\chi^2$  fits to the entire cluster profile, although the core is well fit by

a King profile with  $r_{core} = 0.25\text{pc}$ . As displayed in Figure 4-4, the tail of the cluster profile, i.e., the halo sub-region, is much flatter than either of the analytic profiles. One interpretation, for example, is that the LL95 sub-clusters that constitute the cluster's halo are actual separate entities, rather than simply being statistical fluctuations on a  $1/r$  cluster profile.

Our radial profile and fits likely suffer from two problems. First, we use circular annuli although as we will show in Figure 4-6, the cluster is elliptically elongated in the N-S direction. Second, we rely upon an empirical estimate of the field-star surface density from a region near to IC 348 but that, in principle, could fluctuate between this location and the background relevant to IC 348. Indeed, the surface densities of the two off-cluster locations fluctuate more than expected purely from counting statistics despite their similar galactic latitudes. This spatial fluctuation, however, is exceedingly small relative to the excess surface density of the cluster halo and will not likely affect the cluster boundary we derive. On the other hand, we cannot rule out a somewhat larger cluster radius because the obscuration of background field stars by the parental molecular cloud will lower the expected field star surface density, as we illustrate in Figure 4-4. Reddening the background by the average extinction in the IC 348 region ( $A_V = 4$ ; see Section 4.1.4) only expands the cluster radius by  $1 - 2'$ , however, and the cluster probably does not exceed a radius of  $15'$  (1.4pc), which is a boundary traced very clearly by wide-field X-ray detections (Preibisch et al., 1996).

**Spatial distribution of sources.** With the purpose of characterizing our two cluster sub-regions, we examined the spatial distribution of the IC 348 FLAMINGOS sources, plotting them using separate symbols for different luminosity ranges in Figure 4-5a. By segregating the two sub-regions, we show for example that there are as many members with B & A spectral types within the cluster core as there are in the cluster halo, although o Persei is not a likely cluster member. A similar conclusion is reached about relatively bright sources in IC 348 with as many sources with  $m_K < 10$  in the

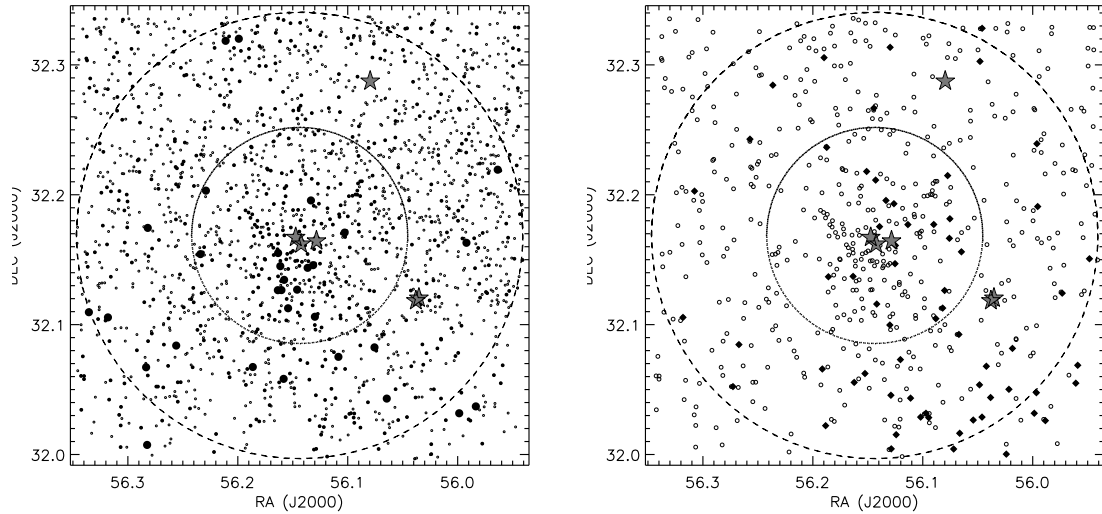


Figure 4–5: Spatial distribution of sources in IC 348. Locations of sources in different magnitude ranges are shown in an equatorial tangent projection of the wide-field FLAMINGOS IC 348 region. The two plots correspond to different samples: A) all sources; B) sources  $m_K < 15$ . Large filled stars correspond to sources with spectral types A5 and earlier including the B0III giant  $\alpha$  Persei. In (A), large filled circles correspond to sources  $m_K < 10$ , smaller filled circles,  $m_K < 15$ , and small open circles,  $m_K > 15$ . In (B), sources  $m_K < 15$  are shown as open circles and sources displaying infrared excess in Figure 4–3 are filled diamonds. The  $R < 5'$  and  $R = 10.33'$  boundaries of the cluster sub-regions are shown as concentric circles. Note the decrease in surface density near the cluster-cloud interface in (A) and the anti-correlation of this decrease with the surface density of infrared excess sources in (B).

cluster core as in the cluster halo. On the other hand, the faintest sources ( $m_K > 15$ ) do show some spatial variations, with a sharp decrease in these sources along the cluster’s southern edge, clearly outlining the interface with the molecular cloud.

In Figure 4–5b we plot the spatial distribution of the 580 sources with  $m_K < 15$  and that were used to construct the cluster’s radial profile. The cluster core is clearly defined, while unlike the faint sources there is no change in the surface density of bright halo stars toward the molecular cloud. We further examine the locations of the 66 sources displaying IR excess. As was found by LL95, the majority of these sources lie outside of the cluster core. Moreover, the surface density of these IR excess sources appears to increase toward the southern interface with the Perseus Molecular Cloud and

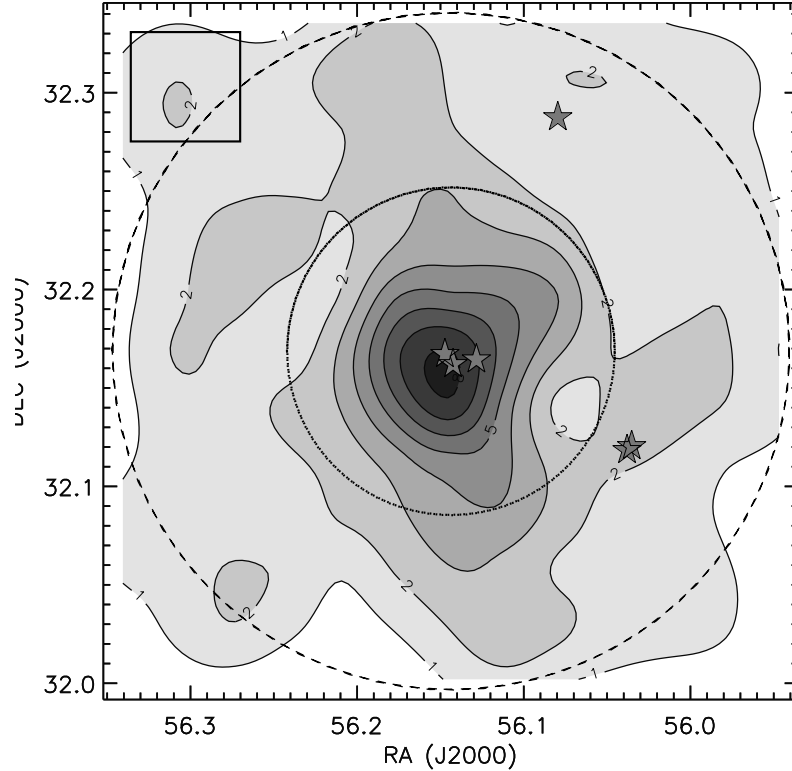


Figure 4–6: Surface density profile of the IC 348 cluster. The surface density of IC 348 sources is shown filtered by a Nyquist sampled box (width =  $200''$ , see upper left) that has an area similar to that used in the bins of the radial profile. Contours are in multiples of the surface density derived by reddening the off-field by  $A_V \sim 4.0$ , yielding a surface density of 2305 stars/sq. deg, the same surface density shown as the shaded band in Figure 4–4. Contours steps at 1, 2, 5, and 10 times the background are labeled.

opposite to the behavior of the faintest objects. This would suggest that many of the IR excess sources are correlated to and likely embedded within the molecular cloud, and may be associated with the most recent star formation in the IC 348 region.

Lastly, in figure 4–6, we construct a surface density plot of the  $m_K < 15$  stars used in the radial profile (Figure 4–4) and in Figure 4–5b. We use a Nyquist sampled box filter that had an area roughly equivalent to the area of the annuli used in the radial profile. We use this relative large box to match the noise in the radial profile as a function of constant area and at this resolution, only a smooth N-S elongated cluster is seen with no significant sub-clusterings. We confirmed, however, that if we

used the same spatial resolution as the [Lada & Lada](#) study ( $90''$ ), we recover most of the sub-clusters identified by LL95 and which now lie in the cluster’s halo. We note, however, that neither map displays any apparent correlation of the surface density to the location of the cluster-cloud interface region.

#### 4.1.4 Cluster Reddening Properties

We also used the sources observed within the IC 348 region as line of sight probes of the parental molecular cloud, allowing us to characterize the reddening that would be seen by cluster members or background field-stars. Building upon the method of [Alves et al. \(1998\)](#) and our recipe(s) described in Chapter 3, we calculated individual extinction estimates for each source by de-reddening the sources’ infrared colors to a locus of assumed intrinsic colors in the (H-K) vs (J-H) color-color diagram. We then examined reddening maps created from these individual extinctions and binned the  $A_V$  estimates into an extinction probability distribution functions (EPDFs) which we will use when estimating the number of interloping field-stars and when calculating luminosity function models to interpret the observations.

**Extinction estimates and maps.** We calculated individual  $A_V$  for sources in two different luminosity ranges, dividing them into sets that are likely dominated by either cluster members or background field-stars. These samples were selected from the (H-K) vs K color-magnitude diagram and were separated into “bright” and “faint” sources by the reddening vector of a source at  $m_K = 15$  (H-K = 0.35). The “faint” sample was also limited to objects brighter than a reddening vector for a source at  $m_K = 17$  (H-K = 0.4).

The two magnitude samples were de-reddened back to different loci of assumed intrinsic colors. The “bright” sources were assumed to be young PMS stars, and those with JHK colors ( $\sim 95\%$ ) were de-reddened back to the classical T-Tauri Star (cTTS) locus in the JHK color-color diagram ([Meyer et al., 1997](#), slope = 0.58; J-H intercept = 0.52), while the remaining 5% were assigned an intrinsic H-K color =

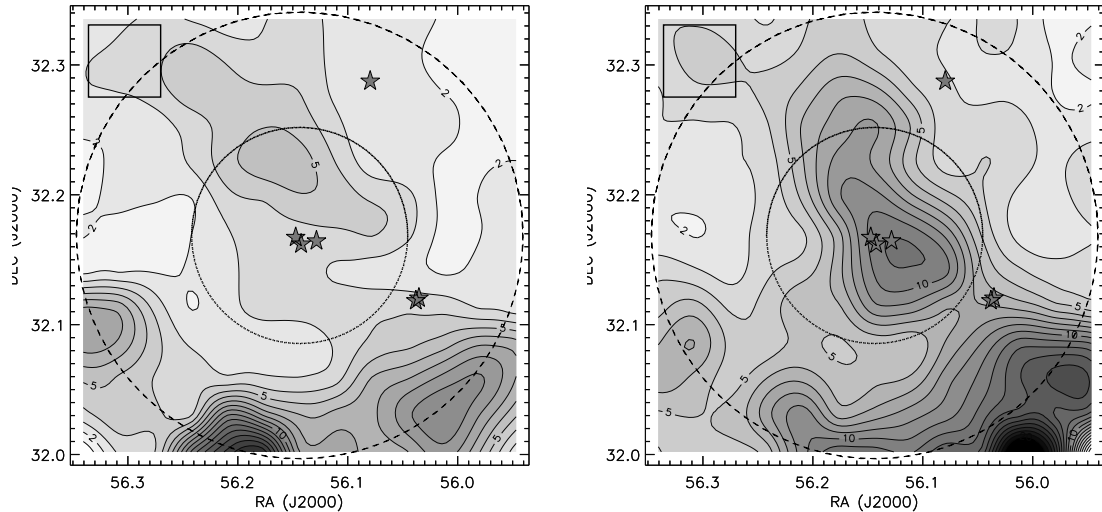


Figure 4–7: Extinction maps of the IC 348 FLAMINGOS region. Individual source  $A_V$  estimates derived in Section 4.1.4 are converted to an extinction map using a Nyquist sampled box filter (width =  $200''$ ; see upper left; same as previous figure). Contours are in steps of  $A_V = 1$  from  $A_V = 1$  to 20; we label the  $A_V = 2, 5, 10$  contours. Left hand panel:  $A_V$  map derived from the bright, likely cluster stars; Right hand panel:  $A_V$  map of the extinction seen by the fainter, likely background stars. See text for sample selection and explanation of reddening estimates.

0.5 and  $A_V$  estimates derived. The “faint” sources were assumed to be dominated by field M dwarfs and those with JHK colors ( $\sim 85\%$ ) were de-reddened back to a linear approximation of the M dwarf branch in the color-color diagram (from K6 to M9, slope = 0.16; J-H intercept = 0.61)<sup>1</sup>, while the remaining 15% lacking J band were assigned an intrinsic H-K = 0.16.

In Figure 4–7 we present the resulting extinction maps derived from these two samples. Both maps clearly define the location of the cluster-cloud interface along the region’s southern border, while they also outline a NE-SW band of reddening that falls across the cluster’s core, similar to the cluster’s N-S elongation. One straightforward conclusion from the spatial variations in either reddening map is that the IC 348 region

<sup>1</sup> These cTTS and M dwarf approximations result in nearly all field giants being de-reddened to the colors of the K1 - K2III spectral class.

cannot be characterized by a single mean  $A_V$  value. Although the two  $A_V$  maps are physically very similar, the reddening seen by the background stars is in general larger than that foreground to the cluster members, suggesting, for example, that there is considerably more material behind the cluster core than in front of it.

**Extinction probability distribution functions (EPDFs).** In Figure 4–8 we plot the normalized histograms of the (H-K) color and of  $A_V$  for sources in the two magnitude ranges defined in the previous section and separate them further by cluster sub-region. As expected from the  $A_V$  maps, the faint sources' color and  $A_V$  distributions are broader and redder than the bright likely cluster stars, although the EPDFs of the likely cluster members in both regions appear somewhat similar. Applying a two-sided Kolmogorov-Smirnov test to the  $A_V$  values derived from bright and faint sources in the cluster core, we found that it is unlikely that they are drawn from the same  $A_V$  distribution, having a KS probability of only 0.00024. This is in contrast to the halo sub-region, where the bright and faint stars have a 0.23 probability of being drawn from the same  $A_V$  distribution. Similarly the bright stars in the core and halo have a 0.043 probability of being drawn from the same distribution while the faint stars in both regions cannot, ruled out at the  $2.0000 \times 10^{-8}$  probability. Taken together, the EPDFs and these statistical tests support two basic conclusions about the reddening seen towards IC 348: 1) there is a measurable difference in the reddening seen by the background stars between the core and halo sub-regions, owing to the substantial material appearing behind the cluster core (also see Figure 4–8b); 2) the bright, likely cluster members of the core and halo appear to have fairly similar reddenings, despite the projection of the entire region onto various pieces of the Perseus GMC.

The normalized  $A_V$  histograms (hereafter known as EPDFs) are generally skewed to  $A_V < 5$  and are quite non-gaussian, again indicating that a single  $\langle A_V \rangle$  value is inappropriate to describe the cluster reddening. On average we find reddenings to the

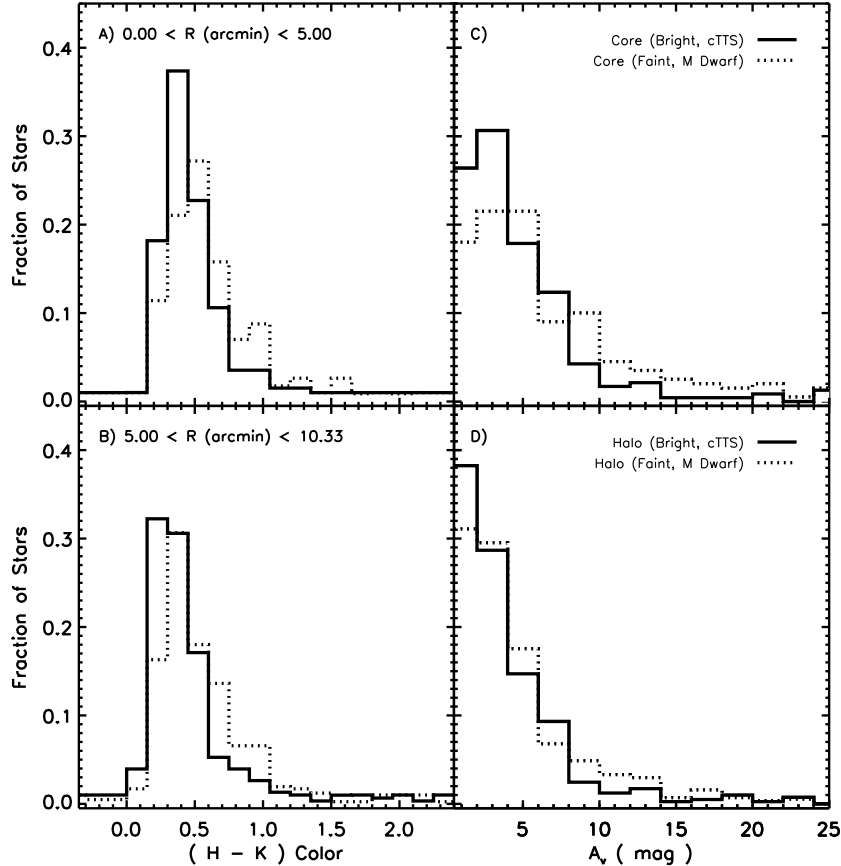


Figure 4–8: Distributions of reddening for IC 348. Panels (A) and (B): the fractional distribution of H-K color divided by sub-region. Panels (C) and (D): the probability distributions of  $A_V$  derived from de-reddening sources in the (H-K)/(J-H) color-color diagram. In all panels, the distributions are divided into the results from magnitude limited “bright” and “faint” samples. See text for sample selection and explanation of de-reddening.

background stars of  $\langle A_V \rangle_{core} \sim 7.2$  ( $1\sigma = 6.3$ , avg. deviation = 4.6, median = 5.3) and  $\langle A_V \rangle_{halo} \sim 4.6$  ( $1\sigma = 4.3$ , avg. deviation = 3.0, median = 3.4), while to the likely cluster members these averages are  $\langle A_V \rangle_{core} \sim 4.9$  ( $1\sigma = 4.2$ , avg. deviation = 2.9, median = 3.8) and  $\langle A_V \rangle_{halo} \sim 4.2$  ( $1\sigma = 4.0$ , avg. deviation = 2.6, median = 3.3). These latter averages are roughly the same as the  $A_K \sim 0.5$  assumed by [LL95](#) for the entire IC 348 region and their skew to lower  $A_V$  is evident in the better agreement of their medians to the median  $\langle A_V \rangle = 2.8$  derived by [Herbig](#) using spectral types for cluster members. Since our observations probe a volume of the cluster region much larger than these prior studies, we will use these EPDFs when correcting for

background field-stars in Section 4.2.2 and in our modeling of the luminosity function in Section 4.3.4.

## 4.2 Infrared Luminosity Functions of IC 348

### 4.2.1 Constructing Infrared Luminosity Functions

In Figure 4–9 we construct the raw infrared luminosity functions (LFs) for sources in the FLAMINGOS IC 348 region. We restrict the sources to the area bounded by the  $10.33'$  radius and use (0.5 mag) bins wider than our photometric uncertainties. We compare the J, H and K band IC 348 LFs and find that all of them display a double peaked structure: the first peak lying at  $J=H=K=13 \sim 13.5$  and the second between  $J = 17.5$  and  $K = 16.5$ . Following our analysis of the cluster’s color-magnitude diagrams in Section 4.1.2, we interpret the brighter of these peaks to be sources in the IC 348 cluster and the fainter peak to be dominated by background field-stars and galaxies.

In Figure 4–10, we display the K band LFs of the IC 348 “core” and the “halo” sub-regions, scaling them to stars per square degree and comparing them to the unreddened field-star KLF constructed from our off-cluster datasets (see also Section 4.2.2). Confirming our preliminary study of the cluster’s color-magnitude diagrams and radial profile, both sub-regions display a considerable excess of sources relative to the field-star KLF for  $m_K < 15$ . Both sub-regions KLFs reach bright peaks although they occur in somewhat different locations with the core KLF, for example, peaking 1.5 magnitudes brighter than the halo. Below these bright peaks, both KLFs flatten or turnover before rising again, parallel to the field-star KLF. While the faint KLF peak of the two sub-regions have nearly identical size and structure, they appear to be smaller and shifted to fainter magnitudes than the field-star KLF. Such differences could certainly be caused by the reddening and obscuration of background field-stars due to the molecular cloud. In the next section we use our detailed study of the cluster reddening properties from Section 4.1.4 to estimate the size of the field-star contribution to the observed KLFs.

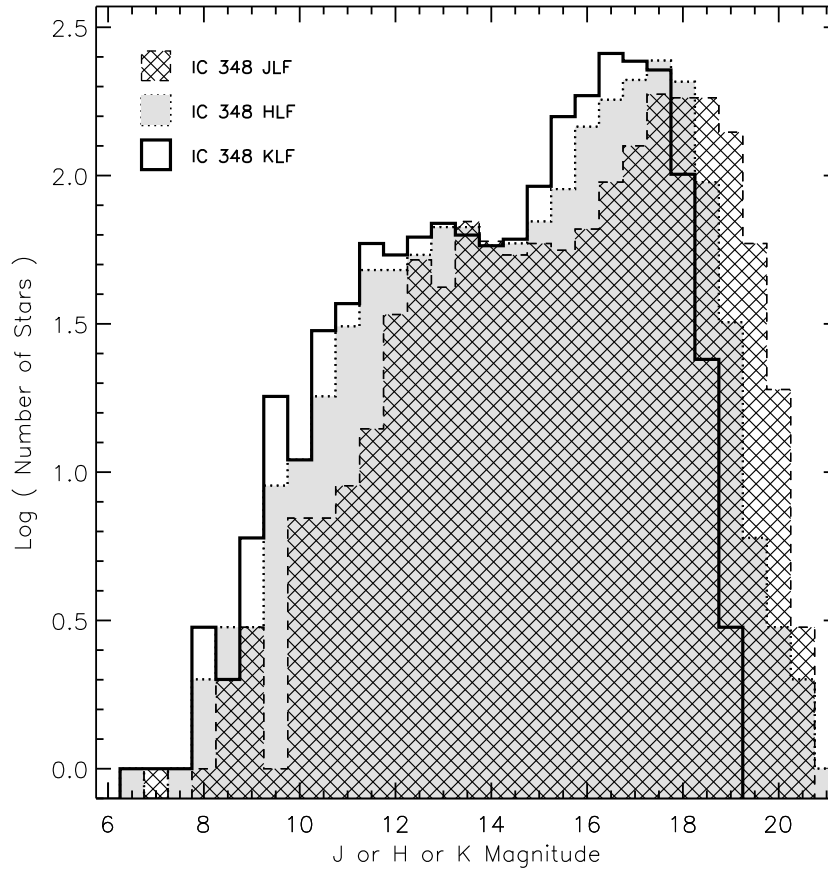


Figure 4–9: Raw infrared luminosity functions for IC 348. We compare the J, H and K band LFs for sources in the entire IC 348 Cluster FLAMINGOS region. Note that all three have similar two peaked structure.

#### 4.2.2 Field-Star Correction to the Cluster KLF(s)

To statistically estimate the field-star contribution to the raw IC 348 KLF(s), we first scaled the observed field-star KLF to the area of the cluster and then convolved it with a reddening probability distribution function that characterizes the effects of the molecular cloud in that region. We used the extinction probability distribution functions derived in section 4.1.4 from the faint stars de-reddened to the M dwarf locus and treated the cluster’s core and halo regions separately. In Figures 4–11ab we compare the raw KLFs to the reddened field-star KLFs appropriate to that sub-region.

The reddened field-star KLFs very closely match the raw KLFs for  $m_K > 15$  in both sub-regions, although they exceed the cluster KLFs at the faintest magnitudes

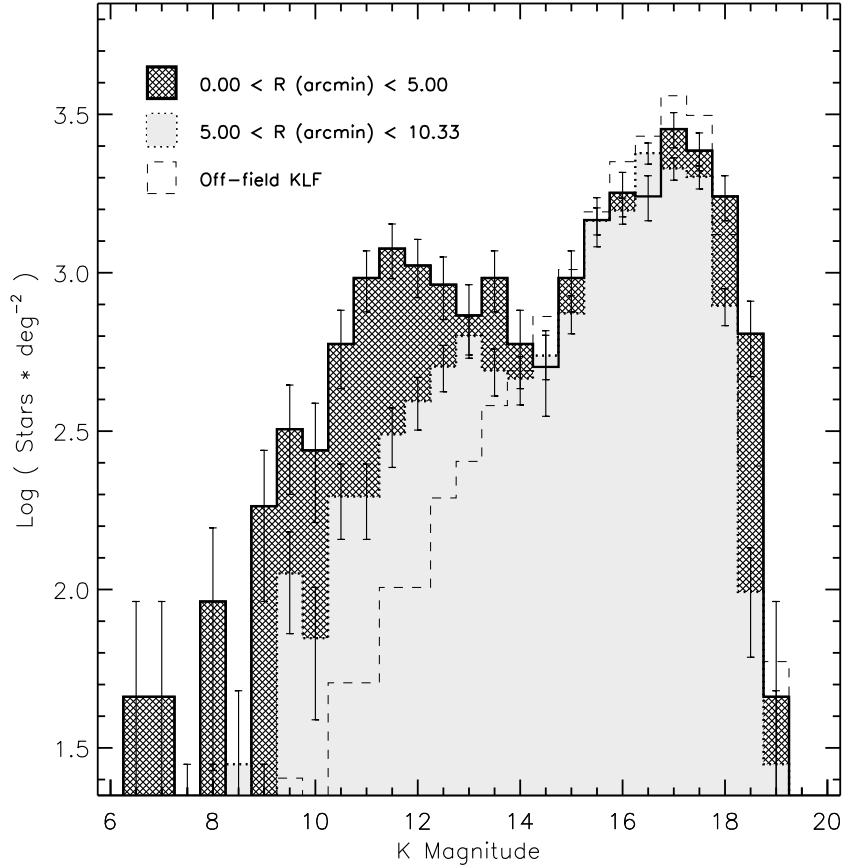


Figure 4–10: K-band luminosity functions by sub-region for IC 348. The KLFs are scaled to stars per square degree and are compared to the observed field star KLF derived by combining the two off-cluster fields. Both the cluster core and halo sub-regions appear to dominate the un-reddened off-field counts for  $m_K < 15$ . Error bars are  $1\sigma$  counting statistics.

because they were not filtered to match our detection limits. We subtracted these reddened field-star KLFs from the raw cluster KLFs, and display the resulting differential KLFs in Figures 4–11cd, constructing error bars that are the  $1\sigma$  counting statistics of the sum of the raw and field star KLFs. The structure of the differential KLFs is significant for the bins containing  $m_K \leq 16.75$ , below which the field-star correction clearly over-estimates the observations. This magnitude limit corresponds to a  $10 M_{Jup}$  brown dwarf at the 2 Myr mean age we assume for IC 348. The two sub-regions have a nearly identical number of members, with the core containing  $153 \pm 16$  sources with  $m_K \leq 15$  ( $172 \pm 24$ ;  $m_K \leq 17$ ) and the halo containing  $150 \pm 23$  sources

with  $m_K \leq 15$  ( $176 \pm 40$ ;  $m_K \leq 17$ ). While the sub-region KLFs are well populated for  $m_K < 15$ , at fainter magnitudes the substantial field-star corrections yield very large uncertainties in the KLF structure.

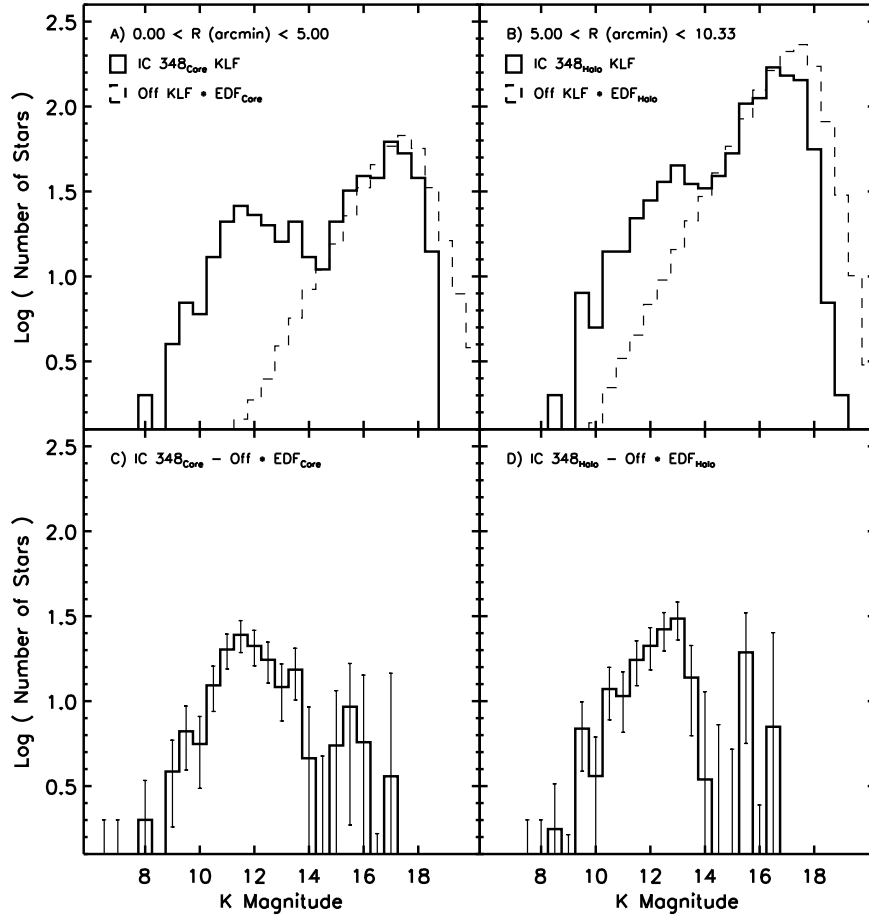


Figure 4–11: Field star correction to cluster KLFs in IC 348 Panels (A) and (B): comparison of the raw sub-region KLFs to the observed field star KLF reddened by the faint star  $A_V$  distributions derived in Section 4.1.4 and displayed in Figure 4–8. The reddening field star KLF(s) were scaled to the area of the cluster sub-region and subtracted to yield the differential KLFs displayed in panels (C) and (D). The differential KLFs are significant for  $m_K \leq 16.5$ , below which we over-estimate the field star correction. Error bars are the square root of the sum of the observed counts and the predicted field star counts for each bin.

In Figure 4–12 we directly compare the sub-region differential KLFs and sum them to construct the overall cluster KLF. Again, the differences in the structure of the two sub-region KLFs are obvious to the eye, with the peak of the halo KLF skewing

significantly to fainter magnitudes, before strongly turning over. While the peaks of the sub-region KLFs are clearly distinct, the KLFs are similar to within their  $1\sigma$  error bars in most bins but separated by 2 to  $3\sigma$  in the  $m_K = 11$  and  $m_K = 13$  bins. A two sample chi-square test of the two histograms (range:  $m_K = 8 - 15$ ) yields a probability of 0.04 that they are drawn from the same parent distribution, indicating that these sub-region KLFs are different at the  $2\sigma$  level.

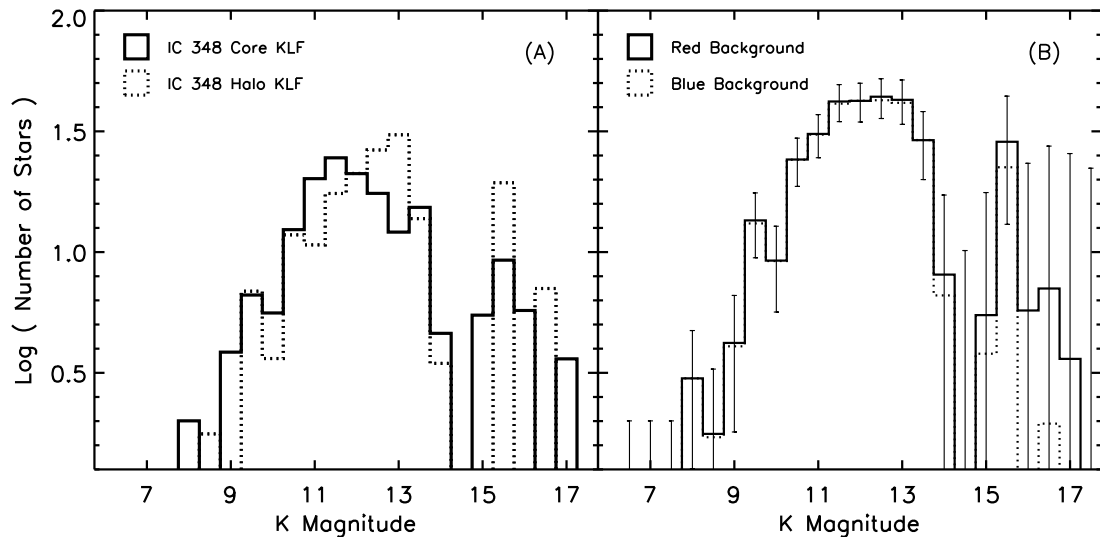


Figure 4–12: Differential KLFs for IC 348. A) Comparison of the differential IC 348 KLFs for the two cluster sub-regions. B) Sum of sub-region differential KLFs into the composite IC 348 KLF. Panel B compares the sum of the sub-region differential KLFs from two different background corrections. The “Red” correction is the field star KLF reddened by the EPDF for the background stars; the “Blue” correction is the field star KLF reddened by the EPDF for the bright cluster stars.

When the two sub-region KLFs are summed together, the complete cluster KLF displays a very broad peak between  $m_K = 11.5$  and 13 before decreasing very sharply to  $m_K = 15$ . In the complete cluster KLF we find that despite the large uncertainties at faint magnitudes the two sub-region KLFs sum to yield a statistically significant number of cluster members with  $m_K > 15$ . Further, we find that if we increase the size of the field-star correction by using a bluer extinction distribution function (one

relevant for the cluster stars), the main cluster KLF characteristics are not substantially altered, although the size of the very faint population is almost halved.

### 4.3 Initial Mass Function of IC 348

To analyze the IC 348 differential K band luminosity function(s) constructed in Section 4.2 we used our model luminosity function algorithm presented in Chapter 2 and expanded in chapter 3. Our goal is to place constraints on the initial mass function of IC 348 by deriving that mass function or set of mass functions whose model luminosity functions best fit the cluster KLF. For the purpose of comparing of our work to other studies, we individually analyzed the KLFs of the two cluster sub-regions as well as the composite cluster KLF. Since a young cluster’s luminosity function is the product of an age dependent mass-luminosity relation and the cluster’s IMF, we detail the star-forming history of IC 348 in Section 4.3.1 and the appropriate theoretical mass-luminosity relations in section 4.3.2, before fixing these quantities and deriving the cluster IMF in Section 4.3.4.

#### 4.3.1 Star Forming History of IC 348

To derive a mean age and age spread appropriate for our luminosity function modeling, we examine published studies of the apparent star-forming history of IC 348. In Figure 4–13, we plot a histogram of the ages derived by Herbig (1998) using the de-reddened V/V-I color-magnitude diagram for candidate pre-main sequence members in an 112 square arc-minute region of IC 348. We merge the ages derived by Herbig for sources with and without detectable H $\alpha$  emission and derive an ensemble cluster mean age of  $\sim 2$  Myr. We approximate the age spread of IC 348 to be  $\sim 3$  Myr, corresponding to constant star formation from 0.5 to 3.5 Myr ago, and note that this age spread is 2.5 times longer than that we used for the younger Trapezium Cluster. We show in Figure 4–13 that our assumed star-forming history closely approximates the bulk of the Herbig SFH, but clips the “older” tail of this distribution. We do not include this “older” tail in our SFH of IC 348 for the following reasons: 1)

Observational errors in the derivation of de-reddened color-magnitude or theoretical HR diagrams can lead to exaggerated star-forming histories, specifically resulting in artificially inflated cluster’s age spreads (Hartmann, 2001; Kenyon & Hartmann, 1990); 2) A number of the “oldest” IC 348 objects analyzed in the Najita et al. (2000) Hubble Space Telescope NICMOS study were also found to be the reddest cluster objects, suggesting that they are background interlopers; 3) Our assumed age spread also very closely approximates that SFH derived by Palla & Stahler (2000), who found that the star formation in IC 348 began approximately 3 Myr ago. Further, Palla & Stahler found negligible star formation at ages greater than 3 Myr and also found no dependence of the SFH on location within IC 348. Thus, we will use the same star formation history when modeling both the ensemble cluster and the cluster’s “core” and “halo” sub-region KLFs.

#### 4.3.2 Cluster Distance and the Mass-Luminosity Relation

Herbig (1998) included an extensive discussion on the distance to IC 348 based upon literature sources existing at that time. Arguing that closer distances ( $\sim 260$  pc) were systematic under-estimates, he chose a distance for IC 348 (of 320 pc) based in part upon the fact that within the current uncertainties, one could not differentiate between the distance to IC 348 ( $316 \pm 22$  pc Strom et al., 1974) and to the Perseus OB2 association Borgman & Blaauw ( $322 \pm 30$  pc 1964). To understand how such distance uncertainties might affect our results, we examined more recent Hipparcos-based proper motion and parallax studies of the cluster and association and then studied the impact of this systematic on the relevant mass-luminosity relation.

The recent use of Hipparcos data, however, does not appear to have resolved the distance uncertainty between the Perseus OB2 association and the IC 348 cluster. de Zeeuw et al. (1999) derived a distance of  $317 \pm 27$  pc for 17 members of the Perseus OB2 association spread over a projected  $37 \times 37$  pc area, while also statistically estimating the number of interlopers. On the other hand, when Scholz et al.

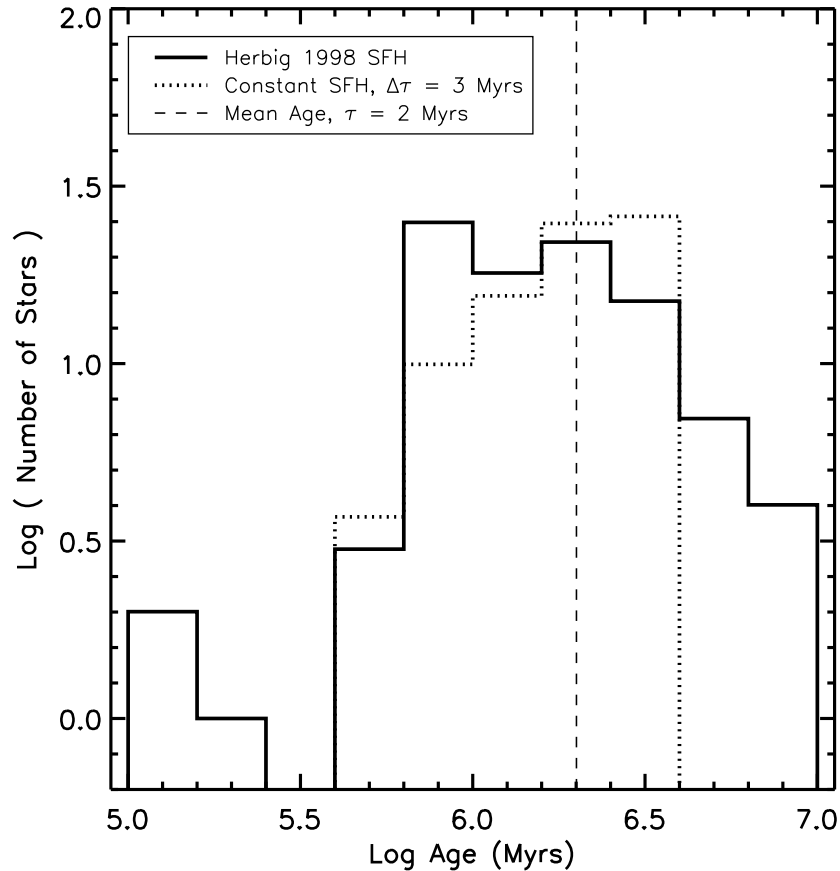


Figure 4–13: Star-forming history of IC 348. The star formation history of IC 348 from [Herbig \(1998\)](#) is compared to that used in our model luminosity function algorithm. The Herbig SFH is the merger of the ages derived for stars with and without detectable H $\alpha$  emission using the de-reddened optical color-magnitude diagram. The SFH assumed for our models has a mean age,  $\tau = 2.0$  Myr with constant star formation from 0.5 to 3.5 Myr ago.

(1999) performed a recent proper motion study of the IC 348 region, they derived a distance of  $\sim 261$  pc using a different set of 9 Hipparcos sources. This latter distance estimate to IC 348 should probably be treated with some caution. Since more than half of the 9 sources with parallaxes were at projected distances of 2.5 - 8 pc from the cluster center, they fall well outside any cluster outer radius we have discussed here and may not be actual members, especially since no statistical estimate of the number of non-members was performed for this sample. Further, [Ripepi et al. \(2002\)](#) very recently reported the discovery of an F star within the IC 348 boundaries that displays

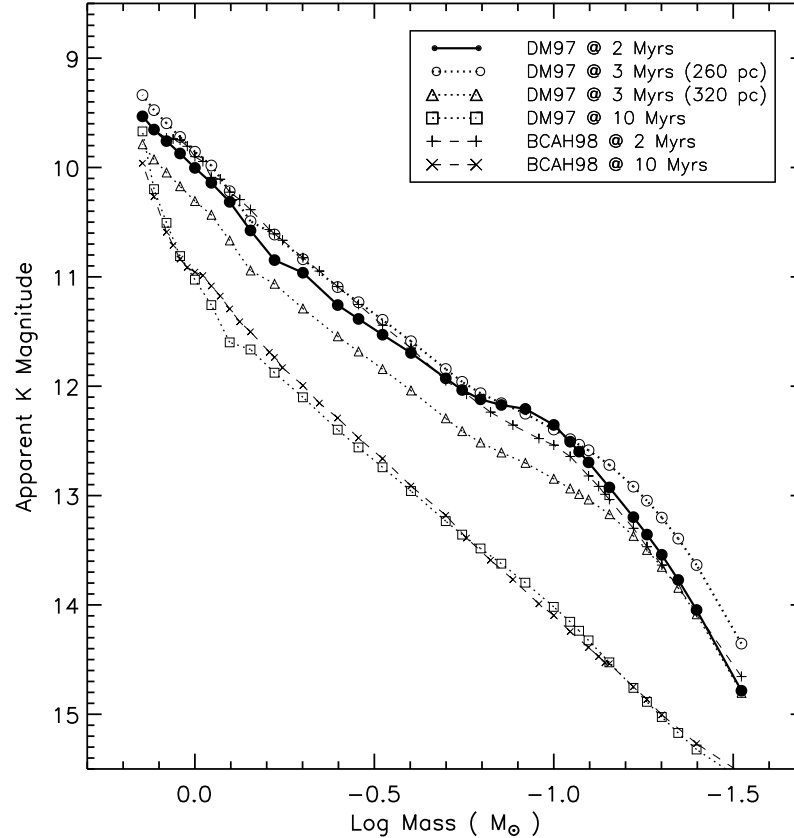


Figure 4–14: Theoretical mass-luminosity relations of IC 348. Mass-K magnitude relations for different ages, distances and set of theoretical evolutionary models are compared to illustrate the sensitivity of our method to assumptions about cluster distance and age. Mass-K magnitude relations from [D’Antona & Mazzitelli \(1997\)](#) are shown at  $\tau = 2, 3$  and 10 Myr for a distance of 320 pc and at  $\tau = 3$  Myr for a distance of 260 pc. Mass-K magnitude relations from the [Baraffe et al. \(1998\)](#) tracks are also compared at 2 and 10 Myr. For all of these comparisons, the PMS tracks were converted to observables using a single set of bolometric corrections.

rapid  $\delta$  Scuti-like variability that is interpreted as the pulsation of a PMS star while in its instability strip ([Marconi & Palla, 1998](#)). The derived pulsation period strongly favors a larger distance to IC 348 of  $\sim 320$  pc. Thus, it remains unclear if the distance to IC 348 can be separated from the distance to the OB association. For our modeling we adopt the distance of 320 pc ( $m-M = 7.5$ ) to IC 348 for consistency with the work of [LL95](#) and [Herbig \(1998\)](#) but we examined how such a distance uncertainty could affect our results.

Such distance uncertainties may translate, for example, into systematics in the derivation of cluster properties such as mean age and possibly the IMF. For example, [Herbig](#) showed that assigning IC 348 a closer distance yielded a systematically older cluster mean age since the cluster appears intrinsically fainter when compared to pre-main sequence evolutionary models. In [Figure 4–14](#), we examine the net effect of this age-distance uncertainty on the theoretical mass-luminosity relations relevant for our luminosity function modeling. Shifting the distance from 320 to 260 pc produces a shift in the mean age from 2 to  $\sim 3 - 4$  Myr (see also [Haisch et al., 2001a](#)). However, the change in the distance modulus ( $-0.42$  magnitudes) is roughly equivalent to the average luminosity evolution of stars ( $1.0 - 0.1 M_{\odot}$ ) between 2 and 3 Myr ( $dK \sim -0.35$ ). By comparing the mass-K magnitude relation at 2 Myr and 320pc to that at 3 Myr and 260 pc, we find that above the hydrogen burning limit, our derived IMF will have little systematic dependence upon the cited age-distance uncertainty for IC 348 and should be a faithful representation of the true cluster IMF. On the other hand, the slope of the substellar mass-K magnitude relation is systematically affected, in part due to a larger mass range undergoing deuterium-burning, and our derived substellar IMF will be less reliable until this age-distance uncertainty is resolved.

Lastly, in [Figure 4–14](#) we compare the theoretical mass-luminosity relations taken from two sets of evolutionary calculations. As we found in [chapter 3](#), the current theoretical mass-K magnitude relations are very consistent between current sets of PMS tracks, meaning that the derived IMF will be mostly independent of which set of modern PMS models we use, although future updates to the input physics may change these conclusions. To provide consistency between our studies of various young clusters, we will derive the cluster IMF using our standard set of PMS tracks, which are based on the [D’Antona & Mazzitelli \(1997\)](#) tracks and fully described in [Section 2.2.3](#).

### 4.3.3 Other Modeling Parameters: Reddening and Binaries

Three additional characteristics of young stars that we can include into our model luminosity function algorithm are the reddening of the cluster members by the parental molecular cloud, excess infrared flux due to optically thick disks around the cluster members, and the frequency of un-resolved companions. First, to account for the reddening of the cluster by the Perseus Molecular Cloud, we used the extinction distribution functions derived in Section 4.1.4 for the bright cluster stars de-reddened to the cTTS locus.

Second, in Section 4.1.2 we confirmed the LL95 finding of  $\sim 60$  infrared excess sources distributed across the IC 348 cluster region. Correcting for field stars and dividing the excess sources by sub-region, we find infrared excess fractions of  $14 \pm 11\%$  (22/153) for the core sub-region,  $24 \pm 17\%$  (36/150) for the cluster halo and  $19 \pm 10\%$  (58/303) for the composite cluster. If we restrict these estimates to those 42 sources which have IR excess greater than their  $1\sigma$  photometric errors, these percentages drop to 9%, 14% and 11%, respectively. Because these excess fractions are very small, we chose to not account for IR excess in our KLF models of IC 348. It is possible, however, that a more substantial fraction of sources could have small K band excesses ( $dK_{irx} \sim 0.1$ ) that are not apparent in the color-color diagram especially since Haisch et al. (2001a) found that 65% of the IC 348 members have inner circumstellar disks as traced at  $3\mu\text{m}$ . We argue such small excesses will not substantially affect the cluster KLF and hence the derived cluster IMF since this flux excess is much smaller than the bins used to create the cluster luminosity function.

The last issue is if we should include the effects of un-resolved binaries, which in our models are instituted using a binary fraction,  $f_{bin}$  and assuming random pairing from a single parental IMF. To parallel our analysis of the Trapezium Cluster in Chapter 3, however, we chose to not include un-resolved binaries into our modeling routine. Thus the IC 348 IMF we derive is the “primary” or “single” star IMF.

Duchêne et al. (1999) found that the binary fraction in IC 348 is very similar to that found in other young clusters and to the field. Further, the consistency of the binary frequency in stellar clusters over a large range of cluster age (Patience et al., 2002), including young clusters like IC 348, suggests that the single star IMFs of star clusters can be readily derived and compared without correction for binaries.

A related issue in our studies of different cluster IMFs is whether or not a significant fraction of *resolved* wide binaries have been included into the cluster KLFs. For example, the physical resolution of our Trapezium study was  $\sim 240$  au, while in IC 348 it is  $\sim 480$  au. Since the binary fraction at these large separations is quite small ( $f < 0.1$ ), the few resolved binary systems that will be included into these cluster KLFs should not significantly modify the single star IMFs we derive.

#### 4.3.4 Modeling the IC 348 Differential KLF(s)

Using these cluster parameters, we produced a suite of model luminosity functions by varying the underlying initial mass functions and then fit these models to the observed cluster KLF(s). Our standard IMF parameterization consists of power-law segments,  $\Gamma_i$ , connected a break masses,  $m_j$ , and for our analysis of IC 348 we used 2 and 3 segment IMFs. We independently calculated and fit model luminosity functions for the cluster’s “core” and “halo” sub-region KLFs and for the composite cluster KLF, varying the extinction distribution function appropriately for each region. Our fitting technique calculates the  $\chi^2$  statistic and probability between the model KLFs and observed KLF over a range of magnitude bins and from these statistical measures, the parameters (mean, standard deviation) of the underlying IMF are derived. We summarize these fits and the resulting IMFs for the two sub-regions in section 4.3.4, and for the overall cluster in Section 4.3.4.

**The IC 348 core and halo sub-region KLFs.** In the left hand panels of Figure 4–15 we display the sub-region differential KLFs compared to the best fit model KLFs derived from our  $\chi^2$  fitting technique. The underlying power-law IMFs are displayed

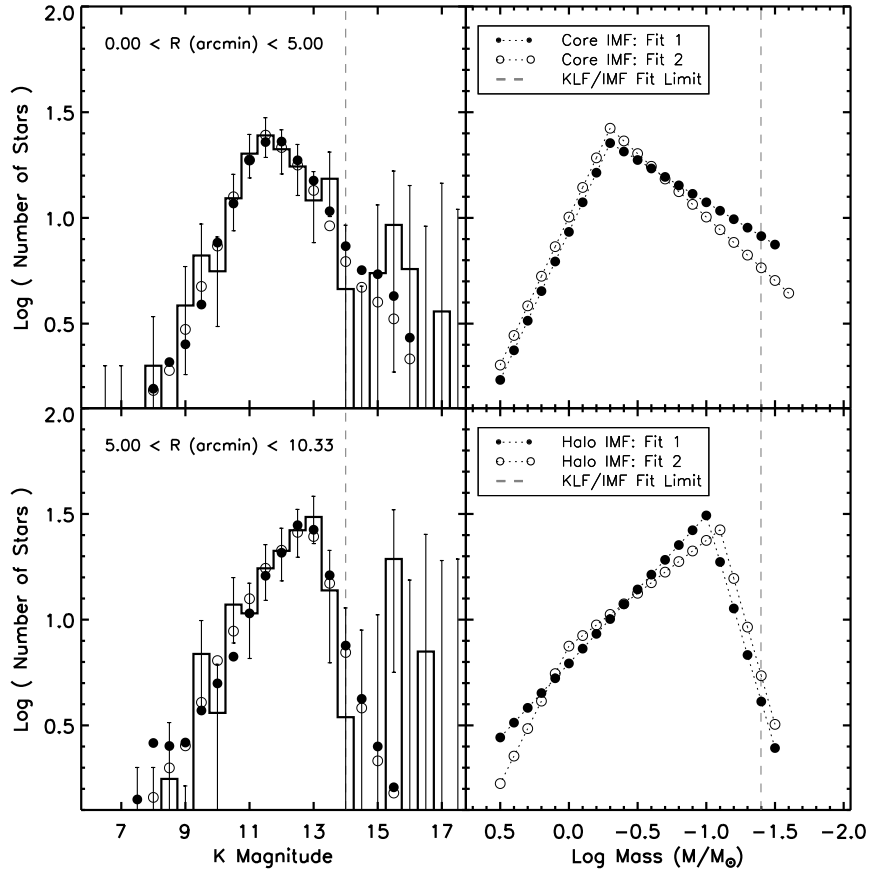


Figure 4–15: Modeling the IC 348 KLF: cluster sub-regions. Left hand panels display model KLFs best fit to the differential IC 348 KLFs of each sub-region (upper: core; lower: halo). The best fit model KLFs are normalized to the observations over a range from  $m_K = 8 - 14$ , corresponding to a mass range from  $2.5$  to  $0.04 M_\odot$ . Right hand panels display the underlying two and three power-law IMFs corresponding to the specific model KLFs (by symbol). Derived IMF parameters are listed in table 4–3.

in the right hand panels of this figure and we list our derived IMF parameters in table 4–3.

We found that model KLFs constructed using 2 power-law IMFs provided satisfactory fits to both sub-region KLFs, while we were able to obtain slightly better fits to the “halo” KLF using a 3 segment IMF. Further, by varying the range of KLF bins fit by our  $\chi^2$  routine, we are able to derive good KLF fits over the luminosity range from  $m_K = 8 - 14$ , corresponding to a mass range from  $2.5$  to  $0.04 M_\odot$  ( $\sim 40 M_{Jup}$ ). Fits down to the  $m_K = 15$  bin are also moderately constrained in the core

sub-region, corresponding to a low mass limit of  $\sim 25 M_{Jup}$ . Owing to the large statistical uncertainties at the faintest magnitudes due to the field star contamination, we could not derive reasonable fits to the differential KLF(s) for  $m_K > 15$ .

For both sub-regions, the  $m_1$  mass break is very strongly constrained by the location of the bright KLF peaks in the 2 power-law IMF fits. The  $\Gamma_1$  IMF slope rises steeply with decreasing mass in the “core” sub-region, but is much shallower in the “halo” region. In our 3 power-law fits to the “halo” sub-region, we found a modest  $\chi^2$  minima that indicated there is an inflection in this high-mass slope near  $0.80 M_\odot$ , yielding a  $\Gamma_1$  similar to that found in the 2 segment “core” IMF. As pointed out before, the two sub-regions have distinctly different IMF peaks, with the core  $m_1$  mass break occurring at  $0.56 \pm 0.18 M_\odot$  and the peak of the halo IMF strongly constrained to lie at  $0.10 \pm 0.02 M_\odot$  (see table 4–3. Below their peaks, both sub-region IMFs steadily fall with decreasing mass down to our  $m_K - M$  fit limit. The  $\Gamma_2$  slope is more tightly constrained for the cluster core IMF than in the halo, where the rapid change in KLF slope between  $m_K = 12$  and 15 yields considerable uncertainty in this IMF parameter. Despite these limitations of our fitting procedure, we find that the resulting substellar IMF slopes are very different in the two sub-regions, although as we discuss in Section 4.4.2, they yield similar fractions of brown dwarfs when integrated over the entire mass range.

**The composite IC 348 KLF.** We examine the best fit model KLFs to the complete cluster KLF in the left hand panel of Figure 4–16. Unlike the simpler structure of the two sub-region KLFs, the composite cluster KLF displays a very broad main peak followed by a sharp turnover at fainter magnitudes. This structure required the use of model KLFs based upon a 3 power-law underlying IMF, and we tabulate the derived IMF parameters as function of the fit range in table 4–3. With these 3 segment underlying IMFs we were able to fit the composite cluster KLF down to  $m_K = 15$ , constraining the IMF from  $2.5 M_\odot$  down to  $\sim 25 M_{Jup}$ .

Table 4–3. IC 348 power-law IMFs derived from model KLFs

Cluster Region	$N_\Gamma$ ( <sup>a</sup> )	$m_K$ Limit	$M/M_\odot$ <sup>(b)</sup> Limit	$\chi^2$ Prob.	IMF Parameters <sup>(c)</sup>									
					$\Gamma_1$	$1\sigma$	$m_1$	$1\sigma$	$\Gamma_2$	$1\sigma$	$m_2$	$1\sigma$	$\Gamma_3$	$1\sigma$
core	2	14.0	0.040	0.93	-1.43	0.38	0.56	0.18	+0.43	0.25	...	...	...	...
core	2	15.0	0.025	0.83	-1.37	0.35	0.47	0.13	+0.59	0.17	...	...	...	...
core	2	16.5	~ 0.01	0.37	-1.47	0.38	0.61	0.19	+0.32	0.19	...	...	...	...
halo	2	14.0	0.040	0.76	-0.72	0.14	0.10	0.02	+1.98	0.46	...	...	...	...
halo	2	15.0	0.025	0.41	-0.75	0.16	0.10	0.01	+2.25	0.26	...	...	...	...
halo	2	16.5	~ 0.01	< 0.01	...	...	...	...	...	...	...	...	...	...
halo	3	14.0	0.040	0.81	-1.23	0.39	0.83	0.28	-0.55	0.14	0.093	0.01	+1.89	0.45
halo	3	15.0	0.025	0.40	-1.25	0.39	0.82	0.29	-0.53	0.14	0.092	0.01	+2.20	0.27
halo	3	16.5	~ 0.01	< 0.01	...	...	...	...	...	...	...	...	...	...
cluster	3	14.0	0.040	0.70	-1.49	0.30	0.79	0.25	-0.19	0.18	0.089	0.02	+1.75	0.53
cluster	3	15.0	0.025	0.63	-1.53	0.28	0.83	0.23	-0.23	0.14	0.086	0.01	+2.28	0.22
cluster	3	16.5	~ 0.01	< 0.01	...	...	...	...	...	...	...	...	...	...
Trap	3	...	0.025	0.99	-1.21	0.18	0.60	0.16	-0.15	0.17	0.120	0.04	+0.73	0.20

<sup>(a)</sup>Number of power-laws,  $\Gamma_i$ , used in the underlying IMF of the model KLFs.

<sup>(b)</sup>Conversion of the  $m_{K,limit}$  to  $M/M_\odot$  using the 2e6 Myr DM97 isochrone. For  $m_{K,limit} = 16.5$ , we converted to mass using the [Burrows et al. \(1997\)](#) and [Baraffe et al. \(2002\)](#) evolutionary models.

<sup>(c)</sup>Units of IMF parametes:  $\Gamma_i$  are slopes for an IMF defined as the number of stars per unit  $\log(M/M_\odot)$ ;  $m_j$  are mass breaks given in units of linear solar mass ( $M/M_\odot$ ).

Note. —  $\chi^2$  probability calculated for best fit model KLF over the range from  $m_K = 8 - m_{K,limit}$ . Average IMF parameters calculated within the 0.35 confidence contour.

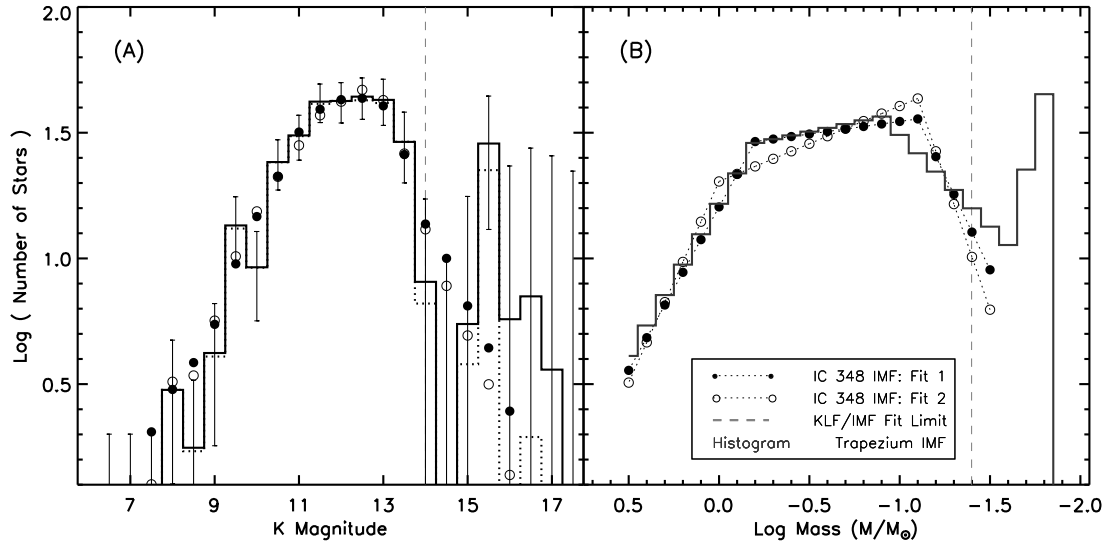


Figure 4–16: Modeling the IC 348 KLF: the composite cluster. The left hand panel compares the best fit model KLFs to the composite differential IC 348 KLF. The right hand panel compares the IMFs of these model KLFs to the IMF derived for the Trapezium cluster from Chapter 3, although the Trapezium is only the  $R < 0.3$  pc core of the larger Orion Nebula Cluster (Hillenbrand, 1997). Model KLFs and IMFs for IC 348 have corresponding symbols.

Over this mass range, our KLF fits yield an IC 348 IMF having a broad peak down to the hydrogen burning limit before rolling over and decreasing sharply into the substellar regime. The high-mass  $\Gamma_1$  slope is moderately constrained with an index of  $\sim -1.5 \pm 0.3$  (Salpeter =  $-1.35$ ) before flattening at  $m_1 = 0.80 M_{\odot}$ . The  $\Gamma_2$  slope and the  $m_2$  mass break are both strongly constrained by the broad KLF peak and the sharp KLF turnover at  $m_K = 13$ , with a very slowly rising  $\Gamma_2 \sim -0.2 \pm 0.15$  across much of the IMF before peaking at the hydrogen burning limit. Similar to the situation for the “halo” KLF/IMF, the  $\Gamma_3$  slope is very steeply falling but poorly constrained, with an index of  $\sim +2.0 \pm 0.4$ .

## 4.4 Discussion

### 4.4.1 The KLFs and IMFs of IC 348 and the Trapezium

**The stellar regime.** We examine the structure of the derived IC 348 KLF and IMF by comparing these cluster characteristics to those we derived for the Trapezium

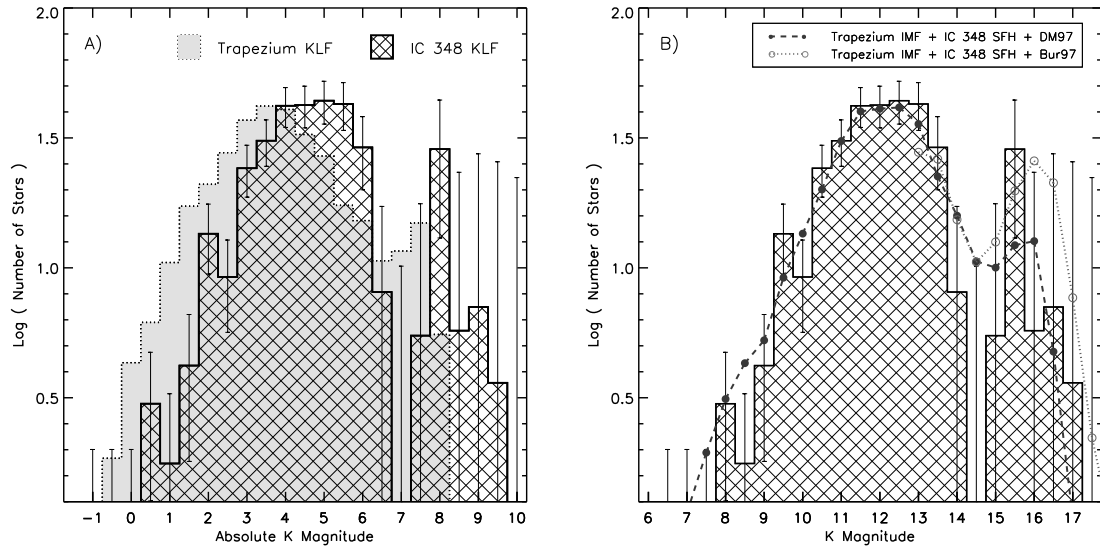


Figure 4–17: Comparison of IC 348 and Trapezium KLFs. Panel (A) compares the K band LFs of IC 348 and the Trapezium, shifted to absolute magnitudes. No reddening corrections have been included but the Trapezium KLF has been scaled to contain the same number of stars as IC 348. Panel (B) compares the IC 348 differential KLF to two model KLFs representing the Trapezium evolved to the age of IC 348. The models use the star-forming history and reddening for IC 348 but substitute the Trapezium IMF derived in Chapter 3 and use two different sets of PMS tracks (D’Antona & Mazzitelli, 1997; Burrows et al., 1997, DM97 and Bur97). This illustrates the predicted location and size of the secondary KLF peak of the Trapezium were this cluster the age of IC 348.

cluster in Chapter 3. By comparing the Trapezium IMF (also reproduced in table 4–3) to the derived IC 348 IMF we find that these two very young clusters have nearly identical IMFs throughout the stellar regime. As illustrated in Figure 4–16, both clusters have IMFs that rise in number with decreasing mass into the subsolar regime, with Salpeter like power-law slopes ( $\Gamma_{1, Trap} = -1.21$  and  $\Gamma_{1, IC348} = -1.53$ ). Their IMFs both flatten around  $0.7 M_{\odot}$ , having slopes of  $\Gamma_2 \sim -0.2$  and forming very broad shallow peaks at subsolar masses. The “peak” or mode of their IMFs varies between  $0.15$  and  $0.08 M_{\odot}$  with the IC 348 IMF skewing to slightly lower masses than the Trapezium.

The strong similarities between these clusters’ stellar IMFs exist despite the significant apparent differences between their cluster KLFs. In Figure 4–17a, we

compare the Trapezium and IC 348 KLFs, shifting them by their respective distance moduli to absolute magnitudes and scaling the Trapezium population to match that of IC 348. The IC 348 KLF is clearly broader and shifted to fainter magnitudes relative to the Trapezium KLF with their primary KLF peaks differing by almost 2 magnitudes. These differences, however, are precisely those predicted by the evolution of the luminosity function with age (Lada & Lada, 1995; Muench et al., 2000). Indeed if we evolve a model KLF of the younger Trapezium to the age of IC 348 and compare it to the IC 348 KLF in Figure 4–17b, we find it agrees with the observed IC 348 KLF extremely well down to  $m_K = 12.5$ , near the unreddened hydrogen burning limit for IC 348 ( $\tau = 2$  Myr,  $m_{K,HBL} \sim 12.7$ )<sup>2</sup>. Fainter than this magnitude the evolved Trapezium KLF moderately under-estimates the IC 348 KLF between  $m_K = 13$  and 13.5, indicative of the slight skewing of the IC 348 IMF mode to lower masses. Below  $m_K = 13$ , both the observed IC 348 KLF and the evolved Trapezium KLF steeply fall in number, marking the transition to the substellar regime that we explore in the next section.

**The substellar regime.** Reviewing Figure(s) 4–16b and 4–17, one immediate similarity between the substellar KLFs and IMFs of IC 348 and the Trapezium is their mutual steep decline towards fainter magnitudes and lower masses. Although the IC 348 IMF mode skews to lower masses than the Trapezium, it turns over and decreases in a much steeper manner than the Trapezium, i.e.,  $\Gamma_{BDs,IC348} = 2.0$  while  $\Gamma_{BDs,Trap} \sim 0.7$ . This is also illustrated by the way that the evolved Trapezium KLF

---

<sup>2</sup> This quantity is fairly independent of current PMS tracks, see Figure 4–14. From various models we find for IC 348 that  $m_{K,HBL}(\text{D'Antona \& Mazzitelli, 1994}) = 12.74$ ,  $m_{K,HBL}(\text{DM97}) = 12.67$ ,  $m_{K,HBL}(\text{Burrows et al., 1997}) = 12.55$ , and  $m_{K,HBL}(\text{Baraffe et al., 1998}) = 12.83$ . For a mean age of 3 Myr at a distance of 260 pc,  $\langle m_{K,HBL} \rangle = 12.68$ .

seems to consistently over-estimate the number faint objects in IC 348, although they do agree within the large statistical uncertainties.

A second similarity between the substellar KLFs of IC 348 and the Trapezium, is the formation of a modest but statistically significant secondary KLF peak, which in IC 348 contains  $42 \pm 29$  sources between  $m_K = 15$  and 17. Further, the secondary KLF peak for IC 348 occurs precisely in the magnitude range predicted by the evolved Trapezium KLF, suggesting they are related features corresponding to sources in the mass range from  $10 - 20 M_{Jup}$ . As was the case for our Trapezium modeling, such KLF structure rejected our fitting of these magnitude bins using models based upon 3 segment power-law IMFs. This is because we are trying to fit this non-power law KLF structure (a dip or gap followed by a secondary peak) with model KLFs that are essentially a power-law throughout the brown dwarf regime because the theoretical mass-luminosity relations that we have used are smooth and do not contain any significant evolutionary features in this mass range. Considering the statistical uncertainties due to the background correction we did not attempt to explicitly fit additional IMF segments to the IC 348 peak although the size of the predicted peak using the Trapezium IMF closely approximates this feature. The similarity of the predicted size of the secondary peak in IC 348 relative to the Trapezium and the similar mass range represented by this feature suggests that they are intrinsically related and may be evidence confirming that such structure exists in the cluster KLF at these ages. We discuss whether this similarity supports our hypothesis of a secondary IMF peak near the deuterium-burning limit or suggests a different origin of this secondary KLF peak in Chapter 7.

One meaningful constraint regardless of detailed IMF structure is the *fraction* of cluster members that are substellar. For example, in the Trapezium we found that  $22^{+4}_{-2}$ % of the clusters members fell between 80 and  $17 M_{Jup}$ , having the interesting implication that only  $\sim 1$  in  $4$  of the cluster members were brown dwarfs! Estimating

this fraction for IC 348 is more difficult because the background correction makes directly counting all the substellar sources difficult. Rather than directly counting sources, we first integrated the derived IMF to calculate the fraction of substellar sources down to the mass limit of our fit. We find that brown dwarfs between 80 and  $25 M_{Jup}$  (the lower mass limit corresponding to our model fits to  $m_K = 15$  and the beginning of the secondary KLF peak) constitute only 14% of the members with 2% uncertainty due to the variation in our fits, and 9% uncertainty due to the counting statistics as dominated by the background correction. For comparison, integrating the Trapezium IMF over the same mass range yields a brown dwarf fraction of 20%.

When we count the number of sources contained in the secondary peak of the IC 348 KLF and not included into the KLF fits, we are able to extend the range of substellar masses down to  $10 M_{Jup}$ , however we also find that the precision of our estimate is significantly worsened by the large field star contamination. Since this secondary KLF peak contains between 26 and 42 sources depending upon the size of the correction for field stars, the total substellar fraction increases to 20 – 25% for IC 348, although the corresponding error bar also increases to  $\pm 14\%$ . Thus despite the uncertainties due to the field star correction, we find that these fractions indicate that IC 348 has anywhere from a moderate dearth to an similar brown dwarf fraction as that found the Trapezium and further, that brown dwarfs are not nearly as populous as stars in either cluster.

#### 4.4.2 Radial Variation of the IC 348 IMF

Our division of the cluster into two sub-regions based on the cluster’s radial profile (see Section 4.1.3) allows us to make important comparisons to past studies of the IC 348 IMF, which have primarily focused on the cluster’s core. For example, when we compare the IMF derived by [Najita et al. \(2000\)](#) for around 100 members of the IC 348a sub-cluster to that we derive for the cluster core in Figure 4–18, we find they agree remarkably well over the mass range from 0.25 to  $0.025 M_{\odot}$ , although the

NICMOS IMF is flatter at higher masses likely due to source saturation or possibly statistical fluctuations since they are not precisely the same samples.

Such a strong similarity is not found, however, when we compare the IMF of the cluster's core to that we derived for the cluster halo. Paralleling the apparent physical differences seen in the KLFs of the IC 348 sub-regions (see figures 4-10 and 4-12), we find that the IMF of the halo skews to lower masses relative to the IMF of the cluster's core. This variation of the IMF is a real representation of the differences in the two sub-regions and is not the product of a variation in some other physical quantity. Reddening due to the molecular cloud and specific to each sub-region is included into these fits, although no meaningful differences exist between the relevant EPDFs of the two regions (see Section 8). Although we did not include the effects of infrared excess, any such effect would actually *increase* the IMF differences, since the larger excess fraction of the halo and would require the halo IMF peak to shift to lower masses. Further, the larger excess fraction in the halo might imply that the halo is younger than the core. However, accounting for such an age difference would again shift the IMF peaks in *opposite* directions from one another and amplify the IMF variations we derive. Lastly, although it would seem to contradict the distribution of infrared excess and H $\alpha$  sources and was not corroborated by the study of Palla & Stahler (2000), Herbig (1998) reported a slight age gradient in IC 348, finding an increasing mean age at larger radii. Such a gradient does act in the correct direction to account for some of the KLF differences, however, even if this age gradient is real, it is considerably too small ( $\tau \sim 1.45$  Myr at  $R = 4'$  to 2.8 Myr at  $R = 10'$ ) to bring the IMFs of the sub-regions into agreement. To align the sub-region IMF peaks given the observed KLFs would require two distinct populations where the halo is 5-10 Myr older than the core. This is a difficult hypothesis to accept considering the populations are of equal size, and while such a model might align the peak of the IMFs by shifting the halo to higher masses, it would further imply that the IMF of the halo is

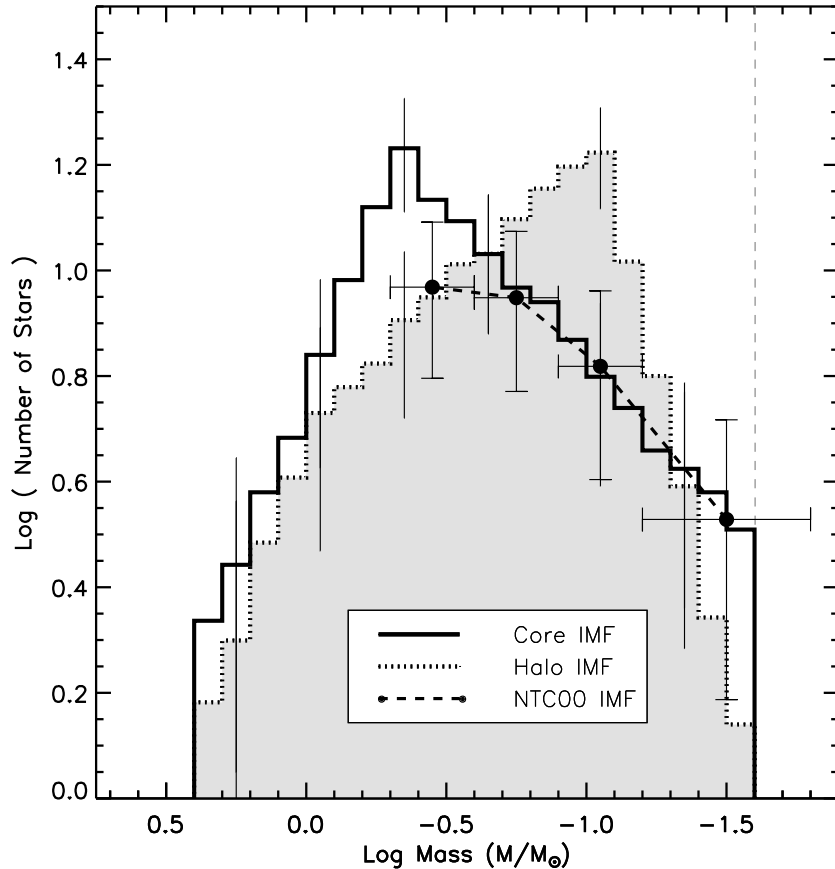


Figure 4–18: Radial variation in the IC 348 IMF. Comparison of the Core and Halo Sub-Region IMFs for IC 348. Shown are Monte Carlo simulations of the derived IMFs for the IC 348 sub-regions and calculated for a sample of 150 stars. Error bars, calculated as the  $1\sigma$  variation in each IMF bin from 100 iterations, are shown every 0.3 dex in log mass for clarity. These sub-region IMFs are also compared to the IMF of the IC 348a sub-cluster derived by [Najita et al. \(2000\)](#) using NICMOS narrow band imaging, with error bars taken directly from this work. The IC 348a sub-cluster is approximately the same area as the IC 348 core sub-region.

radically truncated below  $0.3 M_{\odot}$ . As was originally found in the model fits of [LL95](#), we conclude that such a two age population model cannot explain the IC 348 KLF.

Since the differences between the core and halo sub-regions can only be related to their underlying IMFs and these IMF differences also appear statistically significant as illustrated in figure 4–18, this means that IC 348 displays radial IMF variations on scales of the order of 1pc. Further, these radial IMF differences exist primarily at subsolar masses in IC 348, unlike typical scenarios for mass segregation in very young

clusters in which only the higher mass stars ( $M > 1 M_{\odot}$ ) are thought to be preferentially affected. With these cluster(s) being only a few crossing times old, there is only enough time for the massive stars to sink to the cluster core (Kroupa et al., 2001); otherwise, the massive stars are preferentially born in the cluster center (Bonnell et al., 2001).

Radial variations of a cluster's subsolar mass IMF have also been reported for the Orion Nebula Cluster (ONC), of which the Trapezium is the core. While this cluster displays additional evidence for the segregation of high-mass stars to the cluster core (Hillenbrand & Hartmann, 1998), the low mass ONC IMF varies between the central core and outer cluster halo. This has been shown by Hillenbrand (1997) and Hillenbrand & Carpenter (2000) who found that while the IMF of the central  $r < 0.35$  pc Trapezium core peaks around  $0.2 M_{\odot}$ , the addition of the cluster's halo ( $r_{tidal} = 2.5$  pc) produces a composite ONC IMF that continues to rise down to  $0.1 M_{\odot}$ , the completeness limit of the Hillenbrand spectroscopic survey of the entire ONC cluster. While the difference in the skew of the subsolar IMF as a function of radius appears smaller in the Trapezium than what we have found for IC 348, it proceeds in the same direction, i.e., both the cluster's halo and composite cluster IMFs skew to lower masses than the IMF that would be derived if only the cluster core's were examined.

Lastly, it is important to examine how the substellar sources are radially distributed. Since dynamical effects that could produce the radial IMF variation may operate on the lowest mass sources by skewing them to larger radii, brown dwarfs may correlate with the distribution of low mass sources and be systematically located further from the cluster center. While the slope of the substellar IMF radically varies between the IC 348 core and halo, the percentage of sources that are substellar does not. We find that sources in the mass range from  $80 - 25 M_{Jup}$  constitute roughly 14% of the sources in the cluster core and a similar 16% in the cluster halo. Unless brown

dwarfs preferentially populate the extreme outer regions of IC 348 beyond the  $r = 1$  pc radius of our survey, this finding suggests that the mechanism that is breaking the universality of the IMF on small size scales, whether it is primordial IMF variations or dynamical mass segregation, does not appear to be significantly acting upon the substellar population. Interestingly, the size of the brown dwarf population of the outer  $r > 0.35$  pc region of the ONC is currently unknown and a wider-field IR survey could reveal a similar distribution of the substellar sources. In combination with our results for IC 348 such observations might be used to ascertain the origin of this radial variation of the subsolar IMF in clusters that are still embedded in their parental molecular clouds.

#### 4.5 Conclusions

Using wide-field near-infrared images provided by the FLAMINGOS camera on the Kitt Peak 2.1m telescope, we performed a detailed census of the young 2 Myr IC 348 cluster located on the northeastern end of the Perseus Molecular Cloud. Using the multi-color infrared photometry provided by our observations, we explored this cluster's structure, reddening, and relationship to the parental molecular cloud, and then used these results to construct and to analyze the IC 348 KLF and to correct it for field star contamination. Using our model luminosity function algorithm described in [Muench et al. \(2000\)](#) and [Muench et al. \(2002\)](#), we derived the cluster's initial mass function, providing detailed fits and error estimates. From our analysis of the cluster's structure and luminosity function and by comparison to our earlier study of the Trapezium cluster, we draw the following conclusions about the KLF and IMF of IC 348:

1. We derive an IMF for the composite IC 348 cluster spanning the mass range from 2.5 to  $0.025 M_{\odot}$ . Further, we find that the IC 348 IMF we derive is nearly identical to the Trapezium IMF we derived in [chapter 3](#): The two clusters IMFs rise with decreasing mass, having a Salpeter-like slopes before flattening below  $0.7 M_{\odot}$ . Within

the current uncertainties in PMS evolutionary models, we find that the mode of these cluster IMFs appear to fall at a mass of  $\sim 0.1 M_{\odot}$ .

2. Further, we find that the relative size of the substellar population is very similar in both clusters within the uncertainties of our method, revealing that brown dwarfs constitute only 15 – 25% of the members of either cluster.

3. IC 348 forms a modest but statistically significant secondary KLF peak, corresponding to sources in the same mass range that we found responsible for a similar secondary KLF peak in the Trapezium. The similar KLF features in the Trapezium and IC 348 may signify either the presence of a secondary peak in the substellar IMF between 10 and  $20 M_{Jup}$  as we derived for the Trapezium in Chapter 3, or be the result of a previously undocumented feature in the brown dwarf mass-luminosity relation, as we discuss further in Chapter 7.

4. Radial variations are found in the KLF and IMF of IC 348 on the parsec scale, with a skewing of the KLF to fainter sources and the IMF to lower mass stars in the cluster’s halo, a portion of the cluster whose IMF was previously undetermined. This radial variation in the subsolar IMF is similar to what was found previously for the subsolar mass stars in the Orion Nebula Cluster. It is unclear what process is breaking the universality of the cluster’s IMF on small spatial scales, but it appears different from dynamical mass segregation which primarily acts upon higher mass stars at these young ages. Further, while the slope of the substellar IC 348 IMF varies substantially as a function of radius, the percentage of sources that are brown dwarfs does not.

Finally, we draw the general conclusion that the existence of radial variations of the IMF on parsec scales even at very young ages (1 Myr) may mean that wide-field imaging surveys are a pre-requisite to making meaningful IMF comparisons between different embedded clusters, a fact that has clearly been true in older open clusters for some time.

## CHAPTER 5 THE YOUNG OPEN CLUSTER NGC 2362

In addition to probing the lowest mass populations of nearby clusters, luminosity function studies have the utility that they can be applied to deep surveys of more distant clusters. Using optical luminosity functions, [Phelps & Janes \(1993\)](#), for example, performed a study of the intermediate - solar mass members of a large sample of somewhat older distant clusters. Such studies of distant clusters are vital for determining the degree of uniformity of the initial mass function through space and time, as they are drawn from a much larger volume of the local galaxy and almost certainly sample more varied cluster environments than those found within the local kiloparsec. However, because of their distance, only the brightest, most massive cluster members can be studied spectroscopically. Coupled with the fact that at these young ages few if any such massive stars have begun to evolve, this means that the ages of these clusters are often poorly known.

NGC 2362 is a classic very young open cluster lying at a distance of 1500 pc ([Balona & Laney, 1996](#)). Despite containing various evolutionary signposts suggesting an age younger than 10 Myr, the cluster is not embedded in a molecular cloud. Indeed, as we will show there we could not find evidence of remnant molecular material anywhere near the cluster. Morphologically, NGC 2362 is dominated by the O9Ib super-giant star,  $\tau$  Canis Majoris, often referred to as lying at the cluster's center. The cluster has an extensive B star population which defines the standard observational Zero-Age Main Sequence ([Johnson & Morgan, 1953](#)) and which has been used to derive a cluster distance of  $\sim 1500$  pc ([Johnson, 1950](#); [Balona & Laney, 1996](#); [Moitinho et al., 2001](#)). Modern optical studies have revealed lower mass stars in the cluster ([Wilner & Lada, 1991](#); [Moitinho et al., 2001](#)), yet knowledge of the

cluster’s age has until recently depended upon the post-main sequence evolution of a single star:  $\tau$  Canis Majoris. Fits of post-main sequence evolutionary models to the location of  $\tau$  Canis Majoris in the HR diagram have yielded a cluster age of approximately 5 Myr (Balona & Laney, 1996; Moitinho et al., 2001), yet such fits are very uncertain, mostly because  $\tau$  Canis Majoris is actually a spectroscopic quadruple (van Leeuwen & van Genderen, 1997; Stickland et al., 1998). While the age of NGC 2362 has been improved by a very recent, deep optical study of the pre-main sequence star locus for the cluster (Moitinho et al., 2001), we will consider the uncertainty in the age of NGC 2362 when studying this cluster’s luminosity function. This should allow us to quantify the usefulness of our techniques when applied to regions where even less is known about the age of the cluster.

To construct the infrared luminosity function for NGC 2362 we collaborated with J. Alves who surveyed a  $10' \times 10'$  region around  $\tau$  Canis Majoris (Alves et al., 2001). This infrared census (hereafter referred to as the La Silla survey) reached a depth of  $m_K = 17$  and is briefly detailed in Section 5.1. To estimate the contamination of the cluster KLF by field stars, off-cluster images, totally  $\sim 30\%$  of the on-cluster survey area were also obtained to equivalent depth at K band. These off-fields were located  $1^\circ$  from the cluster, along a line of constant galactic latitude with the cluster.

In addition, we undertook an archival study of NGC 2362 using an existing all-sky infrared survey to examine the cluster over an area much larger than that of the La Silla observations. In Section 5.2, we use this wide-field survey to define the cluster boundaries, to examine the reddening properties toward the cluster and to improve our estimate of the field star contamination. In Section 5.3, we combine this study with the products of the La Silla survey and construct the differential cluster KLF for NGC 2362. In Section 5.4 we compare the NGC 2362 cluster KLF to those KLFs we have derived for the Trapezium and IC 348 clusters. Finally, we model the NGC 2362

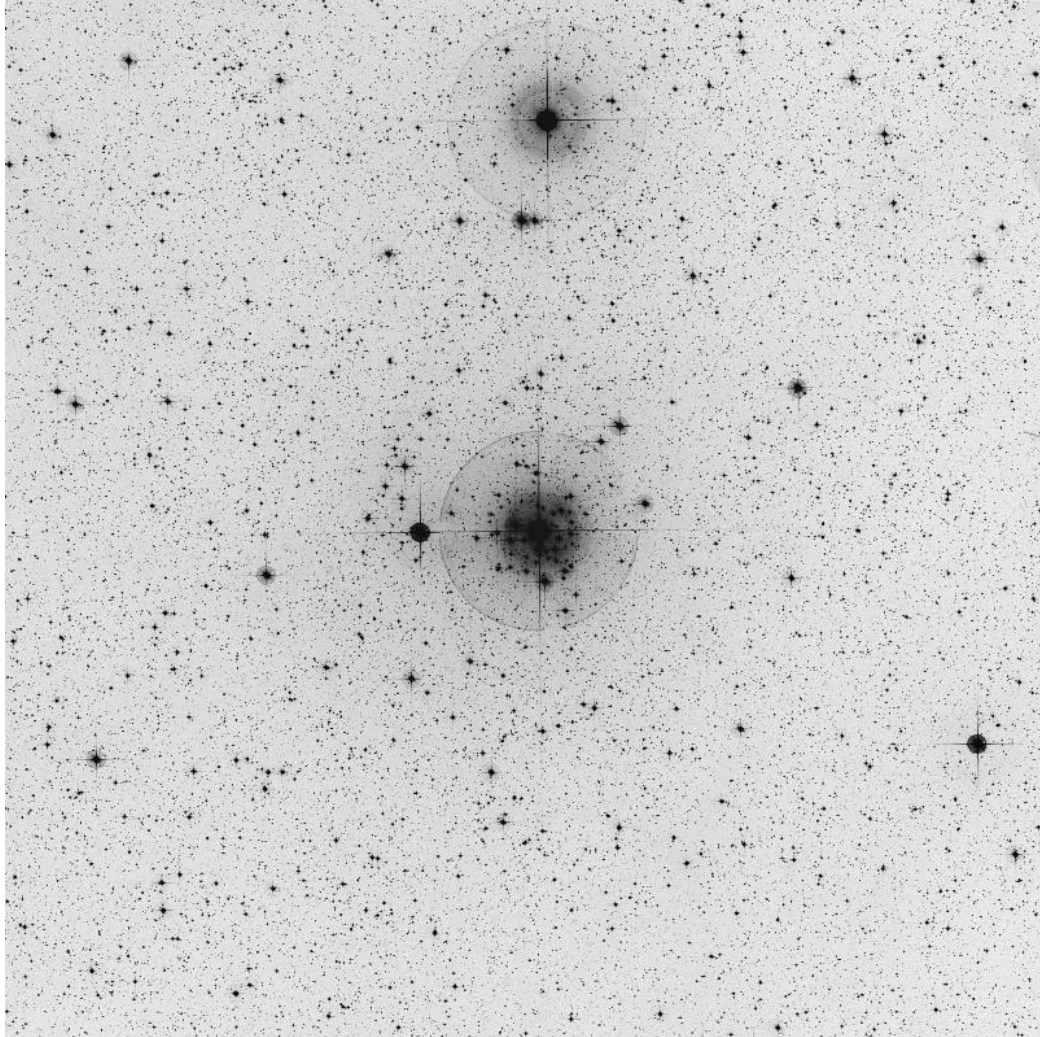


Figure 5–1: Digitalized sky survey image of NGC 2362. For orientation, north is up while east is left and the field of view is  $60.0 \times 60.0'$  on this Schmidt projection of the red “J” band image from the UK Schmidt telescope. Epoch: 1973-1974.

KLF in Section 5.5, exploring the dependence of our results on the cluster’ age and deriving the cluster’s underlying mass function.

### 5.1 La Silla Observations of NGC 2362

Between 27-29 December 1996, a near-infrared (JHK) survey of the central  $10' \times 10'$  region of NGC 2362 was completed by J. Alves using the IRAC-2b infrared camera on the 2.2 meter telescope at the European Southern Observatory (ESO) in La Silla, Chile. The survey consisted of 225 individual images in a  $5 \times 5$  mosaic

grid centered on  $\tau$  Canis Majoris and the IRAC-2b camera was configured to have a  $2\frac{1}{2} \times 2\frac{1}{2}$  field of view and a  $0.51''$  pixel plate scale. The image reduction was performed by J. Alves using the IRAF package(s), and following standard techniques in the infrared. Briefly, nightly dark frames and median local sky frames were subtracted from the individual images before they were flat-fielded using local sky flats. For each mosaic position, individual dithers were stacked and combined using the shift-and-add technique. Final images had an effective integration time of 13.5 minutes, FWHM estimates of  $\sim 1.2''$  and nearly 2200 sources were detected at K band in the cluster region.

Similarly, 72 individual images in 8 different, non-overlapping control fields were observed at K band to provide statistical estimates of the field star population. The fields were located one degree from  $\tau$  Canis Majoris along a line of constant galactic latitude with four each at higher and lower galactic longitude relative to NGC 2362. Figure 5–2 in Section 5.2 illustrates the spatial location of these off-fields.

Aperture photometry was performed using a beamsize of  $4''$  and was corrected out to the sky annulus using aperture corrections derived for each reduced mosaic position. Final calibration (zeropoint and airmass corrections) was performed by comparison to [Elias et al. \(1982\)](#) infrared standards observed throughout each observing night and chosen to sample the range of airmass of the observations. The data were calibrated to this natural system of the IRAC-2b camera and color corrections to a standard system were not subsequently applied. Source extraction and photometry were performed on each individual frame before being mosaicked together using the centers of stars in overlap regions. Astrometry with reasonably high precision was performed by matching the XY pixel locations of a large number ( $\sim 200$ ) of the observed sources on the mosaicked grid to the equatorial positions of these sources listed on the 2MASS world coordinate system and deriving full plate solutions using the IRAF CCMAP. This process was completed in two steps. Rough coordinates were derived by manually

matching 3 sources both on the grid and in the 2MASS catalog, yielding a linear solution applied to all the sources. The rough La Silla database was then matched in full to the 2MASS catalog, yielding a larger number of matches and higher order corrections in the CCMAP routine. The final coordinates have residual errors of  $\sim 0.2''$ .

## 5.2 2MASS Observations of NGC 2362

### 5.2.1 Spatial Structure of NGC 2362

To survey NGC 2362 over an area larger than that covered in the La Silla observations, we made use of archived data in the public domain. The Two Micron All Sky Survey (2MASS) is an infrared survey of the entire sky at J, H and  $K_S$  wavelengths ( $1 - 2.2\mu\text{m}$ ). This survey was completed in December 2000 with the final data release planned for September 2002. The resulting 2MASS source catalog is being released incrementally; for the purposes of this work we will use the 2MASS products from the Second Incremental Data Release (circa March 2000).

From the 2MASS catalog, we downloaded positions and (JHK<sub>S</sub>) magnitudes for sources that have  $K_S$  magnitudes brighter than 14 and lie within  $1^\circ$  of  $\tau$  Canis Majoris. This faint limit was conservatively chosen to be brighter than the nominal (target) completeness limit ( $K_S = 14.3$ ) of the 2MASS survey, although the 2MASS survey is more complete than their target limit in most areas of the sky. A digitalized sky survey of this area of NGC 2362 is shown in figure 5–1 and the spatial distribution of these 2MASS sources around NGC 2362 is shown in Figure 5–2. Sources falling near the locations of extremely bright stars or along these stars' diffraction spikes have been withheld from the public domain until the final catalog release; the resulting gaps in the 2MASS spatial coverage are evident across the survey field. Indeed, within the boundaries of the La Silla infrared observations of NGC 2362, the 2MASS catalog is significantly incomplete with respect to the La Silla observations because of the extreme brightness of  $\tau$  Canis Majoris.

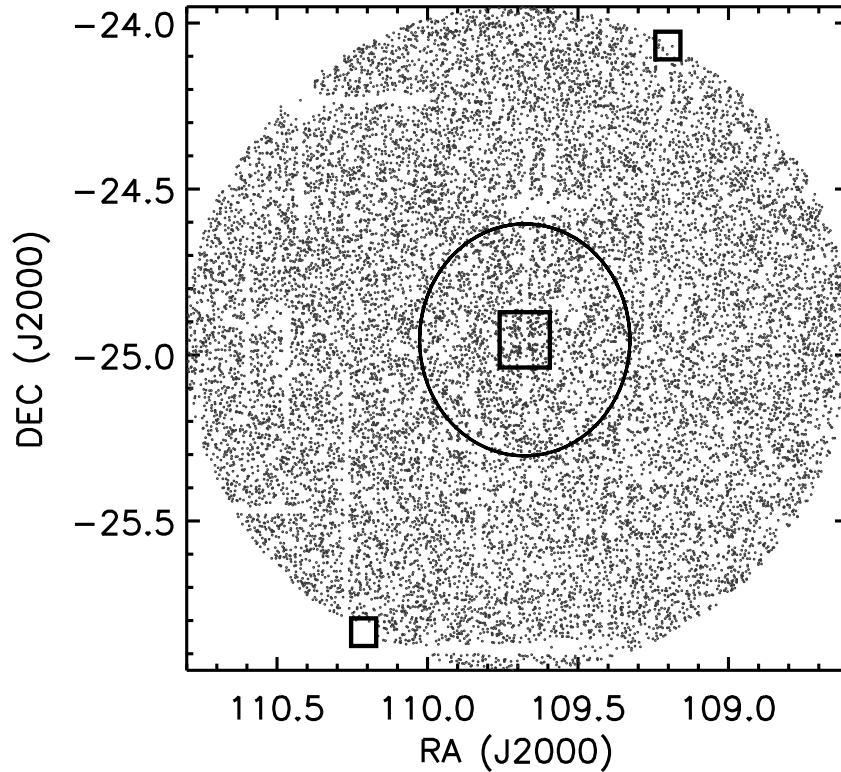


Figure 5–2: Source distribution of NGC 2362 from 2MASS. Surface plot of 2MASS sources surrounding NGC 2362. Large empty areas are regions incomplete in the current 2MASS catalog due to bright star artifacts. The region surveyed by the La Silla observations is indicated by the central square box. The circle, centered on the cluster, represents the area outside of which the 2MASS survey was used to calculate the field star surface density. The two La Silla off-field locations are indicated by small boxes at the periphery of the 2MASS survey.

Using this dataset, we calculated radial profiles for the source distribution in NGC 2362 in an attempt to define the spatial extent of this cluster. We used  $\tau$  Canis Majoris as the cluster’s center, and derived radial profiles of the 2MASS survey region using the same two methods used in Chapter 4: 1) by counting the stars in successive annuli of equal radial separation and 2) counting them in successive annuli having equal areas. While the former is a more common method, the latter gives a better estimate of the noise in the field star surface density for a fixed area. In Figure 5–3, we plot both of these radial profiles from the 2MASS survey, further constructing three sets of profiles for different magnitude intervals. At large radii from the cluster,

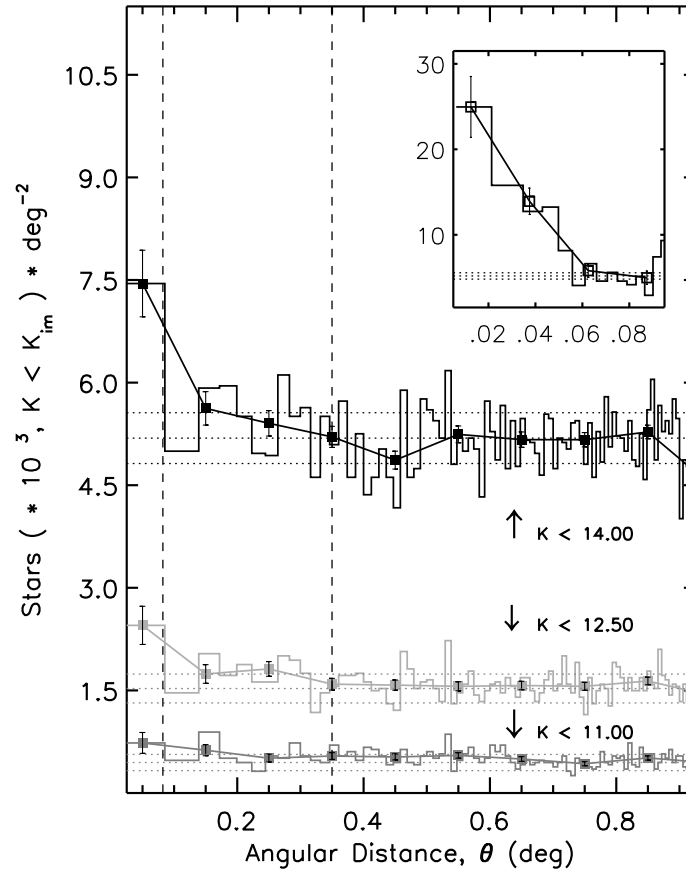


Figure 5–3: Radial profiles of NGC 2362. Three radial profiles (referenced to the location of  $\tau$  Canis Majoris) are displayed corresponding to three different magnitude ranges (see plot). In all cases the radius of the first annulus equaled  $6'$ . The radial profile(s) of 2MASS sources are shown on the full axis; those of the inner  $0.1^\circ$  La Silla dataset are shown in the inset using an  $R_{init} = 1.5'$  and for all sources with  $m_K < 14$ . Artificial dips in the 2MASS radial profile(s) at  $\theta_r = 0.45$  and  $1.0$  result from the gaps in the 2MASS coverage (see Figure 5–2). Three horizontal dotted lines are shown for each profile and correspond to the median field star surface density (for that magnitude range) and the  $\pm 1\sigma$  variation in the off-field surface density in area equivalent to the NGC 2362 La Silla survey. Vertical dashed lines demark the limit of the La Silla survey and an outer boundary where the radial profile intercepts the median field star surface density.

the surface density is well behaved, with a mean(s) of 486 stars per square degree ( $m_K < 11$ ), 1564 stars per square degree ( $m_K < 12.5$ ) and 5188 stars per square degree ( $m_K < 14$ ). Because the 2MASS catalog is very incomplete in the cluster core, we used the La Silla IR catalog to find that the central  $\theta_r = 0.02^\circ$  ( $r=0.5$  pc) reaches a surface

density of  $\geq 2.5 \times 10^4$  stars ( $m_K < 14$ ) per square degree (see inset in Figure 5–3) and does appear to hit the background at a radius of  $\sim 1.5$  pc.

Despite the incompleteness of the current 2MASS catalog in the cluster core, there appears to be a clear central concentration of stars within the ESO survey boundaries. This is true for either radial profile style and any magnitude range. Gaps in the 2MASS coverage extend beyond the cluster core, however, with prominent dips occurring at  $\theta_r = 0.45$  and  $1.0$ . Despite these features, there is a suggestion from all of the 2MASS cluster profile(s) that NGC 2362 extends beyond the ESO survey region. This is in spite of the fact that the central core does appear to go to the background at smaller radii. In all the radial profiles the bins between  $\theta_r = 0.10$  and  $0.35^\circ$  appear elevated relative to the median surface density, and while not all the bins exceed the  $1\sigma$  noise estimate in the background, most of the *structure* of these bins is constant between different magnitude ranges. Since one goal of this archival survey is to improve the field star correction by surveying a larger cluster-free area, we wish to exclude any region that could contain cluster members. While the noise in these profiles do not allow us to determine a precise outer radius for the cluster, we do break the NGC 2362 2MASS into three somewhat arbitrarily named regions based on this profile: 1) the field star population, corresponding to the area well outside any cluster boundary ( $\theta_r > 0.35^\circ$ ); 2) a cluster “halo” region, corresponding to the 2MASS sources between the field star population and that area surveyed by our La Silla observations ( $0.1 < \theta < 0.35^\circ$ ); 3) The cluster “core” ( $\theta < 0.1^\circ$ ), which was surveyed to much greater depths (and completeness) by the La Silla observations.

### 5.2.2 Source Reddening for NGC 2362

Following the procedures used in chapters 3 and 4, we examine the infrared color-color diagram for NGC 2362 to determine the reddening of cluster sources due to interstellar extinction, the parental molecular cloud or by infrared excess from disks. In Figure 5–4 we construct the (H -  $K_S$ ) vs (J - H) color-color diagrams for each of

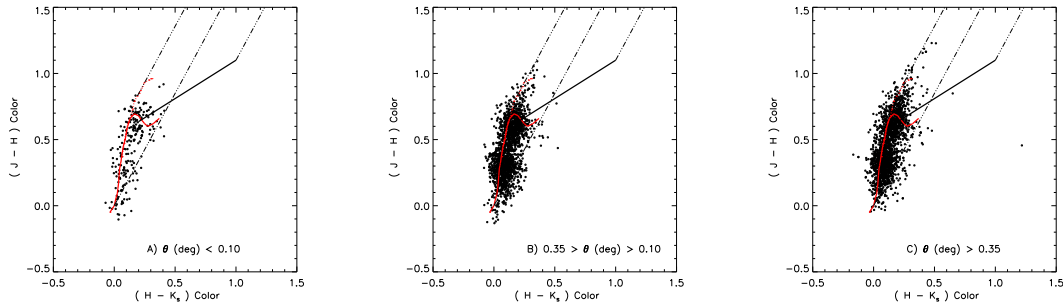


Figure 5–4: Infrared color-color diagrams for NGC 2362. These color-color diagrams were constructed from the 2MASS survey of NGC 2362 for each of the three cluster sub-regions: A) the cluster core; B) the cluster “halo”; C) the field star population. In the last case, only 2000 randomly chosen sources (of the 13000 stars in this region) are shown. The reddening law used is that from [Cohen et al. \(1981\)](#).

the three sub-regions of NGC 2362. Remarkably, neither the effects of interstellar extinction nor infrared excess are evident in any of the diagrams. Not only is there little extinction along the line of sight towards NGC 2362, there is very little if any seen towards the field stars within the cluster’s  $1^\circ$  neighborhood. We attempted to confirm this lack of excess by examining the digital sky survey plates and the dust opacity maps of [Wood et al. \(1994\)](#) and could find no bright or dark nebula, and an apparent “hole” of low opacity appears on the IRAS maps. Further, the lack of infrared excess sources in the cluster core implies that nearly all of the stars have lost their inner disks. This observation was first found by [Alves et al. \(2001\)](#) who studied the color-color diagram of the deep La Silla observations and found that this dearth of infrared excess sources continues down to that survey’s completeness limit ( $m_K = 16.5$ ). It has been subsequently confirmed by [Haisch et al. \(2001b\)](#) who found no sources down to  $m_K = 14$  with  $3\mu\text{m}$  excess.

These findings have two immediate implications for our analysis. First, our modeling procedure will not need to include the effects of source reddening on the cluster members. Second, estimating the contribution of field stars to the cluster KLF will not be complicated by patchy extinction as was the case in our study of

IC 348. On the other hand, the lack of a large background molecular cloud (as was the case for the Trapezium) means the field star contamination will be significant. Thus our statistical subtraction a field star KLF from the on-cluster KLF will result in a meaningful KLF only for that magnitude range where cluster dominates the field star density. Now we combine this wide-field survey with the deeper La Silla observations to construct the cluster and field star K band luminosity functions for NGC 2362.

### 5.3 The NGC 2362 Cluster KLF

#### 5.3.1 Empirical Field Star KLF

In Figure 5–5(a) we construct the field star KLF relevant for the NGC 2362 cluster region. In histogram form we show the KLF (scaled to stars per square degree) of 2MASS sources between the  $0.35^\circ$  cluster boundary and the  $1^\circ$  survey boundary. We compare this “field star” KLF to the KLF derived from our La Silla off-cluster observations, which covers a mere 1/350th the area of the corresponding 2MASS surface area.

Brighter than  $m_K = 12$ , the La Silla off-fields do not cover sufficient area to properly sample the bright population; this is a motivating factor for our use of the 2MASS off-cluster survey. Between  $m_K = 12$  and 14, where the La Silla and 2MASS field star KLFs overlap and are both well sampled, they agree extremely well and have very similar slopes, suggesting the two off-fields can be straightforwardly combined. Below  $m_K = 14$ , however, the slope of the deeper La Silla field star KLF appears change and flatten relative to the La Silla/2MASS KLF for  $m_K < 14$ . We illustrate this change in slope by fitting each KLF with a power-law function and comparing their resulting slopes. From  $m_K = 7 - 14$ , the 2MASS KLF can be characterized as a power law with a slope of  $0.3488 \pm 0.0056$ , while between  $m_K = 12$  and 16.5, the La Silla off-cluster KLF has a slope of  $0.2787 \pm 0.0146$ .

For the purposes of our subsequent analysis, we will assume this change in slope is a real feature of the field star KLF. We construct the field star KLF relevant for

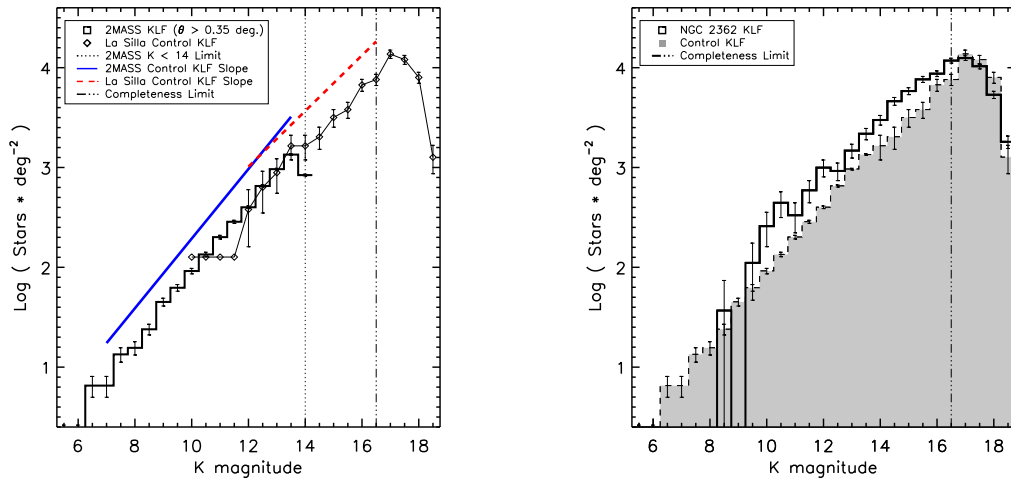


Figure 5–5: Field star and cluster KLFs of NGC 2362. A) Construction of an empirical field star KLF for NGC 2362. The deep La Silla off-field KLF is compared to the 2MASS field star KLF. Error bars are from  $1\sigma$  counting statistics, though the factor of 350 between the 2MASS survey and La Silla off-cluster areas results in smaller statistical errors bars for the 2MASS off-fields relative to those fainter than  $m_K = 14$ . Also shown are power-law indices of the 2MASS and La Silla off-field KLFs, illustrating the flattening below  $m_K = 14$ . B) Comparison of NGC 2362 cluster and field star KLFs (in stars per square degree). The cluster dominates the expected field star counts down to the  $m_K = 16.5$  completeness limit. Error bars are from counting statistics.

NGC 2362 by combining the 2MASS field star KLF brighter than  $m_K = 14$  with the La Silla off-cluster KLF for  $m_K = 14$  and fainter. The power-law index of this combined field star KLF is  $0.3198 \pm 0.0059$ . Uncertainties in the individual bins of the combined KLF are assigned based on the area of the survey from which they were drawn. This means that the error bars for the fainter bins taken from the La Silla off-fields are larger than at the brighter magnitude bins derived from 2MASS.

There are a few concerns with our construction of the field star KLF for NGC 2362; specifically, that the change in slope of the field star KLF could represent some systematic error in its construction. Such an error could come about if, for example, the La Silla observations coincidentally struck a low surface density region or a small patch of molecular material. Yet there is no evidence of reddening in this

region and the La Silla observations came from more than one location relative to the cluster. Further, the mean surface density of stars ( $m_K < 14$ ) in the La Silla and 2MASS regions agree to within 5% as do their KLFs between  $m_K = 12$  and 14.

### 5.3.2 NGC 2362 Differential KLF(s)

In Figure 5–5(b), we compare our empirical field star KLF to the NGC 2362 cluster KLF derived from the La Silla observations. Both are scaled to stars per square degree for this comparison. The cluster counts dominate the field star counts down to and below our completeness limit, however, the field star KLF appears to be somewhat more sensitive. To construct the cluster KLF for NGC 2362, we scaled the empirical field star KLF to the size of the cluster region and subtracted it directly from the on-cluster KLF. The resulting differential NGC 2362 KLF is shown in Figure 5–6(a). One sigma error bars on individual bins carry the quadratic sum of the counting uncertainty in the on-field counts and the field star uncertainties described above and dependent upon the source of field star KLF.

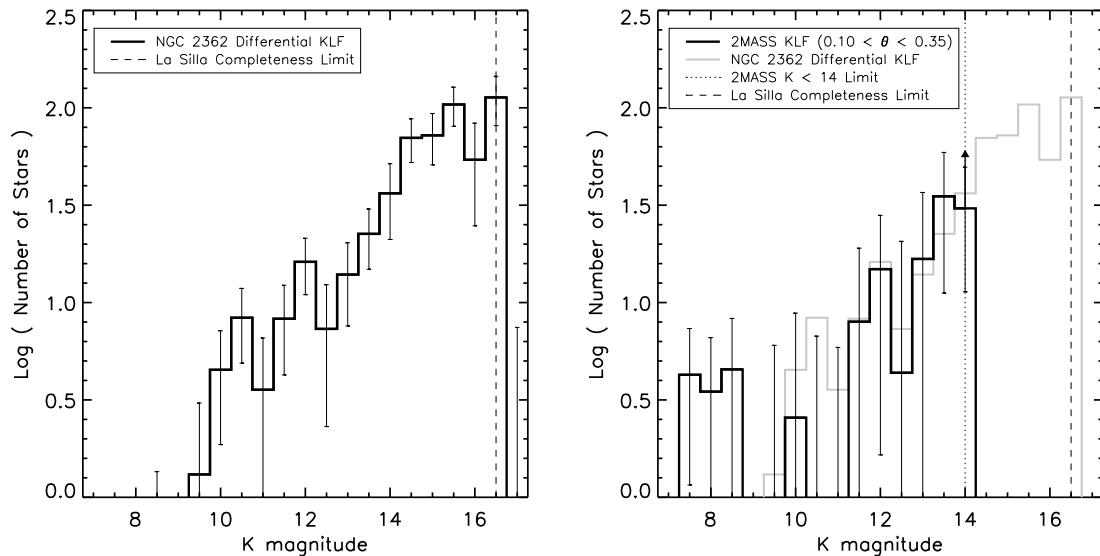


Figure 5–6: Differential KLF(s) of NGC 2362. A) The difference of the on-cluster and the scaled field star KLF.  $1\sigma$  error bars carry the quadratic sum of the cluster counting statistics and the uncertainty in the field star KLF, which depends upon the size of its original survey (See text and Figure 5–5b). B) The difference of the 2MASS cluster “halo” KLF and the scaled field star KLF. Error bars represent the total counting uncertainty for this area.

The NGC 2362 differential KLF contains  $537 \pm 60$  stars above the completeness limit of  $m_K = 16.5$ . The cluster KLF rises in a nearly power-law manner before flattening below  $m_K = 14.5$  and peaking at the completeness limit. We also computed the differential KLF for sources in the 2MASS cluster halo. As seen in Figure 5–6(b), this yields a net positive differential halo KLF, supporting the radial profile suggestion that the cluster extends beyond the La Silla survey. We estimate that there are  $114 \pm 61$  sources  $m_K \leq 14$  in the NGC 2362 cluster halo region, which is roughly the same size population as the cluster core to this depth.

#### 5.4 Comparison to other Young Cluster KLFs

We can compare the NGC 2362 differential KLF constructed here to the K band luminosity functions of the other young clusters that we have studied in detail in this work: IC 348 and the Trapezium. As we have shown, differences between cluster KLFs can be attributed to differences in either the clusters’ mean ages or different underlying IMFs with a small influence from the cluster reddening properties.

In Figure 5–7a we first compare the NGC 2362 KLF to the that of the Trapezium Cluster. We shifted the Trapezium  $M - A_V$  KLF from Section 3.2.2 to the distance of NGC 2362 and brightened it by 0.5 magnitudes to account for the median extinction of the Trapezium sources ( $A_V \sim 4.75$ ;  $A_K \sim 0.43$ ). We did not modify the Trapezium KLF to account for the effects of sources with infrared excess in that cluster.

Clearly, the two KLFs differ both in the peak and breadth with the Trapezium KLF peaking at much brighter magnitudes and being somewhat broader than the NGC 2362 KLF. The differences in the peaks of the KLFs could be easily explained by differences in the ages of these clusters. Based simply upon the evolutionary signposts in NGC 2362, e.g., the lack of a parental molecular cloud or stars with infrared excess, the  $\sim 1$  Myr Trapezium Cluster is almost certainly younger than NGC 2362, and therefore should peak at brighter magnitudes. The difference in the KLF widths, though, is the opposite of that expected from our numerical experiments and is due to

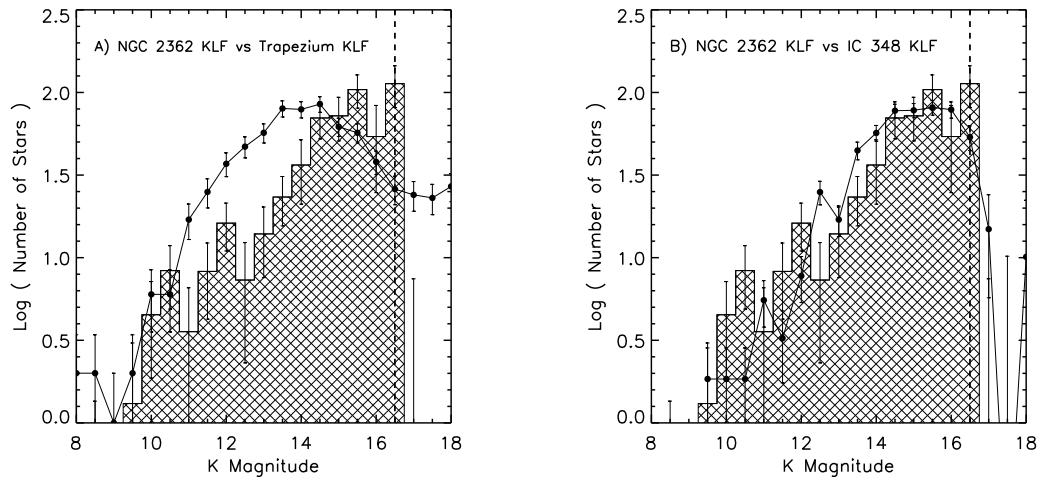


Figure 5–7: Comparing the cluster KLFs of NGC 2362, the Trapezium and IC 348. A) Comparison of the NGC 2362 differential KLF to the Trapezium Cluster KLF. The Trapezium Cluster  $M - A_V$  KLF from Section 3.2.2 was shifted to the distance of NGC 2362 (1500pc) and was brightened by  $A_V = 4.75$  ( $A_K = 0.43$ ) to account for the median extinction seen in the Trapezium. B) Comparison of NGC 2362 differential KLF to the IC 348 Cluster KLF. The IC 348 cluster’s background corrected differential KLF from Section 4.2 was shifted to the distance of NGC 2362 and was brightened by  $A_V = 4.2$  ( $A_K = 0.38$ ) to account for the mean extinction seen in IC 348.

the truncated sensitivity of the NGC 2362 La Silla survey. Since we found in Section 2.5.2 that cluster KLFs broaden with age, the NGC 2362 KLF should be broader than the Trapezium KLF if it were older and the two clusters are drawn from the same underlying IMF. Since our observations of NGC 2362 KLF are not nearly as sensitive in absolute K magnitude as the Trapezium and because infrared excess has likely broadened the Trapezium KLF somewhat we can discard this difference in clusters widths. Only if the two clusters have quite similar ages could these difference in their KLF widths be used to infer something about the cluster’s IMF.

In Figure 5–7(b), we compare the NGC 2362 KLF with the KLF of the IC 348 cluster as derived in Section 4.2. Again we shifted the IC 348 cluster to the distance of NGC 2362 and brightened it to correct for the mean extinction seen in IC 348 ( $A_V \sim 4.2$ ;  $A_K \sim 0.38$ ) The KLFs of the IC 348 and NGC 2362 clusters closely agree,

with the IC 348 KLF slightly shifted to brighter magnitudes but with the NGC 2362 KLF having a few more very bright stars than IC 348. As discussed in Section 4.3.1 IC 348 has an approximate mean age of 2 Myr, or slightly older than the Trapezium. Thus the comparison of these two cluster KLFs means that NGC 2362 is slightly older than IC 348 provided they have similar underlying IMFs. Put a different way, NGC 2362 cannot be significantly older ( $\tau > 10$  Myr) than IC 348 **and** have a similar IMF to IC 348. If NGC 2362 does have a much older age, this KLF comparison would indicate that the IMF of NGC 2362 would be significantly skewed to higher masses than IC 348.

On the other hand even if these two clusters have similar ages, then does appear to be slight excess of bright stars in NGC 2362 relative to IC 348. The observed excess occurs between  $m_K = 9.5$  and 12 (at the distance of NGC 2362) and this luminosity range corresponds to main sequence stars in the mass range of  $\sim 2 - 9 M_\odot$  for either cluster. This excess, however, does not convincingly imply that there is a statistically preference for high-mass stars in NGC 2362. Two issues are important to remember. First, let us assume an universal IMF between these three clusters similar to the IMF we derive for the Trapezium and IC 348. Because the high-mass stars are out on the tail of this probability distribution, the larger the cluster population the greater the statistical likelihood of creating higher mass stars. Since NGC 2362 contains more stars than IC 348 and this excess constitutes only a handful of very massive members, we cannot confidently confirm a variation in the underlying IMFs from this luminosity function comparison alone. Second, we cannot be certain that the bright end of the luminosity function (or the high-mass portion of the IMF) has not been influenced by mass segregation, although we have covered a very large area of NGC 2362 ( $r = 2.4\text{pc}$ ).

## 5.5 Modeling the NGC 2362 KLF

To apply our model luminosity functions to the NGC 2362 KLF we constructed in Section 5.3, we adopt our standard PMS evolutionary models based on a zero age main sequence, and sets of pre-main sequence evolutionary models. We used a fixed cluster distance of 1500pc and did not include any distribution functions of source reddening. We performed a multi-part analysis of the NGC 2362 KLF using our model KLFs, varying both the assumed age and IMF for this cluster. In section 5.5.1 we used our modeling code to derive the cluster’s mean age from its KLF by adopting an underlying IMF. In Section 5.5.2 we examined the dependence of the derived IMF slope on the assumed age of the cluster and find that both parameters can be simultaneously constrained for this cluster. Finally, in section 5.5.3 we adopt a mean age for the cluster and derive the NGC 2362 IMF spanning a mass range from 10 to  $0.2M_{\odot}$ .

### 5.5.1 Deriving a Mean Age Using a Fixed IMF

Since we concluded from our numerical experiments in Section 2.5 that the two most influential parameters on the form of a cluster’s LF are the underlying initial mass function and the cluster’s mean age, one of these parameters must be fixed to derive strong constraints upon the other parameter. As we summarized earlier in this chapter, a mean age may not be known for a distant young cluster simply because no signposts of its age can be quantified. To examine the usefulness of model luminosity functions for studying such young distant clusters, we first examined NGC 2362 as if knowledge of its mean age were not known. By expanding upon the procedure used in Lada & Lada (1995), we will use model luminosity functions and a fixed underlying IMF to derive a mean age for NGC 2362.

To study the mean age of NGC 2362, we created a suite of model luminosity functions employing the Trapezium IMF described in Equation 3.1 and varying the cluster’s mean age by increments of 0.5 Myr. We also ran this experiment for two

different age spreads (coeval and 2 Myr) and for two different binary fractions (no binaries and  $f_{bin} = 0.40$ ). In Figure 5–8, we show the results of  $\chi^2$  fits of the suite of model KLFs to the NGC 2362 KLF. Note, the fits were applied over the entire luminosity range of the observed NGC 2362 KLF.

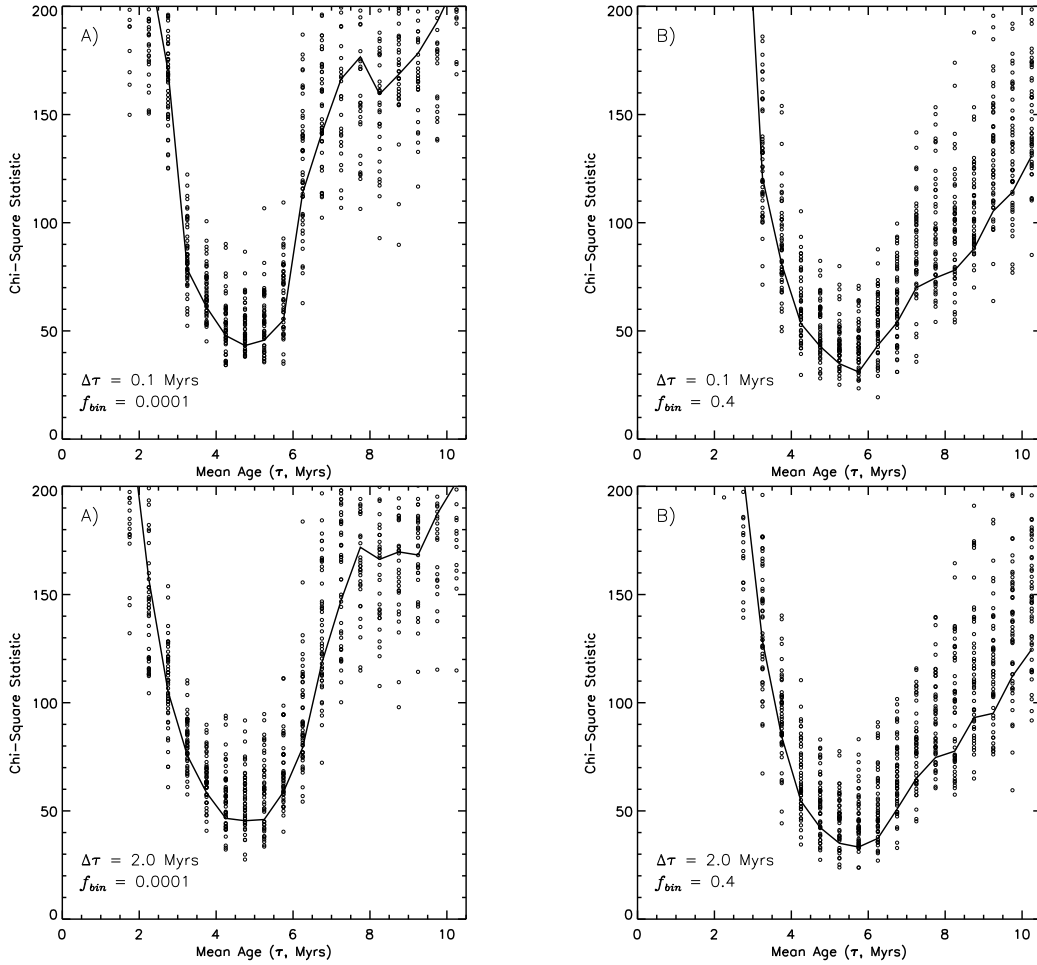


Figure 5–8: Mean age of NGC 2362 derived from the cluster KLF. Each circle represents the fit of a single model iteration to the NGC 2362 differential KLF. The solid black line is the fit the mean model KLF to the NGC 2362 KLF for that set of parameters. A)  $\Delta\tau = 0.1$  Myr (essentially coeval),  $f = 0.00$ ; B)  $\Delta\tau = 0.1$  Myr,  $f = 0.40$ ; C)  $\Delta\tau = 2.0$  Myr,  $f = 0.00$ ; D)  $\Delta\tau = 2.0$  Myr,  $f = 0.40$ .

All of these fits have clear  $\chi^2$  minima and all suggest a mean age for NGC 2362 between 4 and 6.5 Myr, though none of these fits approach a  $\chi^2$  probability of 1. Similar to our numerical modeling experiments, we find that the age spread in the

cluster has very little affect on the fits or on the mean age we derive. On the other hand, the derived mean age is slightly dependent upon the assumed binary fraction. The inclusion of unresolved binaries broadens the  $\chi^2$  minima derived from fitting model KLFs, and yields a slightly older mean age. For example, the mean age derived from models without binaries is between 3.5 and 5.5 Myr, while the fits that include binaries yield ages between 4 and 6.5 Myr. Lastly, we use the statistical sampling that our method naturally provides to examine if simple fluctuations in the cluster KLF could mask the true age. Fitting the NGC 2362 KLF to 50 individual iterations of the model KLF rather than the mean KLF model suggests that the accuracy of this method is 1 - 2 Myr for a cluster of 500 stars.

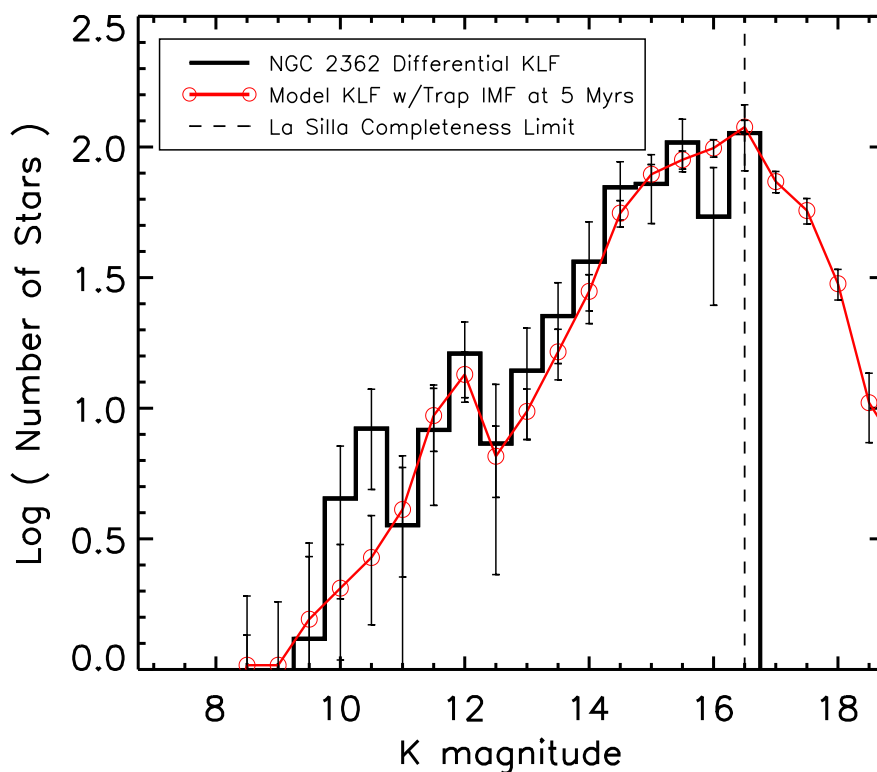


Figure 5-9: Model KLF at 5 Myr with Trapezium IMF fit to NGC 2362. The fit was performed over the luminosity range from  $m_K = 9.5$  to  $m_K = 16.5$ . Error bars on the model KLF correspond to the  $1\sigma$  statistical fluctuation in that KLF bin for 50 iterations of a cluster of 500 stars.

We are able to derive a mean age of  $\sim 5 \pm 2$  Myr for NGC 2362 using our model luminosity function techniques and assuming the IMF of the Trapezium. This age agrees very well with a cluster age of  $\sim 5_{-2}^{+1}$  Myr derived from the evolution of  $\tau$  Canis Majoris or from the cluster's pre-main sequence locus in the color-magnitude diagram (Balona & Laney, 1996; Moitinho et al., 2001). In figure 5–9 we compare the NGC 2362 KLF to a model KLF constructed using the Trapezium IMF at an age of 5 Myr. This model KLF passes through most of the bins of the NGC 2362 KLF above its completeness limit and at this mean age, the  $m_K = 16.5$  completeness limit translates to a mass limit of  $\sim 0.2M_{\odot}$ . Below our completeness limit, the model KLF sharply declines, reflecting the falling substellar IMF of the Trapezium. Were NGC 2362 to have a similar substellar IMF as that of the Trapezium, then the model KLF makes a clear prediction of what deeper observations would reveal.

Two interesting predictions arise from this simple KLF modeling. The first is that the non-power law structure of the bright portion of the NGC 2362 KLF has corresponding structure in the model of the Trapezium KLF at  $\tau = 5$  Myr. This structure in the model KLFs is due to the LMS spike discussed in Section 2.5.1. The small LF peak/dip is the result of a double valuing of the theoretical M-L relation as stars on radiative tracks in the HR diagram reach a maximum luminosity before settling onto the ZAMS. The LMS spike is predicted to be a strong feature in young clusters with mean ages greater than 2-3 Myr, and that it will evolve to fainter magnitudes as the cluster ages. This is because as the cluster ages the subset of stars on radiative tracks in the HR diagram shifts to lower and lower masses, while, assuming a normal IMF, the size of this subset of stars also grows. If no such feature existed in the theoretical mass luminosity relation, then it would be very difficult to fit the bright KLF with a single underlying power-law as we have done here. The second finding is that there appears to be a slight excess of the brightest stars in NGC 2362 relative to the model evolved Trapezium KLF. We discuss this excess in sections 5.5.2 and 5.6.1.

### 5.5.2 Simultaneous Derivation of a Cluster's Age *and* its IMF

Since a young cluster's LF is systematically dependent upon the cluster's age and underlying mass function, it is important to determine how an uncertainty in one of these quantities maps into the derivation of the other. In this section, we allow both the mean age and the IMF of the cluster to vary and use our modeling techniques to simultaneously constrain both of these quantities for NGC 2362.

As seen in Figure 5–6, the NGC 2362 differential KLF has roughly a power-law increase down to  $m_K = 14.5$ , but flattens towards the completeness limit. We learned from our numerical experiments that where a cluster KLF has a power-law form, the underlying IMF also has a power-law form. We use this information to infer that over some mass range, the underlying NGC 2362 IMF is a power-law. To test the dependence of the derived index of this power-law function on the inferred mean age of NGC 2362, we created a suite of model luminosity functions, systematically varying the slope of the power-law IMF and the mean age. We varied the IMF slope from flat to steeply rising, i.e.,  $\Gamma = 0 \rightarrow -2$ , in steps of 0.05. We also varied the cluster's mean age from 1 to 10 Myr in steps of 0.25 Myr. We fixed the age spread at 2 Myr but calculated model KLFs with binary fractions of 0.0 and 0.4. Finally, we fit these models to the observed KLF over the luminosity range down to where the cluster KLF flattens, i.e., from  $m_K = 9.5$  to 14.5.

From these fits we plot the dependence of the power-law IMF on the cluster's mean age in Figure 5–10. We also show this dependence for two different binary fractions. Two results are immediately clear: 1) as expected, there is a systematic relationship between these two parameters (age and IMF); 2) both parameters are simultaneously constrained to a narrow range of best fit values. These results are unchanged by the variation in the binary fraction, though it does slightly affect the final result.

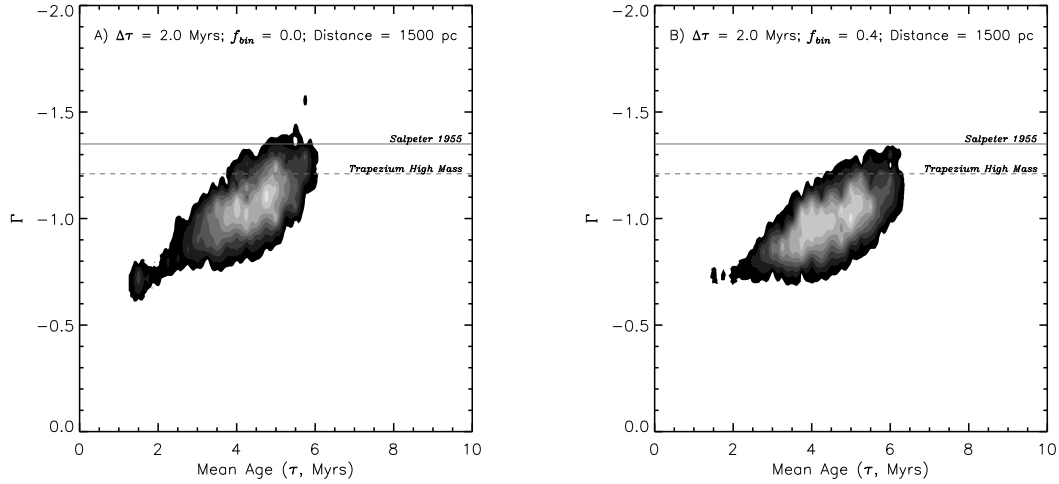


Figure 5–10: Dependence of the NGC 2362 IMF Slope on mean age. We plot contours of  $\chi^2$  probability for fits to the NGC 2362 KLF varying the cluster mean age and power-law IMF slope. Contours range from 0.1 to 1.0 in steps of 0.1. The horizontal lines correspond to the Salpeter field star IMF slope (solid line) and to the high-mass power-law IMF slope derived for the Trapezium (dashed line; from Section 3.3.3) Corresponds to a mass range from  $10M_{\odot}$  to between 1 and  $0.2 M_{\odot}$  depending upon the cluster’s age (see table 5–1). A) Fits without binaries,  $f = 0.0$ . B) Fits with binaries,  $f = 0.40$ .

Examining fits with  $\chi^2$  probabilities greater than 0.6, we find that our technique constrains the mean age of NGC 2362 to lie between 3.5 and 5.5 Myr with a best fit ( $\chi^2$  prob = 0.95) value of  $4.46 \pm 0.51$  (median = 4.5) Myr for fits without binaries. Including binaries actually skews the mean age range very slightly to *younger* ages ( $\tau_{w/binaries} = 4.41 \pm 0.64$  Myr). The derived IMF slope is clearly constrained to lie between -0.8 and -1.3 and has a best fit value of  $\Gamma = -1.08 \pm 0.08$  (median = -1.05). We find, though, that including unresolved binaries results in a slightly flatter IMF slope,  $\Gamma_{w/binaries} = -0.99 \pm 0.09$ .

Because of the PMS nature of the stars in NGC 2362, the luminosity range fit by these models ( $m_K = 9.5 - 14.5$ ) translates into different mass ranges for the power-law IMF as a function of age. We summarize this dependence in Table 5–1. We find that the bright end of this luminosity fit range always corresponds to early B type stars

Table 5–1. Age dependence of the IMF slope in NGC 2362

Cluster Mean Age $\tau$ (Myr)	IMF Mass Range <sup>(a)</sup> ( $M_{\odot}$ )				IMF Slope <sup>(b)</sup>	
	ZAMS	DM97	BCAH98	PS99	$\Gamma$	$\chi^2$ Prob
1.0	$\sim 9$	0.20	0.23	0.23	-0.70	0.10
3.0	$\vdots$	0.56	0.50	0.49	-0.90	0.45
5.0	$\vdots$	0.78	0.66	0.60	-1.00	0.83
7.0	$\vdots$	0.88	0.75	0.80	-1.80	...
10.0	$\vdots$	0.95	0.86	0.90	-1.95	...

<sup>(a)</sup>Corresponding to the K luminosity range fit.  $K = 9.5$  corresponds to a B2.5V main sequence star at the cluster’s distance, which converts to a mass of  $9 M_{\odot}$  (using [Kenyon & Hartmann, 1995](#); [Winkler, 1997](#))  $K = 14.5$  corresponds to pre-main sequence stars whose mass depends upon the cluster’s age and the set of PMS tracks.

<sup>(b)</sup>For fits without binaries. There is no  $\chi^2$  power at ages  $> 7$  Myr.

References. — [D’Antona & Mazzitelli \(1997, DM97\)](#); [Baraffe et al. \(1998, BCAH98\)](#); [Palla & Stahler \(1999, PS99\)](#)

with masses  $\sim 9$  while the faint end of the luminosity range always corresponds to PMS stars. For the range of best fit values of the mean age of the cluster, this low mass limit is between  $0.5$  and  $0.8 M_{\odot}$  and depends very slightly on the set of tracks used for conversion. Within this corresponding mass range ( $10 \rightarrow 1 M_{\odot}$ ) we find that power-law slope for NGC 2362 is constrained to be slightly flatter than that found for the Trapezium or the field star IMF according to [Salpeter](#) under any variations in the assumed mean age or binary fraction.

### 5.5.3 NGC 2362 IMF Derived Using a Fixed SFH

Since there is independent evidence of the age of NGC 2362 available from optical color-magnitude diagrams we can directly derive the cluster IMF. We assume a mean age of 5 Myr and assign an age spread of 2 Myr, based on the spread in age (luminosity) seen in the color-magnitude diagram ([Moitinho et al., 2001](#)) and because this age spread is typical of the other young clusters in our sample. We used multiple

power-law segments for the underlying IMF and varied the fit range over which they were applied. We only performed these fits using model KLFs that did not include unresolved binaries.

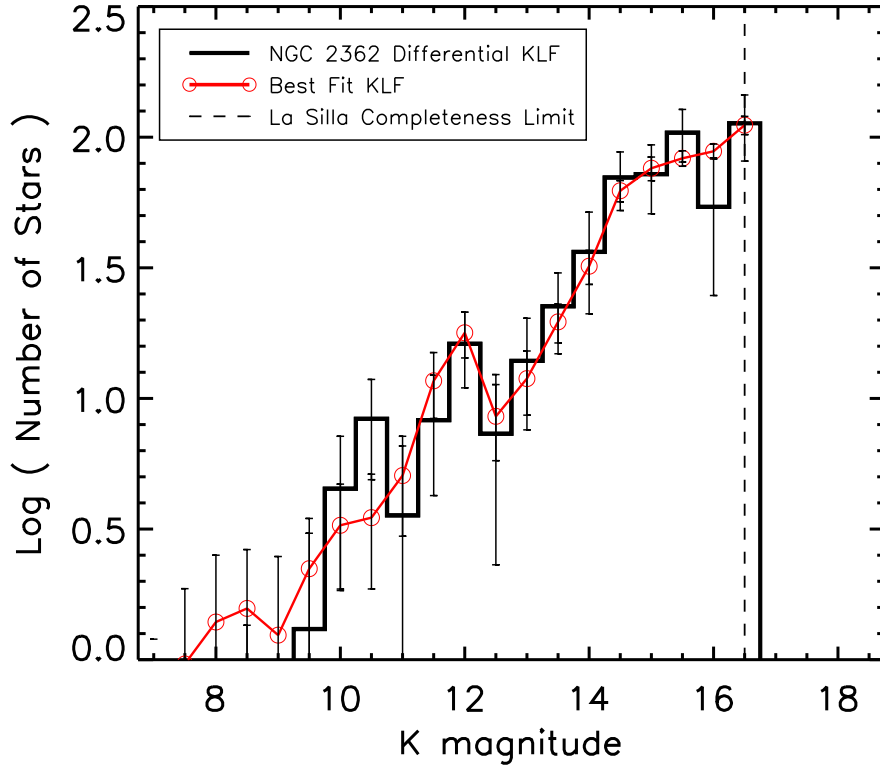


Figure 5–11: Best fit model KLFs to the NGC 2362 KLF. The fit was performed over the luminosity range from  $m_K = 9.5$  to  $16.5$ . Error bars on the model KLF correspond to the  $1\sigma$  statistical fluctuation in that KLF bin for 50 iterations of a cluster of 500 stars.

Single power-law IMFs did not provide good fits over the entire luminosity range from  $K = 9.5$  to  $16.5$ . Fits down to  $m_K = 14.5$  ( $M = 10 \rightarrow 0.8M_\odot$ ) were well fit by a single power-law,  $\Gamma = -1.16 \pm 0.21$  for this fixed age and similar to our findings from the previous section. The break and flattening of the KLF at fainter magnitudes, however, rejected a single power-law over the entire mass/luminosity range.

Two power-law IMFs provided better fits to the form of the cluster KLF. The best fitting model KLF using this 2 power-law IMF is shown in Figure 5–11 compared to the NGC 2362 differential KLF. The model fit is excellent, passing through nearly

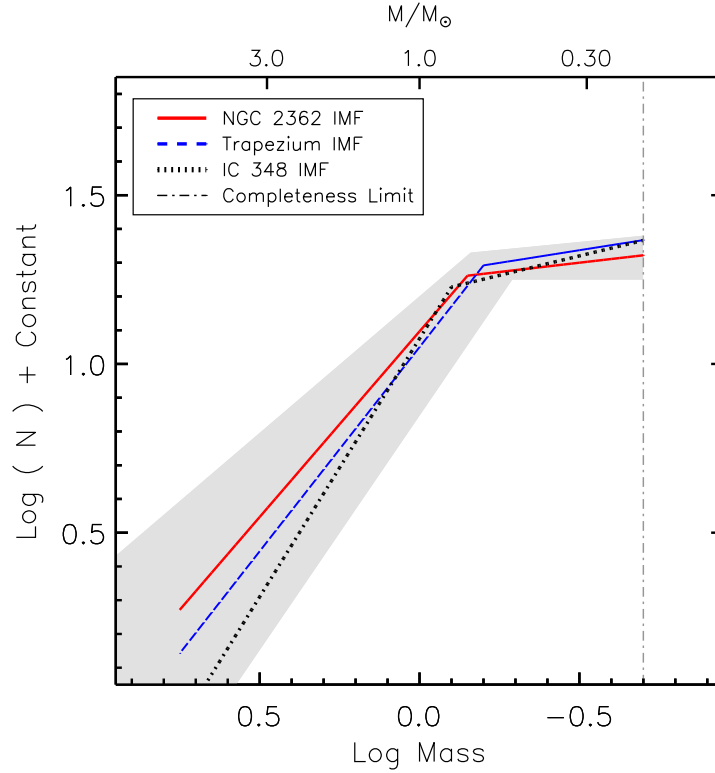


Figure 5–12: Mass Function of NGC 2362. The derived IMF for NGC 2362 is compared to the Trapezium IMF down to the  $0.2M_{\odot}$  limit. The hatched region is a graphical representation of the range of IMFs permitted from by the KLF models.

every bin of the differential KLF, although there is still a modest excess of bright ( $m_K \sim 10$ ) sources relative to model KLF. From these fits with our model KLFs we find a best fit IMF having the form:

$$\frac{dN}{d \log M} = \begin{cases} \Gamma_1 & : -1.10 \pm 0.28 \\ m_1 & : 0.69 \pm 0.18 M_{\odot} \\ \Gamma_2 & : -0.11 \pm 0.11 \end{cases} \quad (5.1)$$

In Figure 5–12 we compare the derived NGC 2362 IMF to that found for the Trapezium (from Equation 3.1) and IC 348 (from Table 4–3). We also graphically display the range of IMFs permitted by the NGC 2362 differential KLF. Clearly, the derived NGC 2362 IMF is very similar to that IMF we derived for the other two younger clusters. All three have power-law inclines toward lower masses, break at

around  $0.6 - 0.8 M_{\odot}$  and flatten at subsolar masses. The NGC 2362 high mass IMF slope,  $\Gamma_1$  is slightly flatter than in the Trapezium, which is also flatter than that derived for IC 348, although all of these differences are smaller than the dispersion in our fits for the high mass slope for each of the clusters.

## 5.6 Discussion

### 5.6.1 Age and IMF of NGC2362

From our construction and modeling of the NGC 2362 KLF, we find that the stellar IMF of this cluster is quite similar to that IMF we found for the IC 348 and Trapezium clusters. While all three rise with power-law slopes into the subsolar regime, the KLF and IMF of NGC 2362 both suggest a slight excess of bright/massive stars relative to these other clusters. The IMF slope in the high to intermediate mass range varies from NGC 2362 -  $\Gamma \sim -1.1$  to the Trapezium -  $\Gamma \sim -1.2$  to IC 348 -  $\Gamma \sim -1.53$ , relative to Salpeter -  $\Gamma = -1.35$ , although all of these slopes are the same within their respective errors.

The NGC 2362 IMF we derived flattens below  $\sim 1 M_{\odot}$ , but continues to rise down to our completeness limit of  $\sim 0.2 M_{\odot}$ , similar to our findings for IC 348 and the Trapezium. Our observations cannot resolve the mode of the NGC 2362 IMF so we cannot compare this measure to that found in the other clusters. Further, we are not able to probe the brown dwarf regime of NGC 2362, though we find that if the substellar IMF of NGC 2362 were similar to that in IC 348 and the Trapezium, i.e. falling, then it would be very difficult to derive from constructing a deeper luminosity function. This is because the statistical noise from the field star surface density would like swamp the counts in the substellar regime. A different mechanism for identifying cluster members, likely in the form of optical-infrared color-magnitude diagrams, will be necessary for determining the size of the brown dwarf population in NGC 2362. Regardless, we note that the lower mass limit of our study of NGC 2362 is nearly the

same as the sensitivity limit of the [Hillenbrand \(1997\)](#) spectroscopic study of the Orion Nebula Cluster despite the fact that NGC 2362 is four times further away.

In addition to deriving the IMF of NGC 2362, we undertook a series of experiments to quantify the usefulness of model luminosity functions for studying distant young clusters where little is known about the cluster's mean age. Expanding on the work of [Lada & Lada \(1995\)](#), we found that by assuming an underlying IMF for NGC 2362, we could derive a mean age for NGC 2362 of 5 Myr, in close agreement with other age estimates that have used the optical color-magnitude diagram. Further the intrinsic sampling error in this age estimate is 1-2 Myr, set by the statistical size of the cluster. From these experiments, we confirmed our earlier findings in [Section 2.5.2](#) that the assumed age spread for the cluster has little effect on the derived age. However, the inclusion of unresolved binaries does affect the derived mean age, shifting the cluster to somewhat older ages for a fixed IMF. This can be understood because unresolved binaries, drawn from an IMF that increases with decreasing mass, will act to brighten the intrinsic KLF, thus, requiring an older age to match the observations.

Lastly, we calculated a series of numerical models of the NGC 2362 KLF in which we made no a priori assumptions about NGC 2362 except for its distance and the functional form of the underlying IMF, basing this latter assumption on the power-law appearance of the KLF. Simultaneous fits of the cluster's mean age and power-law IMF slope were performed, yielding narrow constraints on *both* properties for this cluster. The success of these fits can be understood in part by reviewing our numerical experiments illustrating the evolution of the cluster KLF with mean age. Recalling [Figure\(s\) 2-8](#) and [2-9](#), we showed that cluster KLFs evolve as much during their first 3 Myr of existence as they do in the next 10 Myr. This means that as the cluster ages, the uncertainty in the IMF due to the uncertainty in the age decreases. As we have shown, the systematic errors for a 4-5 Myr old cluster are quite small, 0.5 Myr in age and 0.1 dex in the slope of the IMF. Considering the blurring effects of reddening

on our model KLF fitting technique, such an analysis of distant, younger, *embedded* clusters will likely yield less accurate constraints on both the cluster’s age and IMF. However, the results of such an analysis would become meaningful when looking for radical variations in the IMF even if the IMF/Mean Age errors we derive for a 4 - 5 Myr old open cluster were doubled when studying embedded clusters.

### 5.6.2 Age and Spatial Structure of NGC 2362

In our study of IC 348 we learned that despite the youth of the cluster’s targeted by our study, the spatial structure of a young cluster can influence the form of the IMF we derive because radial variations in the cluster IMF exist even at these young ages. Independent of whether these IMF variations are indicative of dynamical or primordial mass segregation or are simply the product of small samplings of the underlying IMF, their existence implies that the comparison of cluster IMFs as we did in Figure 5–12, requires some idea of the relative areas of the cluster surveyed.

The radii of our surveys of these three clusters are  $r \sim 0.3$  pc for the Trapezium,  $r \sim 0.5$  pc for IC 348 and  $r \sim 2.2$  pc for NGC 2362. For IC 348, this radius is congruent with our radial profile analysis which does not suggest that the cluster is considerably larger than this size. The Trapezium, however, is only the core of the larger Orion Nebular Cluster whose outer radius is  $r_{tidal} \sim 2.5$  pc (Hillenbrand & Hartmann, 1998) and which does appear to have radial IMF variations on these scales. Our survey of NGC 2362 covers an equivalent area to the entire ONC, however because of its advanced age the cluster may have expanded beyond these boundaries. If NGC 2362 were simply the core of an unbound association, then with an initial velocity dispersion of 1 - 2 km/sec imprinted on the stars by the molecular cloud members could have scattered to a radii of 5 - 10 pc. Indeed, we can conclude that there is some evidence in the radial profile of the cluster (Figure 5–3) and the differential 2MASS KLF of the cluster “halo” region (Figure 5–6b) that NGC 2362 extends beyond the boundary of the La Silla survey and to radial distances of 5 - 10 pc.

It is not necessary that the larger size of NGC 2362 be the result of the expansion of an unbound cluster. Indeed, the presence of O stars and the apparently rapid clearing of the parental molecular cloud do not prevent the cluster from emerging as a bound entity as was shown in the recent dynamical modeling of [Kroupa et al. \(2001\)](#). Using N-body models that included the potential energy from the molecular cloud and tuned to have initial conditions (e.g., central stellar density, number of members) similar to the ONC, [Kroupa et al.](#) found that despite the rapid removal of the molecular gas by O stars and with very marginal star formation efficiencies (i.e.,  $\sim 0.3$ ) a bound cluster can form containing approximately 30% of the original members (i.e. 70% of the sources are either ejected or tidally stripped in the first 100 Myr of the cluster's evolution). These models also show that such a cluster undergoes very rapid changes in its structure (i.e., core radius and outer boundary) within the *first few Myr* after the cloud is removed. Since NGC 2362 is near the dynamical relaxation time for the ONC (6.5 Myr, [Hillenbrand & Hartmann, 1998](#)) and both contain O stars, it is possible that NGC 2362 represents a dynamically evolved ONC. In such a model, we already have two pieces of information from our survey. First, the surface density of stars within a radius of 2.0 pc will have decreased from the 164 stars  $\text{pc}^{-2}$  found by [Hillenbrand & Hartmann](#) after averaging over the entire ONC to 11 stars  $\text{pc}^{-2}$  found in our La Silla survey. Second, there are as many stars, one solar mass and greater in the cluster halo as in the cluster core, although much of the dynamical mass segregation to the halo should consist of subsolar mass stars ([Kroupa et al., 2001](#)).

A very wide-field optical study of NGC 2362, merged with a *complete* 2MASS catalog, would improve upon this rough evidence for a dynamically expanding open cluster. Such observations would allow for individual cluster members to be separated from field stars by their location in the optical and optical-infrared color-magnitude diagrams (e.g. [Adams et al., 2001](#); [Moitinho et al., 2001](#)). This would alleviate the need for large background corrections as well as allow for the construction of more

accurate radial profiles which could be fit with analytical profiles (e.g., King models) to determine cluster parameters such as core and tidal radii. Further, the advent of wide field *infrared* imaging such as our use of the FLAMINGOS instrument when studying IC 348, allows us to probe the entire cluster halo to subsolar depths in both the optical and the infrared. Thus, NGC 2362 may be an ideal template for studying the dynamical evolution of young clusters as they emerge from their parental molecular cloud.

### 5.7 Conclusions

Combining model luminosity functions with a near-infrared census of the young, distant open cluster NGC 2362, we explored the usefulness of the luminosity function method when little is known about the age of an open cluster. We found that we are able to place constraints on both the mean age and IMF of this cluster by fixing only basic quantities such as cluster distance. When we assumed a mean age obtained from the cluster's optical color-magnitude diagram, we were able to directly derive the cluster's IMF. From these modeling results and by comparison of the NGC 2362 KLF and IMF to those functions derived for the Trapezium and IC 348 in chapters 3 and 4 we draw the following basic conclusions:

1. From our modeling of the differential NGC 2362 KLF using a fixed mean age, we derive a cluster IMF that spans a mass range from 10 to  $0.2 M_{\odot}$ . Over this range, the cluster's IMF is very similar to the stellar portion of the IMFs that we derived for the other clusters in this study, all of which appear to form broad peaks at subsolar masses. Although our current study of NGC 2362 does not probe the substellar regime, we find that we are able to probe the IMF down to a mass limit very similar to the sensitivity of spectroscopically based IMF studies in nearby clusters, although NGC 2362 is 1.5 kpc away.
2. We find that under the assumption of an universal IMF we can derive the age of NGC 2362 from its luminosity function and that this KLF derived age is very similar

to that found from placing the cluster on the color-magnitude diagram. We find that this method has an intrinsic accuracy of 1-2 Myr set by the statistical size of the cluster. The assumed age spread in a cluster has little effect on the derivation of the mean age, however, ignoring unresolved binaries will tend to produce too young of an age.

3. Simultaneous fits of the cluster's mean age and power-law IMF slope yield reasonable constraints on both parameters. This result is due in part to the fact that LF evolution (to fainter magnitudes) slows with increasing age, reducing the intrinsic uncertainty in the derived IMF. Such a modeling exercise suggests that luminosity function is a powerful tool for studying clusters even when little is known about the cluster's age.

## CHAPTER 6 CIRCUMSTELLAR DISKS AROUND YOUNG BROWN DWARFS

Among the most fundamental issues raised by the existence of brown dwarfs is the question of their origin and genetic relationship to planets and stars. Are brown dwarfs giant planets or small, failed stars, or, something else altogether different? The critical test needed to resolve this question is to determine whether brown dwarfs primarily form within circumstellar disks as companions to stars, similar to planets, or from their own individual cloud cores or fragments, like stars. To date, the most important observations bearing on this question have been: 1) the observed lack of close brown dwarf companions found in radial velocity surveys of nearby field stars (the so-called brown dwarf desert, e.g., [Marcy & Butler, 1998](#)) and 2) the existence of free floating brown dwarfs in young clusters (e.g., [Bouvier et al., 1998](#)). Both facts would appear to implicate a stellar (non-planet like) origin for these objects, i.e., formation from independent, contracting fragments of the parental molecular cloud. However, our understanding of the origin of sub-stellar objects is far from complete. For example, an alternative formation scenario has been recently proposed by [Reipurth & Clarke \(2001\)](#) who suggest that most freely floating brown dwarfs did not form from their own proto-stellar fragments, but instead were initially formed as companions to other protostars and then were dynamically ejected via 3 body encounters before they could grow into stellar mass objects.

The most direct way to address the question of the origin and nature of brown dwarfs is to investigate the properties of extremely young sub-stellar objects in regions of active star and planet formation. For example, finding young brown dwarfs surrounded by their own circumstellar accretion disks would likely implicate a stellar-like formation mechanism (from individual cloud fragments) and place strong

constraints for the theoretical models of their origin (e.g., [Reipurth & Clarke, 2001](#)). Moreover, such a finding would raise the interesting question of whether planetary companions can form around such objects.

Recently, [Lada et al. \(2000\)](#) used near-infrared ( $1 - 3\mu\text{m}$ ) color-color diagrams to show that a large fraction ( $\sim 80 - 85\%$ ) of the stars in the young Trapezium Cluster display thermal infrared excess indicative of circumstellar disks. Further, they found that the fraction of stars with disks remained high with decreasing mass to near the hydrogen burning limit. Below this limit, their observations became incomplete. Does the incidence of circumstellar disks also continuously extend across the hydrogen burning limit to sub-stellar mass objects?

As we have shown in chapters [2](#) and [3](#), deeper infrared observations have revealed a substantial population of faint sources which appear to be free floating sub-stellar objects in this cluster ([McCaughrean et al., 1995](#); [Muench et al., 2000](#); [Lucas & Roche, 2000](#); [Hillenbrand & Carpenter, 2000](#); [Luhman et al., 2000](#); [Muench et al., 2002](#)). As we extensively discussed in Section [3.2.3](#), however, the identifications of these sources as sub-stellar objects are not secure because our observations of nearby un-reddened control fields revealed significant numbers of field stars in the corresponding brightness range (see also Figure [3-4](#)), suggesting that field star contamination could be a severe problem, especially for the faintest candidates. Our attempts in Section [3.2.3](#) to account for the effects of the screen of extinction provided by the molecular cloud behind the Trapezium do suggest the vast majority of the brown dwarf candidates are not reddened field stars, despite the considerable uncertainties intrinsic to that statistical analysis (also see our discussion in Section [3.4.1](#) on the effects of membership uncertainties on the derivation of the cluster's IMF). Thus, independent confirmation of membership is clearly important and could be provided by indications of extreme youth, such as the presence of infrared excess and dusty disks surrounding these objects.

In this chapter, we present an observational analysis of the colors of the brown dwarf population for the Trapezium cluster using the deep NTT infrared data described in Section 3.1. In Section 6.1 we find that a relatively large fraction of the candidate brown dwarfs exhibit infrared excess indicative of circumstellar disks. As we discuss in Section 6.2, this confirms both their membership in the cluster and their status as sub-stellar objects and perhaps suggests an origin for them that is more stellar-like than planetary-like.

### 6.1 Trapezium Brown Dwarfs with Infrared Excess

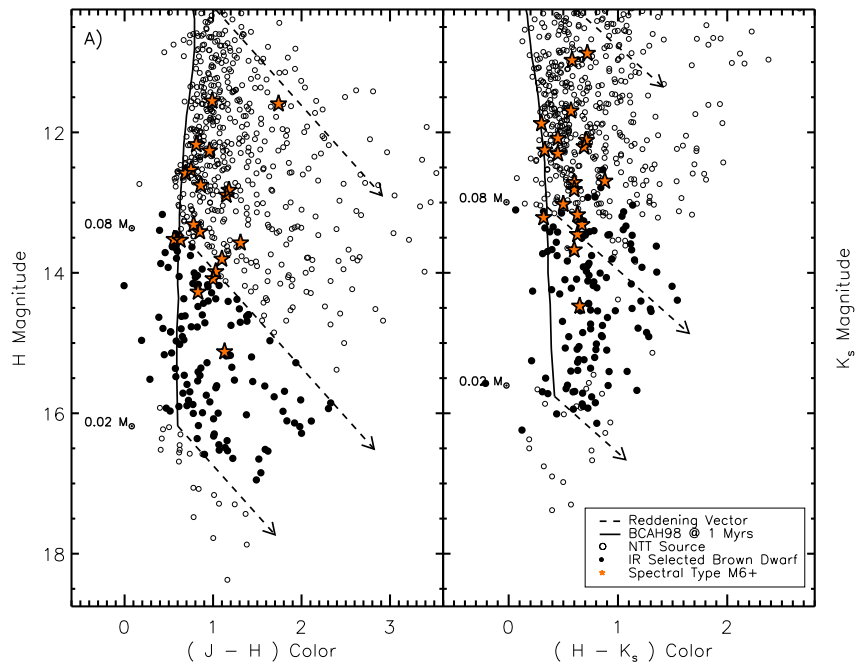


Figure 6–1: Selecting candidate brown dwarfs in the Trapezium. We plot the infrared color-magnitude diagrams for only those Trapezium sources having NTT observations and JH and  $K_S$  magnitudes. The sources are compared to the location of the 1 Myr (at 400pc) isochrone from the BCAH98 evolutionary models and atmospheres. Candidate brown dwarfs (filled circles) were selected by their H band luminosities (and colors) and are marked in both color-magnitude diagrams. Reddening vectors for 1, 0.08 and 0.02  $M_{\odot}$  objects are drawn at visual extinctions of 20, 20 and 10 magnitudes, respectively. Stars with spectral types  $\geq M6$  are identified as filled stars. a) J-H/H color-magnitude diagram. b) H- $K_S$ / $K_S$  color-magnitude diagram.

In Figure 6–1 we construct the infrared color-magnitude diagrams for those NTT Trapezium sources which were simultaneously detected at JHK<sub>s</sub> wavelengths. Thus, the sample shown here differs from that shown in Figure 3.2.2(a) by not including sources that were not detected at J band. In these diagrams, we compare the locations of these sources to the location of the theoretical isochrone from the Baraffe et al. (1998, , BCAH98) non-grey evolutionary models at the assumed mean age ( $\sim 1$  Myr) and distance (400 pc, see appendix B) of the Trapezium cluster. The BCAH98 theoretical isochrone closely follows the near-IR colors of the Trapezium sources, forming an excellent left-hand boundary to the source distribution in this color-magnitude space. The Trapezium sources are reddened away from this boundary with implied extinctions of  $A_V \sim 1 - 35$  mag.

We identified candidate brown dwarfs in the Trapezium Cluster by comparing the infrared luminosities of detected sources to those predicted by the theoretical evolutionary models. We selected all the NTT sources in the J-H/H diagram (Figure 6–1a) fainter than the predicted luminosity of the hydrogen burning limit (hereafter HBL;  $\sim 0.08 M_\odot$ )<sup>1</sup> but brighter than the luminosity of an  $0.02 M_\odot$  object. This lower limit was chosen because the current theoretical evolutionary models do not extend much below this mass, and because we wish to exclude cooler, lower mass objects whose intrinsic colors are not well constrained. Between these two mass/luminosity limits we identified 112 candidate brown dwarfs in the J-H/H diagram. We also indicate in Figure 6–1 the locations of 19 Trapezium Cluster members with spectral types equal to or later than M6 taken from Hillenbrand (1997), Lucas et al. (2001) or Luhman (private communication). The spectral type M6 is an important boundary

---

<sup>1</sup> The predicted colors and magnitudes of the hydrogen burning limit for this distance/age combination are essentially identical to those for a younger assumed age (0.4 Myr) but at a larger distance (470pc).

because recent spectroscopic studies have suggested that it represents the hydrogen burning limit in very young ( $\tau < 10\text{Myr}$ ) clusters (Luhman, 1999). In Figure 6–1(a), these late type sources are on average 1 magnitude brighter than our adopted hydrogen burning limit. The faintness of our IR selected brown dwarfs relative to these late type sources confirms that we are likely selecting sources below the HBL.

We refine our selection of brown dwarf candidates by plotting the J-H/H candidates in the H-K<sub>S</sub>/K<sub>S</sub> color-magnitude diagram in Figure 6–1(b). In this diagram a number of candidates are brighter and redder than the hydrogen burning limit. We retain these as likely brown dwarf candidates because they have photometric errors which are much too small to have scattered them to this location, because they are fainter than most of the M6+ dwarfs, and because excess  $2\mu\text{m}$  flux from circumstellar disks could act to brighten and redden such sources out of the brown dwarf regime in the H-K<sub>S</sub>/K<sub>S</sub> color-magnitude diagram. A few very faint candidates scatter below the  $0.02 M_{\odot}$  limit in the H-K<sub>S</sub>/K<sub>S</sub> diagram, and we exclude these sources from our final sample.

In Figure 6–2, we plot the H-K<sub>S</sub>/J-H color-color diagram for the 109 candidate brown dwarfs. We also plot for comparison the loci of colors for giants and for main-sequence dwarfs from Bessell & Brett (1988). We extended the loci of M dwarf colors in Figure 6–2 from M6 to M9 using the empirical brown dwarf colors compiled in Kirkpatrick et al. (2000). The predicted effective temperatures of 1 Myr brown dwarfs from the BCAH98 evolutionary models are quite warm, e.g.  $T_{eff} \geq 2500\text{K}$  for masses greater than our  $0.02 M_{\odot}$  limit. Therefore, we expect that the intrinsic infrared colors of such young brown dwarfs are no redder than those of M9 dwarfs (J-H = 0.72; H-K<sub>S</sub> = 0.46 Kirkpatrick et al., 2000) which agree well with the H-K colors predicted by

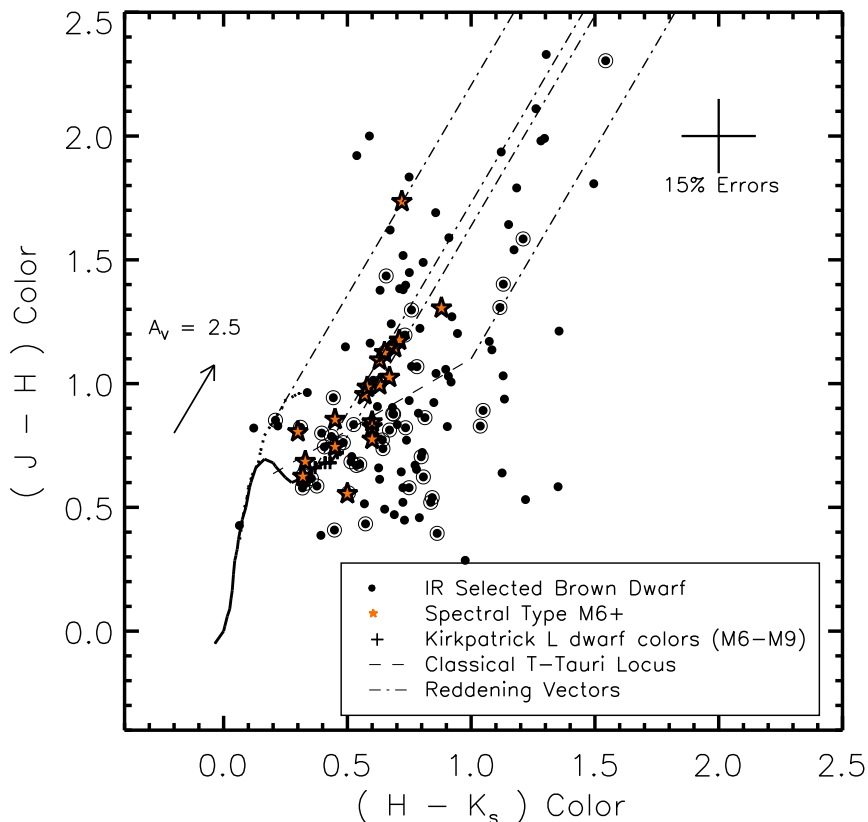


Figure 6–2: Trapezium brown dwarfs with near-infrared excess.  $H-K_s/J-H$  color-color diagram for the 109 sources with NTT  $JHK_s$  magnitudes and which fall into the brown dwarf regime of Figure 6–1. The candidate brown dwarfs are compared to the intrinsic colors of giants and A0-M6 dwarfs from [Bessell & Brett \(1988\)](#), the late M (M6 - M9) color sequence from [Kirkpatrick et al. \(2000\)](#) and the Classical T-Tauri locus from [Meyer et al. \(1997\)](#). Appropriate reddening vectors ([Cohen et al., 1981](#)) are drawn for giants, for M6 stars and for M9 stars. Colors of Trapezium sources with very late (M6+) known spectral types are shown as stars. Circled sources have color errors of less than 10% and the size of 15% uncertainties in color are illustrated at the upper right.

current model atmospheres of low surface gravity, 2600K sources ([Allard et al., 2001, 2](#))

We find  $65\% \pm 15\%$  (71/109) of our candidates fall to the right of the reddening band for M dwarfs and into the infrared excess region of the color-color diagram. We

<sup>2</sup> see also <ftp://ftp.ens-lyon.fr/pub/users/CRAL/fallard/>

further determine that 54% of the candidates have an infrared excess that is greater than their  $1\sigma$  photometric uncertainties in color. In addition to normal photometric uncertainties the measured colors of these sources could be corrupted by the presence of the strong nebular background, and we performed an extensive set of artificial star photometry experiments to test this possibility. We found that nebular contamination can introduce some additional scatter to a star’s measured J-H color and this can explain in part the J-H colors of  $\sim 25\%$  of the excess sources which are bluer than expected for late type sources ( $J-H < 0.6$ ). However, blueward J-H scatter can produce a false excess fraction ( $\sim 10 - 20\%$ ) only for the the faintest artificial stars, i.e.,  $H = K = \sim 16$  mag. Further, we find that such nebular contamination never produces as large a dispersion of the H- $K_S$  colors as found in our observations of the candidate brown dwarfs, and we conclude that the observed infrared excesses are an intrinsic property of these objects.

## 6.2 Discussion and Implications

From analysis of their near-infrared colors, we find that  $\sim 50\%$  of the candidate brown dwarfs in the Trapezium cluster display significant near-infrared excess. This is similar to the behavior of the stellar population of this cluster and suggests the extreme youth of these low luminosity sources. This, in turn, provides independent confirmation of their membership in the cluster and their nature as bona fide sub-stellar objects. As is the case for the more massive stellar members, the most likely explanation for the observed near-infrared excesses around the brown dwarfs in this cluster is the presence of circumstellar disks. Strong, independent support for the disk interpretation derives from the fact that we find 21 of the candidate brown dwarfs to be spatially coincident with optically identified HST “proplyds” (O’dell & Wong, 1996; Bally et al., 2000) which are known to be photo-evaporating circumstellar disks. We illustrate HST images from Bally et al. of three of the IR luminosity selected brown dwarfs that display the proplyd characteristics in Figure 6–3. We note that the proplyd

brown dwarfs display a JHK excess fraction of 71%, while the brown dwarf candidates unassociated with known proplyds have a slightly lower excess fraction of 63%. The proplyd brown dwarfs also display bluer J-H colors than the remaining brown dwarf candidates and account for half the excess sources with J-H color  $< 0.6$ . Despite their relatively blue J-H colors, the proplyd nature of these sources affirms the hypothesis that the observed JHK infrared excess is intrinsic and a signature of the presence of a circumstellar disk.

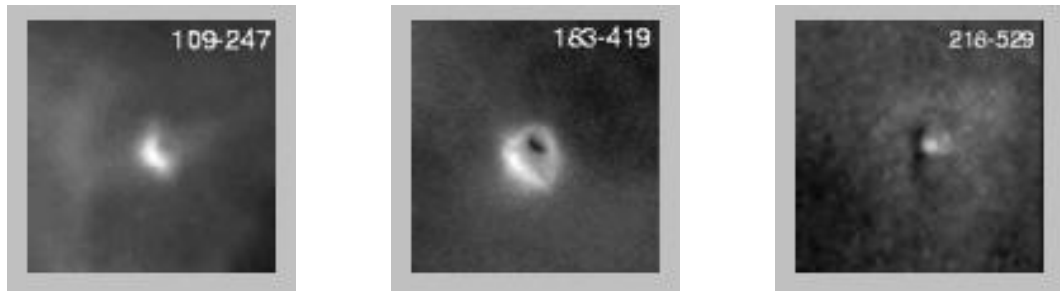


Figure 6–3: Brown dwarf proplyds. HST images (F656N filter) of three infrared selected brown dwarf candidates which are also optical proplyds. Data from [Bally et al. \(2000\)](#) with permission.

The hypothesis that the observed near-IR excess is caused by circumstellar disks is further supported by observations of brown dwarf candidates in other clusters. Late-type brown dwarf candidates in the  $\rho$  Ophiuchi cluster were identified by their water vapor absorption features and display evidence for veiling in their infrared spectra as well as evidence for infrared excesses in their H-K/J-H color-color diagrams ([Wilking et al., 1999](#); [Cushing et al., 2000](#)). ISO ( $6.7\mu\text{m}$ ) observations reveal 4 brown dwarf candidates with mid-infrared excesses in Chamaeleon ([Comerón et al., 2000](#)). [Luhman \(1999\)](#) identified 7 brown dwarf candidates in the IC 348 cluster which, after de-reddening, fall to the right of the main-sequence reddening band but below the cTTS locus similar to the locus of brown dwarfs identified here. Luhman also identified strong  $\text{H}\alpha$  emission ( $W[\text{H}\alpha] > 10\text{\AA}$ ) in a number of these sources and suggested that these are not simply passive circumstellar disks, but that these brown

dwarfs are undergoing accretion. Finally, powerful evidence for accretion disks around very young brown dwarfs was found by [Muzerolle et al. \(2000\)](#) who identified an asymmetric H $\alpha$  emission line profile for the M6 PMS object V410 Anon 13 in Taurus and successfully used magnetospheric accretion models to show that this brown dwarf candidate was indeed accreting but at a rate much lower than has been found in higher mass stars.

Compared to these other studies, our sample of Trapezium Cluster brown dwarfs is the first population that is sufficiently large to statistically estimate the frequency of sub-stellar objects born with circumstellar disks. Indeed, there are now more brown dwarfs identified in the Trapezium cluster than are presently known in all other star-forming regions combined. However, our estimate of the disk frequency from the JHK diagram could underestimate the true disk frequency for a number of reasons. First, JHK observations trace the innermost regions of disks and the particular disk geometry (inclination, presence of inner disk holes, etc.) can act to reduce the efficiency of detecting disks from JHK photometry, especially for late type sources ([Lada & Adams, 1992](#); [Hillenbrand et al., 1998](#)). For example, the  $\sim 50\%$  excess fraction we find for brown dwarfs is nearly identical to the excess fraction found in the JHK diagram of [Lada et al. \(2000\)](#) for objects in the cluster which are above the hydrogen burning limit. However, by employing  $3\mu\text{m}$  photometry, these authors found a much higher,  $\sim 85\%$ , disk frequency even for the faintest members they detected. Similarly, of the 19 M6-M9 sources with known spectral types and displayed in [Figure 6-1](#), 7 display very small near-infrared excesses (37%). But of the 14 such sources with spectral types *and* detections at L band, all but one source displays much stronger evidence for  $3\mu\text{m}$  excess as shown in [Figure 6-4](#), although the intrinsic K-L colors for M6-M9 stars are somewhat uncertain.

Second, as a result of selecting candidate brown dwarfs at all reddenings we may have included reddened background field stars in the sample which would act

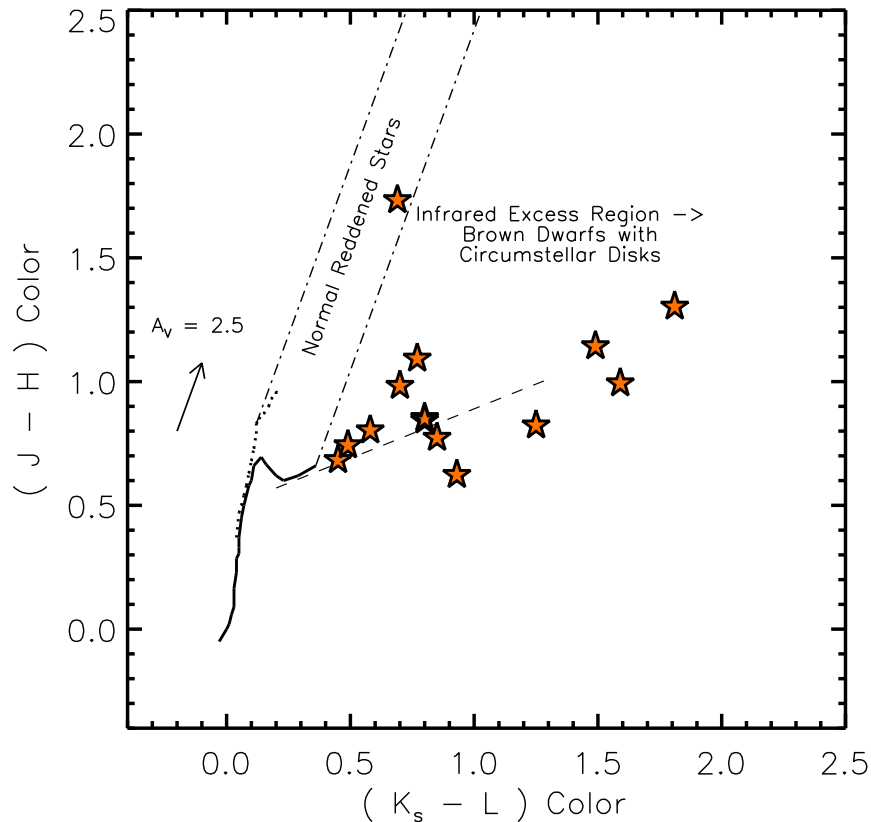


Figure 6–4: L-band observations of brown dwarf candidates. The fraction of brown dwarfs displaying infrared excess is likely a lower limit to the true disk fraction. Longer wavelength observations (L band,  $3\mu\text{m}$ ) such as those used in Lada et al. (2000) are necessary to better understand the spectral energy distributions of these sources and to derive a more secure estimate of the disk fraction. For example, of the 19 late spectral type (M6+) sources, 14 were detected at L band ( $3\mu\text{m}$ ). Though 37% of these sources display IR excess at K band  $2\mu\text{m}$ , 13 of 14 have  $K_s - L$  colors indicative of cool disks.

to decrease the derived disk fraction. When we select candidates at low reddenings ( $A_V \leq 5$  relative to the isochrone in the Figure 6–1a) to exclude background field stars, we find 77% (57/74) of this sample display infrared excess. Further, this sample is an extinction limited sample which is complete at all masses in our selected range and therefore is likely representative of the population as a whole.

We conclude from our current study and from the findings of Lada et al. (2000) that circumstellar disks are present around a high fraction of Trapezium Cluster members *across the entire mass spectrum*. This implies that brown dwarfs and higher mass

stars form via a similar mechanism, e.g., from individual contracting fragments of the parental molecular cloud which, via conservation of angular momentum, form a central star accompanied by a circumstellar disk (Shu et al., 1987). Low & Lynden-Bell (1976) showed that within the conditions of molecular clouds, the minimum Jeans mass for a cloud fragment could be as small as  $0.007 M_{\odot}$ , well below the mass necessary to create the Trapezium brown dwarfs. The free-floating nature of these brown dwarfs rules out their formation as companions in a circumstellar disk. Thus our results seem to implicate a formation mechanism for brown dwarfs in which such objects are formed with circumstellar disks from individual proto-*substellar* cores. Consequently, even sub-stellar objects may be capable of forming with systems of planetary companions.

Confirmation of our hypothesis that a substantial fraction of the brown dwarfs in the Trapezium are surrounded by circumstellar disks requires additional data. Deep  $3\mu\text{m}$  ground-based observations such as those used by Lada et al. (2000) are necessary to permit a more accurate measurement of the excess fraction for the entire brown dwarf population. Longer wavelength infrared observations, such as those that will be possible with Space InfraRed Telescope Facility (SIRTF), would enable the construction of more complete SEDs for these sources which could then be compared directly to theoretical disk predictions. Estimates of the masses of the disks would have interesting implications for the possibility of forming planetary companions around brown dwarfs. Finally, high resolution spectra of these objects would enable searches for accretion indicators, such as H $\alpha$  emission, veiling, etc., which could yield accretion rates and information about the growth and early evolution of these interesting objects.

## CHAPTER 7 DISCUSSION ON THE STRUCTURE OF THE IMF

### 7.1 Young Clusters and the Global IMF

From our current work and by comparison of our work to that of other authors, the general structure of the IMF in these three young stellar clusters is readily apparent: a continuous IMF that rises with a relatively steep slope toward subsolar masses, flattens and forms a broad peak between  $0.3 M_{\odot}$  and the hydrogen burning limit before turning over and declining into the brown dwarf regime. This IMF structure is roughly half-gaussian, though not exactly log-normal (see Figure 3–14b). Further, it is quite consistent with current derivations of the IMF in other star clusters. Mass functions for open clusters such as the Pleiades (Bouvier et al., 1998) and M 35 (Barrado y Navascués et al., 2001) rise with similar power-law slopes and form broad peaks at subsolar masses before apparently rolling over and declining into the brown dwarf regime. Additionally, the color-magnitude diagrams of very luminous clusters such as NGC 3603 (Brandl et al., 1999) and NGC 6231 (Baume et al., 1999) all display evidence of IMFs that peak at subsolar masses, though a more complete discussion awaits detailed derivations of their subsolar and substellar IMFs. Extending this comparison to globular clusters using the study of Paresce & De Marchi (2000) we find that even these older, more populous clusters all have IMFs that form broad peaks at subsolar masses similar to the open and embedded star clusters. On the other hand, the mode of these globular cluster IMFs is consistently around  $0.3 M_{\odot}$  or somewhat higher than that we derive in IC 348 or the Trapezium even after accounting for the range of IMFs permitted by our models. Perhaps more interesting, the form of the IMF in all of these star clusters is very similar to the initial mass function derived for stars in the galactic field (Salpeter, 1955; Miller & Scalo, 1979; Scalo,

1986; Kroupa et al., 1993; Scalo, 1998; Kroupa, 2001; Chabrier, 2001). For example, both the Scalo (1986) and Kroupa et al. (1993) field star IMFs rise in number with decreasing mass in a manner nearly identical to the young clusters, having intermediate ( $1 - 10 M_{\odot}$ ) mass slopes of  $\Gamma_1 = -1.3$  to  $-1.7$ . Further, these field star IMFs flatten between  $1$  and  $0.5 M_{\odot}$  (we derive  $\sim 0.7 M_{\odot}$ ) having subsolar power-law slopes of  $\Gamma_2 = -0.3$  to  $-0.2$ , similar again to that IMF structure we find for the young clusters.

The existence of a peak (or mode or “characteristic mass”) in the field star IMF was first suggested by Miller & Scalo (1979) but it is not yet clear at what mass this IMF mode lies. The most recent study of the V band luminosity function for field stars does not find evidence for a mode or turnover at masses greater  $0.1 M_{\odot}$  (Chabrier, 2001), which would mean that the mode of the IMF in the field is significantly different from and shifted to lower masses relative to that IMF found for globular clusters. In this regard, the field star IMF is more similar to our findings for young embedded clusters than to the older globulars; however, we also learned that the determination of the IMF mode in these young clusters is not straightforward. First, we found in section 3.4.3 that different derivations of the Trapezium IMF yielded IMF modes that varied more than the expected uncertainties from any one method and had a dispersion that spanned the range from the globular cluster IMF mode to the current constraints on the IMF in the field. Second, and perhaps more important, we found and discussed in Section 4.4.2 that there is evidence for radial variations in the *subsolar* IMFs of both the IC 348 and the Orion Nebula Cluster of which the Trapezium is the core. These radial variations, regardless of origin, yield different IMF modes for a cluster depending upon what area of the cluster is sampled. Only when we examine these young cluster’s *composite* IMFs do the modes appear to skew toward the hydrogen burning limit, resulting in IMFs that appear more similar to the constraints placed on the field than to the IMF mode found in the globulars.

Regardless of these potentially meaningful details, if we broadly compare these IMFs we find that all of these stellar systems display remarkable consistency in the form of their IMFs; a similar conclusion has recently been reached by [Kroupa \(2002\)](#). It is not clear, however, the extent to which this documented continuity between the cluster and field star IMFs extends across the hydrogen burning limit and throughout the substellar regime. The aforementioned Pleiades cluster IMF rolls over and declines into the substellar mass regime with a slope slightly flatter,  $\Gamma_{bds} \sim +0.5$  ([Bouvier et al., 1998](#); [Hambly et al., 1999](#)), than that we have derived for these two embedded clusters  $\Gamma_{bds} \sim +0.7 \rightarrow 2.0$ , although the substellar IMFs in these embedded clusters are in fact better populated than in the Pleiades. Although IC 348 and the Trapezium IMFs each decline into the substellar regime with a different IMF slope, they in fact have nearly identical percentages of brown dwarfs as members, i.e.,  $\sim 25\%$ .

On the other hand, the IMF for field brown dwarfs is not yet robustly known as reflected in the two somewhat contradictory results of [Reid et al. \(1999\)](#) and [Chabrier \(2002\)](#). While [Reid et al.](#) suggests a rising substellar IMF (implying brown dwarfs dominate stars by number), [Chabrier \(2002\)](#) determines that a flat substellar IMF is an upper limit and that at most the space density of brown dwarfs equals that of stars (i.e.,  $\sim 0.1 \times 10^{-2} \text{ pc}^{-3}$ ), although this is still twice the frequency of brown dwarfs seen in young clusters.

Two findings in star-forming regions also make it difficult to confirm the universality or stochastic nature of the substellar IMF. First, current surveys find an apparent dearth of brown dwarfs in the isolated star-forming region Taurus ([Luhman, 2000](#)). If this finding is confirmed and is not the product of small number statistics, then the lack of brown dwarfs in a star-forming region that primarily creates only handfuls of solitary or binary stars rather than rich clusters would be solid proof for a variation in the IMF as a function of star-forming environment.

Second, our finding of peaks in the substellar K band luminosity functions of IC 348 and the Trapezium may be very important for testing a hypothesis of an universal IMF drawn from a dominate star formation process. This is because, as we discuss further in the next section, these peaks can be explained by two alternate hypotheses: 1) that a secondary peak forms in the substellar initial mass function near the deuterium-burning limit, suggesting that an alternative mechanism may form the lowest mass objects, or 2) that a previously unknown feature in the evolution of low mass brown dwarfs exists and is not included into current theoretical models on which all derivations of the substellar IMF rely.

## 7.2 Secondary Sub-Stellar Peak in the Cluster LFs

As we derived in Chapter 3, the secondary peak in the substellar regime of the Trapezium KLF can be attributed to a corresponding IMF peak near the deuterium-burning limit using current evolutionary models. Our finding in Chapter 4 of an IC 348 KLF feature having a similar size and corresponding to the same mass range,  $10 - 20 M_{Jup}$ , lends some support to this conclusion. In addition, the nearby ( $\sim 350$  pc) 5 Myr  $\sigma$  Orionis open cluster (Walter et al., 1997) has been the target of recent imaging surveys that are sufficiently sensitive to detect such IMF structure. From an optical and near-infrared survey of  $847 \text{ arcmin}^2$  of this cluster, Béjar et al. (2001) derived a very flat substellar IMF, having a slope of only  $\Gamma_{bds} = +0.2$ , but that appeared to be rapidly rising near the deuterium burning limit. Taking the J band data from this work, we construct the  $\sigma$  Ori JLF in Figure 7–1a. Below a bright LF peak that corresponds to  $0.1 M_{\odot}$  at the cluster’s mean age and that is likely incomplete due to source saturation in the Béjar et al. survey, the  $\sigma$  Ori JLF falls in number with increasing magnitude before forming a very broad plateau.

To make detailed comparisons between the Trapezium and  $\sigma$  Orionis substellar IMFs, we re-derived the  $\sigma$  Orionis IMF using the J band data published in Béjar et al.. We followed their prescription of using a coeval mass-luminosity relation for a 5

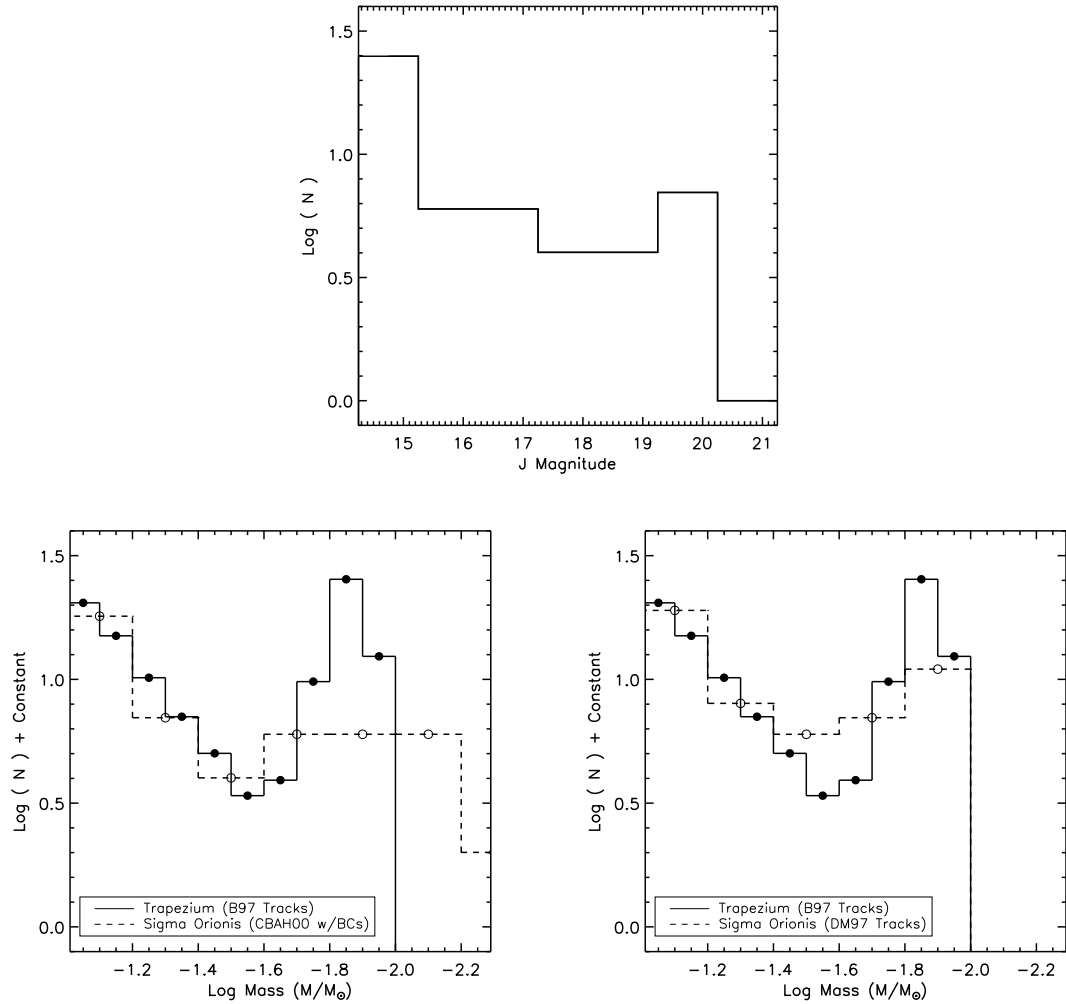


Figure 7–1: Comparison of Trapezium and  $\sigma$  Ori IMF. A) The J band LF of the Sigma Orionis substellar members (photometry from Béjar et al. (2001)) B) Trapezium IMF (using B97 tracks) compared to  $\sigma$  Ori IMF. The  $\sigma$  Ori IMF was derived by directly computing mass estimates from a coeval mass-luminosity relation at 5 Myr. In this panel this M-L relation was from the Chabrier et al. (2000); Baraffe et al. (2002) tracks. C) Trapezium IMF (using B97 tracks) compared to  $\sigma$  Ori IMF (using DM97 tracks).

Myr cluster at 352 pc to derive individual masses for the sources and then binned the resulting *logarithm* of their masses into a evenly spaced histogram. We used the mass-J magnitude relations from the very recent DUSTY PMS tracks of Chabrier et al. (2000) (with updates from Baraffe et al., 2002) because the B97 mass-luminosity relations display a very strong inflection at 5 Myr that is unseen in other PMS tracks (see Figure 3–17e). As shown in Figure 7–1bc, the Trapezium and  $\sigma$  Orionis substellar IMFs

decline in number with decreasing mass in a nearly identical fashion down to around  $0.02$  to  $0.03 M_{\odot}$ . What at first appeared to be large differences in the slope of the substellar IMF of the Trapezium and  $\sigma$  Orionis as derived by [Béjar et al.](#) turned out to be only phenomenological differences due to the random binsizes used by [Béjar et al.](#) in the construction of the  $\sigma$  Orionis IMF and their approximation of this clearly non-power law IMF by a single power-law index. Below this  $30 M_{Jup}$ , the substellar IMFs of both clusters break and form either a secondary peak or a broad plateau at the deuterium-burning limit. As we have already concluded, the morphological details of the secondary peak in the cluster IMF at the deuterium-burning limit are somewhat model dependent. For example, a stronger secondary peak forms in the  $\sigma$  Orionis IMF at the deuterium-burning limit if we use the [DM97](#) tracks (Figure 7–1c). Further, the assumption of coevality for a non-coeval cluster would artificially broaden any potentially sharp secondary peak at the deuterium-burning limit.

Taken as a sum, we have shown that three young clusters at three different ages (1,2 and 5 Myr) all have luminosity functions that form peaks or broad plateaus that could correspond to similar IMF features in the mass range from  $10 - 20 M_{Jup}$ . However, since the observed luminosity function is the product of the IMF and the *slope of the mass-luminosity relation*, it may also be the case that a subtle feature or inflection exists in the empirical mass-luminosity relation that has not been resolved by even the most recent theoretical models of brown dwarfs that we have used (e.g., [Chabrier et al., 2000](#); [Baraffe et al., 2002](#)). Such an undocumented M-L feature could also produce a peak in the luminosity function independent of the structure of the underlying IMF, as was previously found, for example, in the [Kroupa et al. \(1990, 1993\)](#) studies of the  $H^{-}$  and  $H_2$  opacity features in the optical  $M - M_V$  relation for field stars.

There is some observational evidence that seems to point toward an undocumented feature in the evolution of brown dwarfs. After investigating the color-magnitude

diagrams of a number of open clusters with a wide range of ages (1 - 100 Myr) and including  $\sigma$  Orionis, [Jameson \(2002\)](#) pointed out the presence of a gap in the substellar regime of the clusters' loci on the observational HR diagram. Interestingly, this gap occurred at nearly constant color as a function of age, suggesting it is related to the source's temperature and not related to the mass function. This is because after 10 Myr, very low mass stars and brown dwarfs begin to evolve to significantly cooler temperatures with increasing age, and such a color feature, if it were related to the mass function, should also evolve to redder or cooler colors with age. From this data [Jameson](#) hypothesized the existence of a previously unknown feature in the mass-luminosity and mass-color relations for substellar objects, a feature that could be responsible for the secondary JLF and KLF features that exist in  $\sigma$  Ori, IC 348 and the Trapezium.

Regardless, it is clearly uncertain which effect (IMF, M-L relation) will in fact dominate the nature of the secondary LF peaks and features we have observed. Another conclusion from the Kroupa et al studies that is relevant to our deciphering the secondary LF peaks is that until an empirical mass-luminosity feature is accurately constrained, the size of the resulting LF peak due only to the inflection in the mass-luminosity relation (hence independent of the IMF), will be very uncertain ([Kroupa & Tout, 1997](#)). Therefore it remains up to future observations to disentangle these two effects for the very lowest masses in these young clusters and to determine whether a substellar IMF peak may exist. However, since whichever mechanism that is producing this LF peak appears to operate only at the very lowest masses in these very young clusters, it seems unlikely that it will modify the composite cluster IMFs we derive in the stellar regime and down to and across the hydrogen burning limit. Further, a new M-L feature at the deuterium-burning limit, for example, probably will not adjust (inflate or decrease) the percentage of sources that are brown dwarfs in these

clusters. Indeed, in the case of the Trapezium, such a feature cannot change the direct counting of sources that appear substellar.

### 7.3 New Clues to the Origin of Stars and Brown Dwarfs

The continuity of the structure of the IMF across so many environments and the lack of meaningful deviations from this global IMF structure (to which our models would be sensitive) suggests that a single star formation process may be responsible for producing the majority of the mass spectrum. The alternate interpretation of a relatively universal IMF form is that the number of variables or contributing processes to the IMF is sufficiently large that they almost always conspire to produce a single “universal” IMF no matter how they individually vary (Adams & Fatuzzo, 1996). Two important findings from our work may shed light on the origin of the IMF in the context of these hypotheses.

First, we found in Chapter 6 that stars *and* brown dwarfs form with similarly high initial frequencies of circumstellar disks. Combined with the finding that these brown dwarfs disks appear to have very similar properties to those disks found around stars (Natta & Testi, 2001), this evidence suggests that stars and brown dwarfs form via a similar physical mechanism, i.e. as contracting fragments of the molecular cloud. While it may be the case that various physical processes might influence the fine details (e.g., the IMF’s “peak” or mode, for example) of the IMF’s final form ( e.g., Adams & Fatuzzo, 1996), the original fragmentation distribution function of a turbulent molecular cloud probably dominates the final form of the stellar and substellar IMF (Klessen, 2001) down to very low masses.

The second finding from this work that concerns the origin of the IMF is the suggestion that this continuous, globally consistent mass function breaks and forms a secondary peak near the deuterium-burning limit in a number of the youngest clusters. Were a secondary peak in the IMF of the lowest mass brown dwarfs confirmed, then it may provide evidence for a secondary, competing formation mechanism for these

low mass objects. Indeed, the transition in the substellar IMF at  $30 M_{Jup}$  from a steady power-law decline to the secondary peak at the deuterium burning limit may represent the transition from the formation of brown dwarfs as individual fragments of the molecular cloud to their formation, for example, as truncated stellar embryos that were dynamically ejected from hierarchical proto-stellar systems before they had a chance to accrete into higher mass objects (Reipurth & Clarke, 2001). Alternately, the determination that this secondary LF peak is due to an evolutionary feature for brown dwarfs and not the IMF should not inhibit the search for such a transition in the formation mechanisms of brown dwarfs. The Reipurth & Clarke hypothesis for example, makes the prediction that proto-brown dwarfs that are ejected from the initially bound proto-stellar system will have truncated disks with small radii ( $r < 10 - 20\text{au}$ ) and, thus will not have similar disk lifetimes or disk structures relative to those qualities for the disks around stars. Thus, the frequency and characteristics of circumstellar disks around these very low mass brown dwarfs and planetary mass objects may provide an essential test of their formation from individual pre-*sub*-stellar cores or via some entirely different mechanism.

## CHAPTER 8 CONCLUSIONS AND FUTURE WORK

### 8.1 On the Luminosity Functions of Very Young Stellar Clusters

We have conducted an extensive investigation into the usefulness of the stellar luminosity function as a tool for investigating very young ( $\tau < 10$  Myr) star clusters and for deriving the underlying mass functions of these clusters. To accomplish this general goal, we constructed a Monte Carlo based pre-main sequence populations synthesis algorithm for modeling young stellar populations with realistic mass functions and the direct effects of various observational quantities. After performing a series of numerical experiments and through application of this modeling code to the observations of three young clusters, we find that the observed infrared luminosity function for a young cluster is an excellent tool for deriving and comparing the form of the underlying IMFs of young clusters. A cluster's observed luminosity function is also useful for making qualitative comparisons between clusters of different ages and as such can act as a probe of very distant clusters that cannot be examined via other methods.

Summarizing the results of our construction of the population synthesis algorithm for pre-main sequence star clusters, the numerical experiments using these models, and the application of these models to the observed LFs from our observations, we draw the following general conclusions about model luminosity functions:

1. Numerical experiments using our model luminosity function algorithm reveal that the intrinsic cluster luminosity function is most sensitive to the form of the underlying mass function and to a lesser degree on the cluster's assumed mean age.
2. The cluster's model luminosity function evolves to fainter magnitudes as the cluster's age increases. This evolution progresses as much during the cluster's first 3 Myr as it

does during the time from 3 to 10 Myr, meaning that uncertainties in the derived IMF due to uncertainties in the estimate of the mean age decrease for older clusters. This was seen in the case of our NGC 2362 study where reasonable constraints on both parameters (age and IMF) can be obtained provided only basic assumptions such as the cluster's distance.

3. Model luminosity functions do not appear to depend very much upon the assumed set of theoretical mass-luminosity relations used to derive the mass-luminosity relation. The LF differences resulting from changing sets of M-L relations are much smaller than can likely be observed and should not impact our findings. We find that this is because different sets of theoretical evolutionary models for canonical pre-main sequence evolution predict remarkably similar mass-infrared luminosity relations despite significant variations in the fundamental input physics. This is in contrast to the effective temperatures predicted by these evolutionary models, which are very sensitive to input physics.

4. The technique of modeling the cluster luminosity function appears very adept at dis-entangling known mass-luminosity relation features from the form of the underlying IMF. Thus, if future updates to the theoretical mass-luminosity relations change our previous conclusion about the robustness of the M-L relation by including new, previously unknown M-L features, our modeling procedure has the ability to easily include these revisions and resolve the cluster IMF.

Further, we derived a deep near-infrared census of sources in three young star clusters using sensitive near-infrared imaging of these clusters. From these observations we construct the clusters' differential K band luminosity function by correcting the observed luminosity functions for the statistical contribution of interloping field stars. From the construction and comparison of the luminosity functions of these three clusters we draw the following general conclusions about the near-infrared luminosity function of a young stellar cluster:

1. The luminosity function of a very young star cluster can be constructed for sources down to and below the deuterium-burning mass limit ( $\sim 0.01 M_{\odot}$ ) using the products of deep near-infrared surveys.
2. Although young clusters display a number of features in their observed luminosity functions that are physically related to known features in the mass-luminosity relation, we find from our luminosity function modeling of these observations that the overall structure of the cluster's near-infrared luminosity function directly reflects the form of the underlying initial mass function.
3. Three young clusters that have been the targets of infrared surveys sensitive down to the deuterium-burning limit all display structure in their substellar luminosity function in the form of a secondary peak or plateau. These LF features occur in magnitude ranges much brighter than the sensitivity limits of the photometric surveys and cannot be explained by uncertainties in the cluster membership. By comparing clusters of different ages, this feature appears to have evolved to fainter magnitudes with increasing age and thus, appears to be an intrinsic feature of these clusters' infrared luminosity functions.

## **8.2 On the Initial Mass Functions of Very Young Stellar Clusters**

Using our population synthesis models of the young stars and their luminosity functions and deep near-infrared surveys of three young (1-5 Myr) cluster, we are able to derive the underlying initial mass functions for these clusters. In two of these clusters, these IMFs constitute nearly the complete range of stellar and substellar mass, from B stars down to the deuterium-burning limit. In a third cluster we find that we can derive the IMF to a mass sensitivity similar to spectroscopic observations of nearby clusters although our target open cluster is at a distance of 1500pc, four to five times the distance to these nearby clusters. Thus, luminosity function modeling has the ability to study the IMF over a volume nearly two orders of magnitude greater than the use of spectroscopic measurements, illustrating our method's usefulness as a probe of

the universality of the IMF. From these detailed studies, we draw the following basic conclusions about our modeling technique and the IMF of young clusters:

1. We find that the IMF derived from modeling a cluster's infrared luminosity function is in good agreement with that IMF determined either by using spectra to place the stars on the theoretical HR diagram or by other methods that rely upon IR photometry of cluster members.
2. The IMFs we derive for the three young clusters in our survey are remarkably consistent with one another and in good agreement with the IMF found in other open clusters, in globular clusters and in the field. From our current study and through these comparisons to other regions we find no reason to reject the hypothesis for a globally consistent structure of the IMF.
3. We find that the three very young clusters that have structure and secondary peaks in their substellar LFs may reflect the existence of a break from the continuity of the IMF and the formation of a secondary IMF peak near the deuterium-burning limit. Alternately, this feature reflect an unknown feature in the mass-luminosity relation of low mass brown dwarfs.
4. The combination of the sensitive products of the deep infrared surveys performed for this work and the model luminosity function algorithm have allowed us to constrain the IMF of cluster to much greater mass sensitivity than other methods based on the use of spectroscopic measurements. Thus, we are able to use a cluster's luminosity function to sample a much greater volume of the local Galaxy.

Finally, when we combine the robust IMFs we derive for the young clusters and their agreement with the IMF found in other stellar systems with evidence that star and brown dwarfs, independent of mass, are born with circumstellar disks, we conclude that not only is there evidence for a globally consistent formulation of the initial mass function, but that a single star formation process is likely responsible for nearly the entire range of mass. Whether these conclusions extend to the IMF and

formation mechanism of very low mass brown dwarfs near the planetary mass regime, i.e.,  $M < 10 M_{Jup}$ , will be the target of the next generation of IMF studies.

### 8.3 Future Work

There are a number of important questions raised by this work. For example, it is clear that the slope of the substellar IMF is not nearly as robustly determined as the stellar portion of the global IMF. Could it display significant variations from region to region as suggested by the [Luhman](#) Taurus result? Further, what is the nature of the secondary LF peak near the deuterium-burning limit and is there other evidence for a transition in the formation mechanism of brown dwarfs at these lowest masses? We outline a few future projects we are undertaking that might answer similar such questions, as well as future work relevant to the luminosity function models presented here.

#### 8.3.1 Continued Study of the IMF in Young Clusters

Clearly, the luminosity function is a tool that can be efficiently applied to a much larger sample of clusters than the three clusters studied here. Simply increasing the number of clusters studied and the volume of the local Galaxy surveyed would rapidly produce a sufficient sample of homogeneously derived IMFs that can be compared in a statistically meaningful fashion. For example, we can follow the example set by [Kroupa \(2001\)](#) and ask if, the variations in the  $\Gamma_1$  high-mass slope between NGC 2362, the Trapezium and IC 348 are real and reflect something different about the clusters or if they are simply statistical fluctuations. While such fluctuations might be expected out on the high-mass tail of the IMF, they are unlikely to be found near the peak or mode of the IMF since clearly this mass (or mass range) is that portion of the IMF that is most statistically significant for any sized population. With a sufficiently large sample of clusters, surveyed over sufficiently large areas to avoid radial IMF variations, one could easily calculate the robustness of the IMF mode in clusters and compare it in detail to models of the fragmentation of molecular clouds. Further, a statistical

comparisons of the IMF mode in clusters, the field and globular clusters might provide further evidence for stochastic variations in the IMF. Lastly, a larger sample of LF derived cluster IMFs would greatly improve the uncertainty in the substellar IMF.

### 8.3.2 Structure of Young Open Clusters

The existence of the radial IMF variations in IC 348 and the Orion Nebula Cluster has important consequences for making meaningful comparisons between the IMFs of different clusters in our current IMF study. The origin of these radial IMF variations, while beyond the scope of the current work, has important consequences, none the less, on the general understanding of the IMF. For example, if the radial IMF variations are primordial, then they represent a breaking of the universality of the IMF on spatial scales less than a parsec in area, implying that differing processes are acting on the fragmentation of the gas to give different locale IMFs. If the origin of the radial IMF variations is dynamical, then a study of this phenomena in a set of young clusters with a range of ages would reveal what corrections must be applied to convert the observed mass function into the *initial* mass function for a dynamically evolved cluster. On the other hand, determination of the mass function of a cluster's halo reveals one additional piece of information: if most stars are born in clusters then the halo IMF of a cluster constitutes that portion of the IMF being donated to the field in the current epoch.

We will begin such a study of the structural evolution of young clusters by exploring NGC 2362 over a much larger area than the La Silla survey. First we must determine if the cluster's halo as suggested by the 2MASS radial profile is real and what is the subsolar IMF of this halo. This will be accomplished by employing wide-field optical and infrared cameras and the 2MASS catalog to construct optical-infrared color-magnitude diagrams for the cluster halo with the goal of selecting members and estimate masses and mass functions. Since numerical models suggest that significant structural evolution happens within the first 10 Myr after the dispersal of the molecular cloud ([Kroupa et al., 2001](#)) we will extend this study to two other clusters

of similar youth: NGC 3293 ( $\sim 7$  Myr) (Herbst & Miller, 1982) and NGC 1502.

Combining these three clusters with a wide-field IR survey of the Orion Nebula Cluster to determine the mode of this cluster's IMF and the substellar IMF in the cluster halo, we will be able to study how clusters dynamically evolve and are dispersed into the galactic field.

### 8.3.3 Disks around Young Brown Dwarfs

One possible avenue for answering questions about the formation mechanism of brown dwarfs is to investigate the substellar population of an entire Giant Molecular Cloud (GMC). Such an investigation would identify brown dwarfs forming in a variety of environments in a GMC and in sufficient numbers to begin to provide statistical answers to these questions. The Perseus Molecular Cloud is a good candidate cloud for a number of reasons. First, it is known to contain both embedded clusters, e.g., NGC 1333 and IC 348, which we have studied here in Chapter 4, and isolated star forming cores (e.g., LDN 1448). Because Perseus is quite nearby ( $d \sim 300$  pc), very young brown dwarfs across the mass spectrum from the hydrogen to the deuterium-burning limit can be studied both by ground based near-ir imaging and spectroscopy and by mid-infrared imaging using SIRTf. Most vital then is the fact that the Perseus GMC is the target of a complete SIRTf Legacy Science mapping from 3 to 70  $\mu\text{m}$ . The SIRTf Legacy projects are designed to complete large space-based surveys that could not be completed by any single general observer, and they will provide their data products to the general community for archival research immediately after acquisition and processing. For these reasons, a current study of the brown dwarf population of the Perseus GMC has the potential to answer vital questions about the origin and initial mass function of brown dwarfs.

With the goal of obtaining a complete census of young brown dwarfs in a molecular cloud, I am employing the wide-field imaging and spectroscopic capabilities of the FLAMINGOS camera to conduct a ground based photometric and spectroscopic survey

for very low mass stars and brown dwarfs forming throughout the Perseus Molecular Cloud. I am performing this near-infrared survey in advance of the anticipated mid-infrared mapping of this cloud by the SIRTf Legacy Science project entitled, “From Molecular Cores to Planet-Forming Disks” (Evans et al., 2001). The fundamental goal of the proposed research is to identify the substellar population forming within the Perseus Molecular Cloud and to tabulate the composite near- and mid-infrared properties of these sources. The scientific objectives of merging a ground based wide-field near-infrared survey with the products of SIRTf Legacy Science are:

- Identifying where brown dwarfs predominantly form within a Giant Molecular Cloud. By combining near and mid-infrared imaging with spectral classification, low mass and substellar sources can be identified throughout the molecular cloud. Is the nascent Perseus brown dwarf population concentrated in young embedded clusters such as NGC 1333 and IC 348, or in a more distributed population throughout the cloud? How distributed brown dwarfs distributed in and around clusters? Do dynamical or primordial mass segregation produce a brown dwarf population that is primarily found in the halos of these young clusters?
- Determining if the Initial Mass Function of low mass stars and brown dwarfs (from 0.1 to 0.01  $M_{\odot}$ ) varies between the young clusters and the isolated star forming sites within a GMC. Masses for individual young sources will be estimated by comparing luminosities and spectral classifications to theoretical evolutionary models, and the low mass initial mass functions of the Perseus embedded clusters and the distributed population can be compared. Is the formation frequency of brown dwarfs a function of initial stellar density or location within a GMC?
- Establishing the *initial* properties of circumstellar disks around brown dwarfs. Spectral energy distributions from 1 to 24  $\mu\text{m}$  will be constructed for young substellar sources across the mass range from the hydrogen to the deuterium burning limits, allowing for detailed modeling of the brown-dwarf/disk properties. Are the basic physical characteristics (frequency, accretion rate, size and mass) of disks around brown dwarfs the same as for low mass stars? Or do differences exist as a function of mass that might indicate a transition in the formation mechanism from stars to brown dwarfs?

The basic methodology of this project is to derive a complete near-ir census of stellar and substellar objects forming within the Perseus Molecular Cloud will be

combined with the SIRTf Legacy observations. In addition to this near-infrared census, I will conduct an extensive near-infrared spectroscopic study of young embedded substellar sources in this cloud identified both from the near-infrared census and its merger with the SIRTf Legacy observations.

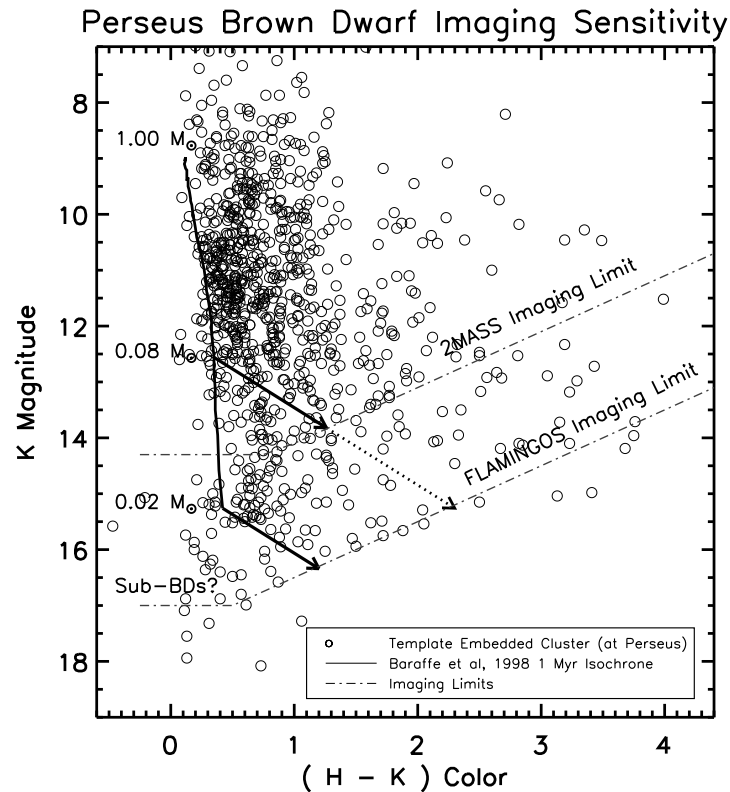


Figure 8–1: Comparison of the 2MASS and FLAMINGOS imaging sensitivity. near-infrared surveys of the Perseus Molecular Cloud. The Trapezium Cluster infrared color-magnitude diagram (from Chapter 3) was shifted to the distance of the Perseus Molecular Cloud to act as a template embedded cluster. 2MASS observations will allow the cloud to be probed to  $A_V \leq 5$  for objects down to  $0.05 M_\odot$ . The deeper FLAMINGOS imaging will probe sources over the entire substellar range to  $A_V \sim 10$ . Based on the nominal  $10\sigma$  sensitivities expected from the SIRTf Legacy Science mapping of the Perseus Cloud, spectral energy distributions will be constructed for objects across the substellar mass range, from the hydrogen to the deuterium-burning limit.

During this project’s first year I will compile a sensitive volume-limited (extinction-limited) near-infrared catalog of *candidate* pre-main sequence stars and

young substellar objects ( $1.0 - 0.01 M_{\odot}$ ) in the cloud. This has already been begun with the wide-field study of IC 348 in Chapter 4 and will be efficiently completed by combining the existing Two Micron All-Sky Survey (2MASS) of the Perseus Cloud with additional deep imaging that employs the wide-field capabilities of FLAMINGOS. As shown in Figure 8–1, the sensitivities of the extant 2MASS database are sufficient to catalog young 1 Myr sources down to  $0.05 M_{\odot}$  in Perseus, though only to relatively low reddenings for the substellar population. Thus, 2MASS can be immediately used to survey the low extinction regions of the cloud. To detect substellar sources from  $0.05 - 0.01 M_{\odot}$  and to probe the more embedded population, I will use FLAMINGOS with a  $21'$  field of view on the 2.1m KPNO telescope to map 36 pointings of the Perseus Cloud in the JHK broadband filters. As shown in Figure 8–2, the FLAMINGOS survey is restricted to the embedded clusters and isolated dense cores as traced by the  $^{13}\text{CO}$  gas (Bachiller & Cernicharo, 1986) and will be obtained in collaboration with the allocated NOAO Survey project, “Toward a Complete Near-Infrared Spectroscopic and Imaging Survey of Giant Molecular Clouds” (E. Lada, P.I.). The combined 2MASS and FLAMINGOS catalogs of Perseus will provide a volume-limited census of young stars down to the hydrogen burning limit seen through 30 magnitudes of extinction, and brown dwarfs as small as  $10\text{-}20 M_{Jup}$  seen through reddenings of  $A_V \sim 10$  magnitudes.

During the project’s second year, I will begin using the multi-object spectroscopic capabilities of the FLAMINGOS camera to obtain spectra of the sources in the 2MASS+FLAMINGOS catalog. FLAMINGOS provides simultaneous spectroscopic measurements of 50 to 100 sources per pointing, and I will use FLAMINGOS to obtain spectra from  $1.25$  to  $2.5 \mu\text{m}$  with spectral resolutions of  $R \sim 1000$ . For example, during one hour on the KPNO 4m, FLAMINGOS can measure the spectra of an unreddened 1 Myr  $0.02 M_{\odot}$  Perseus brown dwarf to a  $S/N = 50$ . Thus, I will be able to derive spectral types for sources across hydrogen burning limit and down to

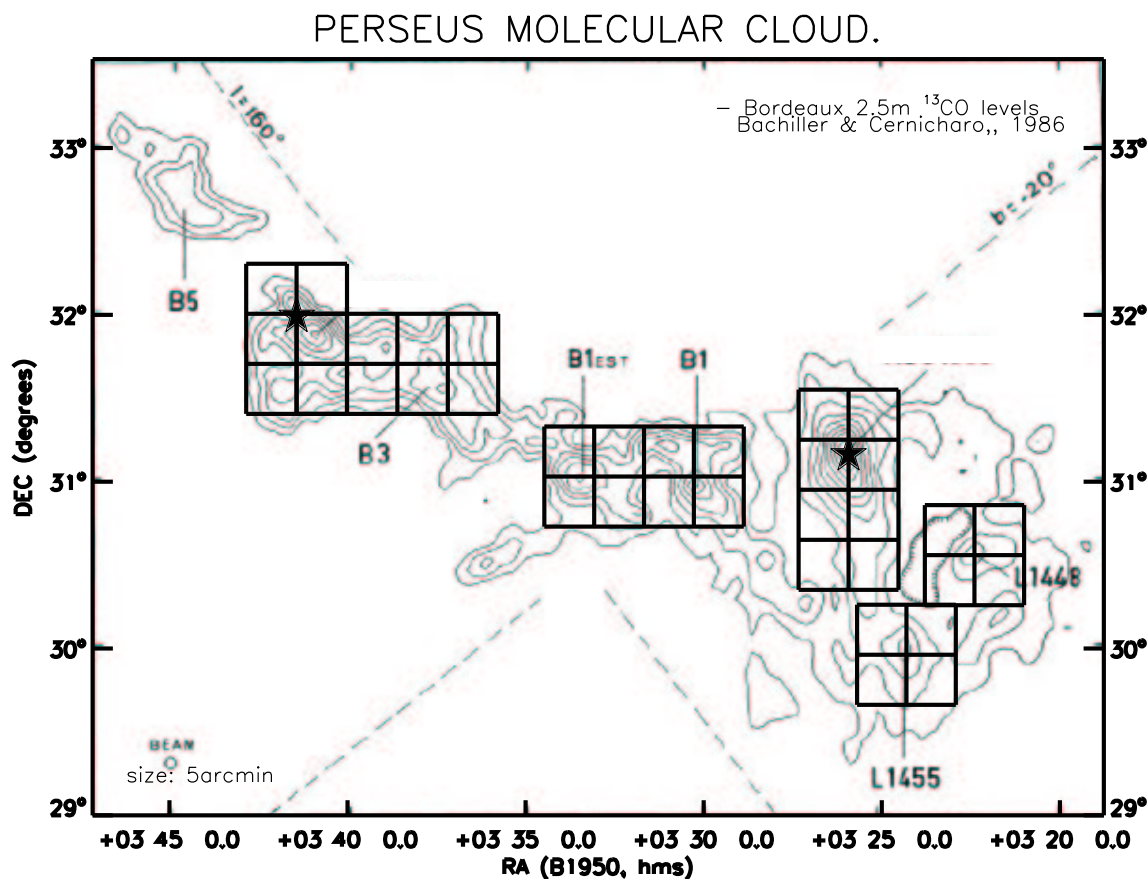


Figure 8-2: Imaging map of the Perseus GMC with FLAMINGOS. Individual pointings are overlapped by  $3'$ . Stars mark the locations of the young embedded IC 348 and NGC 1333 clusters. The SIRTf Legacy Science observations will map the entire  $6.0\text{deg} \times 4.0\text{deg}$  cloud region including both the dense molecular gas and extensive off-cloud areas. The FLAMINGOS mapping concentrates upon the embedded stellar clusters and dense molecular cores and the 2MASS database will be used to catalog potential pre-main sequence stars and young brown dwarfs in off-cloud and in low column density regions of the molecular gas. Deep near-infrared imaging is necessary to catalog the youngest brown dwarfs deeply embedded within the molecular cores and young clusters in the Perseus GMC. The combination of the 2MASS and FLAMINGOS datasets will provide an extinction limited sample of sources sensitive to a  $20 M_{Jup}$  brown dwarf seen through 10 magnitudes of extinction. The SIRTf observations will be able to detect (at the  $20\sigma$  level) the  $5\mu\text{m}$  photosphere of this same reddened low mass brown dwarf.

approximately  $\sim 0.02 M_{\odot}$ . Spectra obtained at J and K wavelengths will be also be searched for evidence of continuum veiling due to disk accretion, and for the Pa $\beta$ ( $1.28\mu\text{m}$ ) and Br $\gamma$ ( $2.17\mu\text{m}$ ) near-infrared hydrogen emission lines which have been shown to be good tracers of the accretion luminosity/rate for embedded T-Tauri stars (Muzerolle et al., 1998). Prior to the SIRTf Legacy mapping, I will concentrate the spectra survey on regions of known star formation such as NGC 1333 and IC 348, or sources selected from the color-color diagram by having infrared colors that lie to the right of the reddening band for M6 stars. This should provide a first cut at isolating both late type stars and brown dwarfs (i.e., those M6 or later), and identifying young sources which display near-infrared excess.

The first pipeline products from the SIRTf Legacy Science project will become publically available beginning roughly 7 months after SIRTf launch, currently scheduled for December 2002. Since this is after the first year of my current project, the near-infrared imaging campaign will be completed and the 2MASS+FLAMINGOS catalog fully tabulated, while the spectroscopic survey will be underway. The initial SIRTf Legacy Science data products will include source photometry at 3.3, 4.5, 5.8, 8, and  $24\mu\text{m}$  and are projected to have nominal  $10\sigma$  sensitivities to sources *at and somewhat below* the limits of the near-infrared catalog. For example, the current predicted sensitivities of the Legacy Science observations will be sufficient to detect (at the  $20\sigma$  level) the *photosphere* at  $5\mu\text{m}$  of a 1 Myr  $20 M_{Jup}$  brown dwarf reddened by 10 magnitudes of extinction. Thus, when the near-infrared catalog and the SIRTf data products are merged, near to mid-infrared spectral energy distributions can be instantly calculated for every source within the extinction-limited near-ir catalog, allowing for efficient separation of young pre-main sequence stars and brown dwarfs from background field dwarfs and giants. After this merger of the SIRTf data with the

2MASS-FLAMINGOS near-infrared catalog, the FLAMINGOS spectroscopic observations will be focused on the revised sample of candidate brown dwarfs in Perseus. This follow-up will continue through the third year of this project.

#### **8.3.4 Model Improvements**

A final, followup to this dissertation is the addition of a few minor improvements to the population synthesis algorithm. The primary goal of these improvements is to make the output more realistic and more varied, giving the code additional uses. These primary improvements include the addition of a photometric noise model for more realistic simulations of color-color and color-magnitude diagrams and improved output parameters for simulation of unresolved binaries so that the colors and magnitudes of individual components can be retrieved. Some secondary improvements will also be implemented to make various model parameters more “random.” This includes drawing random cluster size from a poissonian distribution or drawing random binary fractions. Lastly, the code itself can be improved by instituting a better interpolation scheme for moving between the mass tracks and isochrones of the pre-main sequence evolutionary models. Typically these models are not well spaced, either in mass or age, and the cubic spline routine we are using could be improved upon with a 2-D interpolator, for example.

APPENDIX A  
TABULATED BOLOMETRIC CORRECTIONS

Bolometric corrections, which were used to convert model stars' luminosities and effective temperatures into monochromatic magnitudes, were interpolated from an empirical table of basic stellar properties derived from literature sources. The following formulae were used to convert from these theoretical quantities to the monochromatic pass band magnitude.

$$M_{\lambda} = M_{bol,*} - BC_{\lambda} \quad (\text{A.1})$$

$$M_{bol,*} = M_{bol,\odot} - 2.5 * \log(L/L_{\odot}) \quad (\text{A.2})$$

$$M_{\lambda} = M_{bol,\odot} - 2.5 * \log(L/L_{\odot}) - BC_{\lambda} \quad (\text{A.3})$$

We have adopted the near-infrared colors of dwarf stars. While the temperature scales for young pre-main sequence stars fall somewhere between the temperature scales for main sequence dwarfs and giants, their near-infrared colors are more dwarf-like (Luhman, 1999).

We constructed our initial table of stellar properties beginning with those compiled in Kenyon & Hartmann (1995, hereafter, KH95) . We adjusted this tabulation to reflect the large temperature range of our model stars, to update it with additional observations and to investigate some of the dependencies of our models on this tabulation. For spectral types O3 to B0.5, corresponding to  $T_{eff}$  from 30000 to 50000 K, we used V band bolometric corrections and effective temperatures from Vacca et al. (1996). O star colors were assumed degenerate at all near-infrared bands and assigned the colors of Johnson (1966). B star red and near-infrared colors were taken from a recent tabulation by Winkler (1997). There is presently a significant study in the

literature of the color- $T_{eff}$ -spectral type relation for cool stars with  $T_{eff}$  less than 3500K (Leggett et al., 1996). Because we related the stellar effective temperature directly to the stellar color and bolometric correction and do not assign spectral types to our model stars, we do not need to define any particular spectral sequence. For the color- $T_{eff}$ - $BC_V$  relation of M dwarfs, we used the relations compiled by Bessell (1991, 1995); Bessell et al. (1998). We used the bolometric magnitudes derived by Tinney et al. (1993) for very late type M dwarfs to extend these bolometric corrections to below  $\sim 2000$ K, the approximate temperature of a  $20 M_{Jup}$  brown dwarf at 10 Myrs.

We checked our tabulation against other recent compilations of stellar properties and cool stars observations in the literature. We compared our  $T_{eff}$ - $BC_V$  relation to those polynomial fits recently derived by Flower (1996) and Hillenbrand (1997). We found that our tabulation was in systematic disagreement with these fits. The cause was traced to the original Aller et al. (1982)  $T_{eff}$ - $BC_V$  tabulation used in the KH95 compilation. We refer to the discussion in Bessell et al. (1998, there Appendix D) as to the source of this discrepancy and follow their prescription to add +0.12 to the Aller et al. (1982)  $BC_V$  scale. Combined with our choice of  $M_{bol,\odot}$  equal to 4.75, this yielded a solar  $BC_V$  equal to -0.07 and an absolute  $M_{V,\odot}$  magnitude of 4.81. We then smoothed the  $T_{eff}$ - $BC_V$  relation to match those of Hillenbrand (1997) and Flower (1996). Our tabulation of bolometric corrections as a function of the logarithm of the effective temperature is given in Table A-1.

A more important concern is the accuracy of our tabulation below 3500K. We tested our tabulation for cool stars by compiling the observed colors, effective temperature determinations and bolometric luminosities for a large number of M dwarfs from the literature including published data by Berriman et al. (1992); Tinney et al. (1993); Jones et al. (1994); Leggett et al. (1996). We used repeat observations and derivations of stellar properties (e.g.  $T_{eff}$ ) of the same M dwarfs but by different authors as

reflecting different spectral type to effective temperature scales and variability among late-type stars, as well as fundamental uncertainties in the computation of these values. We also compared our bolometric correction tables to those BCs predicted by recent model atmosphere and evolutionary calculations at 1 Myrs and 10 Gyrs (Baraffe et al., 1998), although the predicted broadband fluxes from model atmospheres have been found to be largely inaccurate (Leggett, 1992; Graham et al., 1992; Kirkpatrick et al., 1993; Tinney et al., 1993; Leggett et al., 1996).

From the comparison of our compilation, the models and the observed M dwarf colors, bolometric corrections, and effective temperatures, we found three main conclusions. First, our comparison indicated that the compiled bolometric corrections were consistent with the observed M dwarf values. Second, although the bolometric corrections inferred from the model atmospheres agreed very well for the coolest objects, the very young models, i.e. those with ages in the range of 1 to 10 Myrs, predicted bolometric corrections that were in substantial disagreement with the observed M dwarfs for temperatures greater than 3500K. Most important, our comparison showed that for the near-infrared bands, specifically the K-band, the bolometric corrections are fairly insensitive to the effective temperature scale for low mass stars and brown dwarfs.

Table A-1. Table of bolometric corrections

$\text{Log } T_{eff}$	$BC_I$	$BC_J$	$BC_H$	$BC_K$
4.70952	-4.92	-5.29	-5.40	-5.50
4.68726	-4.76	-5.13	-5.24	-5.34
4.66389	-4.60	-4.97	-5.08	-5.18
4.63909	-4.42	-4.79	-4.90	-5.00
4.61289	-4.24	-4.61	-4.72	-4.82
4.58490	-4.04	-4.40	-4.52	-4.62
4.55509	-3.83	-4.18	-4.30	-4.40
4.52297	-3.58	-3.94	-4.05	-4.13
4.50596	-3.44	-3.78	-3.89	-3.97
4.40483	-2.87	-3.19	-3.29	-3.37
4.34242	-2.48	-2.75	-2.84	-2.91
4.27184	-2.03	-2.26	-2.34	-2.40
4.23045	-1.87	-2.09	-2.14	-2.21
4.18752	-1.51	-1.71	-1.77	-1.83
4.14613	-1.24	-1.40	-1.46	-1.50
4.11394	-1.03	-1.17	-1.22	-1.26
4.07555	-0.77	-0.90	-0.94	-0.98
4.02119	-0.45	-0.52	-0.54	-0.56
3.97864	-0.17	-0.17	-0.17	-0.17
3.96520	-0.08	-0.04	-0.04	-0.03
3.95279	0.02	0.09	0.10	0.11
3.94052	0.04	0.14	0.17	0.18
3.92737	0.08	0.22	0.25	0.27
3.92169	0.12	0.28	0.34	0.36

Table A-1—Continued

Log $T_{eff}$	$BC_I$	$BC_J$	$BC_H$	$BC_K$
3.91381	0.21	0.34	0.41	0.44
3.89487	0.28	0.40	0.48	0.51
3.87967	0.35	0.48	0.57	0.60
3.86864	0.40	0.53	0.64	0.67
3.85733	0.46	0.58	0.71	0.74
3.84819	0.47	0.61	0.76	0.79
3.83822	0.48	0.65	0.81	0.84
3.82866	0.49	0.70	0.88	0.92
3.81889	0.51	0.76	0.97	1.01
3.80889	0.53	0.82	1.05	1.09
3.80346	0.56	0.85	1.15	1.19
3.79796	0.59	0.95	1.24	1.29
3.79239	0.63	0.97	1.27	1.32
3.78640	0.65	0.99	1.29	1.34
3.78032	0.66	1.00	1.31	1.36
3.77415	0.66	1.02	1.33	1.38
3.76790	0.66	1.02	1.34	1.39
3.76567	0.67	1.04	1.37	1.42
3.76343	0.67	1.07	1.39	1.45
3.76118	0.68	1.08	1.44	1.50
3.75587	0.68	1.09	1.49	1.55
3.75051	0.69	1.17	1.56	1.62
3.74194	0.69	1.16	1.57	1.64
3.73320	0.68	1.15	1.58	1.65

Table A-1—Continued

$\text{Log } T_{eff}$	$BC_I$	$BC_J$	$BC_H$	$BC_K$
3.72016	0.64	1.22	1.67	1.75
3.70586	0.66	1.26	1.73	1.82
3.69020	0.66	1.28	1.78	1.87
3.67486	0.63	1.34	1.88	1.97
3.66181	0.61	1.41	1.99	2.09
3.63849	0.64	1.41	2.02	2.13
3.62377	0.62	1.39	2.02	2.14
3.61278	0.62	1.37	2.03	2.18
3.59106	0.59	1.60	2.27	2.44
3.57749	0.55	1.62	2.28	2.46
3.55630	0.55	1.64	2.30	2.50
3.52634	0.50	1.81	2.45	2.68
3.49554	0.40	1.93	2.55	2.82
3.46982	0.20	2.03	2.65	2.98
3.45637	0.05	2.02	2.66	3.01
3.44248	-0.20	2.00	2.66	3.04
3.43136	-0.50	1.98	2.68	3.10
3.23000	-1.75	1.70	2.72	3.33

## APPENDIX B DISTANCE TO THE TRAPEZIUM CLUSTER

[Minkowski](#) opens his re-analysis of [Trumpler \(1931\)](#) derivation of the distance to Orion with a sentence still applicable today, “All published values of the distance of the Orion nebula are open to some criticism.” This uncertainty can be best seen in the [de Zeeuw et al. \(1999\)](#) Hipparcos study of the region. In what should be the best distance estimate to Orion, [de Zeeuw et al.](#) had difficulties finding the OB associations due to their mostly radial motion away from the Sun. The fact that there are numerous and often distinct associations ([Blaauw, 1964](#)) in a very large region on the sky naturally makes precise distance estimates difficult since the region could be as deep along the line of sight as it is across the sky. This was in fact one positive result from the [de Zeeuw et al.](#) Hipparcos study who found that at least one of the associations was 50-100 pc in front of the others.

We performed a simple historical review of the values for the distance to the Orion Molecular Cloud or the Orion Nebula Cluster, of which, the Trapezium Cluster studied in [Chapter 2](#) and [Chapter 3](#) is the core. We attempted where possible to detail the method used to derive the distance and if error estimates were documented, however, a number of the references were difficult to locate using the resources at hand. We also included a number of commonly cited papers that are not estimates of the distance to this region, e.g., [Jones & Walker \(1988\)](#).

For our modeling, we chose to use a distance of 400pc to the Trapezium and the Orion Nebula Cluster. By inspection of the descriptions and the table below, the reader will note that this is on the near side of the distance to this region, and for example, disagrees to a difference of 80pc with the often used [Genzel et al. \(1981\)](#) distance. The distance we chose to use for the Trapezium places it at distance in agreement with

the Orion 1c population as measured by [Anthony-Twarog \(1982\)](#), [Wolff \(1990\)](#), and [Brown et al. \(1994\)](#). We point out that there is not only a large range in these distance estimates but each is also accompanied by a large error bar. This includes an error bar of 80pc for the [Genzel et al. \(1981\)](#) measurement to the BNKL object(s), meaning our assumed distance is well within the associated error bars of any of other preferred measurement even if 400pc is a systematically closer distance than that assumed by other authors (see table 3–6).

One primary problem that persists in more accurately separating the distance to the Orion Nebula Cluster from the Orion 1c association is that they projected along the same line of sight and the 1c association is primarily concentrated along and parallel to the Orion A Molecular cloud which contains the ONC and the Trapezium. Indeed, they are aligned with such agreement that if we review the [Hillenbrand \(1997\)](#), [Rebull \(2001\)](#), and [Carpenter et al. \(2001\)](#) wide-field studies of this region we find that they show no morphological signatures that can separate the two entities other than their age (the Orion 1c association is of order 2-5 Myrs see [Brown et al. \(1994\)](#)). Thus, the distance spread between the 1c association and the BNKL is interesting since they would have to be separated by 80 pc, yet physically aligned. We leave such a problem to improved radial velocities and proper motions of stars seen toward and within the Orion A molecular cloud.

**[Trumpler \(1931\)](#):** In this work, [Trumpler](#) used a number of diagnostics to estimate the distance of the Orion Nebula. Using the method that will be repeated by numerous authors in their later studies of the distance to Orion, [Trumpler](#) derived a distance modulus of 8.5 magnitudes by comparison of the assumed main sequence magnitudes for the B stars in this cluster.

**[Minkowski \(1946\)](#):** [Minkowski](#) re-calculates the total absorption seen towards the three brightest stars in the Trapezium and derives a distance modulus of 7.38 magnitudes.

**[Sharpless \(1952\)](#):** Performs a survey of B type stars throughout the entire Orion region and derives distances using assumed absolute magnitudes for B type stars.

A distance modulus of 8.5 was derived to all the B stars in Orion with a distance modulus of 8.6 derived for stars near the Orion Nebula. An error estimate of  $\pm 0.3$  was given. This result was revised by [Sharpless \(1962\)](#).

**[Parenago \(1954\)](#)**: A detailed cataloging of stars in the Orion Nebula. A distance modulus of 8.0 was derived by this author according to [Strand \(1958\)](#). (I need to read this paper and determine how it was performed).

**[Johnson & Hiltner \(1956\)](#)**: In this re-calibration of the standard main sequence derived by [Johnson & Morgan \(1953\)](#) using young stellar clusters, [Johnson & Hiltner](#) recognize that some luminosity evolution away from a zero-age main sequence will occur between clusters of different ages. Using their re-calibrated zero-age main sequence, they calculated a distance modulus of 8.0 by de-reddening the data from [Sharpless \(1954\)](#) and stars with spectral types B8-A0 to their revised main sequence. However, their ascertain that A0 stars are on the main sequence is certainly not correct for the Orion Nebula Cluster, leading to an underestimate of the distance.

**[Strand \(1958\)](#)**: A distance of 520pc was derived for the ONC using radial velocities of the 6 OB stars and 135 stars with proper motions. The use of radial velocities of the OB stars in the ONC, which have an average of 1.5 members per star ([Preibisch et al., 1999](#)), likely produces significant distance errors.

**[Sharpless \(1962\)](#)**: Although the analysis was performed on the Orion region by breaking it into two sub-regions, the Belt and the Sword, a single distance modulus of 8.2 magnitudes was calculated. No error bars are given.

**[Blaauw \(1964\)](#)**: A distance of 460pc (distance modulus of 8,3) is quoted in this discussion of the Orion OB association. No distance is derived in this paper, instead referring to a work by [Borgman & Blaauw \(1964\)](#).

**[Johnson \(1965\)](#)**: A distance of 380 pc to the ONC region using 21 stars both with good radial velocities and proper motions.

**[Walker \(1969\)](#)**: Fit the zero-age main sequence of [Johnson \(1963\)](#) to the B stars.

**[Penston \(1973\)](#)**: Fit of the [Johnson \(1963\)](#) ZAMS to the B stars. Revised by [Penston et al. \(1975\)](#).

**[Warren & Hesser \(1978\)](#)**: Stromgren photometry of B stars in the Orion Nebula.

**[Mermilliod \(1981\)](#)**: The well-cited comparison of open cluster color-magnitude diagrams and main sequences. No methodology or errors was listed for the Orion distance in particular but in general distances were from the fitting of the zero age main sequence.

- Genzel et al. (1981):** By observing H<sub>2</sub>O masers embedded within the BNKL objects, these authors were able to calculate a proper motion and a distance to this region.
- Anthony-Twarog (1982):** Revised Warren & Hesser (1978) estimate using a different H<sub>β</sub> calibration. Also used different combinations of sub-groups. In general, these distance estimates are 40-80 pc closer than the original Warren & Hesser findings.
- Walker (1983):** Found no radial velocity dependence on spectral type (in opposition to that found by Johnson (1965)) Slight revision to mean velocity dispersion relative to Johnson (1965) (higher).
- Jones & Walker (1988):** This was not a distance estimate to the Orion Nebula Cluster. These authors showed that 470 pc is a distance more consistent with the rejection of foreground objects via the proper motions distribution than a distance of 250 pc.
- Wolff (1990):** Used H<sub>γ</sub> and the Balmer discontinuity to determine T<sub>eff</sub>, surface gravity and the absolute bolometric magnitude of B stars in Orion. They derived distance estimates to all four OB associations in Orion.
- Brown et al. (1994):** Used VLUBW photometry and ZAMS fitting to derived distance to stars in each sub-region. Also compared the A<sub>V</sub> vs 100μm emission from IRAS to estimate a distance to the Orion A molecular cloud.

Table B–1. Summary of published distances to the Orion 1d association

Work Name	Date Pub.	Region <sup>(a)</sup> Desig.	Distance Modulus	Error	Method <sup>(b)</sup> Used	Number of Stars
Sharpless	1952	ONC	8.50	0.30	B Stars	?
Parenago	1954	ONC	8.00		Unknown	?
Johnson & Hiltner	1956	ONC	8.00		ZAMS	?
Strand	1958	ONC	8.60		PM / RV	6/135
Blaauw	1964	1d	8.00	0.10	ZAMS	?
Johnson	1965	1d	7.90		PM / RV	21
Walker	1969	1d	8.37	0.05	ZAMS	?
Penston	1973	1d	7.80	0.15	ZAMS	?
Penston et al	1975	ONC	8.10	0.13	ZAMS(1)	?
⋮	1975	ONC	7.71	0.21	ZAMS(2)	?
⋮	1975	ONC	7.98	0.12	ZAMS(3)	?
Warren & Hesser	1978	1d	8.40	0.53	B stars	?
⋮	1978	1d+1c*	8.28	0.50	B stars	?
Mermilliod	1981	?	8.20	0.15	ZAMS	?
Genzel et al	1981	BNKL	8.41	0.40	H2O Masers	
Anthony-Tworog	1982	1c	7.86	0.09	B stars	41
⋮	1982	1d+1c*	8.02	0.12	B stars	23
⋮	1982	1d+1c*	8.19	0.10	B stars	15
Wolff	1990	1c	7.70	0.50	B Stars	?
⋮	1990	1d	8.20	0.03	B Stars	2
Brown	1994	1c	8.00	0.49	VBLUW + $\log(g)/T_{eff}$	34
⋮	1994	1d	7.90	0.25	VBLUW + $\log(g)/T_{eff}$	3
⋮	1994	cloud	8.10	0.48	$A_V$ vs 100 $\mu$ m IRAS	...
de Zeeuw et al	1999	1c	8.52	0.25	Hipparcos	?

<sup>(a)</sup>Region corresponded to a variety of “samples.” These included the general Orion region, the Orion A Molecular Cloud, the Orion OB1 associations, the Orion OB1 sub-associations, e.g., 1c or 1d, and the Orion Nebula Cluster itself.

<sup>(b)</sup>Where possible the origin of the distance estimate is given. the listing of ‘B stars’ or to ‘ZAMS’ refers to comparison of observed quantities for these stars to theoretical or empirical estimates to derive distances. PM: proper motions; RV: radial velocities. Since PM and RV are given together, the number of stars used in each estimate is given in the Stars column.

## APPENDIX C SUMMARY OF POPULATION SYNTHESIS FORTRAN CODE

### C.1 FORTRAN Code

We detail the FORTRAN programs written for implementing the population synthesis algorithm for young stars and brown dwarfs. We provide the basic algorithm of the **lumfunc.f** control program and a short summary of any independent subroutines used, including any dependencies and the code's origin if it was scripted from an external source. The structure of input, batch and output files are listed in Section C.2.

The control program and subroutines were compiled into binaries on a desktop computer with an Intel 400 Mhz Pentium II central processor running RedHat Linux (version 6.0, kernel-2.2.16-3). Binaries were compiled using g77 (GNU project Fortran Compiler version(s) egcs-2.91.66 19990314/Linux (egcs-1.1.2 release) (from FSF-g77 version 0.5.24-19981002)) with the `-O3` optimization. On this same machine the program had a runtime of  $\sim 60$  sec (with writing to disk disabled) for 100 iterations of a cluster of 1000 stars.

#### C.1.1 The Control Program

The control program **lumfunc.f** was designed to produce from 1 to N simulations a synthetic cluster of stars using a single set of input parameters passed to it from an external ASCII file. It was also designed to yield a variety of stellar parameters as output. Further, to allow for multiple sets of inputs without having multiple input files, batch versions of the control program were written to allow some parameters to be issued from the command line rather than from an input file.

At the core of the control program algorithm is the random sampling of a series of probability distribution functions to obtain the fundamental (mass, age) or observational (extinction, excess) properties of the synthetic stars in the cluster. We sampled these

distributions using the Monte Carlo rejection method algorithm scripted into a series of logical rejection functions. The rejection method algorithm operates by simply selecting two random numbers from uniform distributions: an abscissa or the variable in question (let us say mass for example) and an ordinate or a “probability” that ranges between 0 and 1. Since the rejection method is simply the integration of the probability distribution function (it would be the initial mass function in this example), one simply must ask if the random ordinate (probability) lies above or below the probability distribution function (IMF) at the abscissa (mass). If it lies below, the abscissa is accepted as a valid mass; the program iterates until the full number of stars have been assigned values (masses).

The rejection functions written for our populations synthesis model simply return logical variables containing **TRUE** or **FALSE** if the random value is accepted or not according to the probability distribution function (PDFs). Rejection functions can sample either analytical PDFs, e.g, gaussian, or they can use normalized histograms that list the relative frequency as a function of the value (referred to as RELFREQs). The type of rejection function for each parameter (age, mass, extinction, excess) is hard-wired into the code, however, and to change the rejection function type, the user is required to edit and recompile the code. Each analytical rejection function is controlled by a set of parameters that are read in from the input file and passed to the rejection function. When the RELFREQ rejection function is used, the code loads and samples a relative frequency histogram contained in an external ASCII file and which can be crafted into any random shape required. We briefly document the steps used in the control program algorithm below and all of the rejection functions are summarized in Section [C.1.2](#).

1. Parameter Input. All relevant cluster parameters are read from an external input file that is passed to the code at the command line. In batch mode, variable parameters are read from screen, otherwise the program reads fixed parameters

from the ASCII file. The batch version of the control program is also adjusted to ignore those parameters which are read from screen.

2. **Parameter Documentation.** The input parameters are echoed to screen (screen echoing can be disabled) and then converted to string variables which will be written to the output file headers. This is one of the two locations in the program that must be manually changed by the user before compiling the binary. The user changes a documentation variable to indicate which rejection functions will be used. The user must also sets logical variables if any of the rejection functions are relative frequency distributions.
3. **Pre-iteration setup.** The program determines the initial seed for the random number generator, opens and reads external files documenting which evolutionary mass tracks to use, loads the theoretical zero age main sequence and bolometric correction tables, reads the files containing relative frequency distribution histograms (if needed) and converts the binary fraction and total number of cluster members into the number of binary systems and solitary stars in the final cluster. The output file is opened and the ASCII header written to it.
4. **Begin Iterations.** The program creates a single synthetic cluster per iteration, sequentially writing the derived cluster quantities to the output file.
5. **Monte Carlo Sampling.** Four parameters, the ages, masses, extinctions and K band excesses of the synthetic stars in the cluster are randomly sampled from probability distributions using Monte Carlo based rejection functions. This is the second location in the control program that must be adjusted by the user for each compiled binary since the rejection functions are hard-wired into the code. The user can select from a set of analytical rejection function which are adjusted by parameters in the input file. Alternately, the user can use a “Relative Frequency” rejection function (see RELFREQ below) which samples a changeable frequency histogram contained in an external ASCII file. Every star is assigned a mass

(and an IR excess if instituted), however, binaries are assigned the same age (and extinction) if necessary.

6. Creation of Isochrones. The program creates a theoretical isochrone at the age of *every* synthetic star by interpolating along the mass tracks of the evolutionary models. The program uses a cubic spline routine, interpolates as a function of log age, and treats the luminosity and effective temperature separately. One potential future improvement to the models is to implement a nearest neighbor, non-linear two dimensional spline to simultaneously derive these quantities.
7. Interpolation along the individual isochrones. For the mass of each star, the program interpolates along its calculated isochrone and between the known mass values given by the tracks. Again, this interpolation uses a cubic spline routine, interpolates as a function of log mass, and treats the luminosity and effective temperature separately. There are more significant potential advantages to implementing a nearest neighbor, non-linear 2D interpolation scheme because of the large separations of the mass tracks provided by the evolutionary models. Note that an input parameter is employed to set the maximum mass interpolated from the pre-main sequence evolutionary models. For higher masses, the luminosity and effective temperature are interpolated from the zero-age main sequence.
8. Conversion to Magnitudes. The luminosity of every synthetic star is first converted to an absolute bolometric magnitude and then to a passband magnitude using bolometric corrections interpolated as functions of effective temperature from look-up tables. Extinction is then added to the absolute magnitude as a function of the reddening law (a parameter in the input file), and an IR excess, in magnitudes, is subtracted at K band. The program then creates two arrays for each passband filter, using four of them to store the IJHK magnitudes of every star. The program then takes the passband magnitudes of individual members

of binary systems, converts them to passband flux, adds them, converts back to passband magnitudes and places these “un-resolved” magnitudes into the second four arrays. All the arrays are then shifted by the distance modulus.

9. Binning Luminosity Functions. Regardless of the type of output requested, the program bins both the single star arrays and the unresolved binary arrays into luminosity functions, according to the binning parameters listed in the input file.
10. Writing to Output File. For each iteration, the program writes to file whatever output data is requested. The output type is specified in the input file and can include tables of any of the star’s parameters calculated throughout the model run. The program then begins the next iteration as necessary. The program closes the output file after completing the last iteration.

### C.1.2 Rejection Functions

We describe each of the relevant rejection functions written for this code. For the analysis undertaken in this work, the IMF was exclusively sampled by the LOGNORMAL function for the experiments in Chapter 2 and by the POWERIMF for fitting data in Chapters 2, 3, 4 and 5. Since the star formation rate was always assumed constant, the SFH was sampled by the UNIFORM function. The extinction distribution functions (EPDF) and infrared excess distributions functions (IXPDF) used in fitting the KLFs of the Trapezium and IC 348 were empirical relative frequency distribution functions derived directly from the data and sampled with RELFREQ. We point out that nearly any probability distribution could be loaded and employed when using the RELFREQ rejection function, although the sampled function will only be as smooth as the size of the bins in the frequency histogram.

**UNIFORM.** Rejection function checks if a random abscissa lies between a minimum and maximum value.

**COEVAL.** Rejection function that always returns a true value. Initially used to derive coeval populations, a similar result can be obtained by using the UNIFORM

function and making the minimum age nearly identical (but NOT the exact same) as the maximum age.

**GAUSS.** Rejection function that tests a gaussian distribution. The function is sampled between two limits and can have up to six terms corresponding to a gaussian distribution plus a quadratic function, e.g.,

$$pdf(x) = p0 + (p1 \times x) + (p2 \times x^2) + (p3 \times \exp - (\frac{x - p4}{\sqrt{2} \times p5})^2) \quad (C.1)$$

where,  $p0$  is a constant term,  $p1$  is a linear term,  $p2$  is a quadratic term,  $p3$  is the normalization of the gaussian,  $p4$  is the mean of the gaussian, and  $p5$  is the width of the gaussian.

**LOGNORMAL.** Rejection function that tests a LOGNORMAL distribution as given in Equation 2.2.

**POWERIMF.** Rejection function that constructs a probability distribution function consisting of four power-laws connected at three break masses. All the segments are normalized together and the rejection function determines which power-law segment governs the random abscissa in question before testing the ordinate.

**RELFREQ.** Rejection function that uses a binned histogram containing the relative frequency of the abscissa. This normalized relative frequency histogram is searched to find which bin the abscissa would fall before testing the ordinate versus the relative probability of that bin. The only requirement is that the bins have equal widths and that the bin centers (in units of the abscissa) increase in value.

**NONEN.** Rejection function that always returns a true value. Used when disabling either the EPDF or IXPDF.

**OTHERS.** Ad hoc combinations of some of these rejection functions were written for testing and are in fact available in the code. These include: MSPOWER, a combination of a Miller-Scalo log-normal IMF, breaking at some mass and changing to

a power-law to the lowest masses; and SALIMF, a sampling of the Salpeter field star IMF over some mass range.

### C.1.3 The FORTRAN Sub-routines

Eleven additional sub-routines were employed in the population synthesis model. These include both newly written sub-routines to handle the loading of various external ASCII files and sub-routines borrowed from Numerical Recipes in Fortran; 2nd ed. Press et al. 1986. We list and summarize each of these sub-routines below.

**ext\_pms.f.** Small subroutine to open and read a simple ASCII file containing a single evolutionary mass track. Each mass track must be a four column array, where the first column is a running number, the second is the log of the age ( $\log \tau$ ), the third is the log of the luminosity in solar units ( $\log L/L_{\odot}$ ), and the fourth is the log of the effective surface temperature ( $\log T_{eff}$ ). Each mass track file must be sorted by increasing time and the user should note the maximum and minimum ages for each mass track. This extraction routine is used by lumfunc.f to read in each of the mass tracks.

**Called by: lumfunc.f; Requires: none**

**ext\_bck.f.** Small subroutine to open and read a simple ASCII file containing the two column bolometric correction table, where the first column is the log of  $T_{eff}$  and the second is the bolometric correction. Bolometric correction file must be sorted by increasing effective temperature. Called four times by lumfunc.f, once each for the four passbands used in the models.

**Called by: lumfunc.f; Requires: none**

**ext\_hist.f.** Subroutine to open and read a simple ASCII file containing a probability distribution function in histogram form that will act as a “Relative Frequency” rejection function for a Monte Carlo integration. The input histogram must have equally sized bins whose centers must increase in value. Subroutine normalizes the probability distribution, if necessary, and returns the bin centers, frequencies, and

limits of the resulting probability distribution function. Used by lumfunc.f when ever the "RELFREQ" Rejection Function is used to sample the IMF, SFH, Extinction or Infrared Excess distribution functions.

**Called by: lumfunc.f; Requires: none**

**spltime.f.** A simple wrapper subroutine to run the cubic spline interpolation routines when lumfunc.f is constructing isochrones from the pre-main sequence tracks at the age of each synthetic star. Splines each mass track (luminosity and effective temperature separately) vs log time ( $\log \tau$ ) to yield an isochrone. Hardwires the first derivative estimates used in the spline routine.

**Called by: lumfunc.f; Requires: spline.f, interp.f**

**splmass.f.** A simple wrapper subroutine to run the cubic spline interpolation routines on the individual isochrones constructed by spltime.f for each of the model stars. Splines each isochrone (luminosity and effective temperature separately) vs log mass ( $\log M$ ) for each individual model star. Hardwires the first derivative estimates used in the spline routine.

**Called by: lumfunc.f; Requires: spline.f, interp.f**

**spline.f.** Subroutine to calculate the second derivative at each point along an  $(x_{in}, y_{in})$  series for use in the cubic spline interpolation of this series. Requires boundary conditions in the form of first derivative estimates. These are hardwired in the wrapper routines (spltime, splmass) used by lumfunc.f. From Numerical Recipes in Fortran; 2nd ed. Press et al. 1986, pg 109.

**Called by: spltime.f, splmass.f; Requires: none**

**interp.f.** Subroutine to take an array of  $(x_{in}, y_{in})$  values and an array of the second derivative at each point and perform the cubic spline interpolation of  $y_{out}$  for an array of  $x_{out}$ . From From Numerical Recipes in Fortran; 2nd ed. Press et al. 1986, pg 110.

**Called by: spltime.f, splmass.f; Requires: none**

**splbck.f.** Subroutine to linearly interpolate on a table of bolometric corrections. Interpolation is performed as a function of the log of the surface temperature,  $\log T_{eff}$ . It interpolates all the model stars of an iteration at one time and is called by lumfunc.f four times (once for each of the four passbands) per iteration.

**Called by: lumfunc.f; Requires: locate.f.**

**mainseq.f.** Subroutine to linearly interpolate along the zero age main sequence. The interpolation is performed as a function of  $\log M$ . Is called if lumfunc.f determines that the mass of a specific model star falls outside (greater or less than) the mass range appropriate for the input pre-main sequence tracks. Note, this mass range is set by the user. This subroutine is run twice in lumfunc.f for each model star, once to interpolate luminosity as a function of  $\log M$ , and again to interpolate surface temperature as a function of  $\log M$ .

**Called by: lumfunc.f; Requires: locate.f.**

**locate.f.** Subroutine to search an ordered list and determine between which two elements and input value lies. Returns the subscript of the position in the list that is less than the input value. From Numerical Recipes in Fortran; 2nd ed. Press et al. 1986, pg 111.

**Called by: mainseq.f, splbck.f; Requires: none.**

**bin.f.** This simple subroutine converts a list of values into a binned distribution. It has three parameters: the binsize and the minimum (dmin) and maximum(dmax) of the sampling range. Bins are created between dmin and dmax and have centers whose value are  $(dmin + (n + \frac{1}{2}) \times binsize)$  and  $n = 1, 2, 3, \dots$ . Values are considered to fall into a specific bin if they are:

$$\left(\text{bin center} - \frac{\text{binsize}}{2}\right) \leq \text{value} < \left(\text{bin center} + \frac{\text{binsize}}{2}\right) \quad (\text{C.2})$$

The subroutine returns a list of bin centers and bin counts.

**Called by: lumfunc.f; Requires: none.**

## C.2 Input Parameters and Output Files

Model parameters were passed to the compiled binary using a simple ASCII input file. This input file contains 1-7 parameters per line and is fully commented. We detail this input file in figure(s) C-1, C-2, C-3 and C-4, breaking it into four parts and discussing any relevant details. When the program was setup to run in batch mode, simple scripts were written to echo those parameters that were being varied, while the remaining fixed inputs were read from a normal input file. We give an example of one line of a batch input in figure C-5.

Lastly, the output files from the population synthesis code consisted of simple ASCII text with informational headers. The results of individual iterations were listed sequentially in the output files and two example output file headers are given with explanation in figure C-6. A current deficiency of the code is that the individual luminosity function simulations cannot be processed and combined by the code into a single luminosity function (and accompanying statistical information, i.e., standard deviations) that can be directly compared to data. Such a procedure would permit smaller output files whose size currently depends upon the type of output chosen and the number of cluster iterations.

```

! *****
! INPUT FILE FOR LUMFUNC MODELING PROGRAM. VERSION: 06/29/2002. A.Muench (@UF)
! *****
! -----
! *****
! BASIC POPULATION PARAMETERS
! *****
! -----
! N_STARS  M_ITERS                               %% SAMPLING PARAMETERS. Max Nstars = 18000
! -----
! 00150    0100
! -----
! MAX_AGE  MIN_AGE                               %% IF COEVAL SFH, ENTER AGE AT MAX_AGE
! -----
! 03.50e+06  00.50e+06
! -----
! DM [m-M(mag)] BIN_FRAC [nbin/(nsing+nbin)]    %% BIN_FRAC < 1/N_STARS = NO BIN
! -----
! 08.00      0.00001
! -----
! AV_MIN  AV_MAX  NORM  <Av>  1SIG  OFFSET  LINEAR  QUAD  %% AV_PARAMS
! -----
! 00.000  03.000  01.00  00.30  00.3000  00.0000  00.0000  00.0000
! -----
! Ai/Av  Aj/Av  Ah/Av  Ak/Av                    %% REDDENING LAW [ = Cohen et al 81]
! -----
! 00.600  00.265  00.155  00.090
! -----
! IRX_MIN  IRX_MAX  NORM  <IRX>  1SIG  OFFSET  LINEAR  QUAD  %% IRX_PARAMS
! -----
! 00.250  50.000  01.00  09.75  02.6845  01.0417  -00.0615  00.0000
! -----
! *****
! IMF PARAMETERS.                               %% P1-P7 = SEVEN PARAMS DEPENDING ON IMF MODEL
! *****
! %% POWERIMF:  P1,P3,P5,P7 = SLOPES, P2,P4,P6 = MASS BREAK [Both linear mass]
! %% LOGNORMAL: P1-P2 = [MEAN, SIGMA]
! P1      P2      P3      P4      P5      P6      P7
! -----
! -2.25   00.820  -1.53   00.092  1.20   00.010  -1.00
! -----
! RANGE OF MASS TO SAMPLE IMF                    %% MUST FIX THE PMS MASS LIMITS BELOW
! IMF_MAX  IMF_MIN                               %% [log mass]
! -----
! 00.4000  -01.6000
! -----

```

Figure C–1: Model input file: basic cluster and IMF parameters. This subset of model parameters includes the number of stars in the cluster and the number of iterations to perform in addition to fixed cluster parameters such as distance, binary fraction, and reddening law. The parameters for functional forms of the cluster’s star formation history, IMF, extinction and excess distributions are listed and these parameters are interpreted differently depending upon the type of rejection function chosen in the compiled binary, or they are ignored if the code is set up to use relative frequency distributions which are listed as inputs in figure C–2. The important parameters, IMF MIN/MAX, specify the range of mass sampled in the functional form of the IMF.

```

! *****
! RELFREQ CALLS: MUST SET LOGICAL IN CODE. ALL FILE NAME LENGTHS LIMITED TO A80
! MUST SET PROPER NUMBER OF COMMENTS (SEE BOTTOM)
! *****
!-----
! IMF RELFREQ FILE.                                %% IMF PARAMS ABOVE IGNORED
!-----
/home/aamn/Models/Distributions/imf_hist.dat
!-----
! STAR FORMING HISTORY RELFREQ FILE.              %% SFH PARAMS ABOVE IGNORED
!-----
/home/aamn/Models/Distributions/sfh_hist.dat
!-----
! EXTINCTION DISTRIBUTION FUNCTION RELFREQ FILE.  %% AV_PARAMS ABOVE IGNORED
!-----
/home/aamn/Models/Distributions/EDF/Trap/trap.edf_lim.hist
!-----
! IXDF RELFREQ FILE. ASSUMED FOR K ONLY.          %% IRX_PARAMS ABOVE IGNORED
!-----
/home/aamn/Models/Distributions/trap.ixdf.hist
!-----
! NUMBER OF COMMENTS IN RELFREQ FILES.           %% INORDER: IMF,SFH,AV,IRX
!-----
00 00 32 20
!-----

```

Figure C–2: Model input file: relative frequency probability distribution files. These parameters are files containing binned histograms that describe the relative frequency of the given parameter (mass, age,  $A_V$  or IR excess). This histograms must have been created with equal sized bins with the bin center in the first column. The bin centers must be listed with positive increasing value but their values (given in the second column) need not be normalized. When RELFREQ distributions are used for a specific cluster parameter, for example, extinction, the other extinction parameters given in the input file are ignored.

```

!*****
! EVOLUTIONARY TRACK / BOLOMETRIC CORRECTIONS FILE POINTERS / PARAMETERS
!*****
!-----
! FILE CONTAINING CHARACTER NAMES OF MASS TRACKS. %% [MAXLEN OF FILENAME = A80]
!-----
/home/aamn/Models/PMS/BMDM/d2.5/char_mass
!-----
! FILE CONTAINING REAL MASSES OF EACH MASS TRACK. %% [MAXLEN OF FILENAME = A80]
!-----
/home/aamn/Models/PMS/BMDM/d2.5/real_mass
!-----
! PREFIX TO MASS TRACK FILE. %% [MAXLEN = A50]
!-----
/home/aamn/Models/PMS/BMDM/d2.5/Comp_
!-----
! SUFFIX TO MASS TRACK FILE. %% MASS TRACK FILE=PREFIX+CHAR_MASS[i]+SUFFIX
!-----
.25
!-----
! IJHK BOLOMETRIC CORRECTION FILES. %% (Teff,BC) LINEAR INTERP. [MAXLEN = A80]
!-----
/home/aamn/Models/BCS/bci_comp_4.dat
/home/aamn/Models/BCS/bcj_comp_4.dat
/home/aamn/Models/BCS/bch_comp_4.dat
/home/aamn/Models/BCS/bck_comp_4.dat
!-----
! MAIN SEQUENCE FILE. %% LOGMASS vs (L, Teff). LINEAR INTERP. [MAXLEN = A80]
!-----
/home/aamn/Models/PMS/MainSeq/mainseq_4
!-----
! RANGE OF MASS TO USE PMS MODELS. %% ABOVE PMS_MAX = MAIN_SEQUENCE
! PMS_MAX PMS_MIN %% REQ: PMS_MIN LE IMF_MIN. [log mass]
!-----
00.5000 -01.7000
!-----

```

Figure C–3: Model input file: pointers and parameters for evolutionary tracks. The evolutionary models, bolometric corrections and theoretical main sequence are all stored in separate ASCII files. For example in the case of the evolutionary models, individual ASCII files exist for individual mass tracks. This set of parameters and pointers are used when opening and reading in these evolutionary files while the code is running. Further, since there are an unknown number of evolutionary tracks, each corresponding to a specific mass object, the code is passed lists of the individual masses that it uses in both opening the files and in the interpolation of the tracks. An important parameter is the PMS MIN/MAX parameters which set the range of the tracks to use relative to the range of masses sampled from the IMF. The user is required to ensure that the IMF is not sampled less than the minimum mass of the evolutionary models, else interpolation will fail. For masses greater than PMS MAX, the code interpolates along the theoretical zero-age main sequence.

```

!*****
! OUTPUT PARAMETERS
!*****
!-----
! OUTPUT TYPE.                                %% SEE README or CODE HEADER
!-----
JHKLf
!-----
! BIN_SIZE  BIN_MIN  BIN_MAX                    %% OUTPUT LUMFUNC BINNING PARAMETERS
!-----
! 00.500    03.250   21.250
!-----
! OUTPUT FILE.                                %% [MAXLEN = A80]
!-----
/home/aamn/Models/Data/example.dat
!-----
! SCREEN INFORMATION TURNS OFF/ON SCREEN WRITING INFORMATION.
!-----
ON
!-----
! EXPERIMENT RUN TITLE OR OTHER INFO.          %% [MAXLEN = A50]
!-----
Example of Input File
!-----
!*****
! USER NAME OR OTHER USER INFO                %% MAXLEN + A50
!*****
! A. Muench (@UF)
!-----
!

```

Figure C–4: Model input file: output parameters. The ASCII output files can contain a variety of physical or observable cluster properties depending upon the setting of the OUTPUT TYPE parameter. All iterations are written sequentially to the OUTPUT FILE, while other comments, titles or username are also added to the output file. If screen writing is enabled, all input parameters are echoed to screen.

Example of one line of batch file input to luminosity function modeling:

```
echo -e " -2.30 10.00 -2.30 01.00 -2.30 00.10 -2.30\n
          2.00e+06 1.00e+06\n
          10.88 0.40\n
          /home/aamn/Models/Data/Fits/NGC2362/ngc2362.T02.DT2.all_lf\n
          /home/aamn/Models/IFiles/lf_batch_age_imf.param" |
          /home/aamn/Models/lumfunc_batch_age_imf_v0
```

which translates into:

```
echo -e " The seven IMF parameters \n
          Maximum and Minimum Ages \n
          Distance Modulus and Binary Fraction \n
          Output Filename \n
          Input Filename containing other static parameters |
          binary file
```

Figure C–5: Example batch file. The control program **lumfunc.f** was modified to accept certain parameters echoed to the command line from scripts while operating in batch mode. In this example, the parameters of a four segment power-law IMF, the star forming history, the distance, the binary frequency and the output file are all being varied in batch mode. The other parameters are fixed and listed in a normal input file. Echoed variables are listed but ignored in the input file in batch mode.

Example 1: No Extinction or Excess used, although parameters listed.  
JHK LFs are the output.

```
# Output from lumfunc.f FORTRAN program
#
# Last written:      20:43:24
# On date of:       6/29/2002
# By user:          A. Muench (@UF)
# Run title:        Example of Output File
#
# FUNCTIONS: imf[POWERIMF] sfh[UNIFORM] av[NONEN] irex[NONEN]
# GENPARAMS: N: 150 M: 100 DM: 8.0000
# BINPARAMS: Nsing: 150 Nbin: 0 Nsystem: 150
# SFHPARAMS: Min Age: 0.50E+06 Max Age: 0.35E+07
# IMFPARAMS:  -2.250000  0.820000  -1.530000  0.092000  1.200000  0.010000
# AVPARAMS :   0.000  3.000  1.000  0.300  0.300  0.00000  0.00000  0.00000
# IXPARAMS :   0.250 50.000  1.000  9.750  2.684  1.04170 -0.06150  0.00000
# DATAFILE :  JHKLF      /home/aamn/Models/Data/example.dat
```

Example 2: Extinction and Excess histograms were used. Binary fraction was  
non-negligible. Output included masses, ages, luminosities and  
effective temperatures.

```
# Output from lumfunc.f FORTRAN program
#
# Last written:      2:22:59
# On date of:       5/16/2002
# By user:          A. Muench (@UF)
# Run title:        Testing IMF
#
# FUNCTIONS: imf[POWERIMF] sfh[UNIFORM] av[RELFREQ] irex[RELFREQ]
# GENPARAMS: N: 1000 M: 50 DM: 10.9000
# BINPARAMS: Nsing: 818 Nbin: 91 Nsystem: 909
# SFHPARAMS: Min Age: 0.25E+07 Max Age: 0.35E+07
# IMFPARAMS:  -2.350000  0.100000  -1.000000  0.020000  -1.000000  0.010000
# AVPARAMS : hist file: /home/aamn/Models/Distributions/EDF/Trap/trap.edf.hist
# IXPARAMS : hist file: /home/aamn/Models/Distributions/trap.ixdf.hist
# DATAFILE :  MSAGE_LT  /home/aamn/Models/Data/check_imf.dat
```

Figure C–6: Example(s) of output file headers. The program writes simple ASCII file containing the sequentially listed output from each sampling iteration of a model run. Simple headers containing relevant information are appended to the beginning of each output file. Two example headers are given, containing very different sets of input parameters.

## REFERENCES

- Adams, F. C. & Fatuzzo, M. 1996, *ApJ*, 464, 256
- Adams, J. D., Stauffer, J. R., Monet, D. G., Skrutskie, M. F., & Beichman, C. A. 2001, *AJ*, 121, 2053
- Alexander, D. R., Augason, G. C., & Johnson, H. R. 1989, *ApJ*, 345, 1014
- Alexander, D. R. & Ferguson, J. W. 1994, *ApJ*, 437, 879
- Ali, B. & Depoy, D. L. 1995, *AJ*, 109, 709
- Allard, F., Hauschildt, P. H., Alexander, D. R., Tamanai, A., & Schweitzer, A. 2001, *ApJ*, 556, 357
- Aller, L. H., Appenzeller, I., Baschek, B., Duerbeck, H. W., Herczeg, T., Lamla, E., Meyer-Hofmeister, E., Schmidt-Kaler, T., Scholz, M., Seggewiss, W., Seitter, W. C., & Weidemann, V., eds. 1982, *Landolt-Börnstein: Numerical Data and Functional Relationships in Science and Technology - New Series* "Gruppe/Group 6 Astronomy and Astrophysics" Volume 2 Schaifers/Voigt: Astronomy and Astrophysics / Astronomie und Astrophysik "Stars and Star Clusters / Sterne und Sternhaufen
- Alves, J. ., Lada, C. J., & Lada, E. A. 1999, *ApJ*, 515, 265
- Alves, J. ., Lada, C. J., Lada, E. A., Kenyon, S. J., & Phelps, R. 1998, *ApJ*, 506, 292
- Alves, J. ., Lada, C. J., Lada, E. A., & Muench, A. A. 2001, *A&A*
- Anthony-Twarog, B. J. 1982, *AJ*, 87, 1213
- Béjar, V. J. S., Martín, E. L., Zapatero Osorio, M. R., Rebolo, R., Barrado y Navascués, D., Bailer-Jones, C. A. L., Mundt, R., Baraffe, I., Chabrier, C., & Allard, F. 2001, *ApJ*, 556, 830
- Bachiller, R. & Cernicharo, J. 1986, *A&A*, 166, 283
- Bally, J., O'Dell, C. R., & McCaughrean, M. J. 2000, *AJ*, 119, 2919
- Balona, L. A. & Laney, C. D. 1996, *MNRAS*, 281, 1341
- Baraffe, I., Chabrier, G., Allard, F., & Hauschildt, P. H. 1998, *A&A*, 337, 403
- . 2002, *A&A*, 382, 563

- Barrado y Navascués, D., Zapatero Osorio, M. R., Béjar, V. J. S., Rebolo, R., Martín, E. L., Mundt, R., & Bailer-Jones, C. A. L. 2001, *A&A*, 377, L9
- Baume, G., Vázquez, R. A., & Feinstein, A. 1999, *A&AS*, 137, 233
- Belikov, A. N., Hirte, S., Meusinger, H., Piskunov, A. E., & Schilbach, E. 1998, *A&A*, 332, 575
- Belikov, A. N. & Piskunov, A. E. 1997, *Astronomy Reports*, 41, 28
- Bernasconi, P. A. 1996, *A&AS*, 120, 57
- Bernasconi, P. A. & Maeder, A. 1996, *A&A*, 307, 829
- Berriman, G., Reid, N., & Leggett, S. K. 1992, *ApJ*, 392, L31
- Bertin, E. & Arnouts, S. 1996, *A&AS*, 117, 393
- Bessell, M. S. 1991, *AJ*, 101, 662
- Bessell, M. S. 1995, in *The Bottom of the Main Sequence – and Beyond*, Proceedings of the ESO Workshop Held in Garching, Germany, 10-12 August 1994., ed. C. G. Tinney, ESO Astrophysics Symposia (Berlin Heidelberg New York: Springer-Verlag), 123
- Bessell, M. S. & Brett, J. M. 1988, *PASP*, 100, 1134
- Bessell, M. S., Castelli, F., & Plez, B. 1998, *A&A*, 333, 231
- Blaauw, A. 1964, *ARA&A*, 2, 213
- Bonnell, I. A., Bate, M. R., Clarke, C. J., & Pringle, J. E. 2001, *MNRAS*, 323, 785
- Borgman, J. & Blaauw, A. 1964, *Bull. Astron. Inst. Netherlands*, 17, 358
- Boulard, M.-H., Caux, E., Monin, J.-L., Nadeau, D., & Rowlands, N. 1995, *A&A*, 300, 276
- Bouvier, J., Stauffer, J. R., Martin, E. L., Barrado y Navascues, D., Wallace, B., & Bejar, V. J. S. 1998, *A&A*, 336, 490
- Brandl, B., Brandner, W., Eisenhauer, F., Moffat, A. F. J., Palla, F., & Zinnecker, H. 1999, *A&A*, 352, L69
- Bromm, V., Coppi, P. S., & Larson, R. B. 2002, *ApJ*, 564, 23
- Brown, A. G. A., de Geus, E. J., & de Zeeuw, P. T. 1994, *A&A*, 289, 101
- Burrows, A., Hubbard, W. B., Saumon, D., & Lunine, J. I. 1993, *ApJ*, 406, 158
- Burrows, A., Marley, M., Hubbard, W. B., Lunine, J. I., Guillot, T., Saumon, D., Freedman, R., Sudarsky, D., & Sharp, C. 1997, *ApJ*, 491, 856

- Canuto, V. M., Goldman, I., & Mazzitelli, I. 1996, *ApJ*, 473, 550
- Canuto, V. M. & Mazzitelli, I. 1991, *ApJ*, 370, 295
- . 1992, *ApJ*, 389, 724
- Carpenter, J. M. 2000, *AJ*, 120, 3139
- Carpenter, J. M., Hillenbrand, L. A., & Skrutskie, M. F. 2001, *AJ*, 121, 3160
- Chabrier, G. 2001, *ApJ*, 554, 1274
- . 2002, *ApJ*, 567, 304
- Chabrier, G., Baraffe, I., Allard, F., & Hauschildt, P. 2000, *ApJ*, 542, 464
- Cohen, J. G., Persson, S. E., Elias, J. H., & Frogel, J. A. 1981, *ApJ*, 249, 481
- Comerón, F., Neuhäuser, R., & Kaas, A. A. 2000, *A&A*, 359, 269
- Comerón, F., Rieke, G. H., & Rieke, M. J. 1996, *ApJ*, 473, 294
- Cushing, M. C., Tokunaga, A. T., & Kobayashi, N. 2000, *AJ*, 119, 3019
- D'Antona, F. 1998, in *ASP Conf. Ser. 142: The Stellar Initial Mass Function (38th Herstmonceux Conference)*, ed. G. Gilmore & D. Howell, 157
- D'Antona, F. & Mazzitelli, I. 1994, *ApJS*, 90, 467
- . 1997, *Memorie della Societa Astronomica Italiana*, 68, 807
- de Zeeuw, P. T., Hoogerwerf, R., de Bruijne, J. H. J., Brown, A. G. A., & Blaauw, A. 1999, *AJ*, 117, 354
- Duchêne, G., Bouvier, J., & Simon, T. 1999, *A&A*, 343, 831
- Duquennoy, A. & Mayor, M. 1991, *A&A*, 248, 485
- Eddington, A. S. 1924, *MNRAS*, 84, 308
- Elias, J. H., Frogel, J. A., Matthews, K., & Neugebauer, G. 1982, *AJ*, 87, 1029
- Elmegreen, B. G. 1997, *ApJ*, 486, 944
- Elmegreen, B. G. & Mathieu, R. D. 1983, *MNRAS*, 203, 305
- Elston, R. 1998, in *Proc. SPIE Vol. 3354, p. 404-413, Infrared Astronomical Instrumentation*, Albert M. Fowler; Ed., Vol. 3354, 404-413
- Evans, N. J., Allen, L. E., Blake, G. A., Harvey, P. M., Koerner, D. W., Mundy, L. G., Myers, P. C., Padgett, D. L., Sargent, A. I., Stapelfeldt, K., & van Dishoeck, E. F. 2001, *American Astronomical Society Meeting*, 198, 0

- Figer, D. F., Kim, S. S., Morris, M., Serabyn, E., Rich, R. M., & McLean, I. S. 1999, *ApJ*, 525, 750
- Fletcher, A. B. & Stahler, S. W. 1994a, *ApJ*, 435, 313
- . 1994b, *ApJ*, 435, 329
- Flower, P. J. 1996, *ApJ*, 469, 355
- Frerking, M. A., Langer, W. D., & Wilson, R. W. 1982, *ApJ*, 262, 590
- Fruchter, A. S. & Hook, R. N. 2002, *PASP*, 114, 144
- Genzel, R., Reid, M. J., Moran, J. M., & Downes, D. 1981, *ApJ*, 244, 884
- Goldsmith, P. F., Bergin, E. A., & Lis, D. C. 1997, *ApJ*, 491, 615
- Graham, J. R., Matthews, K., Greenstein, J. L., Neugebauer, G., Tinney, C. G., & Persson, S. E. 1992, *AJ*, 104, 2016
- Haisch, K. E., Lada, E. A., & Lada, C. J. 2001a, *AJ*, 121, 2065
- . 2001b, *ApJ*, 553, L153
- Hambly, N. C., Hodgkin, S. T., Cossburn, M. R., & Jameson, R. F. 1999, *MNRAS*, 303, 835
- Hartmann, L. 2001, *AJ*, 121, 1030
- Hauschildt, P. H., Allard, F., & Baron, E. 1999, *ApJ*, 512, 377
- Hayashi, C. 1961, *PASJ*, 13, 450
- Henry, L. G., Lelevier, R., & Levée, R. D. 1955, *PASP*, 67, 154
- Herbig, G. H. 1998, *ApJ*, 497, 736
- Herbst, W., Maley, J. A., & Williams, E. C. 2000, *AJ*, 120, 349
- Herbst, W. & Miller, D. P. 1982, *AJ*
- Hillenbrand, L. A. 1995, PhD thesis, University of Massachusetts Amherst
- . 1997, *AJ*, 113, 1733
- Hillenbrand, L. A. & Carpenter, J. M. 2000, *ApJ*, 540, 236
- Hillenbrand, L. A. & Hartmann, L. W. 1998, *ApJ*, 492, 540
- Hillenbrand, L. A., Strom, S. E., Calvet, N., Merrill, K. M., Gatley, I., Makidon, R. B., Meyer, M. R., & Skrutskie, M. F. 1998, *AJ*, 116, 1816
- Iben, I. J. 1965, *ApJ*, 141, 993

- Jameson, R. F. 2002, in IAU Symp. 211: Brown Dwarfs, ed. E. Martín (San Francisco: Astronomical Society of the Pacific)
- Johnson, H. L. 1950, *ApJ*, 112, 240
- , ed. K. A. Strand (Chicago: University of Chicago Press), 225
- , 1966, *ARA&A*, 4, 193
- Johnson, H. L. & Hiltner, W. A. 1956, *ApJ*, 123, 267
- Johnson, H. L. & Morgan, W. W. 1953, *ApJ*, 117, 313
- Johnson, H. M. 1965, *ApJ*, 142, 964
- Jones, B. F. & Walker, M. F. 1988, *AJ*, 95, 1755
- Jones, H. R. A., Longmore, A. J., Jameson, R. F., & Mountain, C. M. 1994, *MNRAS*, 267, 413
- Kenyon, S. J. & Hartmann, L. 1995, *ApJS*, 101, 117
- Kenyon, S. J. & Hartmann, L. W. 1990, *ApJ*, 349, 197
- Kirkpatrick, J. D., Kelly, D. M., Rieke, G. H., Liebert, J., Allard, F., & Wehrse, R. 1993, *ApJ*, 402, 643
- Kirkpatrick, J. D., Reid, I. N., Liebert, J., Cutri, R. M., Nelson, B., Beichman, C. A., Dahn, C. C., Monet, D. G., Gizis, J. E., & Skrutskie, M. F. 1999, *ApJ*, 519, 802
- Kirkpatrick, J. D., Reid, I. N., Liebert, J., Gizis, J. E., Burgasser, A. J., Monet, D. G., Dahn, C. C., Nelson, B., & Williams, R. J. 2000, *AJ*, 120, 447
- Klessen, R. S. 2001, *ApJ*, 556, 837
- Kroupa, P. 2001, *MNRAS*, 322, 231
- , 2002, *Science*, 295, 82
- Kroupa, P., Aarseth, S., & Hurley, J. 2001, *MNRAS*, 321, 699
- Kroupa, P., Gilmore, G., & Tout, C. A. 1991, *MNRAS*, 251, 293
- Kroupa, P. & Tout, C. A. 1997, *MNRAS*, 287, 402
- Kroupa, P., Tout, C. A., & Gilmore, G. 1990, *MNRAS*, 244, 76
- , 1993, *MNRAS*, 262, 545
- Lada, C. J. & Adams, F. C. 1992, *ApJ*, 393, 278
- Lada, C. J., Alves, J., & Lada, E. A. 1996, *AJ*, 111, 1964

- Lada, C. J., Muench, A. A., Haisch, K. E., Lada, E. A., Alves, J. ., Tollestrup, E. V., & Willner, S. P. 2000, *AJ*, 120, 3162
- Lada, E. A. 1990, PhD thesis, University of Texas Austin
- Lada, E. A., Evans, N. J., Depoy, D. L., & Gatley, I. 1991, *ApJ*, 371, 171
- Lada, E. A. & Lada, C. J. 1995, *AJ*, 109, 1682
- Leggett, S. K. 1992, *ApJS*, 82, 351
- Leggett, S. K., Allard, F., Berriman, G., & Dahn, C. C. and Hauschildt, P. H. 1996, *ApJS*, 104, 117
- Low, C. & Lynden-Bell, D. 1976, *MNRAS*, 176, 367
- Lucas, P. W. & Roche, P. F. 2000, *MNRAS*, 314, 858
- Lucas, P. W., Roche, P. F., Allard, F., & Hauschildt, P. H. 2001, *MNRAS*, 326, 695
- Luhman, K. L. 1999, *ApJ*, 525, 466
- . 2000, *ApJ*, 544, 1044
- Luhman, K. L. & Rieke, G. H. 1999, *ApJ*, 525, 440
- Luhman, K. L., Rieke, G. H., Lada, C. J., & Lada, E. A. 1998, *ApJ*, 508, 347
- Luhman, K. L., Rieke, G. H., Young, E. T., Cotera, A. S., Chen, H., Rieke, M. J., Schneider, G., & Thompson, R. I. 2000, *ApJ*, 540, 1016
- Marconi, M. & Palla, F. 1998, *ApJ*, 507, L141
- Marcy, G. W. & Butler, R. P. 1998, *ARA&A*, 36, 57
- McCaughrean, M., Zinnecker, H., Rayner, J., & Stauffer, J. 1995, in *The Bottom of the Main Sequence - and Beyond*, Proceedings of the ESO Workshop Held in Garching, Germany, 10-12 August 1994., ed. C. G. Tinney, ESO Astrophysics Symposia (Berlin Heidelberg New York: Springer-Verlag), 209
- McCaughrean, M. J., Rayner, J. T., & Zinnecker, H. 1994, *ApJ*, 436, L189
- McCaughrean, M. J. & Stauffer, J. R. 1994, *AJ*, 108, 1382
- Megeath, S. T. 1996, *A&A*, 311, 135
- Mermilliod, J. C. 1981, *A&AS*, 44, 467
- Meyer, M. R. 1996, PhD thesis, University of Massachusetts Amherst

- Meyer, M. R., Adams, F. C., Hillenbrand, L. A., Carpenter, J. M., & Larson, R. B. 2000, in *Protostars and Planets IV*, ed. V. Mannings, A. P. Boss, & S. S. Russell (Tucson: University of Arizona Press), 121
- Meyer, M. R., Calvet, N., & Hillenbrand, L. A. 1997, *AJ*, 114, 288
- Mihalas, D., Dappen, W., & Hummer, D. G. 1988, *ApJ*, 331, 815
- Miller, G. E. & Scalo, J. M. 1979, *ApJS*, 41, 513
- Minkowski, R. 1946, *PASP*, 58, 356
- Moitinho, A., Alves, J., Huélamo, N., & Lada, C. J. 2001, *ApJ*, 563, L73
- Muench, A. A., Alves, J. ., Lada, C. J., & Lada, E. A. 2001, *ApJ*, 558, L51
- Muench, A. A., Lada, E. A., & Lada, C. J. 2000, *ApJ*, 533, 358
- Muench, A. A., Lada, E. A., Lada, C. J., & Alves, J. . 2002, *ApJ*, 573, 366
- Muzerolle, J., Briceño, C., Calvet, N., Hartmann, L., Hillenbrand, L., & Gullbring, E. 2000, *ApJ*, 545, L141
- Muzerolle, J., Hartmann, L., & Calvet, N. 1998, *AJ*, 116, 2965
- Najita, J. R., Tiede, G. P., & Carr, J. S. 2000, *ApJ*, 541, 977
- Natta, A. & Testi, L. 2001, *A&A*, 376, L22
- O'dell, C. R. & Wong, K. 1996, *AJ*, 111, 846
- Palla, F., Salpeter, E. E., & Stahler, S. W. 1983, *ApJ*, 271, 632
- Palla, F. & Stahler, S. W. 1990, *ApJ*, 360, L47
- . 1993, *ApJ*, 418, 414
- . 1999, *ApJ*, 525, 772
- . 2000, *ApJ*, 540, 255
- Parento, P. P. 1954, *Trudy Gosudarstvennogo Astronomicheskogo Instituta*, 25, 1
- Paresce, F. & De Marchi, G. 2000, *ApJ*, 534, 870
- Parker, J. W. 1991, *PASP*, 103, 243
- Patience, J., Ghez, A. M., Reid, I. N., & Matthews, K. 2002, *AJ*, 123, 1570
- Penston, M. V. 1973, *ApJ*, 183, 505
- Penston, M. V., Hunter, J. K., & O'Neill, A. 1975, *MNRAS*, 171, 219

- Persson, S. E., Murphy, D. C., Krzeminski, W., Roth, M., & Rieke, M. J. 1998, *AJ*, 116, 2475
- Phelps, R. L. & Janes, K. A. 1993, *AJ*, 106, 1870
- Pols, O. R., Tout, C. A., Eggleton, P. P., & Han, Z. 1995, *MNRAS*, 274, 964
- Preibisch, T., Balega, Y., Hofmann, K., Weigelt, G., & Zinnecker, H. 1999, *New Astronomy*, 4, 531
- Preibisch, T., Zinnecker, H., & Herbig, G. H. 1996, *A&A*, 310, 456
- Rebull, L. M. 2001, *AJ*, 121, 1676
- Reid, I. N., Kirkpatrick, J. D., Liebert, J., Burrows, A., Gizis, J. E., Burgasser, A., Dahn, C. C., Monet, D., Cutri, R., Beichman, C. A., & Skrutskie, M. 1999, *ApJ*, 521, 613
- Reipurth, B. & Clarke, C. 2001, *AJ*, 122, 432
- Reipurth, B. & Zinnecker, H. 1993, *A&A*, 278, 81
- Ripepi, V., Palla, F., Marconi, M., Bernabei, S., Arellano Ferro, A., Terranegra, L., & Alcalá, J. M. 2002, in 7 pages, including 7 postscript figures, accepted for publication on *A&A*, 6115
- Rogers, F. J. & Iglesias, C. A. 1992, *ApJS*, 79, 507
- Rogers, F. J., Swenson, F. J., & Iglesias, C. A. 1996, *ApJ*, 456, 902
- Salpeter, E. E. 1955, *ApJ*, 121, 161
- Saumon, D. & Chabrier, G. 1991, *Phys. Rev. A*, 44, 5122
- . 1992, *Phys. Rev. A*, 46, 2084
- Saumon, D., Chabrier, G., & van Horn, H. M. 1995, *ApJS*, 99, 713
- Scalo, J. 1998, in *ASP Conf. Ser. 142: The Stellar Initial Mass Function (38th Herstmonceux Conference)*, ed. G. Gilmore & D. Howell, 201
- Scalo, J. M. 1986, *Fundamentals of Cosmic Physics*, 11, 1
- Schaller, G., Schaerer, D., Meynet, G., & Maeder, A. 1992, *A&AS*, 96, 269
- Scholz, R.-D., Brunzendorf, J., Ivanov, G., Kharchenko, N., Lasker, B., Meusinger, H., Preibisch, T., Schilbach, E., & Zinnecker, H. 1999, *A&AS*, 137, 305
- Sharpless, S. 1952, *ApJ*, 116, 251
- . 1954, *ApJ*, 119, 200

- . 1962, *ApJ*, 136, 767
- Shu, F. H., Adams, F. C., & Lizano, S. 1987, *ARA&A*, 25, 23
- Siess, L., Dufour, E., & Forestini, M. 2000, *A&A*, 358, 593
- Stahler, S. W. 1983, *ApJ*, 274, 822
- Stetson, P. B. 1987, *PASP*, 99, 191
- Stickland, D. J., Lloyd, C., & Sweet, I. 1998, *The Observatory*, 118, 7
- Strand, K. A. 1958, *ApJ*, 128, 14
- Strom, K. M., Strom, S. E., & Merrill, K. M. 1993, *ApJ*, 412, 233
- Strom, S. E., Strom, K. A., & Carrasco, L. 1974, *PASP*, 86, 798
- Tinney, C. G., Mould, J. R., & Reid, I. N. 1993, *AJ*, 105, 1045
- Trumpler, R. J. 1931, *PASP*, 43, 255
- Vacca, W. D., Garmany, C. D., & Shull, J. M. 1996, *ApJ*, 460, 914
- van Leeuwen, F. & van Genderen, A. M. 1997, *A&A*, 327, 1070
- Walker, M. F. 1969, *ApJ*, 155, 447
- . 1983, *ApJ*, 271, 642
- Walter, F. M., Wolk, S. J., Freyberg, M., & Schmitt, J. H. M. M. 1997, *Memorie della Societa Astronomica Italiana*, 68, 1081
- Warren, W. H. & Hesser, J. E. 1978, *ApJS*, 36, 497
- Wilking, B. A., Greene, T. P., & Meyer, M. R. 1999, *AJ*, 117, 469
- Wilner, D. J. & Lada, C. J. 1991, *AJ*, 102, 1050
- Winkler, H. 1997, *MNRAS*, 287, 481
- Wolff, S. C. 1990, *AJ*, 100, 1994
- Wood, D. O. S., Myers, P. C., & Daugherty, D. A. 1994, *ApJS*, 95, 457
- Yoneyama, T. 1972, *PASJ*, 24, 87
- Zinnecker, H. 1984, *MNRAS*, 210, 43
- Zinnecker, H., McCaughrean, M. J., & Wilking, B. A. 1993, in *Protostars and Planets III*, ed. E. H. Levy & J. I. Lunine (Tucson: The University of Arizona Press), 429–495

## BIOGRAPHICAL SKETCH

August was born in the city of Tampa in the state of Florida during August of 1973 to Elizabeth Ealer and August Albert Muench, Jr. He spent most of his current life in the tiny, tomato-infested town of Ruskin on the eastern shores of Tampa Bay where he attended East Bay High School by some natural twist of Florida fate. Two astronomical high points during this period are worth noting. The first was his memory of staring into the steamy, scintillating Florida sky trying in vain to see Halley's Comet in 1986. The second was respectfully telling his father that he had purchased, as a wonderful gift for his sons, the wrong kind of telescope.

In September 1991, August began as an undergraduate at the Georgia Institute of Technology in Atlanta, Georgia. Despite the good intention of attending this school to become a chemical engineer and to actually begin to earn a decent salary by the age of 23, August instead became disenchanted by the probabilistic nature of the equations used to determine reaction rates for various chemical processes. Seeking a higher standard of precision, he shifted his studies to those of Physics although it seems likely at the  $2\sigma$  level that during this paradigm shift his subconscious was shifting toward the opposite end of the precision scale. That being toward astronomy.

After four years in Atlanta, August was admitted under generous pretexts to the master's program of the Department of Astronomy at the University of Florida. Roughly two years later, after another paradigm shift from observational cosmology to infrared star and planet formation and being admitted to the doctoral program as a graduate student working with Dr. Elizabeth Lada, he departed Gainesville to begin as a Smithsonian Predoctoral Fellow at the Harvard-Smithsonian Center for Astrophysics (CfA) in Cambridge, Massachusetts where he worked with Dr. Charles Lada. Thus, the

CfA was where August spent three years enjoying the pedestrian (only in the best way) city of Boston, living in various attics in Somerville, and enjoying the hearty winters.

After finishing this fellowship but not sadly his dissertation, he left Boston to return to Gainesville (i.e., Florida) while his fiancée' Laura Nasrallah also left Harvard and Cambridge to begin as an assistant professor in Religious Studies at Occidental College in Los Angeles (i.e., California). A bit less than a year later, Laura and August were married in Baltimore, Maryland and after a trip to Tuscany they became Muench-Nasrallah via the progressive courts of Gainesville. The last year of his dissertation was spent with alternating periods working from their home in LA and long stretches spent in Gainesville. After the defense of this dissertation, August will begin a post-doctoral research position at the Space InfraRed Telescope Facility (SIRTF) Science Center in Pasadena, California.